UNIVERSITY OF SOUTHAMPTON

Faculty of Engineering, Science and Mathematics

Optoelectronics Research Centre

Optical properties of long photonic crystal fibre tapers

by

Natasha Vukovic

A thesis submitted for the degree of
Doctor of Philosophy

March 2010

UNIVERSITY OF SOUTHAMPTON

ABSTRACT

FACULTY OF ENGINEERING, SCIENCE AND MATHEMATICS
OPTOELECTRONICS RESEARCH CENTRE

Doctor of Philosophy

Optical properties of long photonic crystal fibre tapers

by Natasha Vukovic

In this thesis I investigate optical properties of metre - long tapers. Microstructured optical fibre technology has created new opportunities in a broad range of science and technology. In the work presented in this thesis I have combined the microstructured optical fibre technology with a novel tapering facility in order to develop new applications in the field of nonlinear optics.

This thesis concerns development of a novel tapering facility, capable of achieving intermediate length (few tens of cm to ≈10 m) tapers. In comparison with systems presented to date, the novel system has the advantage of the increased control over the desired taper profile and enables efficient fabrication of intermediate taper lengths of potentially arbitrary profiles. During the fabrication the fibre diameter exhibits significant variations, due to various disturbances. A design of the feedback loop for the enhanced control of the output diameter variation is proposed. The system capabilities have been tested and demonstrated in many different examples. The presented results show that the variation of the fibre diameter is within ≈1%, which offers possibilities to use the system in various applications.

As an example of the intermediate taper length design and application, parabolic pulse generation was investigated. It represents a very attractive pulse shape, since it can propagate at high peak powers while avoiding wave-breaking effect and have a flat and broad spectrum, which could lead to pulse compression applications. This thesis presents numerical modelling and experimental results (restricted to a set of parameters of fibres available from 'stock') concerning this phenomena.

Supercontinuum generation is an area of research that has been attracting scientific interest over several decades. This thesis shows results of a study of supercontinuum generation in intermediate length tapered microstructured optical fibres. A simulation tool has been developed and the procedure to efficiently determine optimum conditions for improving flatness of the supercontinuum spectra has been proposed. The proposed method concerns a 'standard' microstructured optical fibre, but generally can be extended to different fibre designs.

Contents

List of Figures

List of Tables

Acronyms

CL	confinement loss
DS	dispersion slope
ERGO	Erbium glass oscillator
FEM	finite element method
FROG	frequency resolved optical gating
FWHM	full width at half maximum
GNLSE	generalized nonlinear Schrödinger equation
GVD	group velocity dispersion
HF	holey fibre
HP-EDFA	high power Erbium doped fibre amplifier
IG	index guidance
l-FROG	linear frequency resolved optical gating
LMA	large mode area
MOF	microstructured optical fibre
MT	meso taper
NLSE	nonlinear Schrödinger equation
OSA	optical spectrum analyzer
PBG	photonic bandgap
PC	polarisation controller
PCF	photonic crystal fibre
RK4IP	Runge Kutta interaction picture method
SBS	stimulated Brillouin scattering
SC	supercontinuum
SEM	scanning electron micrograph
SHG	second harmonic generation
SMF	single mode fibre
SPM	self phase modulation
SRS	stimulated Raman scattering
SSFM	split step Fourier method
TOD	third order dispersion
XPM	cross phase modulation

DECLARATION OF AUTHORSHIP

I, Natasha Vukovic declare that the thesis entitled *Optical properties of long photonic crystal fibre tapers* and the work presented in the thesis are both my own, and have been generated by me as the result of my own original research. I confirm that:

- this work was done wholly while in candidature for a research degree at this University;
- where I have consulted the published work of others, this is always clearly attributed;
- where I have quoted from the works of others, the source is always given. With the exception of such quotations, this thesis is entirely my own work;
- I have acknowledged all sources of help;
- where this thesis is based on work done by myself jointly with others, I have made clear exactly what was done by others and what I have contributed myself;
- parts of this work have been published in the journal articles and conference proceedings reported in the List of publications at the end of the thesis.

Natasha Vukovic

January 2010

Acknowledgements

The ORC is a place where, without any doubt, everyone who loves science, could easily find the inspiration for work. I have the pleasure, at this final stage of my thesis, to thank some of the exceptional people who helped me throughout my thesis.

Firstly, I would like to thank my supervisor Dr Neil Broderick for guidance and support during the last three years. His help was invaluable to me and I am indebted to Neil for providing me with all the equipment, introducing to me the world of Mac computers and for proof reading all my papers and this thesis.

I am grateful to Professor David Richardson for welcoming me into his group and for constructive weekly discussions about my work during the group meetings, that helped me to be focused and organised. My special thanks to Dr Marco Petrovich, who helped me so many times resolving different problems in the lab, who fabricated great fibres that I was able to use and who lent me many pieces of equipment for my experiments. I would like to thank Sonali, Francesco, Peter and other group members, whose helpful and constructive comments played an important role in the development of this thesis. My warmest thanks to Dr Gilberto Brambilla for the use of his lab space and equipment and helping me many times resolve many doubts and practical issues in the lab. I appreciate very much and want to thank Dr Periklis Petropoulos for giving me the opportunity to work in the telecom group labs and for lending me the equipment. Dr Francesca Parmigiani helped me with the crucial experiments in my thesis and I am so grateful to her. I admire her dedication to science and enthusiasm and appreciate very much her friendly and helpful attitude. I would like to thank my colleague Angela Camerlingo for sharing her lab with me and helping me on many occasions. A big thank you to other members of the ORC with whom I had the pleasure of discussing ideas, borrowing equipment and who generally helped me with my work. Thanks to Trevor Austin for his help in building the power supply and testing the equipment for my taper rig and Kevin Sumner for help with computer troubles.

Words can not say how indebted I am to my parents for their love and encouragement through all the years. I am eternally grateful to Pedja for always being supportive. This whole journey wouldn't be possible without you. My warmest thanks and my love go to my children Bane and Jelena for having patience and for giving me joy.

In memory of my father Aleksandar

Chapter 1

Introduction

Modern fibre optics was born in 1950s and revolutionized the field of telecommunications. Since then a lot of effort has been put into the design of new fibres, using new materials and improved control of fibre optical properties. Of particular importance was the development of low loss silica fibres which contributed to the development of the new field of nonlinear fibre optics [1]. Many different nonlinear phenomena have been studied over the years including self phase modulation, stimulated Raman scattering, four wave mixing etc. The combination of different nonlinearities has also been considered, leading to new developments in the field of nonlinear optics.

Microstructured optical fibres (MOF) have attracted much attention since the first demonstration of optical guidance in a MOF in 1996, [2] - [5]. MOFs have shown potential for many practical applications, due to their novel optical properties and have been in the focus of research over the recent years [2]. Light guidance in MOF is provided by a periodic arrangement of holes, acting as a cladding, running along the full length of the fibre. A potentially unlimited range of geometric arrangements (hole shape, dimension and position) permits control of optical properties (dispersion, nonlinearity, birefringence), improving some of the characteristics in comparison to conventional optical fibres. Already MOFs have significant applications in various scientific domains, such as nonlinear optics, telecommunications or medical science.

Many of the above mentioned nonlinear effects are enhanced by tapering optical fibres and particularly by tapering MOF. Nowadays, many important optical fibre components and many advanced applications are based on tapered optical fibres. Tapered MOFs have been widely used over the recent years in a variety of applications in the field of nonlinear optics, such as supercontinuum generation, soliton pulse compression or parabolic pulse generation in the normal dispersion regime [2], [3]. The fabrication techniques in the field of fibre tapers were mainly focused on fabrication methods for short taper lengths (<10 cm), based on heating and stretching of the fibre, and for long taper lengths (>10 m), based on fibre drawing technique. These processes are well

understood and allow wide variety of tapers to be fabricated. However, these methods can not be easily extended to allow fabrication of intermediate length tapers (range between tens of cm and 10 m). Moreover, the performance of the fibre devices and the influence of different effects on pulse propagation can be enhanced by a carefully engineered profile of the fibre taper and by improved control of the parameters that affect tapering. This thesis presents results of developing a novel fibre tapering system, which enables fabrication of intermediate length tapers, particularly for applications where required diameter change is less than 10%. The full capabilities of the novel fibre tapering rig were demonstrated in this thesis. Such metre - long tapers offer precise control of the effective nonlinearity, dispersion, Brillouin threshold etc. In particular, I have studied parabolic pulse generation in the tapered microstructured optical fibre, which is an attractive way to produce flat spectra, which allows efficient compression in the time domain. Another important nonlinear application is the supercontinuum generation in microstructured fibres, which has been in the focus of scientific interest and demonstrated frequently. However there is still a need to improve its performance by extending the bandwidth, improving the spectra flatness or decreasing the power requirements, which can be achieved using tapered microstructured optical fibres, too. The possibility of having tapering facility able to fabricate intermediate length tapers is beneficial and potentially can revolutionise the field of optical fibre tapering.

The work described in this thesis is motivated by the need to explore theoretically and experimentally new fibre tapers designs and to correlate them to the physical and optical properties that can be achieved. The final aim of this research work is to expand the current knowledge of how the new system facility can be used in the existing and new applications in the field of nonlinear optics. In addition, the ultimate goal of the research presented in this thesis is to propose some new tapered MOF designs which could be fabricated using the tapering rig and to experimentally validate some pre-determined optical properties.

Outline

Chapter 2 provides the general background of the thesis. An introduction of the microstructured optical fibres, with the emphasis on the guidance mechanisms and most important definitions, as well as an introduction to tapered fibres, is given. Brief overview of the fundamental properties, materials and fabrication techniques, is presented. This chapter describes the foundations of the dispersive and nonlinear effects in standard and MOF. The nonlinear effects, such as self phase modulation and stimulated Raman scattering, are briefly reviewed, as their comprehension is of fundamental importance for understanding different nonlinear phenomena studied in this thesis. Furthermore, for an understanding of the nonlinear phenomena it is necessary to consider the basic equations

that determine the propagation constant and govern the propagation of optical pulses. The derivation procedures of the wave equation and the NLSE equation are shown.

The nonlinear pulse propagation in optical fibres is simulated using both the split step Fourier method and a fourth order Runge Kutta interaction picture method, therefore both methods are described in this chapter. The techniques for complete optical pulse characterisation, FROG and l-FROG, are introduced.

Chapter 3 presents the results of design, configuration and demonstration of a novel optical fibre tapering rig. The most important steps in the designing procedure, including the mathematical theory of the control problem formulation, are explained in detail. The system description with all relevant parameters is given. A particularly important achievement in this thesis is the inclusion of the control feedback loop, and hence the detailed design of the feedback loop is given. Moreover, different experimental results of tapering of both step-index and MOF fibres are presented. The quality of tapering is quantified using the mean error and error standard deviation. Specifically, the experimental results of the MOF fibre taper are examined.

Chapter 4 introduces the theoretical background of the parabolic pulse generation in the normally dispersive optical fibre, which relies on the theory of self similarity. Furthermore, the results of modelling and simulation of tapered normally dispersive MOF are presented. Two normal dispersion regions of the MOF are identified using an optical map. The procedure for choosing the parameters of the taper profile for efficient parabolic pulse generation is proposed. The procedure is essentially based on creating a set of 2D maps which relate the measure of pulse being parabolic and the taper's corresponding length as a function of input pulse peak powers and temporal widths. It is shown that Gaussian input pulse of various peak powers and widths can evolve into the parabolic shape with a linear chirp coefficient in both cases. The improvement of the misfit parameter, which quantifies the parabolic pulse evolution in the MOF, when compared to the standard optical fibre, is demonstrated.

Chapter 5 shows numerical and experimental results of the three sets of experiments that I have done towards the parabolic pulse generation in a tapered microstructured optical fibre with the normal dispersion. The first two experiments were performed using the fibre that wasn't specifically designed for this analysis and experiment. An attempt to accommodate the existing MOF to suit the purpose of the experiment and the initial experimental results were shown. Further in this chapter I have presented numerical and experimental results of the third experiment of the parabolic pulse shaping in a tapered MOF. Results of numerical modelling and taper parameter determination were shown. Consequently, the 1.8 m long taper was successfully fabricated. The experimental results of parabolic pulse generation have been compared with the numerical simulations. The nonlinear pulse propagation through the taper was characterized using linear FROG

technique. The results of the experimental investigation suggest that parabolic pulse shaping can be obtained if the optimum launching conditions can be achieved.

Chapter 6 presents results of investigation of the supercontinuum generation in tapered MOF. The novelty of this research relies in the proposed procedure for improving flatness of a supercontinuum based upon tapering of the microstructured optical fibres. This approach provides a simple way for determination of the taper parameters (pitch and relative hole size), to achieve the required dispersion regime. The modelling procedure was based on the simulation of the sech pulse propagation of various FWHM and peak powers in the tapered MOF of different lengths. The generalised nonlinear Schrödinger equation was solved numerically using a fourth order Runge Kutta in the interaction picture method. I calculated the supercontinuum spectra bandwidth and the ratio of spectra width and spectra standard deviation. This measure is associated with the figure of merit of the spectra flatness. Some enhanced supercontinuum spectra features are obtained for the fibre tapering from anomalous to normal dispersion regime. It is shown that by taking into account the spectra standard deviation it is possible to find conditions to significantly improve flatness of the supercontinuum with respect to the untapered fibre. The method proved to be efficient for easy determination of the optimum launching conditions, thus providing a simple way of enhancing the spectra properties of SC, which is of the fundamental and practical interest.

The thesis concludes with Chapter 7 in which I summarise the results and discuss the possible directions of future work.

Chapter 2

Background

2.1 Introduction to microstructured optical fibres

The microstructured optical fibre (MOF) is a novel class of optical fibre which exhibits a wide range of optical properties that were impossible to achieve using standard optical fibres. MOFs can be made using a single type of glass, in contrast to conventional technology, and light guidance is achieved by introducing an air hole lattice that runs longitudinally along the fibre length. Microstructured optical fibres were proposed in 1995 [4] and the first demonstration of optical guidance was published in 1996 [5]. Since the breakthrough in the fabrication process of these fibres in the late 1990 these fibres' unusual optical properties attracted significant interest and initiated huge scientific research [2] - [18].

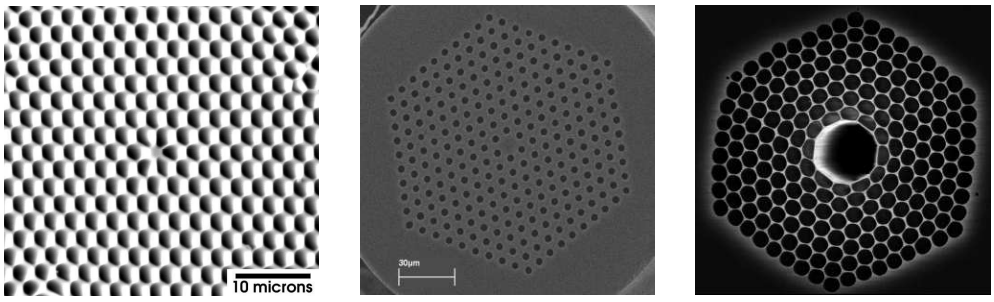

(a) Small core index-guiding holey fibre

(b) Large mode area silica holey fibre

(c) Hollow core photonic bandgap fibre

FIGURE 2.1: SEM images of microstructured optical fibres realised at the ORC

One of the most important MOF configurations consists of an arrangement of holes running longitudinally along the fibre, acting as a cladding, typically in a hexagonal arrangement, guiding light in either a solid or hollow core. Such fibres are also known as Holey Fibres (HF) or Photonic Crystal Fibres (PCF), as the microstructure is often

highly periodic. Figure 2.1. shows a few examples of practical fibres of very different topological structures allowed by current fabrication techniques.

- ***Fundamental properties:*** An important property of index-guiding MOF is that they can, under certain circumstances, be endlessly single moded [2], [3], [8]. In addition, due to the flexibility in their structural design and the large index contrast, for many physical parameters, MOF can generally span a larger achievable range than standard fibres [2], [19], [20]. It is therefore possible, for example, to target more efficiently either non-linear applications, employing a small core design, or high power delivery applications using large mode area fibres [2], [3], [21]. Also, dispersive properties are "tailorable", enabling dispersion-flattening across a very broad spectral region allowing, for example, anomalous dispersion down to the visible region or normal dispersion with either very low or very high values.

- ***Materials:*** The significant advantage of MOFs is that they can be realised in a single material, usually pure silica, but can be also made using different materials. This eliminates the problem of doping certain areas to modify the refractive index in order to achieve light guidance, and allows a broader range of materials to be potentially employed. Pure silica remains the material of choice for most of the applications in the near infrared wavelength range due to the low intrinsic loss. However, for applications requiring extremely high nonlinear coefficients, compound glasses have been employed (bismuth, tellurite or chalcogenide glasses) [2], [3].

- ***Fabrication techniques:*** Since the first fabrication of MOFs associated with 1996, [5], a variety of different techniques was used. The first stage of the process is fabrication of a preform (which is a macroscopic version of the targeted structure). The preform is usually produced by stacking circular capillaries (shown in Figure 2.2).

FIGURE 2.2: The capillaries stacked around a rod

The common approach is based on a drawing tower techniques where the stack is then drawn down into fibre on a fibre drawing tower. Alternatively, the stack can be drawn into cane, which can be inserted into a jacket and drawn to a fibre. Different structures can be made by varying pulling speed, temperature or by doping the central rod (active fibres) etc. [2].

2.2 Single mode optical fibres

In order to properly understand the novel properties of PCFs I first review the common step-index fibre. The geometry of step-index fibre is used in most conventional single mode fibres (SMFs). The step-index fibre (shown in Figure 2.3) has a central core, with a refractive index n_{core}, surrounded by a cladding layer with a refractive index n_{clad}. The light is guided via the principle of total internal reflection in the higher refractive index core, while the cladding refractive index is lowered ($n_{core} > n_{clad}$).

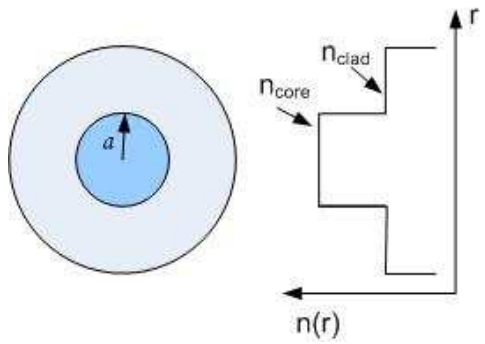

FIGURE 2.3: Schematic diagram of the step-index fibre cross section and refractive index profile

The two important parameters that characterise a step-index fibre are the relative core-cladding index difference, Δ, and the normalized frequency, V. The relative core-cladding index difference is:

$$\Delta = \frac{n_{core}^2 - n_{clad}^2}{2n_{core}^2} \tag{2.1}$$

In conventional fibres it is the normalized frequency, V, that determines the second order cut-off between the single mode and multimode guidance [1], given by the following equation:

$$V = \frac{2\pi}{\lambda} a \sqrt{n_{core}^2 - n_{clad}^2} \tag{2.2}$$

where a is the core radius.

According to the geometrical optics analysis, the difference in refractive index gives rise to total internal reflection at the core-cladding interface, which will confine light in the core region. Alternatively, Maxwell's equations enable finding a finite set of guided modes whose energy is concentrated in the core. The number of guided modes is $N \sim V^2/2$ and is determined by the wavelength of light and the fibre structural parameters. It has been shown [1], that by reducing the core radius until $V < 2.405$, only one transverse mode is guided by the fibre, i.e. the single mode propagation regime. The guided modes have a propagation constant β which is related to the effective index, n_{eff}, using the following expression:

$$\beta = \frac{2\pi n_{eff}}{\lambda} \tag{2.3}$$

where λ is the optical wavelength ($k_0 = 2\pi/\lambda$ is the wavenumber of light in vacuum). For a step-index fibre with an infinite cladding propagation constants satisfying $n_{clad} < \beta/k_0 < n_{core}$ give strictly guided modes. In this theoretical, ideal case of having an infinite cladding, n_{eff} is real. However, due to the cladding finite size, all modes are leaky because of confinement (tunnelling) losses [20]. In this case the propagation constant takes small imaginary part, so that these modes would satisfy $n_{clad} < Re(\beta)/k_0 < n_{core}$. However, we can assume that most well-confined leaky modes of the fibre with the finite cladding are similar to the guided modes of a fibre with the same parameters but an infinite cladding [20]. The fundamental mode of a step index fibre is the mode with largest β.

2.3 Guiding mechanisms in microstructured optical fibres

The fundamental difference between standard and microstructured optical fibres is associated with the wavelength dependence of the effective cladding index in the MOFs [11], [15]. Whilst in conventional fibres it is largely independent of wavelength, in MOFs the large index contrast between air and glass and small structure dimensions combine [11], thus in MOFs there is a small effective index difference between the core and cladding at shorter wavelengths and the effective index contrast is larger at longer wavelengths. This phenomena leads to the unusual optical properties in these fibres. In MOFs, as long as guidance is due to the finite number of layers of holes, light leakage from the core to the outer layers of holes is unavoidable [20]. Therefore, in MOFs, all modes are leaky modes and both β and n_{eff} are complex and imaginary part of n_{eff} is related to

the confinement loss. The effective index is associated with the largest possible value of the propagation constant β for a given frequency.

In contrast to conventional optical fibres however, MOFs can confine light in the core due to a number of different physical mechanisms. Most common guidance mechanisms are index guidance (IG) and photonic bandgap guidance (PBG) [2], discussed further below.

2.3.1 Index guiding MOFs

The typical cross section of the hexagonal structure MOF with equal sized holes is shown in Figure 2.4. There are two parameters, Λ and d/Λ, used to define the structure geometry, where d is the hole diameter, and Λ is the hole-to-hole spacing (pitch). The omission of the central hole is used to define the solid (silica) fibre core.

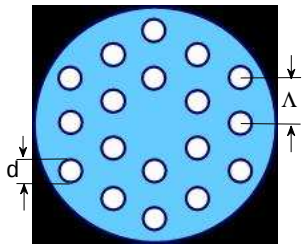

FIGURE 2.4: Schematic diagram of the MOF cross section. Note that only two rings of holes are shown for clarity.

The principle of index-guiding mechanism in MOF relies on the modified total internal reflection which confines light in the MOF core (shown in Figure 2.5). Similarly to conventional optical fibres, the effective refractive index of the cladding is lower than the core, due to the presence of air holes. Thus, the equivalent of step index fibre, with the refractive index of the core, n_{core}, surrounded by a cladding (refractive index n_{clad}), is created. In case of MOFs, the refractive index of the core is $n_{core} = n_{silica}$ and the effective index of the fibre n_{clad} is defined as the effective modal index of the lowest-order cladding mode (this is a good approximation to the fundamental mode of an infinitely periodic structure), which is fundamental space filling mode (FSM), so that $n_{clad} \simeq n_{FSM}$. The FSM becomes more confined to the silica regions as the wavelength decreases [6], and so the effective cladding index increases until $n_{FSM} \simeq n_{silica}$ for $\lambda \ll \Lambda$. In the opposite regime when $\lambda \gg \Lambda$, n_{FSM} is given by [22]:

$$n_{FSM} = n_{air} d/\Lambda + n_{silica}(1 - d/\Lambda) \tag{2.4}$$

(a) (b)

FIGURE 2.5: a.) Scanning Electron Micrograph (SEM) of a typical structure of a solid core index guiding MOF; b.) Simulated fundamental guided mode of the same fibre (2 dB contours)

Therefore, a strong wavelength dependence of the refractive index of the cladding structure can be observed [7], which leads to the unique properties of MOFs, most importantly, to an endlessly single mode guidance phenomenon. This was first reported in 1997 by Birks et al. [8] and they showed that a MOF can be single moded at all wavelengths. Analogously to the concept of the normalized frequency applied in conventional fibres, the V-parameter of MOF was proposed in the following way [6]:

$$V_{MOF} = \frac{2\pi}{\lambda}\Lambda\sqrt{n_{eff}^2 - n_{FSM}^2} \tag{2.5}$$

This equation implies that the condition for cut-off is $V_{MOF} \leq \pi$ [20], [22].

2.3.2 Photonic Bandgap Effect guiding MOFs

The idea of guiding light through a photonic bandgap mechanism originates from the fact that in periodic arrangements of dielectrics, the propagation of light can be suppressed at certain wavelengths. The frequency range where propagation is forbidden, regardless of propagation direction and polarisation, is called the photonic bandgap. By breaking the periodicity of the cladding (by adding an extra hole to form a defect), it is possible to confine light within the defect [2], [3]. Such a defect acts as a core in photonic bandgap (PBG) fibres, as shown in Figure 2.6.

(a) (b)

FIGURE 2.6: a.) SEM of a typical structure of a typical photonic bandgap fibre; b.) Simulated intensity levels of the Poynting vector of the fundamental mode of the same fibre

PGB fibres confine light due to the principle of Bragg reflection. Therefore, in order to understand this concept, we could consider first a Bragg mirror. It is the simplest device whose operational principle relies on photonic bandgap effect, which consists of a periodic stack of two alternating dielectric layers. Light propagating in a direction normal to the layers undergoes reflections and transmissions at each interface. For each choice of layer thickness and refractive index, maximum reflection is achieved when the different contributions from each interface are in phase with each other [2]. For an infinite structure the reflection becomes unity on resonances and therefore, light in a certain wavelength range can be totally reflected. Photonics crystals with two or three dimensional periodicity can be analysed as the generalisation of Bragg mirrors [20]. A photonic bandgap fibre is a 2D photonic crystal i.e. a dielectric with a refractive index that varies periodically in space, with a period of the order of optical wavelength [4]. In such fibre, for certain values of frequencies and directions, light can not propagate due to the photonic bandgap effect. In such cases Bragg reflection takes place and light can only propagate longitudinally down the core (defect). These fibres are the focus of much research interest as they offer novel properties beyond conventional fibres which can be exploited in applications such as high power and energy transmission, sensing, fibre lasers, wideband communication for optical network system etc.

2.4 Introduction to tapered optical fibres

Optical fibres are usually designed and fabricated to be uniform along the direction of propagation. If a structure changes smoothly in the direction of propagation, light can pass gradually from one part of fibre structure to another with low loss (otherwise, abrupt changes in the structure features can cause coupling to higher order modes and consequently loss in transmission) [23]. A tapered fibre is one with gradually reduced dimensions in a direction of propagation.

Conventionally, tapers are fabricated by a process of heating and simultaneously stretching the fibre in opposite directions. A typical tapering facility that enables short fibre tapers with two transition regions (smoothly varying sections of a fibre) is shown in Figure 2.7. This is often done using a flame torch while monitoring the fibre diameter. By tapering, heated part of the fibre narrows to form a waist that is connected to untapered fibre ends by taper transitions. For example, the standard SMF is made non-uniform and the end result is a fibre whose diameter narrows down from 125 μm in two transition regions of $\sim$ 4 cm to 5 cm length [23]. The length of central region (waist) is usually limited to 20 cm to 30 cm.

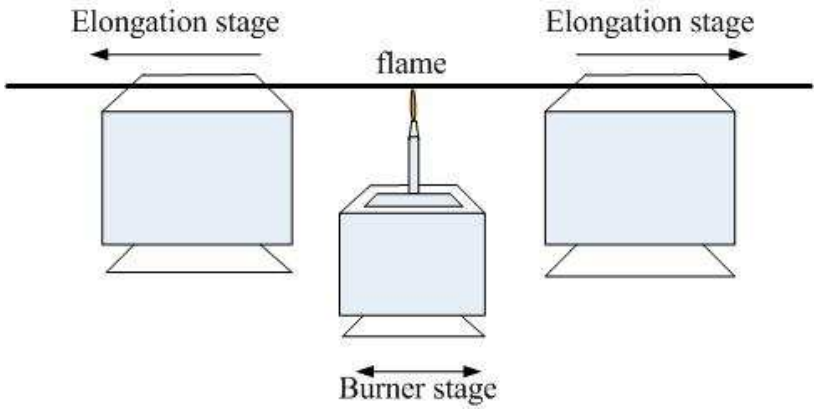

FIGURE 2.7: Conventional fibre tapering rig

In contrast to the short tapers described above, long (range between 10 m and 40 km) tapers have also been manufactured, by the drawing tower technique [26]. In this case, the fibre is pulled from the heated preform down the tower and the diameter of the fibre is continuously monitored. By changing of draw speed different tapering ratios can be achieved.

Microstructured optical fibres can also be tapered, however, whereas SMFs are only reduced in scale, in MOFs the holes change size relative to the fibre as a whole [2]. There have been reported different techniques to control the process of tapering and to characterise tapered fibres (such as optical microscopy, SEM and transmission measurements) [24] - [27]. Tapered fibres represent a convenient way of generating white light radiation and e.g. it has been demonstrated [28], [29], that the supercontinuum light with the spectrum more than two octaves broad ($\sim$ 375 nm to $\sim$ 1750 nm) is possible using tapered MOFs. Also, soliton pulse compression was observed using tapered MOFs, where for example, nearly transform - limited output pulses with duration 90 fs have been generated from 195 fs input pulse using 8 m of the tapered hollow-core photonic crystal fibre [30]. The use of tapered MOFs has been demonstrated to control the gain of the Brillouin signal or to enable Brillouin suppressed frequency shift [31] - [33]. Optical fibre

tapers have been used in many applications, ranging from pulse compression in a soliton regime, to the supercontinuum generation [34] - [43].

2.5 An overview of linear and nonlinear effects in optical fibres

Here I briefly explain the different physical effects that happen during light propagation down a fibre.

2.5.1 Fibre losses

The first effect we consider is the fibre loss or attenuation. The attenuation constant, α, is a measure of energy loss during the transmission in the fibre. It is calculated using the following equation:

$$\alpha[dB/m] = -\frac{10}{L}\log(\frac{P_t}{P_0}) \tag{2.6}$$

where P_0 is the power launched at the input of a fibre, P_t is the transmitted power, L [m] is the fibre length. Factors that contribute to the loss spectra of a standard fibre are material absorption and Rayleigh scattering [1].

In MOFs, the major attenuation mechanisms are: absorption, scattering, bend loss and confinement loss [2], [7], [44]. Since pure silica has a lower Rayleigh scattering loss than standard germanium-doped fibres, thus pure silica MOFs have potentially lower loss than standard fibres. To date, small core highly nonlinear MOFs with losses less than $\sim$ 50 dB/km have been fabricated [2] and an order of magnitude smaller losses are achievable with larger core designs. However, bend loss becomes the major limiting factor in the large mode area (LMA) fibres limiting the obtainable mode area at a given wavelength. Bend loss occurs when fibre is bent beyond a certain critical radius, which mainly depends on wavelength [44]. Under these conditions all guidance is lost for wavelengths longer than a certain value, according to the comprehensive study by Baggett et al. [45]. Moreover, due to the finite size of the MOF structure, modes are leaky and both the propagation constant and effective index are complex, as implied previously. Physically, we can imagine the light leaking from the core to the cladding region through the bridges between the holes [20]. Losses due to the finite extent of the cladding are confinement losses. For example, the power density of the fundamental mode has maximum value at the centre of the core and in the cladding the power density decays exponentially with increasing distance from the core, until the outer boundary of the cladding is reached. The confinement loss associated with the mode can be extracted from the imaginary part of the complex effective index and can be calculated as [18]:

$$CL[dB/m] = \frac{20 \times 10^6}{\ln 10} \frac{2\pi}{\lambda[\mu m]} Im(n_{eff}) \tag{2.7}$$

For a MOF with a finite cladding, the losses of the fundamental mode are smallest, which corresponds to the minimum $Im(n_{eff})$, whilst having largest $Re(n_{eff})$. The confinement loss is determined by the geometry of the structure and it has been shown that increasing number of rings in the small core fibre can reduce the fibre loss by improving the confinement of the mode [18]. Typically, including one extra ring of holes in the MOF design, leads to the reduction of the confinement loss e.g. from 1 dB/km to 0.01 dB/km. By careful design, the confinement loss can be made as low as required.

2.5.2 Fibre dispersion

In any material the refractive index depends on frequency and this is called chromatic dispersion. In an optical fibre there are two effects that account for chromatic dispersion: the material dispersion (intrinsic to medium and caused by the wavelength dependent interaction between light and matter) and waveguide dispersion (can be changed to control the chromatic dispersion). The material dispersion is related to the characteristic resonance frequencies at which material absorbs electromagnetic radiation through the oscillations of bound electrons [1]. Far from the medium resonances, the refractive index is approximated by the Sellmeier equation [1].

Fibre dispersion is of critical importance for the propagation of ultrashort pulses as different spectral components associated with the pulse travel at different speeds [1]. The effects of fibre dispersion are expressed by applying Taylor expansion for the propagation constant about the angular frequency ω_0:

$$\beta(\omega) = n_{eff}(\omega)\frac{\omega}{c} = \beta_0 + \beta_1(\omega - \omega_0) + \frac{1}{2}\beta_2(\omega - \omega_0)^2 + \frac{1}{6}\beta_3(\omega - \omega_0)^3 ... \tag{2.8}$$

where: $\beta_1 = 1/v_g$ (v_g is the group velocity), implying that the envelope of the pulse moves at group velocity, β_2 represents the dispersion of the group velocity and is responsible for pulse broadening (shows how the group velocity of a pulse changes as a function of frequency), while β_3 is the third-order dispersion (TOD) coefficient. Since it is more common to work in wavelength than in the frequency domain, the group velocity dispersion (GVD), β_2, is often related to the dispersion parameter D, via the equation:

$$D[ps/nm/km] = -\frac{\lambda}{c}\frac{d^2}{d\lambda^2}[Re(n_{eff})] = -\frac{2\pi c}{\lambda^2}\beta_2 \tag{2.9}$$

If parameter D is negative, this is the normal dispersion regime where the red components of the pulse travel faster than the blue components, i.e. positive chirp. Similarly,

if D is positive, i.e. anomalous dispersion regime, where the red components of the pulse travel slower than the blue components, i.e. negative chirp. When $D = 0$, which corresponds to the zero dispersion wavelength, all frequency components of the pulse travel at the same speed (to lowest order) and the pulse maintains its shape, whilst for $D \neq 0$ the pulse spreads in time. This is of high importance in communications as it can lead to pulse overlapping in time and intersymbol interference, which causes the degradation of information transfer. In some applications (with broad bandwidth), it is important how the dispersion changes with wavelength, which is calculated as the dispersion slope (DS), using the following equation:

$$DS[ps/nm^2/km] = \frac{dD}{d\lambda} = (\frac{2\pi c}{\lambda^2})^2\beta_3 + \frac{4\pi c}{\lambda^3}\beta_2 \tag{2.10}$$

The waveguide dispersion is strongly dependent on the fibre structure. In MOFs the waveguide contribution to the chromatic dispersion can be large and is determined by the choice of d and Λ. For example, by decreasing the pitch value, Λ, and increasing the relative hole size d/Λ, the zero dispersion wavelength can be shifted down to visible range [4], [29], which opens a whole new range of applications, such as soliton generation and propagation [2]. By carefully controlling the structural parameters of the fibre, different dispersion characteristics of MOFs can be obtained, signifying the unique property of MOFs in tailoring (shift or flatten) the dispersion characteristics.

2.5.3 Nonlinearities in optical fibres

The response of any dielectric (including optical fibres) to light becomes nonlinear for intense electromagnetic fields [1]. The origin of nonlinear response is related to the aharmonic motion of bound electrons under the influence of an applied field [1]. The total induced electric polarization **P** is related to the electric field **E(r,t)** (far from medium resonances), through the nonlinear equation:

$$\mathbf{P_i} = \sum_j \varepsilon_0 {\chi_{ij}}^{(1)} E_j + \sum_{j,k} \varepsilon_0 {\chi_{ijk}}^{(2)} E_j E_k + \sum_{j,k,l} \varepsilon_0 {\chi_{ijkl}}^{(3)} E_j E_k E_l + \cdots = \mathbf{P_1} + \mathbf{P_2} + \mathbf{P_3} + \cdots \tag{2.11}$$

where (i) defines the order and each coefficient is a tensor of rank $i + 1$ and ε_0 is the vacuum permittivity. The first order susceptibility is $\chi^{(1)}$, which represents the dominant contribution to **P**, [1], and its effects are taken into account through the refractive index n and the attenuation coefficient α. $\chi^{(2)}$ is the second order nonlinear optical susceptibility which is zero in a material with inversion symmetry (such as silica), so that $\mathbf{P_2}$ is zero. $\chi^{(3)}$ is the third order nonlinear optical susceptibility. The lowest order nonlinear effects in optical fibres originate from the third order susceptibility, such as: nonlinear

refraction, third-harmonic generation (THG), four-wave mixing (FWM). Processes such as THG and FWM require phase matching, otherwise they are not efficient and so can in general be ignored. Nonlinear refraction arises from the intensity dependence of refractive index and is given as:

$$\tilde{n}(\omega, |E|^2) = n(\omega) + n_2|E|^2 \tag{2.12}$$

where $n(\omega)$ represents the linear part which is well approximated by the Sellmeier equation [1], $|E|^2$ is the optical intensity inside the fibre and n_2 is a measure of the fibre nonlinearity given by:

$$n_2 = \frac{3}{8n} Re(\chi^{(3)}_{xxxx}) \tag{2.13}$$

where the optical field is assumed to be linearly polarized so that only one component $\chi^{(3)}_{xxxx}$ of the fourth-rank tensor contributes to the refractive index. Note that nonlinear refraction is always phase matched and so most nonlinear effects originate from nonlinear refraction.

The nonlinear refraction leads to nonlinear effects, such as Self-Phase Modulation (SPM) and Cross-Phase Modulation (XPM). These nonlinear effects are elastic, which implies that no energy is exchanged between the electromagnetic field and the dielectric medium. Nonlinear effects that result from inelastic interchange of energy between the electromagnetic field and the medium are Stimulated Raman Scattering (SRS) and Stimulated Brillouin Scattering (SBS).

2.5.3.1 Self Phase Modulation

The simplest effect due to nonlinear refraction is Self Phase Modulation (SPM) in which the optical field modulates its own phase. It is due to the intensity dependence of the refractive index in a nonlinear optical medium (optical Kerr effect), in accordance to Equation 2.12 [1]. For the electric field given by its complex amplitude $E(t) = A_0 \exp(-i\phi(t))$ (where A_0 is the peak intensity), the phase of an optical field changes by $\phi = (n + n_2|E|^2)k_0 L$. The intensity dependence leads to nonlinear phase shift $\phi_{NL}(t)$ given by:

$$\phi_{NL}(t) = \frac{2\pi}{\lambda} n_2 |E|^2 L \tag{2.14}$$

where L is the propagation distance. SPM creates new frequencies and can lead to the spectral broadening of optical pulses, which arises due to the time dependence of the

nonlinear phase shift ϕ_{NL} i.e. the instantaneous optical frequency changes across the pulse (chirp). The frequency difference from its central value ω_0 is given by:

$$\delta\omega(t) = -\frac{\partial\phi_{NL}}{\partial t} \propto \frac{\partial|E|^2}{\partial t} \tag{2.15}$$

The time dependence $\delta\omega(t)$ is frequency chirping. The chirp induced by SPM increases in magnitude with the distance, implying that new frequency components are generated continuously as the pulse propagates along the fibre, so that the nonlinear phase shift becomes [1]:

$$\phi_{NL}(L,t) = \gamma P_0 L_{eff}|u(0,t)|^2 \tag{2.16}$$

where the nonlinearity coefficient γ=2 $\pi n_2/(\lambda A_{eff})$, $u(L,t) = u(0,t)exp(i\phi_{NL}(L,t))$ is a normalized slowly varying envelope of the electric field and A_{eff} is the effective area. The input pulse peak power is P_0 and effective fibre length is $L_{eff} = (1-\exp(-\alpha L))/\alpha$, where α accounts for the fibre losses.

These new frequency components broaden the pulse spectra. Generally, the chirp depends on the input pulse shape. For Gaussian pulses, the chirp rate is linear and positive over the central region of the pulse, it is negative near the leading edge and is positive near the trailing edge of the pulse. The chirp gets larger for pulses with steeper edges [1], as can be seen in Figure 2.8.

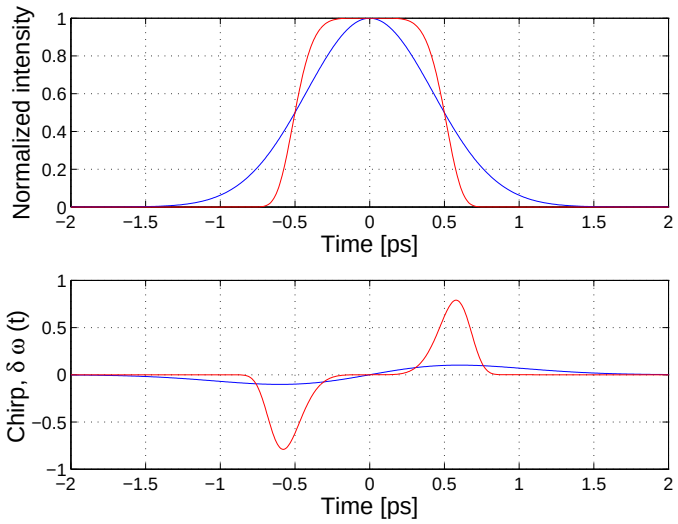

FIGURE 2.8: Top: Normalized intensity for a Gaussian pulse (blue) and super Gaussian when m=3 (red); Bottom: Frequency chirp $\delta\omega(t)$ for Gaussian pulse (blue) and super Gaussian (red)

The input pulse chirp in combination with the effect of SPM plays a significant role in the pulse propagation. A positive input pulse chirp parameter causes increased spectral broadening, whilst the opposite occurs in case of a negative chirp. For shorter pulses it is necessary to consider the combined effects of GVD and SPM [1]. The SPM generates new frequency components that are red shifted near the leading edge and blue shifted near the trailing edge (positive chirp). In the normal dispersion regime the red components travel faster than the blue components (positive chirp). Then along with the effect of SPM, this causes increased temporal broadening. The opposite occurs in the anomalous dispersion regime, where the interplay between the GVD and SPM leads to the generation and propagation of optical solitons. In this case, the GVD induced chirp is negative, whilst SPM induced chirp is positive (also for sech pulses), so that the pulse shape adjusts itself during the propagation while cancelling out two opposite sign chirp effects. Therefore, a soliton is formed, a chirp-free pulse that propagates while keeping both time duration and frequency spectra constant during the propagation.

Tapered fibres are particularly attractive for nonlinear applications, as the SPM is enhanced in tapered fibres due to the reduction of the effective area and increase of the Kerr nonlinear phase shift of the fundamental mode [48].

2.5.3.2 Cross Phase Modulation

The Cross Phase Modulation (XPM) is another result of Kerr nonlinearity in optical fibres, which arises from the intensity dependence of the refractive index $n = n_0 + n_2(|E_1|^2 + |E_2|^2)$. Two optical pulses at different wavelengths can couple in the process of XPM without any energy transfer among them. XPM is similar to SPM but the origin of spectral broadening is in mutual interaction of the different optical fields of different wavelengths. XPM initiate different nonlinear effects in optical fibres. For example, in case of normally dispersive fibre with the specially designed dispersion profile (dispersion flattened fibre), the modulation instability occurs as the consequence of XPM. The beneficial applications of XPM modulation include XPM-induced pulse compression, optical switching etc. [1].

2.5.3.3 Four Wave Mixing

Four Wave Mixing (FWM) describes a nonlinear process in which four optical waves interact with each other as the consequence of the third order susceptibility $\chi^{(3)}$. Such process is characterized as a parametric effect as it modulates refractive index. The origin of FWM is in the nonlinear response of bound electrons of a material to an electromagnetic field [1].

FWM process involve nonlinear interaction between four optical waves oscillating at frequencies ω_1, ω_2, ω_3, ω_4. Generally, there are two types of FWM process. First

corresponds to the case in which three photons transfer their energy to a single photon at the frequency $\omega_4 = \omega_1 + \omega_2 + \omega_3$. Second corresponds to the case in which two photons at frequency ω_1 and ω_2 are annihilated, while two photons at frequencies ω_3, and ω_4 are created simultaneously, so that $\omega_3 + \omega_4 = \omega_1 + \omega_2$. The efficiency of FWM depends strongly on the phase matching of the frequency components and consequently relies on dispersion properties of the fibre. The phase matching condition requires matching of the wave vectors, i.e. $\Delta k = 0$. The particularly interesting is degenerate case, in which $\omega_1 = \omega_2$, so that a single input beam can be used to initiate FWM i.e. to generate a Stokes and anti-Stokes photon:

$$2\omega_{pump} = \omega_s + \omega_{as} \tag{2.17}$$

In this case, the phasematching condition is expressed as:

$$\Delta k = (2n_{pump}\omega_{pump} - n_s\omega_s - n_{as}\omega_{as})/c = 0 \tag{2.18}$$

where n_j is the effective mode index at the frequency ω_j and c is the speed of light. Note that due to dispersion $n_{pump} \neq n_s$ and so FWM is in general not phasematched.

Similarly to stimulated Raman scattering (SRS), the process of FWM can be used to convert the input light into light at one or more different frequencies [49]. In comparison with SRS, parametric frequency conversion is more useful as the range of frequencies is broader and both frequency up-conversion as well as down-conversion is possible. The gain coefficient for FWM is larger than for SRS [1] and it can be expected that FWM always dominate over SRS when it is phase matched.

2.5.3.4 Stimulated Raman Scattering

Raman scattering is a phenomenon that results from stimulated inelastic scattering. On a fundamental level it is related to the scattering of one photon by one of the molecules to a lower frequency photon, while the molecule makes the transition to a higher energy vibrational state. A photon of the incident field (pump) is annihilated to create a photon at a lower frequency (Stokes wave) and a phonon with the right energy and momentum to conserve the energy and the momentum [1]. Stimulated Raman Scattering (SRS) is a combination of Raman scattering with stimulated emission, which leads to Raman amplification. The SRS can occur in both directions of a single mode optical fibre. The initial growth of the Stokes wave can be described by the equation:

$$\frac{dI_s}{dz} = g_R I_P I_S \tag{2.19}$$

where g_R is the Raman gain coefficient, I_S is the Stokes intensity, while I_P is the pump intensity.

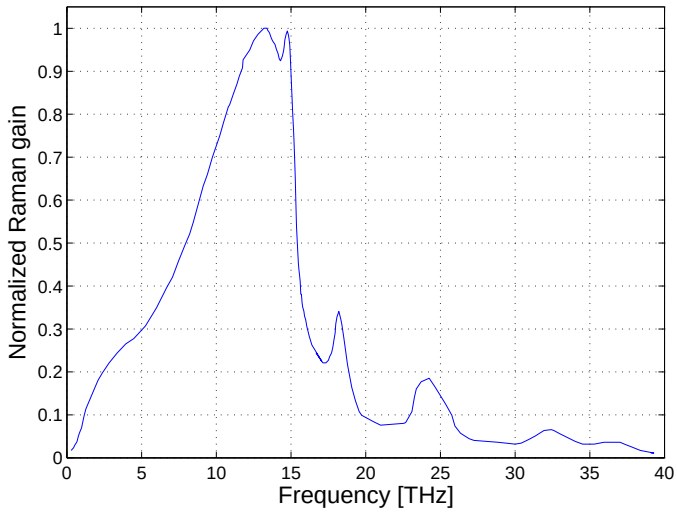

FIGURE 2.9: Normalized Raman gain for fused silica when pump and Stokes wave are copolarized (After [1])

The Raman gain spectrum for silica, $g_R(\Omega)$, where Ω is the frequency difference between the pump and Stokes waves, shown in Figure 2.9, is found to be very broad, extending up to 40 THz with a peak located near 13 THz [49]. As long as the frequency difference Ω lies within the bandwidth of the Raman-gain spectrum, the beam launched at the fibre input will be amplified because of the Raman gain. The maximum gain in silica is achieved for the frequency component downshifted by about 13 THz from the pump frequency. SRS exhibits a threshold-like behaviour, implying that significant conversion of pump energy to Stokes energy occurs when the pump intensity exceeds a threshold level. For a single mode fibre, assuming Lorentzian shape approximation for the Raman gain spectrum, the SRS threshold pump intensity is given by:

$$I_P^{th} \approx 16 \frac{A_{eff}}{g_R L_{eff}} \tag{2.20}$$

The threshold pump intensity is inversely proportional to the effective fibre length and e.g. the typical Raman threshold is ≈ 600 mW for a standard telecommunication fibre, when $L_{eff} \approx 20$ km. Note that the Raman effect in optical fibres can be used to amplify a weak signal if that signal is launched together with a strong pump, such that their frequency difference lies within the bandwidth of Raman gain spectrum [50]. The Raman response time of fused silica is extremely short, it occurs over a time scale of 60 - 70 fs. When ultrashort pulses are used (≤ 1 ps), which have a wide spectrum, the Raman effect can amplify low frequency pulse components by transferring energy from the high frequency components of the same pulse. Consequently, the spectrum shifts towards

the low frequency side as the pulse propagates inside the fibre (self frequency shift - intrapulse Raman scattering) [1]. The frequency shift increases linearly along the fibre and it becomes very large for short pulses (it scales with the pulse width as T_0^{-4}).

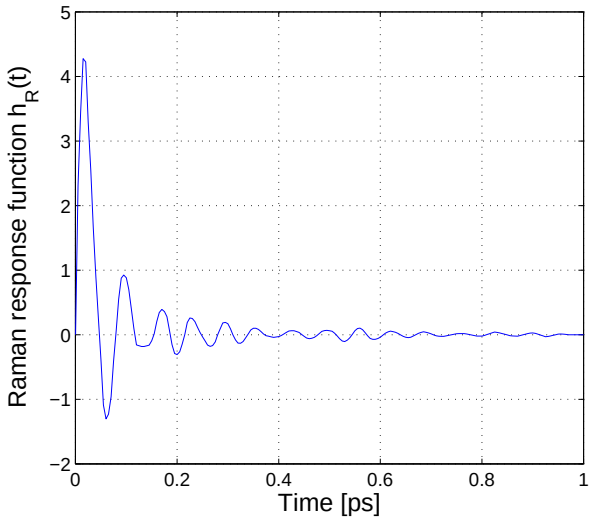

(a)

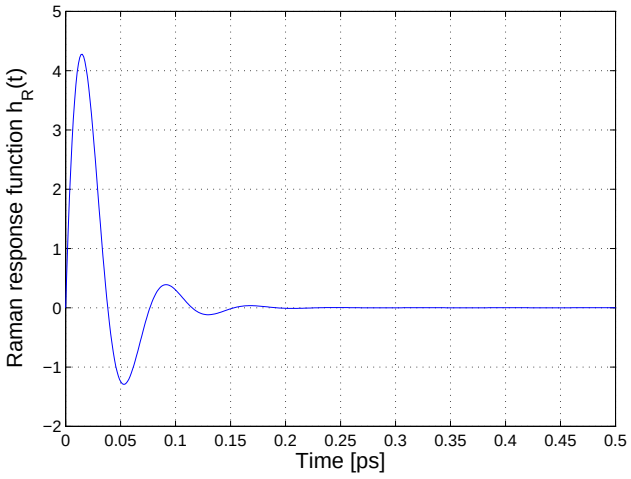

(b)

FIGURE 2.10: Raman response function a.) After Ref. [49]; b.) After Equation 2.22

The functional form of the nonlinear response function is given using the following equation:

$$R(t) = (1 - f_R)\delta(t) + f_R h_R(t) \tag{2.21}$$

where $(1 - f_R)\delta(t)$ accounts for the instantaneous electronic and $f_R h_R(t)$ is a delayed Raman contribution, where $f_R = 0.18$ (determined using the known numerical value of peak Raman gain) [49]. Raman response function $h_R(t)$ (set by vibrations of silica molecules induced by the optical field) is deduced from the experimentally measured

spectrum [49], but also the analytical form of the Raman response function can be used [1], [50]:

$$h_R(t) = \frac{(\tau_1^2 + \tau_2^2)}{(\tau_1 \tau_2^2)} \exp(-\frac{t}{\tau_2}) \sin(\frac{t}{\tau_1}) \tag{2.22}$$

where τ_1=12.2 fs ($1/\tau_1$ gives the optical phonon frequency) and τ_2=32 fs ($1/\tau_2$ gives the bandwidth of the Lorenzian line). Figure 2.10 shows the Raman response function of fused silica, obtained by using the experimentally measured spectrum (after Ref. [49]) and using analytical form of Equation 2.22.

2.5.3.5 Self steepening and optical shock effect

Self steepening is a higher order nonlinear effect which results from the intensity dependence of the group velocity. It causes an asymmetry in the SPM broadened spectra of ultrashort pulses as the pulse moves at a lower speed than the wings of the pulse [1]. Therefore, as the pulse propagates inside the fibre, the peak shifts towards the trailing edge and the trailing edge becomes steeper with increasing distance. Self steepening of the pulse creates an optical shock and is only important for short pulses.

2.6 Light propagation in optical fibres

In order to study nonlinear effects related to tapered microstructured optical fibres, including parabolic pulse generation in MOFs or supercontinuum generation in MOFs etc, it is necessary to consider the theory of electromagnetic wave propagation in optical fibres. A brief overview of the derivation of wave equation, starting from Maxwell's equations, as well as the derivation of nonlinear pulse propagation equation with numerical solutions, will be presented in this section.[1]

2.6.1 Maxwell's equations

All electromagnetic effects are governed by the four Maxwell equations, whose differential form in case of a dielectric medium when no free charges or currents are present in the entire domain is [1]:

$$\nabla \times \mathbf{E} = -\frac{\partial \mathbf{B}}{\partial t} \tag{2.23}$$

$$\nabla \times \mathbf{H} = \frac{\partial \mathbf{D}}{\partial t} \tag{2.24}$$

$$\nabla \cdot \mathbf{B} = 0 \tag{2.25}$$

[1] A more detailed derivation can be found in many books, for example Ref. [1].

$$\nabla \cdot \mathbf{D} = 0 \tag{2.26}$$

where **E** and **H** are respectively the vectorial electric and magnetic fields, **D** and **B** the electric displacement and magnetic induction fields. All these fields are functions of both space and time. All of the cases of interest for this research involve isotropic materials, and it is often a good approximation to assume propagation in the linear regime. For a nonmagnetic isotropic medium such as an optical fibre, the flux densities **D** and **B** are related to **E** and **H** via the constitutive equations:

$$\mathbf{D} = \varepsilon\mathbf{E} + \mathbf{P} \qquad \mathbf{B} = \mu\mathbf{H}. \tag{2.27}$$

where ε is the electric permittivity and μ is the magnetic permeability and **P** is the induced electric polarization. For the dielectric materials of interest to us, μ can be assumed to be a constant, equal to its free-space value. The electric permittivity ε is generally a function of frequency (ω). The imaginary part of ε accounts for material-related losses (absorption), but in case of low-loss dielectrics such as silica in the near infrared part of the spectrum, ε can be assumed to be purely real.

By applying the operator *curl* (*rotor*) on the Equation 2.23 and using Equation 2.24 and Equation 2.27 into the result, the following wave equation for the electric field can be obtained:

$$\nabla \times \nabla \times \mathbf{E} = -\frac{1}{c^2}\frac{\partial^2 \mathbf{E}}{\partial t^2} - \mu_0 \frac{\partial^2 \mathbf{P}}{\partial t^2} \tag{2.28}$$

where the induced electric polarization **P** is related to the electric field **E(r,t)** (far from medium resonances), given by the Equation 2.11.

The electric field **E(r,t)** can be expressed in terms of slowly varying envelope approximation as:

$$\mathbf{E}(\mathbf{r}, \mathbf{t}) = \frac{1}{2}\hat{x}[E(r,t)exp(-i\omega_0 t) + c.c.] \tag{2.29}$$

where $E(r,t)$ is a slowly varying complex envelope, $\hat{x}$ is the polarization unit vector, *c.c.* stands for complex conjugate and ω_0 is an angular optical frequency.

The linearity of Maxwell's equations permits the application of Fourier analysis. By using Fourier analysis, the wave equation Equation 2.28 expressed in the frequency domain is in the form of [1]:

$$\nabla^2 \tilde{\mathbf{E}} + \varepsilon(\omega) k_0^2 \tilde{\mathbf{E}} = 0 \tag{2.30}$$

where the free-space wave number is defined as:

$$k_0 = \frac{\omega}{c} = \frac{2\pi}{\lambda} \tag{2.31}$$

and the frequency dependent dielectric constant is:

$$\varepsilon(\omega) = 1 + \tilde{\chi}^{(1)}(\omega) + \varepsilon_{NL} \tag{2.32}$$

where ε_{NL} is the nonlinear contribution to the dielectric constant (treated as a constant during the pulse propagation) and is defined by:

$$\varepsilon_{NL} = \frac{3}{4}\chi^{(3)}_{xxxx}|E(r,t)|^2 \tag{2.33}$$

$\tilde{\chi}^{(1)}(\omega)$ is the Fourier transform of $\chi^{(1)}(t)$. Its real and imaginary parts can be related to the refractive index $\tilde{n}(\omega)$ and the attenuation coefficient $\alpha(\omega)$ by the equation:

$$\varepsilon = (\tilde{n} + \frac{i\alpha c}{2\omega})^2 \tag{2.34}$$

From Equation 2.32, Equation 2.34 and Equation 2.12, the following equations are obtained:

$$n(\omega) = 1 + \frac{1}{2}Re[\tilde{\chi}^{(1)}(\omega)] \tag{2.35}$$

$$\alpha(\omega) = \frac{\omega}{nc}Im[\tilde{\chi}^{(1)}(\omega)] \tag{2.36}$$

where Re and Im are real and imaginary parts, respectively. Since the imaginary part of $\varepsilon(\omega)$ is negligible in comparison to the real part (due to the low losses in fibres), then $\varepsilon(\omega)$ can be replaced by $\tilde{n}^2(\omega)$ ($\tilde{n}^2(\omega)$ is often independent of the spatial coordinates in both the core and cladding of step-index fibre), so that Equation 2.30 becomes:

$$\nabla^2\tilde{\mathbf{E}} + \tilde{n}^2(\omega)k_0^2\tilde{\mathbf{E}} = 0 \tag{2.37}$$

λ is the vacuum wavelength of the optical field oscillating at the frequency ω and $\tilde{E}$ is defined as:

$$\tilde{\mathbf{E}}(\mathbf{r},\omega) = \int_{-\infty}^{\infty} \mathbf{E}(\mathbf{r},\mathbf{t}) \exp i\omega t dt \tag{2.38}$$

In search for solutions of the optical field, it is useful to use method of separation of variables, so that the envelope $E(r,t)$ is in a form:

$$E(r,t) = F(x,y)A(z,t)exp(i\beta_0 z) \tag{2.39}$$

where $F(x,y)$ is transverse mode distribution, $A(z,t)$ is a slowly varying function of z and $\beta_0 = \beta(\omega_0)$ is the wavenumber at the carrier frequency. Substitution of Equation 2.39 into the wave equation leads to two equations, for $F(x,y)$ and $A(z,t)$ [1]. The wavenumber β is determined by solving the eigenvalue equation for the modes $F(x,y)$, whilst the temporal characteristics of the optical pulse are obtained using the solutions for $A(z,t)$. For step-index fibre $F(x,y)$ is obtained as a solution of differential equation for Bessel functions (note that in practice, the fundamental fibre mode is often approximated by a Gaussian distribution of the form $F(x,y) \approx \exp[-(x^2+y^2)/w^2]$, where w is the width parameter [1]).

The propagation constant β is generally a complex number, where the imaginary part accounts for the losses of the mode as it propagates along the fibre. In the case of a conventional optical fibre, the wave equation with the appropriate boundary conditions can be solved analytically [20]. However, for MOF fibres, expressing the boundary conditions in an analytical formula is usually very difficult. Therefore, numerical methods must be applied in order to calculate eigenvalues, eigenvectors and hence the optical properties of the structure. There are different numerical methods that can be used to treat this problem, having different advantages or disadvantages. A commonly used approach is based on the Finite Element Method (FEM). This method is a general technique for numerical solving of partial differential equations. It is based on discretising the domain and solving the problem on each subdomain to obtain exact solution on a discrete number of points. Using a linear combination of basis functions, usually linear, the unknown field or functions can be approximated. The FEM elements are flexible from both geometric point of view (easy treatment of any shape of structure) and the material point of view (inhomogeneous, anisotropic or non-linear characteristics could be incorporated) [20]. At the ORC a variety of methods for tackling the design of MOF was investigated and different comparative tests on both accuracy and speed were conducted. As a result, it was decided that the FEM implementation of `Comsol Multiphyics`® represented significant advantages over other methods [22].

2.6.2 Nonlinear pulse propagation equation

In order to be able to observe different nonlinear effects in the MOF and tapered MOF, it is necessary to solve the pulse propagation equation, which originates from the wave equation in the frequency domain. To solve the wave equation (Equation 2.30) in the frequency domain, the method of separation of variables can be used [1], [51]. The solution of the Equation 2.30 can be assumed in the following form:

$$\tilde{\mathbf{E}}(\mathbf{r}, \omega - \omega_{\mathbf{0}}) = F(x, y)\tilde{A}(z, \omega - \omega_0)\exp(i\beta_0 z) \tag{2.40}$$

where $\tilde{A}(z, \omega)$ is a slowly varying function of z, β_0 is the wavenumber and $F(x, y)$ corresponds to the modal distribution in the fibre. Preceding the derivation, the following assumptions are made to simplify the Equation 2.28. Firstly, $\mathbf{P_3}$ is treated as a small perturbation to $\mathbf{P_1}$ because the nonlinear changes in the refractive index are very small compared to the linear effect. Secondly, the optical field is assumed to maintain its polarization along the fibre length so that a scalar approach can be used. Substituting Equation 2.40 into the Equation 2.37, leads to the following equations [1]:

$$\frac{\partial^2 F}{\partial x^2} + \frac{\partial^2 F}{\partial y^2} + [\varepsilon(\omega)k_0^2 - \tilde{\beta}^2]F = 0 \tag{2.41}$$

$$2i\beta_0 \frac{\partial \tilde{A}}{\partial z} + (\tilde{\beta}^2 - \beta_0^2)\tilde{A} = 0 \tag{2.42}$$

where the second derivative $\frac{\partial^2 \tilde{A}}{\partial z^2}$ is ignored, since $\tilde{A}(z, \omega)$ is a slowly varying function of z. The wavenumber $\tilde{\beta}$ is determined by solving the Equation 2.41 (this gives the modes of the fibre, as discussed previously). The eigenvalue $\tilde{\beta}$ can be written by $\tilde{\beta}(\omega) = \beta(\omega) + \Delta\beta$, where $\Delta\beta$ is found to satisfy the relation:

$$\Delta\beta = k_0 \frac{\int\int_{-\infty}^{\infty} \Delta n |F(x, y)|^2 dxdy}{\int\int_{-\infty}^{\infty} |F(x, y)|^2 dxdy} \tag{2.43}$$

where $F(x, y)$ is the modal field distribution and x and y are the transverse coordinates.

Equation 2.42 can be well approximated by replacing $(\tilde{\beta}^2 - \beta_0^2)$ with $2\beta_0(\tilde{\beta} - \beta_0)$ as:

$$\frac{\partial \tilde{A}}{\partial z} - i[\beta(\omega) + \Delta\beta - \beta_0]\tilde{A} = 0 \tag{2.44}$$

By transforming Equation 2.44 back to the time domain, the propagation equation for $A(z, t)$ can be obtained. However, it is necessary to know the functional form of $\beta(\omega)$. Note that $\beta(\omega)$ can be expanded in a Taylor series about the centre frequency ω_0 as:

$$\beta(\omega) = \beta_0 + (\omega - \omega_0)\beta_1 + \frac{1}{2!}(\omega - \omega_0)^2\beta_2 + \frac{1}{3!}(\omega - \omega_0)^3\beta_3 + \cdots \tag{2.45}$$

where β_k is k^{th} order dispersion coefficient defined as:

$$\beta_k = (\frac{d^k \beta}{d\omega^k})_{\omega=\omega_0} \qquad\qquad k = 1, \cdots, n \tag{2.46}$$

Equation 2.45 reflects the dispersion character of an optical fibre (β_2 is the group velocity dispersion (GVD) and β_3 is the third order dispersion).

Equation 2.45 is substituted into Equation 2.44 and after taking the inverse Fourier transform [during the transform $\omega - \omega_0$ is replaced by $i(\partial/\partial t)$], the resulting propagation equation is obtained:

$$\frac{\partial A}{\partial z} = -\beta_1 \frac{\partial A}{\partial t} - \frac{i}{2}\beta_2 \frac{\partial^2 A}{\partial t^2} + \frac{1}{3!}\beta_3 \frac{\partial^3 A}{\partial t^3} + \cdots + i\Delta\beta A \tag{2.47}$$

where $\Delta\beta$ is evaluated by using Equation 2.12 and Equation 2.43, so that the following is obtained:

$$\frac{\partial A}{\partial z} + \beta_1 \frac{\partial A}{\partial t} + \frac{i}{2}\beta_2 \frac{\partial^2 A}{\partial t^2} - \frac{1}{3!}\beta_3 \frac{\partial^3 A}{\partial t^3} + \cdots + \frac{\alpha}{2}A = i\gamma|A|^2 A \tag{2.48}$$

The nonlinearity coefficient γ is:

$$\gamma = \frac{n_2 \omega \int_{-\infty}^{\infty}\int_{-\infty}^{\infty} |F(x,y)|^4 dxdy}{c(\int_{-\infty}^{\infty}\int_{-\infty}^{\infty} |F(x,y)|^2 dxdy)^2} \tag{2.49}$$

Equation 2.49 is equivalent to:

$$\gamma = \frac{2\pi n_2}{\lambda A_{eff}} \tag{2.50}$$

where A_{eff} is the effective area, introduced to estimate the optical field concentration inside the fibre [13], [18]. A_{eff} is defined as:

$$A_{eff} = \frac{(\int_{-\infty}^{\infty}\int_{-\infty}^{\infty} |F(x,y)|^2 dxdy)^2}{\int_{-\infty}^{\infty}\int_{-\infty}^{\infty} |F(x,y)|^4 dxdy} \tag{2.51}$$

Conventional step-index, single mode fibres have $A_{eff} \simeq 80\ \mu m^2$, which corresponds to $\gamma \simeq 1\ W^{-1}km^{-1}$. Smaller values of A_{eff} enhance the nonlinearity of the fibres and significantly increase γ, by the strong confinement of light in the core region of the fibre.

Equation 2.48 is called the nonlinear Schrödinger equation (NLSE) and it describes pulse propagation in an optical fibre. It takes into account the effect of dispersion through β_k, the effect of nonlinearity through γ and fibre loss through parameter α. The pulse amplitude A is normalized such that $|A|^2$ is the optical power. To solve the NLSE equation it is useful to introduce a new reference (t, z) (new t is retarded time), which travels with the pulse at group velocity v_g ($v_g = 1/\beta_1$). So, the new variable t is $t = t - z/v_g = t - \beta_1 z$, and the NLSE can be written as:

$$\frac{\partial A}{\partial z} + \frac{i}{2}\beta_2\frac{\partial^2 A}{\partial t^2} - \frac{1}{3!}\beta_3\frac{\partial^3 A}{\partial t^3} + \cdots + \frac{\alpha}{2}A = i\gamma|A|^2 A \tag{2.52}$$

Equation 2.48 should also be modified for ultrashort optical pulses (width $\leq$ 100 fs). The NLSE equation in the generalized form, which includes the effect of Kerr nonlinearity, SRS, self-steepening and optical shock effect, in addition to the fibre loss and dispersion, is given by the following expression:

$$\frac{\partial A}{\partial z} + \frac{i}{2}\beta_2\frac{\partial^2 A}{\partial t^2} - \frac{1}{3!}\beta_3\frac{\partial^3 A}{\partial t^3} + \cdots + \frac{\alpha}{2}A = i\gamma(1 + \frac{i}{\omega_0}\frac{\partial}{\partial t})(A(z,t)\int_0^\infty R(t')|A(z,t-t')|^2 dt') \tag{2.53}$$

where $R(t)$ is Raman response function. For broad band application, such as supercontinuum generation, it is necessary to include higher order dispersion terms up to β_{10} [23], [52].

The retarded time can be normalized with the initial pulse width T_0 so that $\tau = t/T_0$ (t - retarded time). The normalized distance is $\xi = z|\beta_2|/T_0^2$ and at the same time a normalized amplitude u can be introduced, when α=0, using [1] :

$$u(z,\tau) = A(z,\tau)/\sqrt{P_0} \tag{2.54}$$

where P_0 is the peak power of the incident pulse.

Using the normalized amplitude u, the NLSE Equation 2.52, when $\beta_3 = 0$ and $\alpha = 0$, becomes :

$$\frac{\partial u}{\partial \xi} + i\frac{s}{2}\frac{\partial^2 u}{\partial \tau^2} - iN^2|u|^2 u = 0 \tag{2.55}$$

where $s = \mathrm{sgn}(\beta_2)$=+1 (when $\beta_2 > 0$) and $s = -1$ (when $\beta_2 < 0$) and $N^2 = \gamma P_0 T_0^2/|\beta_2|$.

2.6.2.1 Different propagation regimes

Different propagation regimes can be distinguished in optical fibres [1]. Depending on the initial pulse temporal width T_0 and the peak power P_0 either dispersive or nonlinear effect can dominate along the fibre. Two length scales over which the dispersion or nonlinearity effects become important for pulse propagation are the dispersion length, L_D, ($L_D = \frac{T_0^2}{|\beta_2|}$) and nonlinear length, L_{NL}, ($L_{NL} = \frac{1}{\gamma P_0}$), where γ is nonlinearity coefficient, defined by Equation 2.50 and β_2 is GVD.

In a case if fibre length L is such that $L \ll L_D$ and $L \ll L_{NL}$ then neither dispersive nor nonlinear effects dominate pulse evolution and pulse propagates maintaining its shape during the propagation. As pulses become shorter and more intense, both L_D

and L_{NL} become smaller. If $L \ll L_D$ and $L \sim L_{NL}$, the pulse evolution is dominated by SPM that spectrally broadens the pulse. The opposite is true, if $L \ll L_{NL}$ and $L \sim L_D$, when the pulse evolution is governed by the dispersive effect (GVD). For example, at $\lambda = 1.55$ μm, parameters of the standard telecommunication fibre are $|\beta_2| \approx 20\ ps^2/km$ and $\gamma \approx 1\ W^{-1}km^{-1}$, so one can determine T_0 and P_0 to obtain the dominant propagation regime. To achieve dispersion dominant regime, P_0 should be $\ll$ 1 W for 1 ps pulses, whilst to achieve the SPM dominant regime, pulses of temporal widths $T_0 > 100\ ps$ should be used for peak powers of $P_0 \sim 1\ W$ [1].

2.6.2.2 Numerical Solution to the NLSE - the split step Fourier method

There is a number of different methods, [53] - [56], that could be used to solve the NLSE. The most commonly employed method is the split-step Fourier method (SSFM) [1], [53]. The SSFM is a pseudo-spectral method which is faster by up to two orders of magnitude compared to finite difference methods [1]. For the pulse widths of the order of *ps* this method is shown to work efficiently and accurately [1], [53]. In this thesis the SSFM is employed to solve the NLSE to observe parabolic pulse generation in tapered microstructured optical fibres (Chapter 4 and Chapter 5). This method relies on the steps that will be explained briefly. Mathematically, Equation 2.52 can be expressed in the following form:

$$\frac{\partial A}{\partial z} = [\hat{D} + \hat{N}]A \tag{2.56}$$

where $\hat{D}$ is linear differential operator that takes into account dispersion and absorption in the medium and $\hat{N}$ is a nonlinear operator that accounts for the effect of fibre nonlinearities on pulse propagation [1]. These operators are defined as:

$$\hat{D} = -\frac{\alpha}{2} - i\frac{\beta_2(z)}{2!}\frac{\partial^2}{\partial t^2} + \frac{\beta_3(z)}{3!}\frac{\partial^3}{\partial t^3} \tag{2.57}$$

$$\hat{N} = i\gamma(z) \mid A \mid^2 \tag{2.58}$$

Both the linear and the nonlinear parts have analytical solutions. Under the assumption that a small step h is taken along z, two parts can be treated to act separately with only a small numerical error. One can therefore first take a small nonlinear step while $\hat{D} = 0$ and in the second step, dispersion acts alone and $\hat{N} = 0$. Mathematically, for the standard SSFM, the solution of the differential equation at step $z = jh$ is given by:

$$A(t, z + h) = IFFT[\exp(h\hat{D}(i\omega))FFT\{\exp(h\hat{N})A(t, z)\}] \tag{2.59}$$

where j is an integer, $j = 1, 2, \cdots N$, number of steps of length h is $N = L/h$ and L is the total fibre length.

The operation of $\hat{D}$ is performed in the frequency domain. By taking the inverse Fourier transform the pulse has thus been propagated a small step h. Next, the procedure is repeated so the pulse can be propagated over a total length of L. The Fourier transforms of this algorithm can be computed relatively fast using the fast Fourier transform (FFT). The SSFM is accurate to first order in the step size h [53]. The accuracy of the SSFM can be improved by adopting a different procedure (symmetrised SSFM) to propagate the optical pulse over one segment from z to $z + h$. At $z = jh$ the pulse envelope is described as:

$$A(t, z+h) = IFFT[\exp(\frac{h}{2}\hat{D}(i\omega))FFT\{\exp(\int_{z}^{z+h}\hat{N}(z')dz')IFFT\{\exp(\frac{h}{2}\hat{D}(i\omega))FFT\{A(t,z)\}\}\}] \tag{2.60}$$

For the symmetrised SSFM, first the dispersion over a distance $h/2$ is computed, the effect of nonlinearity occurs at the step mid-point and the effect of dispersion is computed again over $h/2$. The integral of nonlinearity operator is treated as a constant as it accounts for the change of γ over the step h. This procedure is repeated until the end of the fibre is reached.

2.6.2.3 Numerical Solution to the NLSE - the Runge Kutta interaction picture method

In order to simulate supercontinuum generation in the optical fibre, the generalized NLSE (GNLSE) has to be solved. I used an alternative method to the SSFM to solve the GNLSE - the fourth order Runge Kutta in the interaction picture method (RK4IP) [54]. The `Matlab` code that I have written, which models supercontinuum generation in tapered MOF (presented in Chapter 6), is based on the mathematical interpretation that will be briefly explained.

The GNLSE that describes pulse propagation in tapered optical fibre, in the co-moving frame, can be written as:

$$\frac{\partial A}{\partial z}+\frac{i}{2}\beta_2(z)\frac{\partial^2 A}{\partial t^2}-\frac{1}{3!}\beta_3(z)\frac{\partial^3 A}{\partial t^3}+\cdots+\frac{\alpha}{2}A = i\gamma(z)(1+\frac{i}{\omega_0}\frac{\partial}{\partial t})(A(z,t)\int_0^\infty R(t')|A(z,t-t')|^2dt') \tag{2.61}$$

where $A(z, t)$ is the slowly varying envelope of the electric field, z is the distance along the fibre, t is time in a copropagating time-frame.

The RK4IP method is closely related to the SSFM and the studies showed that it is the most accurate and efficient when compared to the standard methods [54]. The RK4IP

procedure is based on transforming the problem into an interaction picture, which allows the use of the explicit techniques to progress the solution forward [54].

Similarly to the SSFM method, the GNLSE Equation 2.61 can be expressed mathematically in the following form:

$$\frac{\partial A}{\partial z} = [\hat{D} + \hat{N}]A \tag{2.62}$$

where $\hat{D}$ is linear differential operator that takes into account dispersion and absorption in the medium and $\hat{N}$ is a nonlinear operator that accounts for the effect of fibre nonlinearities on pulse propagation, self steepening, shock effect and SRS effect. These operators are defined as:

$$\hat{D} = -\frac{\alpha}{2} - i\frac{\beta_2(z)}{2!}\frac{\partial^2}{\partial t^2} + \frac{\beta_3(z)}{3!}\frac{\partial^3}{\partial t^3} + \cdots \tag{2.63}$$

$$\hat{N} = i\gamma(z)(1 + \frac{i}{\omega_0}\frac{\partial}{\partial t})(A(z,t)\int_0^\infty R(t')|A(z,t-t')|^2 dt') \tag{2.64}$$

In this method the GNLSE is transformed into an interaction picture in order to separate the effect of dispersion contained in $\hat{D}$ from the nondispersive terms contained in $\hat{N}$. This allows the use of explicit techniques to propagate the solution. The field envelope A is transformed into the interaction picture representation A_I by the following equation [54]:

$$A_I = \exp(-(z-z')\hat{D})A \tag{2.65}$$

where z' is the separation distance between the interaction and normal pictures (the more detailed explanation of the method given in [57]). Differentiating the Equation 2.65 gives the evolution of A_I:

$$\frac{\partial A_I}{\partial z} = \hat{N}_I A_I \tag{2.66}$$

where $\hat{N}_I = \exp(-(z-z')\hat{D})\hat{N}\exp((z-z')\hat{D})$ is the nonlinear operator in the interaction picture. The differential equation Equation 2.66 can now be solved using conventional explicit schemes, such as Runge Kutta, as the stiff linear part have been moved into the interaction picture [54]. The step mid-point is chosen as the separation distance $z' = z + h/2$. The algorithm that advances $A(z,T)$ to $A(z+h,T)$ in a spatial step h, expressed in a normal picture now, is given by following equations:

$$A_I = \exp(\frac{h}{2}\hat{D})A(z,T) \tag{2.67}$$

$$k_1 = \exp(\frac{h}{2}\hat{D})[h\hat{N}(A(z,T))]A(z,T) \tag{2.68}$$

$$k_2 = h\hat{N}(A_I + \frac{k_1}{2})[A_I + \frac{k_1}{2}] \tag{2.69}$$

$$k_3 = h\hat{N}(A_I + \frac{k_2}{2})[A_I + \frac{k_2}{2}] \tag{2.70}$$

$$k_4 = h\hat{N}(\exp(\frac{h}{2}\hat{D})(A_I + k_3))[A_I + k_3] \tag{2.71}$$

$$A(z+h,T) = \exp(\frac{h}{2}\hat{D})[A_I + \frac{k_1}{6} + \frac{k_2}{3} + \frac{k_3}{3}] + \frac{k_4}{6} \tag{2.72}$$

In this method the number of FFTs per step is reduced by half compared to the required number of FFTs if the classical fourth order Runge Kutta has been employed. Also, the method has a local error which is a fifth order accurate and is globally fourth order accurate [54].

The `Matlab` implementation of the RK4IP method is shown in Appendix D.

2.7 Pulse measuring techniques

In order to be able to better understand the behaviour of pulses propagated in optical fibres, it is necessary to have well established methods that would provide measurements of the pulses' electric field (amplitude and phase). This is of importance to the verification of numerical models and simulations. There are several different methods used for pulses characterisation applicable in the field of communications. The methods commonly used at the ORC are Frequency Resolved Optical Gating (FROG) and linear FROG (l - FROG).

2.7.1 Frequency Resolved Optical Gating

Measuring the intensity profile in the time domain is much more challenging than in the frequency domain [58], [59]. The measurement technique that allows the complete characterisation of optical waveform is Frequency Resolved Optical Gating. This method is classified as the spectrographic method and the technique requires more postprocessing of the measured traces and involves an inversion step in which the intensity and phase are retrieved from a set of measurements. It is commonly used technique in the area of

pulsed laser characterisation. The operating principle of FROG in shown in Figure 2.11. The method is based on the nonlinear interaction in a second harmonic generating (SHG) crystal, between two replicas of the same pulse [58]. The input pulse is split into two replicas and one passes through variable delay stage. The two pulses are recombined within the second harmonic generating crystal. At the overlap (temporal and spatial) between the two pulses after the SHG crystal, the photons are generated at the sum-frequency of the two overlapping photons [58].

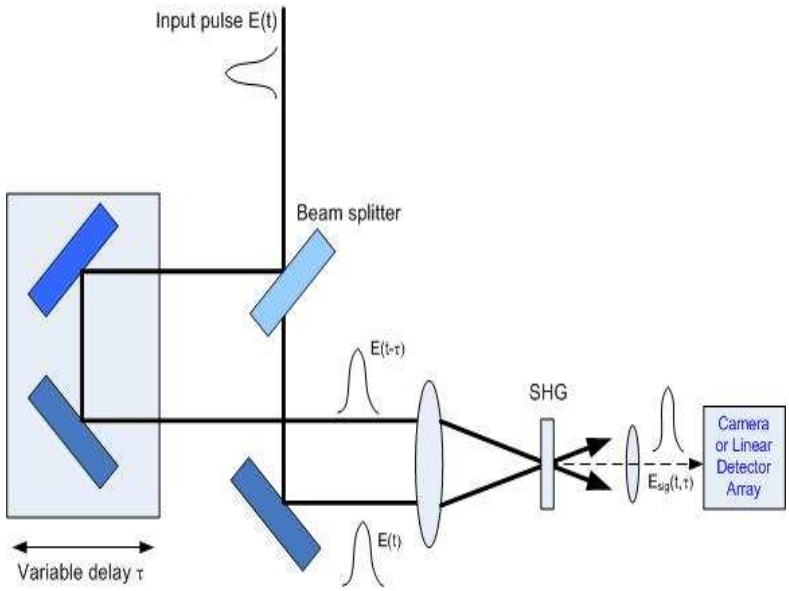

FIGURE 2.11: Block diagram of the operating principle of the FROG; After Ref. [58]

The SHG pulse is spectrally resolved with a spectrometer, as an intensity spectrum in a function of delay between the two replicas of the original pulse. Spectrogram is a time-frequency distribution of a pulse, or a pair of pulses. The intensity spectrum of a pulse $E(t)$ is measured after gating as a function of the delay τ between the gating function and the pulse under test. The experimental trace is mathematically represented as:

$$S(\tau,\omega) = \mid \int E(t)E(t-\tau)exp(i\omega t)dt \mid^2 \tag{2.73}$$

The next step is to apply a retrieval algorithm which attempts to find a pulse shape that would have the same spectrogram as the one that is measured. However, the main disadvantage of second harmonic generation FROG is that the two-dimensional FROG trace is a time symmetrical function, which leads to the ambiguity in the direction of time. This problem could be overcome by taking another measurement of the pulse after

introducing a certain known distortion (as by propagating through a known dispersive medium), so that such a pulse will establish a direction of time of the retrieved pulse. Another disadvantage of this method is that it requires careful free space alignment and that the method relies on nonlinearities. For these reasons the linear FROG method is preferably in use within the ORC telecom lab and the same one was used in the work conducted in Chapter 5 of this thesis.

2.7.2 Linear Frequency Resolved Optical Gating

It has been shown that it is possible to implement the gating with a modulator [60], instead of relying on nonlinear optics and the technique is commonly known as Linear Frequency Resolved Optical Gating (l-FROG). This technique was developed in the ORC telecom lab by Dr M. Roelens and Dr B. Thomsen, [59], and has been used since. The pulse characterisation throughout the Chapter 5 of this thesis was taken using l-FROG technique.

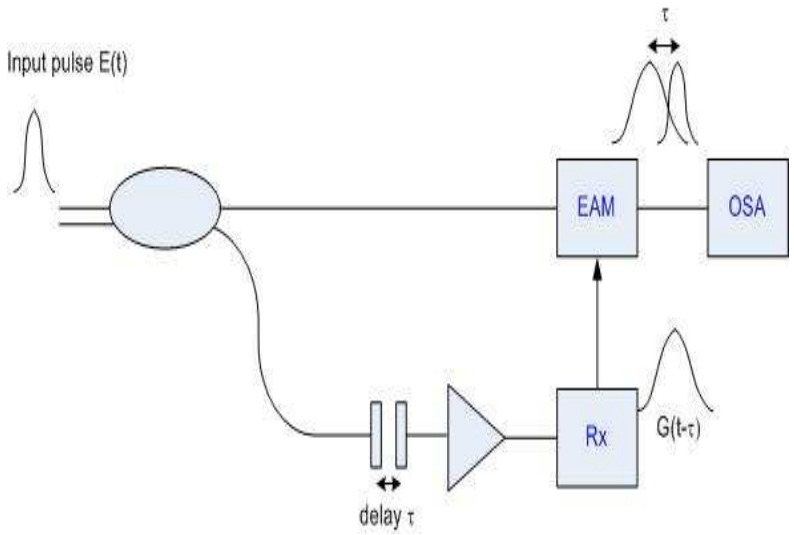

FIGURE 2.12: Block diagram of the operating principle of a l-FROG; After Ref. [59]

The schematic diagram of this technique, incorporating the Electro Absorption Modulator (EAM), is shown in Figure 2.12. The input pulse under test is split of with an optical fibre coupler into two replicas. One is the probe signal which passes through the EAM. The other one, a gate signal, is delayed by a motorized variable time delay (G(t-τ)) stage and used to drive the EAM. The gated signal is spectrally resolved by an OSA and the resulting signal can be expressed by Equation 2.73. The choice of fast

photodetector and a broadband amplifier allows creation of the short electrical pulses, which consequently enables creation of a shorter sampling windows in the modulator. Electro absorption modulator is suitable as it provides very fast switching speeds and can be polarisation insensitive [58].

After the measurement phase to acquire a spectrogram, the retrieval of the intensity and phase of the measured pulses from the spectrogram is performed. In order to speed up the convergence of the reconstruction algorithm, the retrieved gating function of a particular spectrogram is fed into the retrieval of the following spectrogram as an initial guess. The retrieval procedure is explained in detail in [59].

2.8 Conclusion

This Chapter gives a theoretical overview of the main topics that need to be known to allow understanding of the work presented in this thesis.

An introduction of the microstructured optical fibres, with the emphasis on the guidance mechanisms and most important definitions, as well as an introduction to tapered fibres, is given. Brief overview of the fundamental properties, materials and fabrication techniques, is shown. The general background of the dispersive and nonlinear effects in standard and MOFs is described in this Chapter, too. Nonlinear effects, such as self phase modulation and stimulated Raman scattering, are briefly reviewed. Furthermore, for an understanding of the nonlinear phenomena it is necessary to consider the basic equations that determine the propagation constant and governs the propagation of optical pulses. The derivation procedures of the wave equation and the NLSE equation are shown. The nonlinear pulse propagation in optical fibres is simulated using both split step Fourier method and fourth order Runge Kutta interaction picture method, therefore both methods are described in this chapter. The introduction of the techniques for the complete optical pulse characterisation, FROG and l-FROG, is given.

Chapter 3

A Novel Method for the Fabrication of Optical Fibre Tapers

3.1 Introduction

Over the past decade the tapering of optical fibres (both step index and PCFs) has been widely investigated [61] - [67] and have found many applications, particularly in nonlinear optics. While short (<10 cm) and long (>10 m) tapers have been successfully manufactured by the flame−brushing [68] and by the drawing tower techniques [26], no method has been demonstrated for the manufacture of tapers of arbitrary profiles in the intermediate length range, meso-tapers (MT)[1]. Flame - brushing technique has a limited translational range of the elongation stages, therefore only short tapers can be produced. The total taper length is also restricted by the fibre initial diameter, target waist diameter, length and temperature uniformity of the hot zone [66], [68]. Moreover, with traditional techniques it is very difficult to achieve accurate control of the fibre diameter over long lengths and to manufacture tapers with a non-monotonically decreasing/increasing profile.

Long optical tapers could be used to improve results of the pulse compression in a soliton system [69] - [74], for parabolic pulse generation in the normal dispersion regime [75] - [77], supercontinuum generation [78] - [80] or to control many other nonlinear processes, such as stimulated Brillouin scattering [31], where tapered fibre could be used to control the growth of the Brillouin signal. The single mode fibre tapers proposed in the literature and used for applications such as sensors, directional couplers or beam expanders, are usually short lengths (several cm). The taper shape has to be considered as it is relevant

[1]Donlagic in Ref. [66] suggested the possible approach.

to the particular application [81] - [83]. Many other applications of tapered fibres were considered in the literature, from different applications in controlling nonlinear optical properties of the fibres [84], [85], photonic nanowires fabrication [86], or spot-size and numerical aperture conversion [87]. The theoretical fundamentals of the tapering fluid dynamics, as well as the characterisation of the tapering process is explained in Refs. [88] - [92].

In this Chapter, I present in detail a novel taper rig to manufacture MT and demonstrate that it is possible to make intermediate - length tapers with potentially arbitrary profiles. Compared to other tapering rigs which simultaneously elongate the fibre from both ends, this taper rig feeds in the fibre continuously from one side and heats and stretches it before respooling it on the far side. This new system is analogous to the tapering method using the fibre drawing tower, but scaled down to the intermediate fibre lengths. The new system performs process of fibre stretching horizontally, whilst there is vertical stretching in the drawing tower technique. Moreover, in the drawing tower technique the control accuracy is limited, due to the large drawing speeds and large time constant of the process, which set the controllability to tens of centimetres, which implies that there is no control when the total tapering length is of the order of 1 m. From this reason, there is a need to develop a tapering facility capable of producing intermediate length tapers with the enhanced control accuracy. In addition, we anticipate that this system could be of particular importance in a soliton compression systems using dispersion decreasing fibres [34] - [38]. In particular, if the input pulse temporal width of $\sim$1 ps is used, it yields the dispersion length L_D $\sim$100 m, so that the fibres could be tapered using the fibre drawing tower method. However, for the input pulse power in the range of $\sim$100 fs, L_D $\sim$1 m, such as in [35], where the efficient soliton pulse compression could be achieved in a few meters of tapered fibre. In this case it is of high importance to minimize the fibre length, due to the presence of realistic fibre losses, while maintaining high compression [35]. This specific application contributes to our motivation and justifies the need for fabricating intermediate length optical fibre tapers.

Here I show an improved control over the taper diameter when a feedback loop is built into the system. The optical properties of fibres such as dispersion, nonlinearity etc., strongly depend on the fibre diameter, therefore it is very important to have a good accuracy over the fibre diameter during the tapering process and to reduce the ripple in it. The accuracy of the system is illustrated on several different tapering experiments. The examples include a non−monotonically linear profile for the step index fibre, a step-index fibre taper with a periodically varying diameter profile, step index fibre tapered linearly 70% at 20 cm length and a linearly tapered microstructured optical fibre with 50% decrease in diameter over the 60 cm length.

3.2 System Description

The block diagram of the experimental set-up for the fabrication of MT is shown in Figure 3.1 and the system as set-up is shown in Figure 3.2.

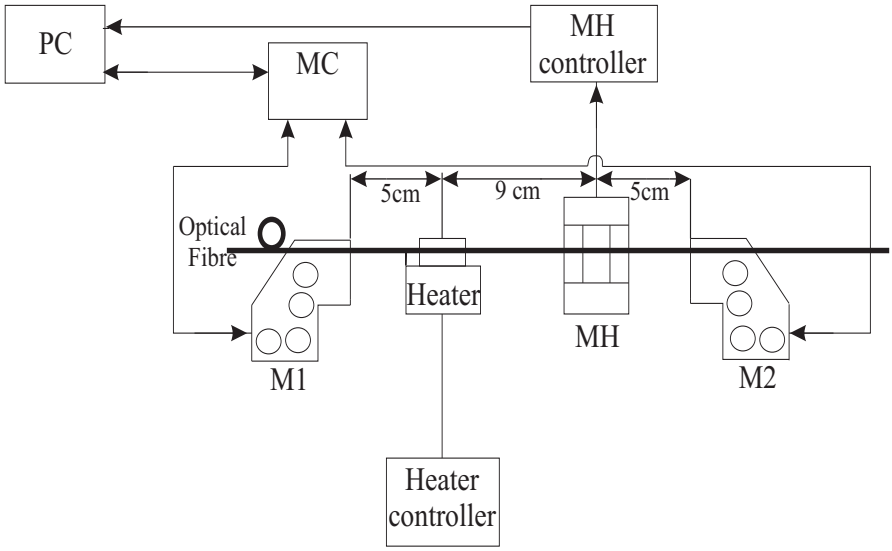

FIGURE 3.1: Experimental set-up; MH - Measuring Head, MC - Motors Controllers, M1- feeding motor, M2 - drawing motor

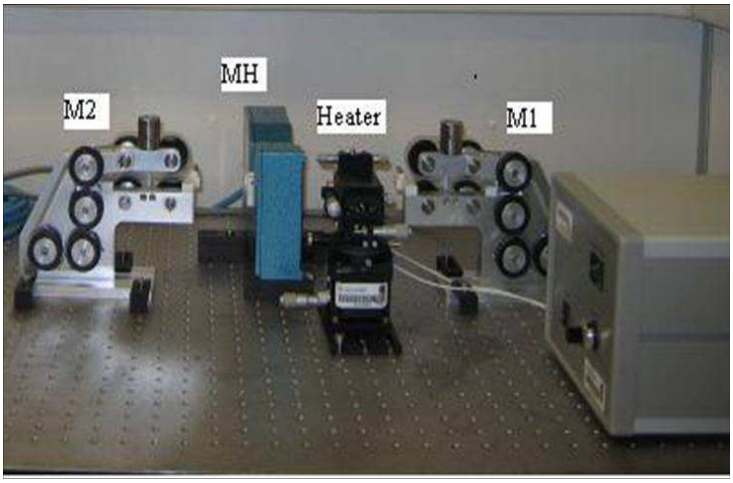

FIGURE 3.2: Photo of the experimental set-up; MH - Measuring Head, M1- feeding motor, M2 - drawing motor

The tapering rig comprises two rotary controllers which control the feed and draw speed of the fibre, a heating element, an accurate diameter measuring gauge and a computer to control the system. The part of the system comprising the controllers is based on a high performance digital signal processor (DSP), which enables a high control quality, precise positioning and very low speeds (4.5 - 45 mm/min), using RS - 232 interface for PC command and communication. The drive can be operated via RS-232 interface

or independently, if the desired function has been previously programmed via analogue input. The system has two rotating units - DC motors (M1 and M2) in combination with optical encoders. The commercial measuring head is based on using a laser beam to accurately measure (resolution up to 0.1 μm) the fibre diameter, and the signal is continuously sent to the processor unit. A linear measurement precision of 9.1 μm per motor rotation is achieved with this system. Although the current system does not allow for easy tension monitoring in the fiber, this might be possible via future improvement of the system. Due to the high temperature of the ceramic microheater (heater unit $\sim$1500 °C), the diameter measurement unit is spaced by a distance l_m (currently 9 cm) away from the heater. As a result, there is a pure transport delay in measuring the exit diameter d_e equal to $\tau = \frac{l_m}{v_e}$ (v_e is the exit speed). This delay limits the response speed of the feedback controller.

3.3 Control Problem Formulation

Generally, the output fibre diameter, d_e, on the average, is governed by the low of mass conservation in steady state [66], [68]:

$$d_e = \sqrt{\frac{v_f}{v_e}} d_f \tag{3.1}$$

where v_f is the preform feeding speed, d_f is the preform diameter, v_e is the fibre drawing (exit) speed and $d_e = d$ is a fibre diameter. However, at any instant of time or distance, the diameter is influenced by various factors, such as the state of the glass or other process conditions, in a random manner [89]. Figure 3.3 shows a schematic diagram of the tapering operation used to build a model for the control problem formulation.

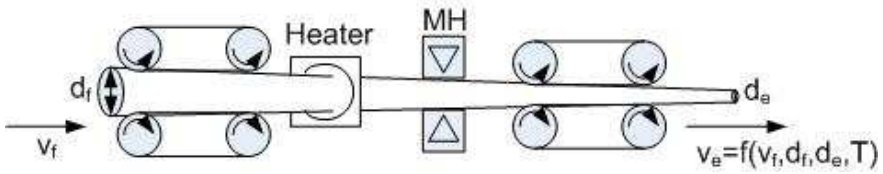

FIGURE 3.3: Schematic diagram of tapering operation; v_f - feeding speed, d_f - preform diameter, v_e - fibre drawing (exit) speed, d_e - exit fibre diameter, MH - Measuring Head

Equation 3.1 was used to build a `Matlab` based application that controls the feeding and drawing motors. During the initialization phase, serial ports for communication with feeding/drawing motor (M1, M2) and measurement head (MH) are initialized. Next,

motor controllers are initialized to velocity control mode, so that controllers follow the speed profile set by serial communication. At the same time, internal controller position counters are reset to zero. The desired tapering profile is specified as a function of exit diameter $d(l), l \in [0, L]$ as function of the tapering length l. The taper length (L) is divided into a (large) number of segments, and desired tapering profile across the segment is assumed to be constant i.e. $d_i(l_i) = d_i, i = 1, \cdots, N$. The length of the segments can be set according to required precision in specifying the taper shape. Knowing the preform diameter d_f, and desired exit diameter d_i, we have the ratio of feeding to exit speed (v_f/v_e) determined $(\frac{d}{d_f})^2 = \frac{v_f}{v_e}$, but the initial value of one of these speeds is arbitrary, and has to be specified according to the desired tapering time. With one of the speeds, v_f, v_e, specified, the other one is determined according to Equation 3.1. In this way, we have discretised the continuous taper length space. However, to enable application of control/signal processing algorithms, sampling in time should be used. Therefore, the `Matlab` timer is initialized with sampling period $T_s = 0.5\ s$, and started. On every timer expire period, measurements of the M1/M2 position, current and velocity are sampled. The current distance is compared to the segment boundaries, and (precomputed) velocity setpoint corresponding to the current segment sent to motor controller. Several sets of measurements on both step index and microstructured optical fibres performed while testing the system have shown that the fibre cladding variation of the untreated fibre is within $\pm\ 1\ \mu m$, which is in good agreement with the fibres manufacturers' specifications. During the first 9 cm distance (see Figures 3.11, 3.15, 3.16), which corresponds to the delay between the measuring head and the heater, there is a small diameter variation of an untreated fibre. In this thesis I have assumed $d_f = const$ during tapering.[2]

There are three possible speed profiles: 1.) Feeding motor M1 speed (v_f) remains constant during the tapering and exit motor M2 speed changes in accordance with Equation 3.1; 2.) Exit motor M2 speed (v_e) remains constant during the tapering and feeding motor M1 speed changes in accordance with Equation 3.1; 3.) Both the exit motor and the feeding motor speeds change so that the drawing speed remains bellow pre-specified limit v_{dmax}. Figure 3.4.a illustrates the first case, Figure 3.4.b represents the second case and Figure 3.4.c shows the speed profiles according to the third case. The case illustrated in Figure 3.4.c is based on the modification of the algorithm, such that at the point l_i, where $v_d(l_i) = v_e - v_f = v_{dmax}$, we first calculate the desired diameter ratio $d_f/d(l_i)$ and the desired drawing ratio $v_f(l_i)/v_e(l_i)$ and then with the specified 'head-room' parameter $h_d \in [0, 1]$, the drawing speed can be calculated in the following equation:

$$v_d = v_e - v_f = v_f((\frac{d_f}{d(l)})^2 - 1) = h_d v_{dmax} \tag{3.2}$$

[2]The measurement of the diameter variation of the untreated fibre will be affected by the inevitable presence of disturbances in the system and therefore it was much simpler to assume constant diameter of the untreated fibre.

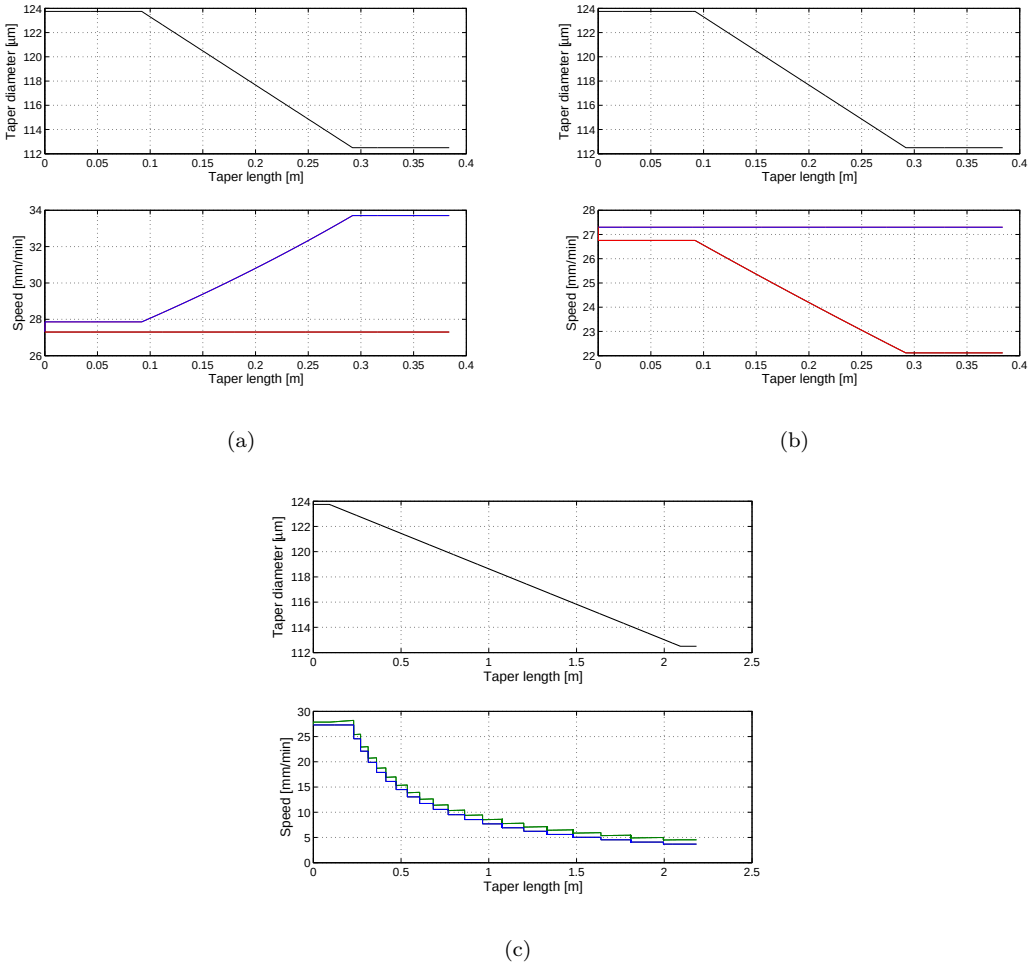

FIGURE 3.4: a.) Taper diameter and speed profile, v_f = const, red - v_f, blue - v_e; b.) Taper diameter and speed profile, v_e = const, red - v_f, blue - v_e; c.) Taper diameter and speed profile, v_f and v_e change, green - v_e, blue - v_f

The second and the third case are particularly useful when we want to achieve higher tapering ratios (more than 50%), when the major limitation of the first case is that the maximum velocity of the motors (limited to 5000 rpm) would be exceeded. In the third case we can see that both feed and exit speed are now changing during tapering, with desired profile remaining the same but the drawing speed is confined to region $v_d \in [h_d v_{dmax}, v_{dmax}]$, where $h_d \in [0, 1]$. Using Equation 3.2 we can solve for v_e and v_f. For h_d close to 1, v_d is essentially constant. The tapering time depends only on the exit motor speed and therefore the first taper case is the fastest of the three possible profiles. The second taper case should be used for deep tapering when the first can not be used because it would lead to the motor speed exceeding the 5000 rpm limitation.

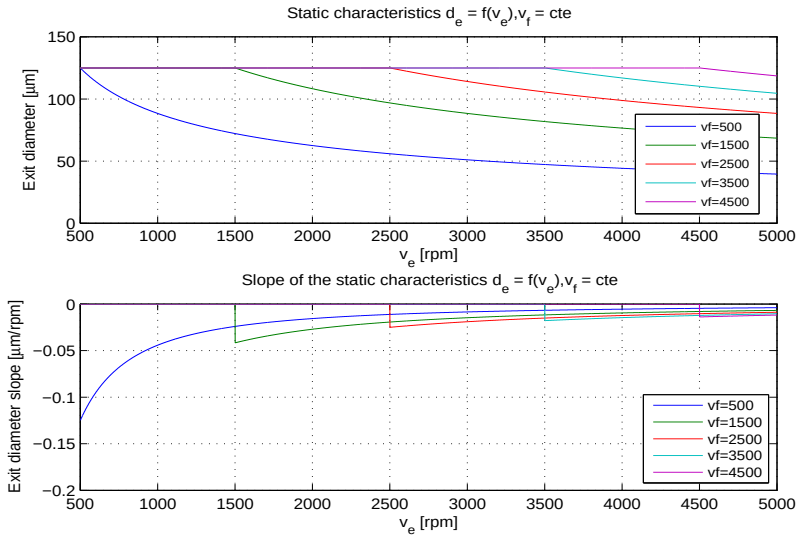

FIGURE 3.5: Family of static gain characteristics

The third tapering case is characterized with nearly constant drawing speed v_d, therefore a constant fibre tension is provided. However, steps in this profile can provoke oscillation in the system which could reduce the tapering quality.

Since during the tapering feed diameter d_f and feed motor velocity v_f are kept constant, the relationship between the exit diameter d_e and the exit velocity v_e is $d_e = c/\sqrt{v_e}$, where $c = d_f\sqrt{v_f}$, it is possible to plot the family of static gain (d_e/v_e) characteristics, shown in Figure 3.5.

Figure 3.5 (top) shows the d_e as a function of the exit velocity v_e for a range of feed velocities v_f. Figure 3.5 (bottom) shows that the slope of these characteristics changes, too. We can use the first characteristics to find the feed speed for which the desired tapering ratio is in the middle of the curve range. Also, we can use the bottom family of curves to find the exit speed for which the change of the curve slope is small. If the change of the slope is large, this will lead to difficulties with feedback control (as the gain of the control system changes).

Figure 3.6 shows the range (minimum, maximum) of the exit diameter as a function of a feed motor velocity and it enables us to choose an appropriate v_f so that we could achieve the desired tapering ratio. Figure 3.5 and Figure 3.6 do not allow for unique determination of $[v_e, v_f]$ for a given tapering ratio. Figure 3.5 shows that with smaller feed speed we have larger change in the slope of the curve $d_e = f(v_e)$, implying that the tapering system is more sensitive to uncontrolable speed changes. From Figure 3.6 we see that for the deeper tapering maximum feed speeds are limited from above.

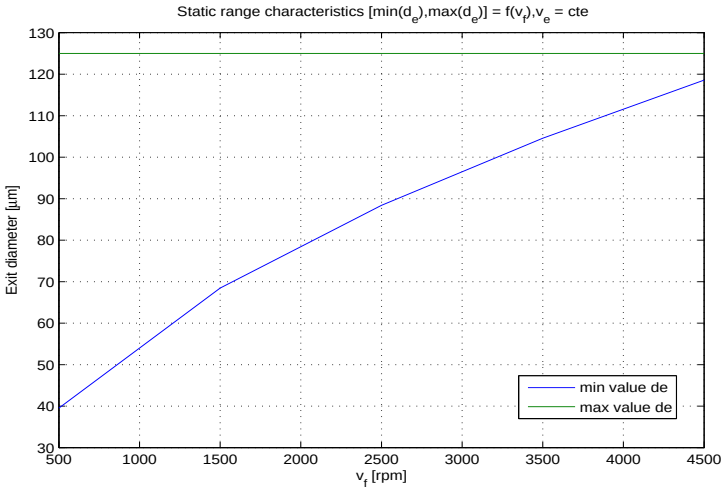

FIGURE 3.6: Range of the exit diameter as a function of the feed motor velocity

3.3.1 Control feedback loop design

In order to obtain consistent transmission properties along the taper length, the fibre must be tapered very precisely. Therefore, the control feedback loop is designed, aiming to suppress the unwanted diameter fluctuations. The block diagram of the implemented taper control system is shown in Figure 3.7. Generally, the control system task is to track the desired profile and eliminate disturbances represented by the signal v_d, [85]. In Figure 3.7, the signal which represents nominal value of the fibre diameter d_{des}, in addition with (constant) feed diameter d_f and feed speed v_f, is used to calculate the exit motor speed reference v_e, according to Equation 3.1.

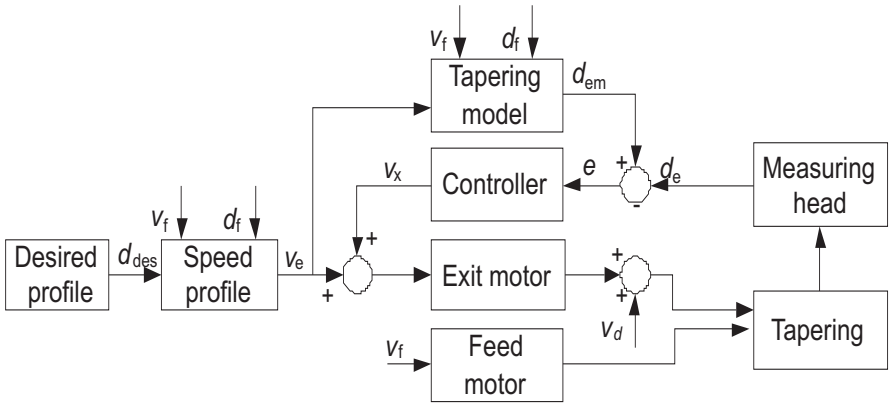

FIGURE 3.7: Block diagram of the tapering control system

This speed is used to predict the exit diameter d_{em} and compare it to the measured exit diameter d_e. The difference $e = d_{em} - d_e$, representing an error, is fed back into a controller block and used to calculate the correction speed v_x. The correction speed v_x is added to the v_e and sent to the exit motor. The disturbance might have changed

v_f, v_e and d_f, but we will assume that there exist equivalent exit speed disturbance v_d, which if should have been applied it would create same change in the exit diameter. The control system task then is to cancel the effect of the disturbance signal v_d by the way of changing v_x. If we assume that due to the effect of disturbances affecting the exit speed v_e, the exit diameter d_e is changed by e, then Equation 3.1 requires that:

$$d_e + e = \sqrt{\frac{v_f}{v_e + v_x}} d_f \tag{3.3}$$

And dividing it by Equation 3.1 we obtain:

$$\frac{d_e}{d_e + e} = \sqrt{\frac{v_e + v_x}{v_e}} \tag{3.4}$$

Solving for v_x from Equation 3.4 one obtains:

$$v_x = v_e(\frac{d_e}{(d_e + e)^2} - 1) \tag{3.5}$$

or after normalizing e with d_e:

$$v_x = v_e(\frac{d_e - (d_e + e)^2}{(d_e + e)^2}) = v_e(\frac{(1 - (1 + \frac{e}{d_e})^2)}{(1 + \frac{e}{d_e})^2}) \tag{3.6}$$

Equation 3.6 states that to cancel the effect of disturbances resulting in diameter error, e, exit speed has to be modified by v_x.

As in the real system the measurement of the exit profile is located at a distance l_m from the heater, there is a pure transport delay τ in the tapering that is determined with the exit speed. Therefore, the model described by Equation 3.1 is augmented with a pure transport delay τ. From the open-loop step response measurements, it has been determined that the disturbance signal has a constant term in addition to several harmonic components located in the frequency range between 1/1000 s and 1/10 s. To effectively cancel a DC type of disturbance one needs to include PI (Proportional Integral) controller in the feedback loop. The PI controller's transfer function in the complex (s) domain, with $U_{PI}(s)$ the Laplace transform of the controller output $u_{PI}(t)$ and $E(s)$ the Laplace transform of the exit diameter error $e(t)$, is described by:

$$G_{PI}(s) = \frac{U_{PI}(s)}{E(s)} = \frac{K_I}{s} + \frac{1}{K_P} = \frac{1}{K_P}\frac{K_P K_I + s}{s} = \frac{1}{K_P}\frac{(s + \alpha)}{s}, \qquad \alpha = K_I K_P \tag{3.7}$$

The controller has two tuning parameters: (inverse) proportional K_P and integral gain K_I. The product of K_P with K_I is labelled α and determines the frequency where the integral action effectively stops being active.

If we choose $K_I = 2\pi/2000$ and $K_P = 2$ the transfer function of the controller is:

$$G_{PI}(s) = \frac{U_{PI}(s)}{E(s)} = 0.5\frac{s + 0.006283}{s} \tag{3.8}$$

The Bode diagram of Equation 3.7 is shown in Figure 3.8. For low frequencies, controller magnitude slope is $-20\ dB/dec$, up to a frequency $\omega = \alpha = 0.006283\ rad$ ($f = 10^{-3}Hz$), where the controller zero becomes active, reducing the controller action to pure proportional $1/K_P = 0.5 = -6\ dB$.

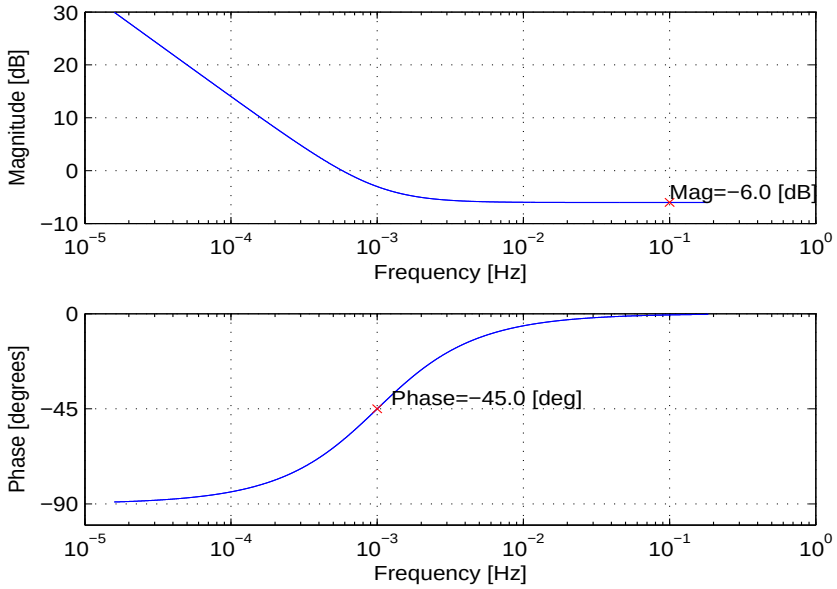

FIGURE 3.8: Bode diagram of the PI controller

To implement the PI controller as a software controller, we have to find the discrete time equivalent of the Equation 3.7 for a selected sampling time T_s (set to $T_s = 0.5\ s$). Chosen sampling period enables a small discretisation error with respect to the analogue controller without setting too restrictive real time requirements on a `Matlab` application which implements the controller. This can be achieved by applying the method of finite differences on the controller transfer function in Equation 3.7. Firstly, we rearrange Equation 3.7 such that we obtain:

$$sU_{PI}(s) = \frac{1}{K_P}sE(s) + \frac{1}{K_P}\alpha E(s) \tag{3.9}$$

Secondly, the backward difference method is applied by approximating the first order differential with a first order difference operator ($dx/dt = sX(s) - x(0) = \frac{x(k)-x(k-1)}{T_s}$) to Equation 3.9 and we have:

$$\frac{u_{PI}(k) - u_{PI}(k-1)}{T_s} = \frac{1}{K_P}\frac{e(k) - e(k-1)}{T_s} + \frac{1}{K_P}\alpha e(k) \tag{3.10}$$

where $e(k)$ is the discrete time equivalent of the error and $u_{PI}(k)$ is the discrete time equivalent of the controller output. From Equation 3.10 we finally obtain:

$$u_{PI}(k) = u_{PI}(k-1) + \frac{1}{K_P}(\beta e(k) - e(k-1)) \tag{3.11}$$

where $\beta = 1 + T_s\alpha$.

After the Z transform applied to Equation 3.11, we obtain:

$$U_{PI}(z) = z^{-1}U_{PI}(z) + \frac{1}{K_P}(\beta E(z) - z^{-1}E(z)) \tag{3.12}$$

where z^{-1} is the delay operator.

Finally, the noise filter is added, to limit the highest frequency where controller is still active. The noise filter transfer function is:

$$G_{nf}(s) = \frac{U(s)}{U_{PI}(s)} = \frac{\omega_{nf}}{s + \omega_{nf}} \tag{3.13}$$

For $\omega_{nf} = 4\alpha$ Bode diagram of the noise filter is shown in Figure 3.9.

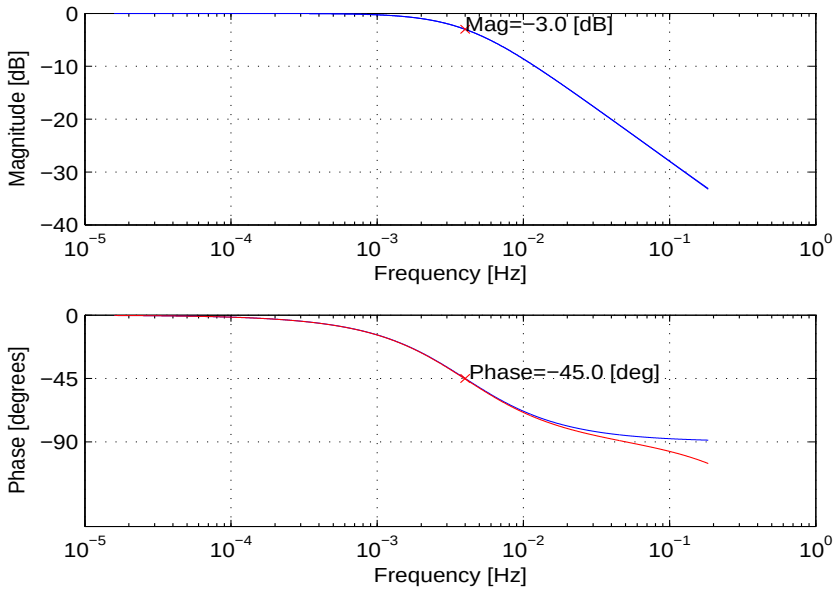

FIGURE 3.9: Bode diagram of the noise filter transfer function, blue - continuous time, red - discrete time

After applying the backward difference scheme on the filter transfer function, we get:

$$u(k) = \gamma u(k-1) + \delta u_{PI}(k) \tag{3.14}$$

where $\gamma = \frac{1}{1+\omega_{nf}T_s}$ and $\delta = \frac{\omega_{nf}T_s}{1+\omega_{nf}T_s}$. After the Z transform applied to Equation 3.14, we obtain:

$$U(z) = \gamma z^{-1}U(z) + \delta U_{PI}(z) \tag{3.15}$$

The transfer function of the controller is then obtained by multiplying Equation 3.12 with Equation 3.15 and Bode diagram is shown in Figure 3.10.

In summary, a software PI controller with a NF (Noise Filter) filter can be implemented using two equations:

$$u_{PI}(k) = u_{PI}(k-1) + \frac{1}{K_P}(\beta e(k) - e(k-1)) \tag{3.16}$$

$$u(k) = \gamma u(k-1) + \delta u_{PI}(k) \tag{3.17}$$

and a PI controller with noise filter has three tunable parameters: integrator gain K_I , proportional gain K_P and noise filter cut off frequency ω_{nf}.

The relevant bits of the code for the control of the taper fabrication that I have written in `Matlab`, are given in Appendix B.

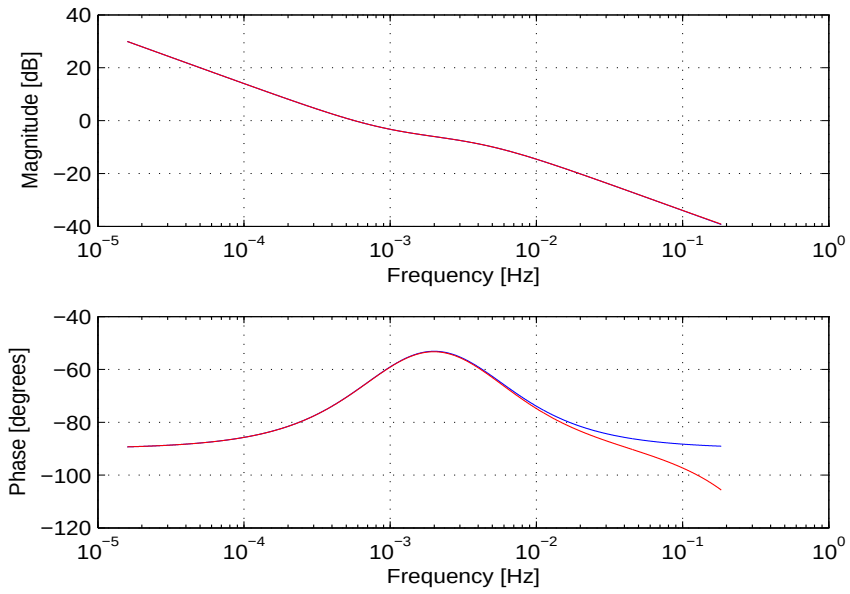

FIGURE 3.10: Bode diagram controller, blue - continuous time, red - discrete time $T_s = 0.5s$, when $K_I = 2\pi/2000, K_P = 2$ and $\omega_{nf} = 4\alpha$

3.4 Experimental Analysis of Optical Fibre Tapering

In order to test the system I tapered both step index fibres and microstructured optical fibres with a number of well specified tapering profiles. Figure 3.11 shows a non -

monotonically varying diameter profile, where the fibre diameter changes from 125 μm to 112.5 μm in the taper transition regions (10% change in the fibre diameter), over the length of 1 m.

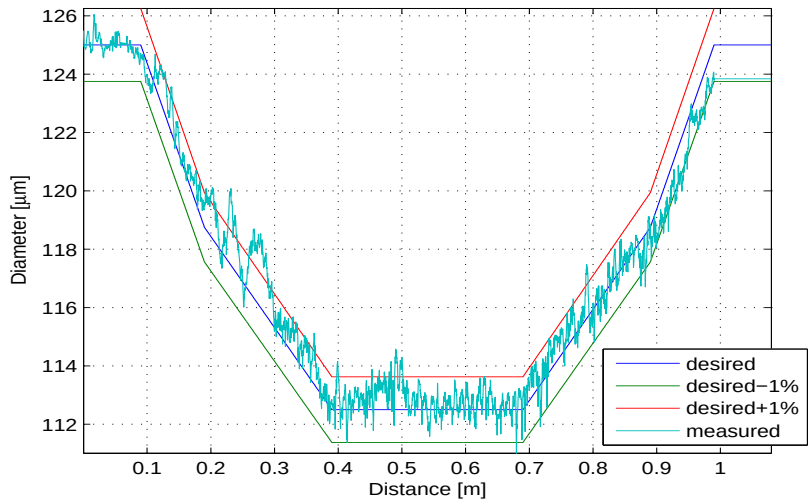

FIGURE 3.11: The non-monotonically linear profile, feedback on.

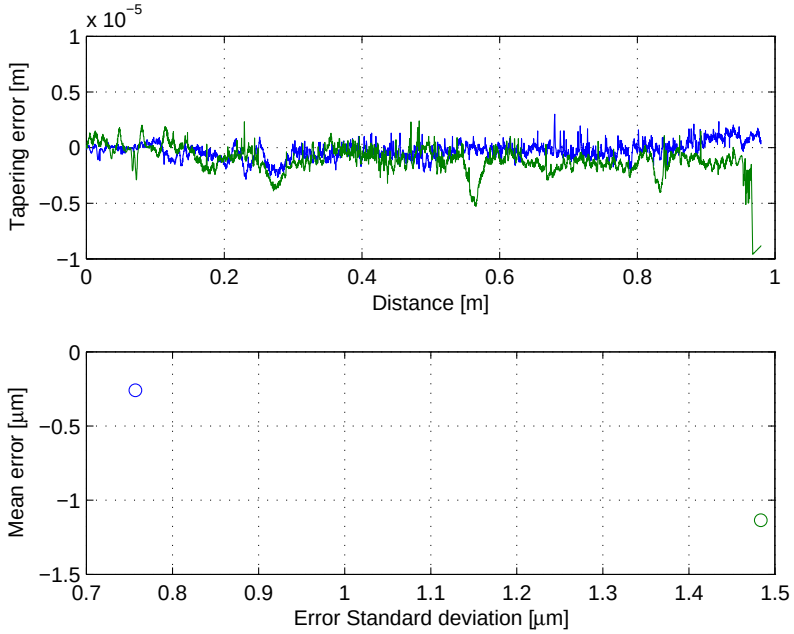

FIGURE 3.12: Tapering error and error mean and standard deviation, green - no feedback, blue - feedback.

The comparison of the experimental measurements with and without feedback control (see Figure 3.12), shows that the tapering error (calculated as the difference between desired and measured fibre diameter) is within ± 2 μm for the most of the time with active

feedback control, whilst it is in the range of ± 5 μm when there is no feedback control of the diameter. For the case of applied feedback the mean error value is -0.26 μm and standard deviation is 0.75 μm, while for the case when there is no feedback applied the mean is -1.1 μm and standard deviation 1.48 μm.

This clearly shows the benefit of the feedback loop. However, due to a large measurement delay ($\approx$ 3 min) due to the distance between the heater and the measuring head, the feedback loop reduces only the effects of slow variations developing over a period greater than $\approx$ 3 min. With the equipment currently available the distance between the measuring head and the heater can not be reduced as high temperature can damage the measuring gauge. This drawback could be improved by choosing an alternative (faster) way to monitor the fibre diameter and thus maximizing the dynamic response of the control loop.

Many sets of experiments were done to find the optimum parameters of the PI regulator and noise filter. Figure 3.13 shows the tapering error and the mean error value for three different sets of values of K_I, K_P and ω_{nf}. The results show that the minimum tapering error can be achieved with $K_I = 2\pi/2000$, $K_P = 2$ and $\omega_{nf} = 2\pi/500$.

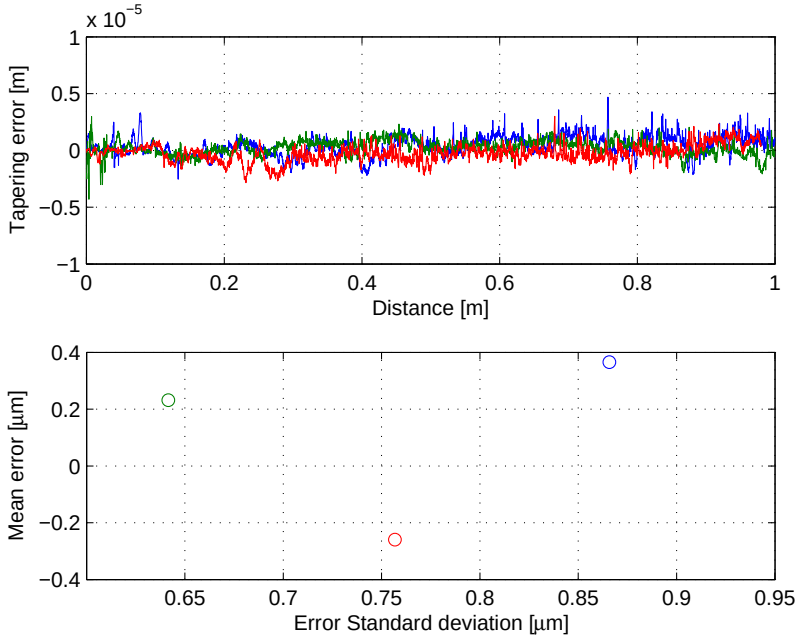

FIGURE 3.13: Tapering error and error mean and standard deviation for 1 m taper length, green - $\omega_{nf} = 2\pi/500, K_I = 2\pi/2000, K_P = 2$, blue - $\omega_{nf} = 2\pi/1600, K_I = 2\pi/3200, K_P = 2$, red - $\omega_{nf} = 2\pi/500, K_I = 2\pi/3000, K_P = 2$.

Figure 3.14 shows the experiment of tapering a step - index fibre with the periodically varying diameter profile tapered along 60 cm length. The diameter variation of a step - index fibre tapered linearly 70% along 20 cm length is shown in Figure 3.15.

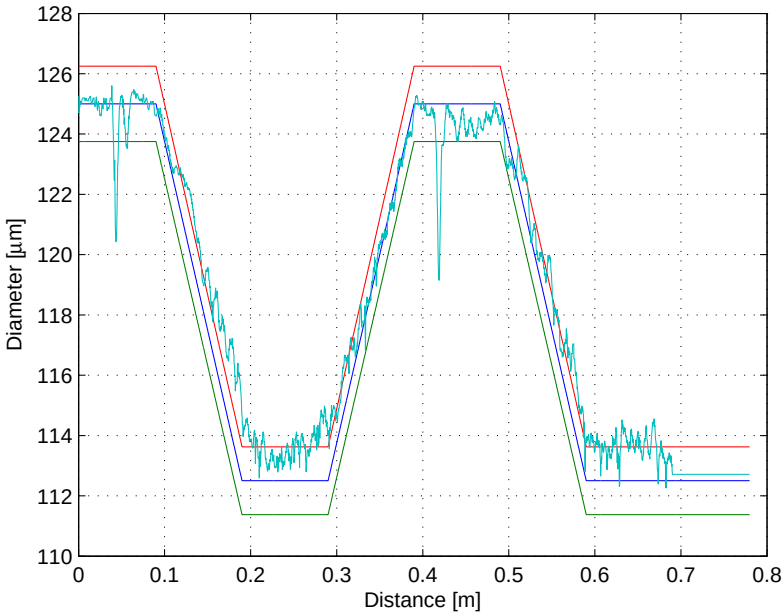

FIGURE 3.14: Step - index fibre taper with a periodically varying diameter profile, red - desired diameter+1%, green - desired diameter-1%.

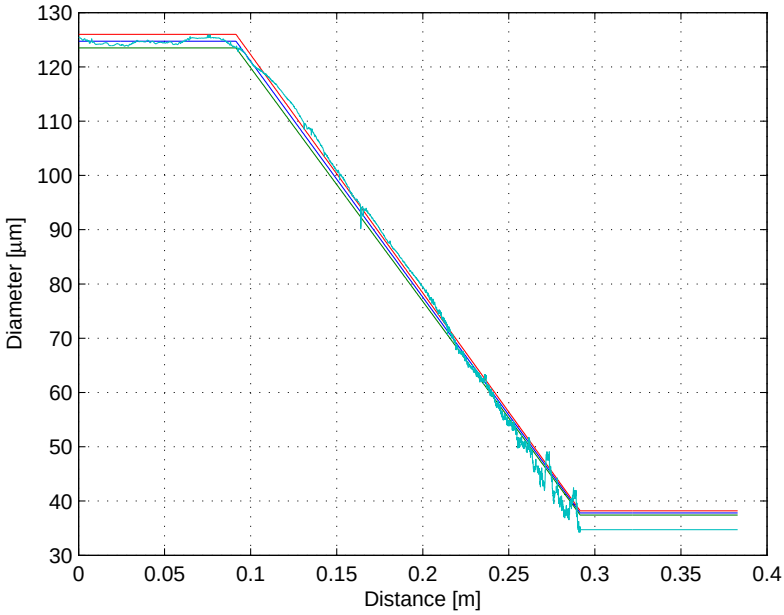

FIGURE 3.15: Step - index fibre tapered linearly 70% at 20 cm length, red - desired diameter+1%, green - desired diameter-1%.

In another experiment, using the feedback control system, I tapered a solid core MOF along a 60 cm length with the tapering ratio of 50% (Figure 3.16), where the speed profile was such that the exit motor speed remains constant and the feeding motor speed changes according to the mass conservation law. The corresponding tapering error is

shown in Figure 3.17, with a mean error of 0.09 μm and the error standard deviation is 1.68 μm.

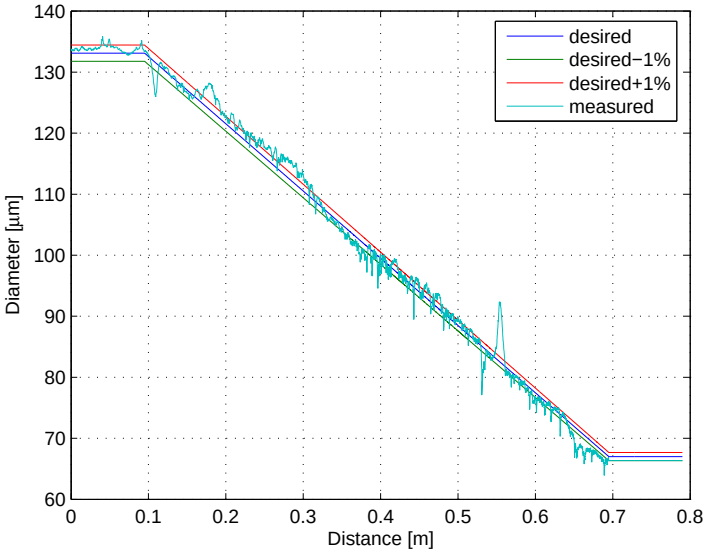

FIGURE 3.16: Taper diameter profile (50% tapering)

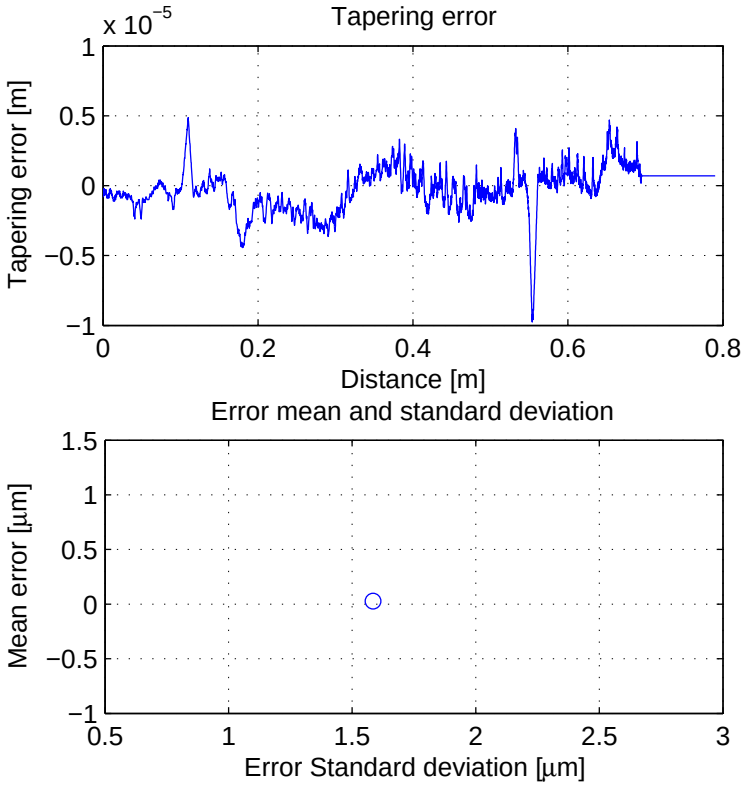

FIGURE 3.17: Tapering error and error mean and standard deviation

Of interest in this case is the reduction of the relative hole size as the outer diameter reduces. Using SEM images I examined (using the program described in the Appendix A,

which automatically determines the MOF geometry parameters) the structural change of the taper along its length, shown in Figure 3.18. It can be seen that up to a tapering ratio of $\sim 10\%$, the air-filling factor (d/Λ) of the MOF remains unchanged. This has been confirmed by the observation of the SEM images of different tapers (for brevity reasons, the SEM images of one taper are shown here). I anticipate that even very small variation in the structural parameters can cause large change in both the dispersion and/or nonlinearity, however at this stage of the development of the system the only method that was available to use was the SEM destructive measurement. Therefore, this assumption that the structure parameters of the fibre are preserved in the transition, is the approximation used in this thesis.

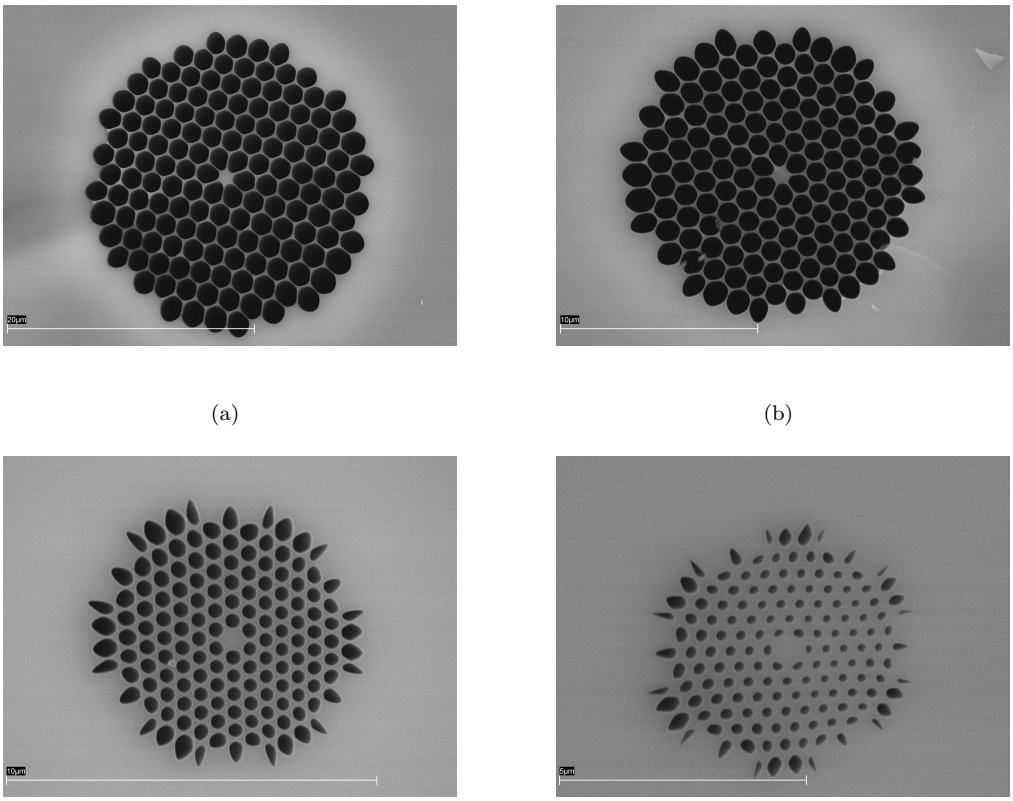

(a) (b)

(c) (d)

FIGURE 3.18: SEM images at the a.) taper start, scale 20 μm; b.) 30 cm from the start, scale 10 μm; c.) 50 cm from the start, scale 10 μm; d.) taper end, scale 5 μm

It can be observed from Figure 3.18 that for tapering ratios >10% d/Λ changed. In the example given, d/Λ is 0.95 at the beginning of the taper, 0.92 after 30 cm tapering length and 0.54 after 50 cm. The pitch values are: 1.8236 μm at the beginning, 1.084 μm after 30 cm and 0.5234 μm after 50 cm length. Although the hole collapse was observed at the taper end due to the high tapering ratio, it can be avoided by reducing the temperature or by applying pressurisation (this is a future direction for system improvement) in the fibre's holes. The result shows that it is possible to produce shallow tapers over long

lengths whilst maintain structural integrity and hence that it would be possible to change the dispersion of the fibre significantly (over the first 10 cm the dispersion changes from 173.67 ps/nm/km to −126.93 ps/nm/km) along the taper in a predictable way.

3.4.1 Experimental Set-up Including the Optical Fibre Coating System

Despite achieving very good accuracy in tapers fabrication using the tapering facility introduced above, the drawback of the proposed tapering system was the lack of a recoater. Although bare fibres can be handled with care, they are extremely fragile and potentially can not be incorporated into practical devices. Therefore, need to incorporate fibre coater into the tapering rig has been identified and addressed. The commercial optical fibre recoater was incorporated into the system. The block diagram of the experimental set-up incorporating the recoater, for the fabrication of metre-length fibre tapers, is shown in Figure 3.19.

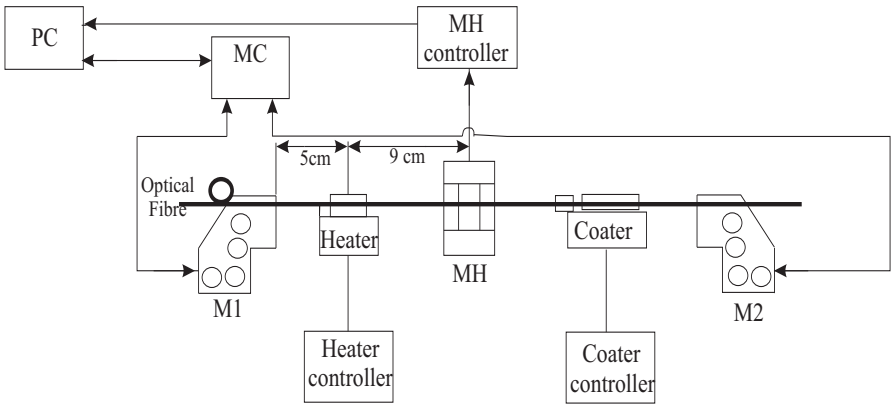

FIGURE 3.19: Experimental set-up with the inclusion of the optical fibre coating system; MH - Measuring Head, MC - Motors Controllers, M1- feeding motor, M2 - drawing motor

The system comprises components already introduced in Figure 3.1 (two DC motors, measuring head, ceramic microheater), with the inclusion of the optical fibre coating system after the measuring head. The coater is designed to overcoat optical fibre with a UV cured material and ultimately to improve the strength of the fabricated taper. The operating principle of the fibre coating system starts with the phase in which fibre passes from the fibre feed reel into the input guide roller. The guide roller is positioned such that the fibre can pass directly through the coating polymer. Then the fibre passes the UV LEDs which are used to cure the applied coating material. The fibre feeds out of the coating station to the output fibre guide.

Figure 3.20 shows the diameter variation of the step-index fibre tapered linearly 10% along 2 m length and consequently recoated.[3] The significant diameter variations can be observed in the beginning of the tapering due to some problems with the alignment of the coating system with the feed and exit motors of the tapering rig. The origin of the oscillations shown in Figure 3.20 is in the inappropriate manual handling of the fibre while it was passing through the motorised stages. Nevertheless, the expected effect of increasing the fibre strength and robustness was achieved and a long taper (2m length) was successfully recoated after the fabrication. This is a promising result as the fabricated tapers could be handled and delivered to the potential customers.

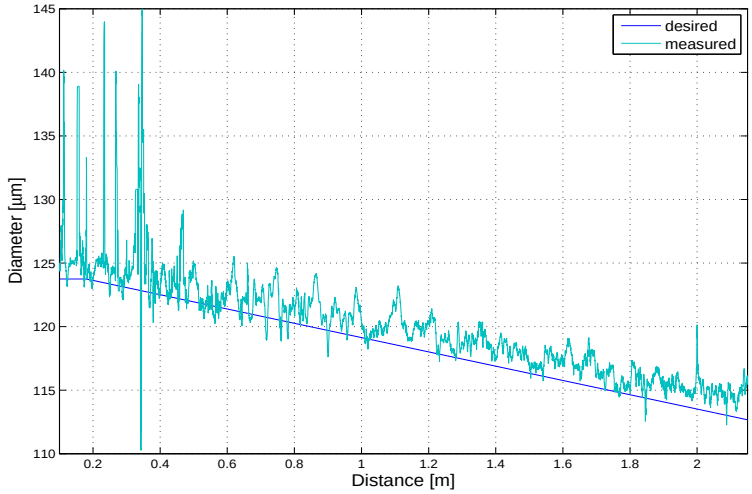

FIGURE 3.20: Diameter profile of the step - index fibre tapered linearly 10% along the 2 m length

3.5 Conclusion

In this chapter a novel system for optical fibres tapering is presented. In comparison with systems shown to date, the novel system has the advantage of increased control over the desired taper profile and enables efficient fabrication of intermediate taper lengths (few tens of cm to ∼10 m) of arbitrary profiles. I have demonstrated a design of the feedback loop for the enhanced control of the output diameter variation. The system has been tested in many different examples and presented results show that the variation of the fibre diameter is within 1%, which offers possibilities to use the system in different applications. The experimental results of tapering of both step index and MOF fibres are shown with the statistical parameters of mean error and error standard deviation.

[3]The optical coating system became available at the time when the equipment was about to be moved to a new laboratory, therefore the system had to be dismounted and transferred. This tapering result is presented for the illustrative purposes, to show the capability of the new recoating system.

These results show values for mean error close to zero when the feedback is applied and low value of standard deviation in all cases is being demonstrated.

There are several important points arising from tapering using novel tapering rig. Firstly, active feedback is essential to reduce the error in the diameter variation of the fibre taper. Secondly, tapering of MOFs is possible without changing d/Λ for shallow tapers. Finally, using this method large changes in the fibres dispersion can be produced in a controllable fashion.

The main developments that have taken place, leading to a clearer understanding of the general problem and to some innovative results can be summarised by:

1. Design and setting - up the experimental tapering facility for fabrication of intermediate length tapers;
2. Generating `Matlab` script, based on the control system approach, to control the fabrication of tapered fibres (Appendix B); Development of different speed profiles that could be implemented in accordance to the desired taper profile or tapering ratio;
3. Designing the control feedback loop to enhance the control over the taper diameter variation;
4. Generating `Matlab` script for automatic post - processing of the SEM images, for the determination of the MOF fibres geometry parameters (Appendix A).

Chapter 4

Numerical Investigation of Parabolic Pulse Generation in Tapered Microstructured Optical Fibre

4.1 Introduction

Parabolic pulse generation has been the focus of much research activity (both theoretical and experimental) over the past years [75] - [77]. Due to the interaction between dispersive and nonlinear effects on a high intensity pulse in the normal dispersion regime, propagating pulse suffers wave breaking, manifesting itself as oscillations on the pulse's tail [1], [93]. However, if the pulse possesses a linear chirp such that the rate of change of the time separation is the same for all parts of the pulse, the pulse preserves its shape [94]. Linearly chirped parabolic pulses can be efficiently compressed and are used in many telecommunications applications such as optical regeneration [95] or temporal Fourier transforms [96]. Such pulses are also useful for applications such as pulse compression, and indeed compression of picosecond parabolic pulses down to femtosecond range have been experimentally demonstrated [95], [97].

Different approaches to the generation of parabolic pulses have been studied and include: optical amplifiers [98] - [101], similariton lasers [102], [103], dispersion decreasing fibre in the normal dispersion regime [104], [105] and fibre gratings [95], [97], [106]. Applications requiring high power parabolic pulses often rely on an optical amplifier as parabolic pulses are automatically generated in these amplifiers. On the other hand, there is a range of applications, particularly related to optical signal processing, where a high signal power is undesirable, since it requires a high power pump source and adds costs

and complexity to the system [107]. Another drawback of using an active system is that it introduces amplified spontaneous emission noise. Hence the need for other ways to generate parabolic pulses using passive fibres. The passive methods to generate parabolic pulses described above usually require relative long lengths of fibre (> 1 km) and are suitable for picosecond pulse widths (> 1 ps). In [108], however, it was shown that using a comb-like dispersion decreasing profile also leads to parabolic pulse generation, in a few metres of fibre. Such comb-like profiles are complicated to produce (relying on multiple splices) and hence, there is a need for a different approach for efficient generation of parabolic pulses in relative short lengths and with the flexibility of coping with differing input pulse widths and energies.

I chose to investigate tapered optical fibres, since, as it was pointed out in [99], [105], [109], that in a system described by the ideal lossless nonlinear Schrödinger equation (NLSE) with decreasing dispersion, optical pulse evolution is formally similar to that of a medium with a constant gain. As a consequence, an asymptotic self-similar parabolic pulse solution is found to exist in a dispersion decreasing fibre with normal group velocity dispersion i.e. a taper [109]. Using a linear dispersion profile parabolic pulses are generated after a finite propagation length, with the parabolic pulse remaining stable for some length before becoming distorted. Formally my approach doesn't correspond to an asymptotic self-similar parabolic pulse, since I used a linear taper profile and not a hyperbolic dispersion profile. However, a linear taper profile is a good approximation to the hyperbolic dispersion profile in the case of shallow tapering.

We use MOFs as the tapered fibre because they are characterized by the exceptional optical properties and tapered MOFs have been used in various applications. Therefore, tapered MOFs have attracted our interest to investigate parabolic pulse generation in such fibres, aiming to find a way to efficiently generate parabolic pulses in relatively short fibre lengths, with the flexibility of coping with varying input pulse widths and energies.

This chapter starts with introducing the theoretical background of the parabolic pulse generation in the normally dispersive optical fibre, which relies on the theory of self similarity. It was first described by Kruglov [99] and his derivation is summarised below. According to this theory, in a system described by the ideal lossless NLSE with the hyperbolic profile dispersion decreasing optical fibre, optical pulse evolves into a parabolic pulse after a certain propagation length. This theoretical introduction was used for understanding the fundamental principles of parabolic pulse evolution and the derivation of analytical expressions. Next, I investigated parabolic pulse evolution in tapered normally dispersive MOFs and the results of modelling and simulation are shown. I have identified two normal dispersion regions, and outlined a procedure for choosing the parameters of the taper profile for efficient parabolic pulse generation. Then in Section 4.3, based on the numerical solution of the NLSE, I show how initial Gaussian pulses of various input powers and widths evolve into parabolic pulses with a linear

chirp, for two different tapers. Results are quantified using the misfit parameter, which measures the root mean square error between the propagated pulse and its parabolic fit in the time domain. The procedure enables efficient determination of the best parabolic fit and taper's length, for a wide range of initial pulse parameters.

4.1.1 Theory of self-similar propagation in normally dispersive optical fibre

The basic principle behind the parabolic pulse generation in a passive optical fibre relies on the theory that in a system described by the ideal lossless nonlinear Schrödinger equation with decreasing dispersion (taper), optical pulse evolution is formally similar to that of a medium with a constant gain [99], [105], [109]. When a high intensity optical pulse is launched into the fibre, the pulse evolves into a linearly chirped, parabolic pulse in which the nonlinear chirp introduced by the self phase modulation is linearized gradually by normal group velocity dispersion.

In this chapter the relevant parts of the derivation[1] of the parabolic pulse envelope for the normal dispersive hyperbolically tapered fibre will be shown. The propagation of optical pulses in a normal dispersion decreasing fibre is described by the NLSE in the following form [99], [105], [109]:

$$i\frac{\partial A}{\partial z} - \frac{\beta_2}{2}D(z)\frac{\partial^2 A}{\partial t^2} + \gamma \mid A \mid^2 A = 0 \tag{4.1}$$

where $A(z,t)$ is the slowly varying envelope of the pulse in the copropagating frame, $D(z)$ describes variation in the group velocity dispersion due to dispersion tapering and is normalized such that $D(0) = 1$ and $\beta_2 > 0$. The nonlinearity coefficient is considered to be uniform along the taper length.

Using the new variable: $\zeta = \int_0^z D(z')dz'$, we have $\partial\zeta = \partial(\int_0^z D(z')dz') = D(\zeta)\partial z$. Then, $\partial z = \partial\zeta/D(\zeta)$, which is substituted into the Equation 4.1 and we get:

$$iD(\zeta)\frac{\partial A}{\partial \zeta} - \frac{\beta_2}{2}D(\zeta)\frac{\partial^2 A}{\partial t^2} + \gamma \mid A \mid^2 A = 0 \tag{4.2}$$

After dividing Equation 4.2 by $D(\zeta)$ we have:

$$i\frac{\partial A}{\partial \zeta} - \frac{\beta_2}{2}\frac{\partial^2 A}{\partial t^2} + \frac{\gamma}{D(\zeta)} \mid A \mid^2 A = 0 \tag{4.3}$$

Another change of variables could be introduced [99]: $\psi(\zeta,t) = A(\zeta,t)/\sqrt{D(\zeta)}$, so that: $A(\zeta,t) = \sqrt{D(\zeta)}\psi(\zeta,t)$ can be substituted into Equation 4.3.

[1] More details of the derivation steps can be found in Ref. [99].

This transforms Equation 4.1 into a NLSE with constant coefficients and an effective gain depending on ζ [99].

$$i\frac{\partial\psi}{\partial\zeta} - \frac{\beta_2}{2}\frac{\partial^2\psi}{\partial t^2} + \gamma \mid \psi \mid^2 \psi = i\frac{\Gamma(\zeta)}{2}\psi \tag{4.4}$$

where:

$$\Gamma(\zeta) = -\frac{1}{D}\frac{dD}{d\zeta} = -\frac{1}{D^2}\frac{dD}{dz} \tag{4.5}$$

With $\Gamma > 0$ since D is a decreasing function ($dD/dz < 0$), so the right hand side of Equation 4.4 adds gain to the normalized pulse amplitude.

With the choice of a hyperbolic dispersion profile $D(z) = 1/(1+\Gamma_0 z)$, the gain coefficient becomes constant [109]:

$$\Gamma = -\frac{1}{\frac{1}{(1+\Gamma_0 z)^2}}\frac{d}{dz}(\frac{1}{1+\Gamma_0 z}) = -(1+\Gamma_0 z)^2\frac{-\Gamma_0}{(1+\Gamma_0 z)^2} = \Gamma_0 \tag{4.6}$$

Equation 4.4 becomes:

$$i\frac{\partial\psi}{\partial z} = \frac{\beta_2}{2}\frac{\partial^2\psi}{\partial t^2} - \gamma \mid \psi \mid^2 \psi + i\frac{\Gamma_0}{2}\psi \tag{4.7}$$

Following this derivation, it is anticipated, [99], that there will exist a linearly chirped solution to Equation 4.4 that, after some period of initial evolution, scales self-similarly as it propagates in z. A self-similar solution, by definition [99], is one in which the functional form of the solution is invariant so that the solution at one point (space or time) can be found from a solution at another point by a similarity transformation. To find such solution, the field can be expanded in terms of an amplitude and phase: $\psi(z,t) = q(z,t)\exp[i\phi(z,t)]$ and be substituted into Equation 4.7, which leads to the a pair of coupled equations in q and ϕ, as follows:

$$\frac{\partial q}{\partial z} = \beta_2\frac{\partial q}{\partial t}\frac{\partial\phi}{\partial t} + \frac{\beta_2}{2}q\frac{\partial^2 q}{\partial t^2} + \frac{\Gamma_0}{2}q \tag{4.8}$$

$$[\frac{\beta_2}{2}(\frac{\partial\phi}{\partial t})^2 - \frac{\partial\phi}{\partial z}]q = \frac{\beta_2}{2}\frac{\partial^2 q}{\partial t^2} - \gamma q^3 \tag{4.9}$$

Mathematically, self-similar solutions are found by the technique of symmetry reduction [99]. This involves reformulating a problem in terms of a certain combination of the original variables (similarity variables), so that the number of degrees of freedom of the system is reduced. This means that the original problem of solving partial differential equations can be changed into a problem of solving a system of differential equations. In general, the similarity variables can be found using techniques based on Lie algebra

theory [99]. Kruglov et al. [99] constructed the symmetry variable based on the combined results of high intensity wave breaking free propagation in normal dispersive fibres and those obtained for radial pattern formation in a laser cavity. The NLSE with gain (Equation 4.7), can be analyzed using symmetry reduction. The solutions obtained in this way represent exact self-similar solutions which appear in the asymptotic limit $z \to \infty$.

The coupled equations Equation 4.8 and Equation 4.9 can be simplified with the assumption of self-similar evolution in the dispersion decreasing fibre. The key step in self-similarity analysis is to reduce number of degrees of freedom of the system by rewriting these equations in terms of carefully chosen combinations of original variables. The searching for linearly chirped solution is conducted in the following form [99]:

$$q(z,t) = f(z)F(z,t) = f(z)F(\nu) \tag{4.10}$$

$$\phi(z,t) = \varphi(z) + C(z)t^2 \tag{4.11}$$

where self-similarity variable ν is in the form:

$$\nu = f^2(z)\exp(-\Gamma_0 z)t \tag{4.12}$$

$f(z)$ has the same dimensions as $A(z,t)$ and describes the evolution of the peak amplitude of the pulse with propagation distance z, whereas $F(\nu)$ is a normalized, dimensionless function that describes the evolution of the temporal profile. The phase term $\varphi(z)$ and $C(z)$ are the z-dependant phase offset and chirp parameter. The explicit form of the amplitude term was found based on the constraint that, for the particular choice of ν, the energy conservation integral is satisfied [99]. After substitution into Equation 4.8 and Equation 4.9, these become:

$$\frac{df}{dz} = \beta_2 f C + \frac{\Gamma_0}{2} f \tag{4.13}$$

$$(2\beta_2 C^2 - \frac{dC}{dz})\frac{\nu^2}{f^6} exp(2\Gamma_0 z) - \frac{1}{f^2}\frac{d\varphi}{dz} = \frac{\beta_2}{2}\frac{f^2}{F}\frac{d^2F}{d\nu^2} exp(-2\Gamma_0 z) - \gamma F^2 \tag{4.14}$$

Thus, by reducing the number of degrees of freedom, the original problem involving partial differential equations has been reduced into a system of ordinary differential equations. These equations can be simplified in the asymptotic limit, allowing explicit analytic solutions for F, f, φ and C to be obtained. The term proportional to $\frac{d^2F}{d\nu^2}$ can be neglected as $z \to \infty$. Equation 4.14 can be simplified into two coupled equations [99]:

$$(2\beta_2 C^2 - \frac{dC}{dz})\frac{1}{f^6} exp(2\Gamma_0 z) = a\gamma \tag{4.15}$$

$$\frac{1}{f^2}\frac{d\varphi}{dz} = \gamma \tag{4.16}$$

From the derivation of Equation 4.15 and Equation 4.16 it follows that the solution for $F(\nu)$ has the following form:

$$F(\nu) = \begin{cases} \sqrt{1-a\nu^2}, & \mid \nu \mid \leq \frac{1}{\sqrt{a}} \\ 0 & \text{elsewhere} \end{cases} \tag{4.17}$$

where a is a constant that depends on the input parameters and F obeys the normalization condition $F(0) = 1$.

Equation 4.13 is substituted into Equation 4.15, leading to the equation:

$$\frac{d}{dz}(\frac{1}{f}\frac{df}{dz}) - 2(\frac{1}{f}\frac{df}{dz} - \frac{\Gamma_0}{2})^2 + \beta_2 a\gamma f^6 exp(-2\Gamma_0 z) = 0 \tag{4.18}$$

which has the solution [99], [109]:

$$f(z) = q_0 exp(\Gamma_0 z/3) \tag{4.19}$$

where q_0 is a constant (peak amplitude) that depends on the parameters of the system. The form of f(z) given by Equation 4.19 can be substituted into Equation 4.12, yielding the explicit form of self similarity variable $\nu = q_0^2 \exp(\frac{-\Gamma_0 z}{3})t$.

Substituting Equation 4.19 for $f(z)$ and Equation 4.17 for $F(\nu)$ into Equation 4.10 yields the asymptotic evolution of the amplitude $q(z,t)$ (parabolic pulse), which can be written as:

$$q(z,t) = \begin{cases} q_0 \exp(\frac{\Gamma_0}{3}z)\sqrt{1-\frac{t^2}{T_0^2(z)}}, & if \mid t \mid \leq T_0(z) \\ 0 & \text{elsewhere} \end{cases} \tag{4.20}$$

where T_0 is the pulse width. To determine the general form of the phase of self-similar pulse, solution for $f(z)$ Equation 4.19 is substituted into Equation 4.13, which gives the following:

$$C = -\frac{\Gamma_0}{6\beta_2} \tag{4.21}$$

$\varphi(z)$ could be derived from Equation 4.16 and Equation 4.11, so that we have:

$$\phi(z,t) = \varphi + \frac{3\gamma A_0^2}{2\Gamma_0} exp(\frac{2\Gamma_0}{3}z) - \frac{\Gamma_0}{6\beta_2}t^2 \tag{4.22}$$

The linear chirp can be calculated as:

$$\Omega_c(t) = -\frac{\partial \phi}{\partial t} = \frac{\Gamma_0}{3\beta_2} t \tag{4.23}$$

Therefore, the self-similar asymptotic pulse solution is: $\psi(z,t) = q(z,t)\exp[i\phi(z,t)]$, with amplitude defined by Equation 4.20 and phase defined by Equation 4.22. These results predict that the asymptotic behaviour of the parabolic pulses is related with the exponential growth of the pulse amplitude and width and are conditioned by the energy of the initial pulse [99]. The linear chirp is independent of z, but as the pulse is temporarily broadening, the pulse's spectral width increases.

Although formally this solution is valid for the hyperbolic dispersion profile, the approximation of linearly tapered dispersion decreasing fibre is suggested [105]. This theoretical introduction was used for clearer understanding of the fundamental principles of parabolic pulse evolution and provides a background for the investigation conducted in this chapter. Following this analytical derivation, in the next section we turn to a practical implementation and observe parabolic pulse evolution in tapered normally dispersive MOFs.

4.2 Microstructured Optical Fibre and Taper Modelling

Clearly, to investigate MOF for parabolic pulse generation, we need to know how the optical properties depend on the structure (i.e. to solve Maxwell's equations). It was stated earlier that in microstructured optical fibres, light is confined in the core by a microstructured cladding. The finite element method (FEM), implemented in the commercial software package `Comsol Multiphysics`, was used to solve for dispersion, effective area and confinement loss of the lowest order mode [20], [22], [110]. The geometry of the MOF used in the analysis was a hexagonal pattern with 11 layers of holes, (see Figure 4.1.a). According to a group theoretic analysis [111], [112], a minimum waveguide sector can be assigned to determine all the modes in a symmetry e.g. C_{6v} symmetry class, 6-fold rotational symmetry with at least one plane of reflection symmetry, by applying the appropriate boundary condition. For the fundamental mode this allows the restriction of the computational domain to only one quarter of the structure (minimum waveguide sector, 90 °) with no loss of information about the modes, thus saving considerable amount of the computational time [112]. The magnitude of Poynting vector of the fundamental mode of a MOF, for illustrative purposes, is shown in Figure 4.1.b. It can be observed that the light is well confined to the core region and penetrates only slightly into the cladding region.

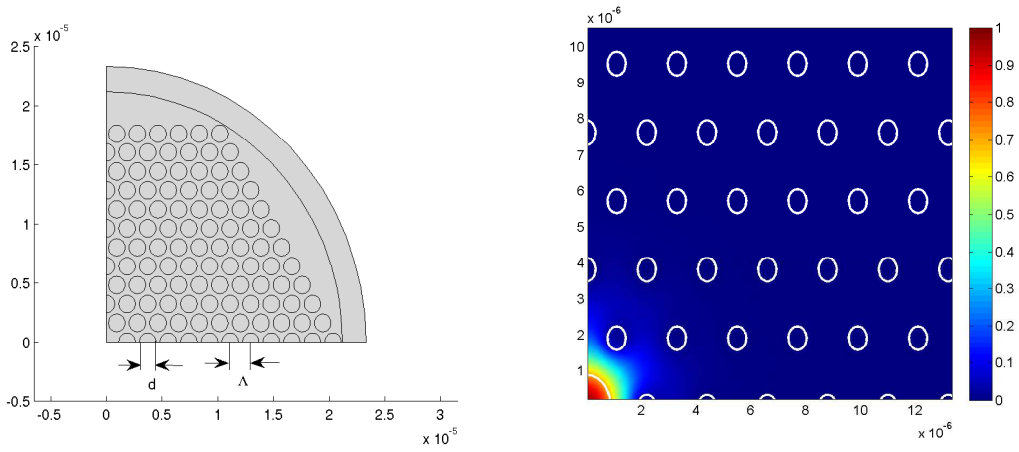

(a) (b)

FIGURE 4.1: a.) Cross section of the MOF with 11 rings of holes b.) The magnitude of the Poynting vector for the fundamental mode

Using the mode analysis, where the wavelength is fixed, the propagation constant β is calculated, which is related to the effective index of the propagation mode n_{eff} by:

$$\beta = \frac{2\pi n_{eff}}{\lambda} \tag{4.24}$$

where λ is optical wavelength.

Note that for a finite structure n_{eff} is a complex number with the imaginary part giving the confinement loss of the mode [110]. In the FEM analysis, a perfectly matched layer (PML) to treat the open boundaries is used. Using the complex effective index, the confinement loss is calculated using the Equation 2.7. The chromatic dispersion is taken into account through the dispersion parameter D, using the Equation 2.9.

Fibre design using optical property maps has been shown to be a very powerful when the number of design parameters is limited to two or three, each one plotted on one axis of a bidimensional rectangular map [22]. In hexagonally structure of the MOF with equal hole size (as seen in Figure 4.1.a) two parameters (hole size d and pitch Λ) completely describe optical properties[2]. Figure 4.2 shows an optical map of the calculated dispersion (dispersion parameter D [ps/nm/km]) of various MOFs at 1.55 μm (the wavelength of interest) as a function of Λ and d/Λ. This plot enables us to find the range of values for Λ and d/Λ that would provide normal dispersion regime (D<0) of the fibre. It can be seen that almost any value of d/Λ can be used assuming that the correct value of Λ is chosen and so we need to choose a range that can be easily fabricated. Importantly, the dispersion characteristics of any fibre taper can be immediately read off the contour

[2]Technically, λ is important through Sellmeier equation but we ignore it here. Note that optical map is calculated for a single wavelength.

graph as each fibre taper corresponds to a path in (Λ, d/Λ) space. However, for ease of taper fabrication, only vertical paths are considered here as these correspond to fibre tapers with a constant d/Λ which can be made by simply heating and stretching the fibre. More complicated profiles which can be made by pressuring the taper during fabrication are not considered here.

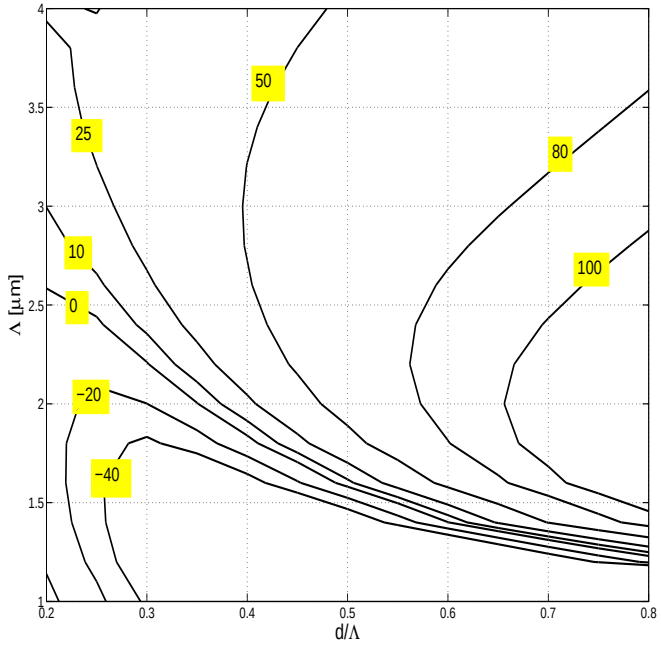

FIGURE 4.2: Dispersion, D [ps/nm/km], contour plot at λ=1.55 μm

Since our fibre tapers have a fixed d/Λ we can compress the 2D map in Figure 4.2 into a series of overlapping curves as shown in Figure 4.3. From Figure 4.3 it can be seen that there are several regions of d/Λ that can be chosen so that a fibre operates in the normal dispersion regime. I chose to examine three regions with d/Λ = 0.2, 0.3 and 0.8 respectively, as these regions have a low absolute value of dispersion, (as seen from Figure 4.3).[3] Importantly, both the nonlinearity and the third order dispersion differ by an order of magnitude in the different regions. Thus these regions allow us to observe the effects of different fibre parameters on the pulse shaping. For these regions the maximum and minimum values of Λ were determined in accordance to the constraint that the absolute value of the dispersion is lower than 40 ps/nm/km (as this level of dispersion can be acceptable in communications applications), according to Figure 4.3. Next, the effect of the confinement loss for each region was examined. Figure 4.4 shows plots of the dispersion and confinement loss versus pitch (Λ) for a fixed d/Λ =0.2, d/Λ =0.3 and d/Λ =0.8, respectively.

[3]It can be observed that there is a large number of different d/Λ and the corresponding pitch values that can be chosen for the analysis.

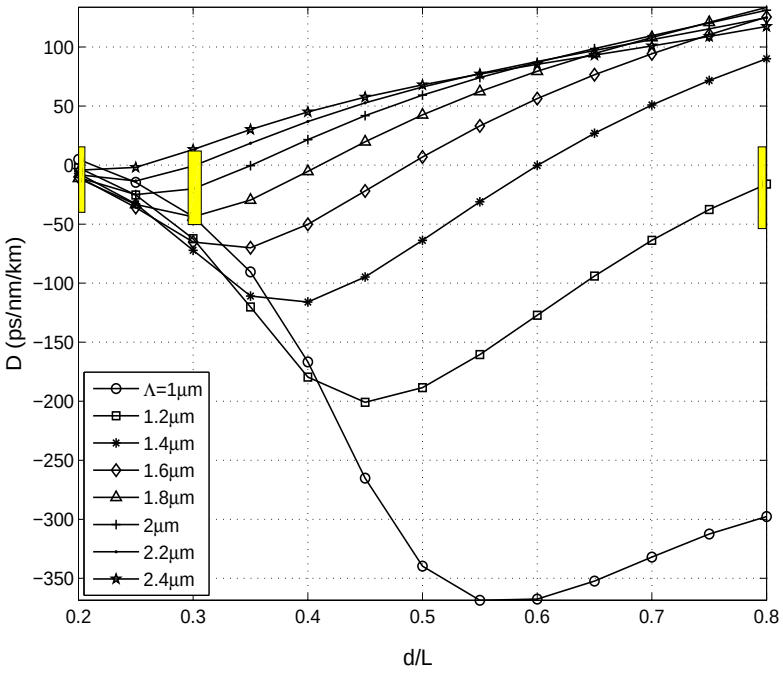

FIGURE 4.3: Dispersion vs. d/Λ for different Λ. Yellow shaded regions emphasize the choice of d/Λ, which fall in the region of low dispersion for the chosen Λ parameters.

From Figure 4.4 it can be seen that although the dispersion is limited to the absolute value of 40 ps/nm/km, the confinement loss changes by several orders of magnitude for different d/Λ, being the lowest for d/$\Lambda = 0.8$ and the highest for d/$\Lambda = 0.2$ (as expected). The results obtained for d/$\Lambda = 0.2$ (Figure 4.4.a) show that although the dispersion is low, the confinement loss of up to 100 dB/m is the crucial factor making this region useless for practical experiments. Therefore, I concentrated on the regions of d/$\Lambda = 0.3$ and d/Λ =0.8, as both the dispersion and confinement loss lie within acceptable limits.

From Figure 4.4.b the parameters of the first taper were chosen, with starting pitch 1.85 μm and finishing pitch 2.2 μm. In the same manner, from Figure 4.4.c, the parameters of the second taper were chosen, the starting pitch 1.18 μm and finishing pitch 1.22 μm. Even knowing the starting and finishing values of the dispersion there is still an infinite range of possible tapers to consider. For the sake of simplicity, a linear profile for the taper is chosen, determined by fibre pitch at the beginning and the end, from the equation:

$$\Lambda = \frac{(z_{max} - z)\Lambda(0) + z\Lambda(z_{max})}{z_{max}} \tag{4.25}$$

where z_{max} is the taper length, $\Lambda(0) = 1.85$ μm and $\Lambda(z_{max})$=2.2 μm, for case when d/$\Lambda = 0.3$ and $\Lambda(0) = 1.18$ μm and $\Lambda(z_{max}) = 1.22$ μm, for case when d/$\Lambda = 0.8$. In the normal dispersion regime smaller absolute values of dispersion correspond to larger

core diameters and therefore taper should be used from the narrow end. Other taper profiles are possible (such as hyperbolic dispersion profile).

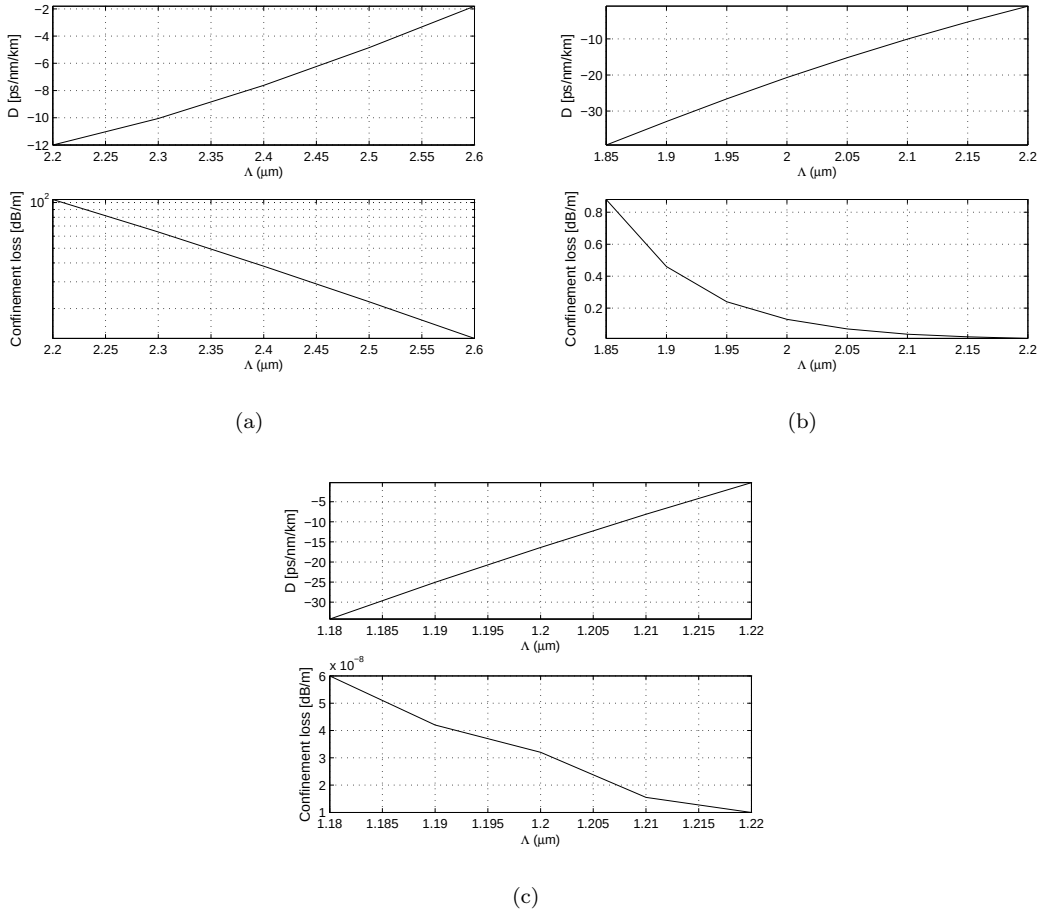

FIGURE 4.4: Dispersion and loss vs. pitch when: a.) d/Λ=0.2; b.) d/Λ=0.3 and c.) d/Λ=0.8.

The parameters of the MOF that change with tapering are the chromatic dispersion β_2, third order dispersion β_3 and nonlinear coefficient γ. Note that it is the effective area that changes along the taper and hence γ does as well. Table 4.1 and Table 4.2 summarize taper parameters for regions d/Λ = 0.3 and d/Λ = 0.8, respectively. β_2, β_3 and γ in function of pitch are used as the interpolation points to calculate the parameters versus taper length (distance), using linear interpolation.

	$\Lambda[\mu m]$	$\beta_2[ps^2/m]$	$\beta_3[ps^3/m]$	$\gamma[W^{-1}km^{-1}]$
Start	1.85	0.050367	-0.0001886	4.1
End	2.2	0.001167	-0.0000761	4.6

TABLE 4.1: Parameters of the tapered fibre ($d/\Lambda = 0.3$)

	$\Lambda[\mu m]$	$\beta_2[ps^2/m]$	$\beta_3[ps^3/m]$	$\gamma[W^{-1}km^{-1}]$
Start	1.18	0.0436	-0.001131	45.1
End	1.22	0.00031	-0.0009118	44.1

TABLE 4.2: Parameters of the tapered fibre ($d/\Lambda = 0.8$)

Setting z_{max} = 10 m, then the final linear taper profile and change of parameters β_2, β_3 and γ with the distance, are shown in Figure 4.5 and Figure 4.6 for d/Λ=0.3 and d/Λ=0.8, respectively.

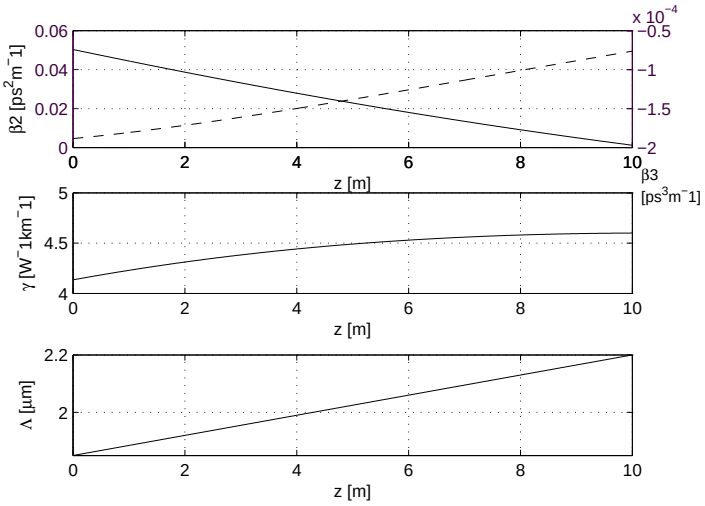

FIGURE 4.5: β_2 and β_3 ($--$) vs. distance (top), γ vs. distance and pitch (Λ) vs. distance (bottom), for d/Λ = 0.3.

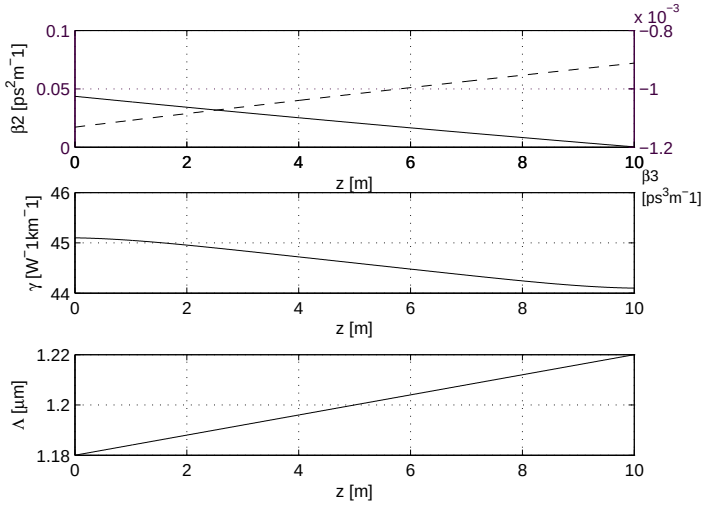

FIGURE 4.6: β_2 and β_3 ($--$) vs. distance (top), γ vs. distance and pitch (Λ) vs. distance (bottom), for d/Λ=0.8.

In this section the suitable linear taper parameters were chosen, following the MOF modelling and generation of the optical map. Next step in the procedure is to numerically simulate the propagation of various peak power and widths pulses along the tapers of different lengths. Consequently, the comparison with the parabolic fit will be performed and the taper which gives the best parabolic pulse determined. Those steps are presented in the following section.

4.3 Simulation results and discussion

The propagation of optical pulses in an optical fibre with variable dispersion and nonlinearity is described by the NLSE:

$$\frac{\partial u}{\partial z} + \frac{\alpha}{2}u + i\frac{\beta_2(z)}{2!}\frac{\partial^2 u}{\partial t^2} - \frac{\beta_3(z)}{3!}\frac{\partial^3 u}{\partial t^3} - i\gamma(z) \mid u \mid^2 u = 0 \tag{4.26}$$

where u is the complex electric field envelope, z is the distance along the fibre, t is time in a copropagating time-frame, α is fibre loss, β_2 is a group velocity dispersion, β_3 is the third order dispersion and γ is the nonlinear coefficient.

The NLSE Equation 4.26 is solved numerically, using the symmetrised split-step Fourier method [53], for the two tapers. In order to quantify the evolution towards parabolic pulse, the evolution of the misfit parameter M^2 between the pulse intensity profile $\mid u \mid^2$ and the parabolic fit $\mid p \mid^2$ was computed, using [101]:

$$M^2 = \frac{\int [\mid u \mid^2 - \mid p \mid^2]^2 d\tau}{\int \mid u \mid^4 d\tau} \tag{4.27}$$

where $p(t)$ is the generalized expression for the parabolic pulse:

$$p(t) = \begin{cases} \sqrt{P_p}\sqrt{1 - 2\frac{t^2}{T_p^2}}\exp(-i\frac{C}{2}t^2), & \mid t \mid \leq \frac{T_p}{\sqrt{2}} \\ 0 & \text{elsewhere} \end{cases} \tag{4.28}$$

where P_p is the peak power of the pulse, T_p is the temporal full-width at half maximum (FWHM) and C the linear chirp coefficient. The linear chirp coefficient can be found as:

$$C = -\frac{\partial \varphi}{\partial t} \tag{4.29}$$

where φ is the electric field envelope phase. A local misfit parameter which looks at the difference between the pulse and an ideal parabolic pulse at that particular instant

in time is also calculated. A Nelder-Mead nonlinear optimization algorithm is used to ensure the best fit of the output pulse to a parabolic profile.

The initial pulse launched into the fibre was a Gaussian pulse with various peak powers and temporal widths. I chose to examine pulse propagation in a taper of z_{max}=10 m length. This value determines slope of the linear taper profile in Equation 4.25, as my aim was to investigate possibility of obtaining best parabolic fit in a longer taper length. I observed propagation of the pulse along the taper from the narrow end, with Λ= 1.85 μm to Λ= 2.2 μm, in the first case, when d/Λ= 0.3. The range of input pulse peak power was 2 kW to 20 kW and range of input pulse FWHM was 200 fs to 5 ps. The range of input pulse peak powers and widths ensured nonlinear propagation in all cases and prevented pulse distortion at higher pulse energies.

It has been shown in [107] that pulse reshaping is possible using nonlinear propagation in a length of a normally dispersive step index fibre. The best misfit parameter obtained in that study was 0.033, for a pulse energy of 31 pJ. My aim, to prove this method to be useful, was to improve upon this figure. In fact, I found that for a range of parameters the minimum misfit parameter for different input energies is less than 0.002 - for the example chosen when d/Λ= 0.8, it is 0.0015. By carefully adjusting input pulse peak power and width it is possible to reach values corresponding to $M^2 < 0.001$, i.e. significantly better than that obtained with a step index fibre.

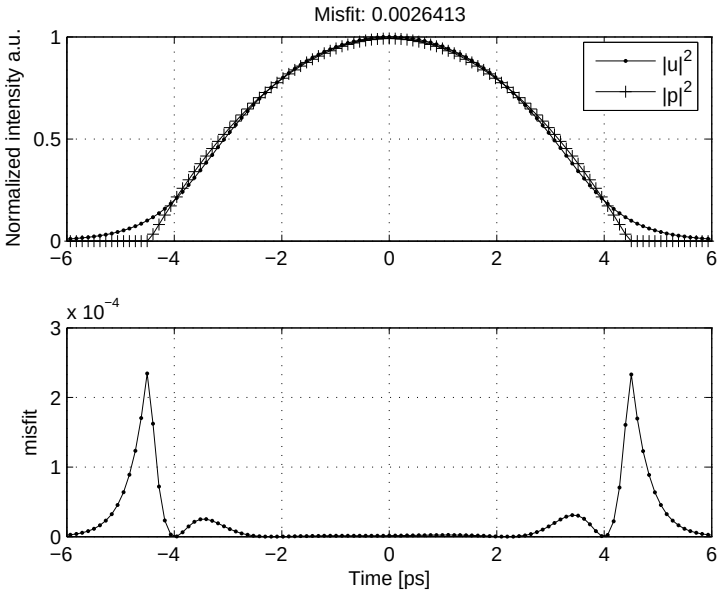

FIGURE 4.7: Top: pulse envelope (normalized $\mid u \mid^2$) against parabolic fit (normalized $\mid p \mid^2$), and bottom: local misfit parameter, d/Λ= 0.3

A typical result is presented in Figure 4.7, which shows a plot of the intensity profile of the output pulse for a taper length of 2.2 m (peak power 2.8 kW and the pulse FWHM width 4.5 ps) and the best parabolic fit, as well as plot of the local misfit. The

pulse envelope is almost perfectly parabolic, apart from the pulse edges, as expected. The local misfit parameter is of the order of 10^{-4} which should be acceptable for most applications.

The minimum values of M^2 along the length of the taper (for d/Λ= 0.3) are shown in Figure 4.8.a (assuming no loss) for differing initial conditions. Figure 4.8.b shows distance along the taper where the misfit parameter has its minimum value. Importantly, the shape of the contours is dependent on the value of z_{max}, which determines the taper slope in Equation 4.25, and is chosen to be 10 m in this case as my motivation was to observe parabolic generation in the longer fibre taper, as it was previously implied. The procedure presented in this chapter can be generalised and used for different taper lengths as well as for different launching conditions.

Similarly, Figure 4.9.a shows the result obtained for the same taper with an artificially high fibre loss taken into account as $\alpha = 0.5$ dB/m. Also, Figure 4.9.b shows distances that correspond to the minimum misfit parameter from Figure 4.9.a.

Comparing these two sets of graphs only minor differences can be seen showing that realistic fibre losses will not significantly affect the parabolic pulse generation. From Figure 4.8.a. and Figure 4.8.b, or from Figure 4.9.a and Figure 4.9.b, we can extract the taper length that will provide best misfit parameter i.e. where the best parabolic pulse is generated. From the contour plots given it can be concluded that there is a range of values of input pulse widths and powers that will enable generation of parabolic pulses. The minimum value of misfit parameter, from Figure 4.8.a, is 0.002, obtained for input powers of around 3 kW, for different input pulse widths. From Figure 4.8.a it can be seen that misfit parameter is a function of the peak power, whilst it is mostly independent on the value of the pulse width. The taper length that corresponds to the chosen pulse peak power and width can be determined from Figure 4.8.b. Therefore, from Figure 4.8.a and Figure 4.8.b it is possible to choose values for input pulse power, width and the taper length (this choice depends on the choice of the equipment used in the particular application).

Figure 4.10 shows parabolic pulse evolution for the chosen parameters of the taper, when $d/\Lambda = 0.3$ and peak power $P_0 = 2.8$ kW, FWHM width $T_0 = 4.5$ ps and the taper length $z_{max} = 2.2$ m.[4]

Figure 4.11 shows the pulse envelope, spectrum, phase and chirp, for the chosen values. The spectra broadening factor is calculated as $B/B0 = 28$ (where B is a 3 dB - bandwidth calculated at $z_{max} = 2.2$ m and $B0$ is bandwidth when z= 0 m) [70]. From the bottom plot in Figure 4.11, which represents instantaneous frequency, or chirp, it

[4]These parameters are chosen for illustration purposes, and it is obvious that the low values of M^2 could be obtained for different choice of the input pulse width, peak power and taper length. The procedure presented represents a proof of principle that parabolic pulses can be generated in tapered microstructured optical fibres.

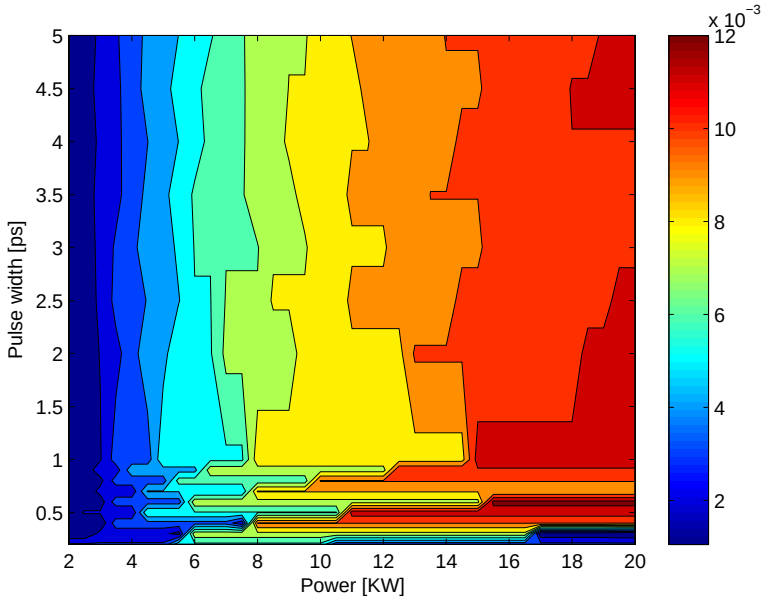

(a)

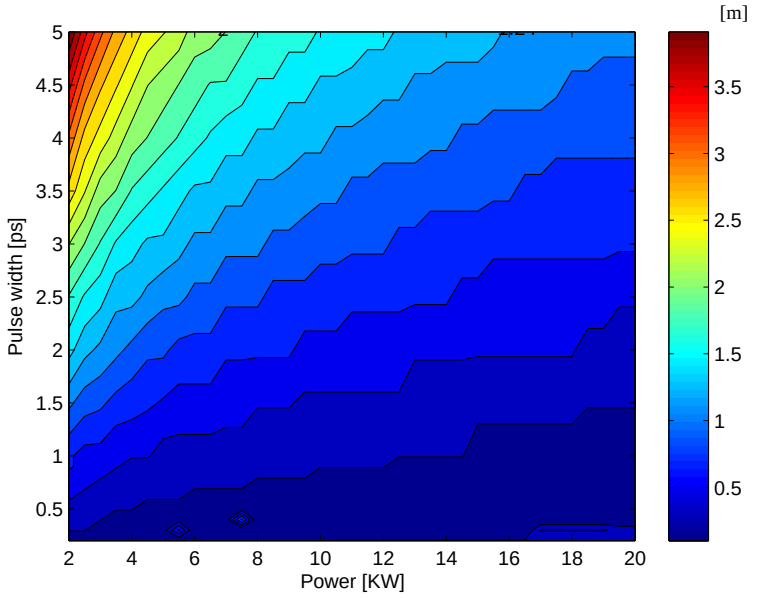

(b)

FIGURE 4.8: a.) Misfit parameter (minimum) for input Gaussian pulse; b.) Taper length where best (minimum) misfit parameter is obtained for input Gaussian pulse, α=0, d/Λ= 0.3

can be seen that, as expected, the generated parabolic pulse has a linear chirp across it and therefore can be useful for practical applications. Figure 4.12 shows the result of the pulse compression performed numerically (using ideal pulse compression) [70], [71], where initial pulse FWHM is 4.5 ps and after compression 310 fs, so that a compression ratio (calculated as the ratio of the FWHM of the input pulse to that of the compressed pulse) of 14.5 is obtained.

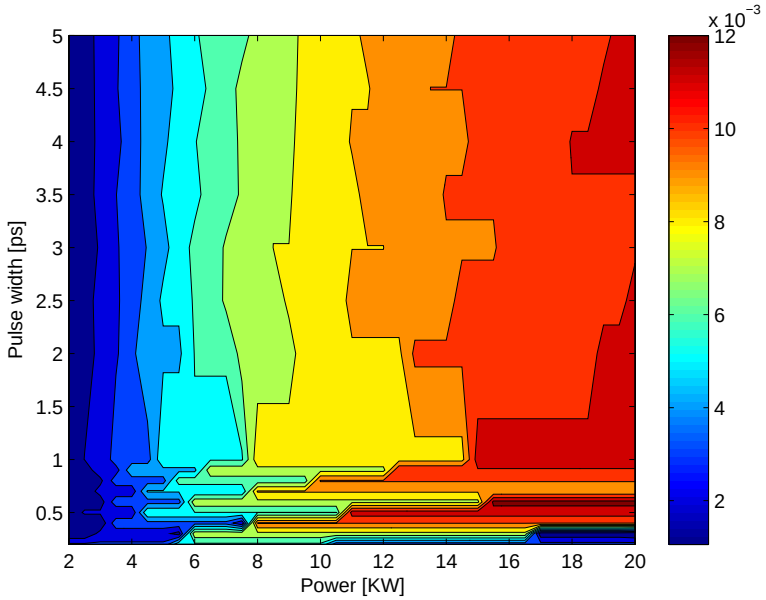

(a)

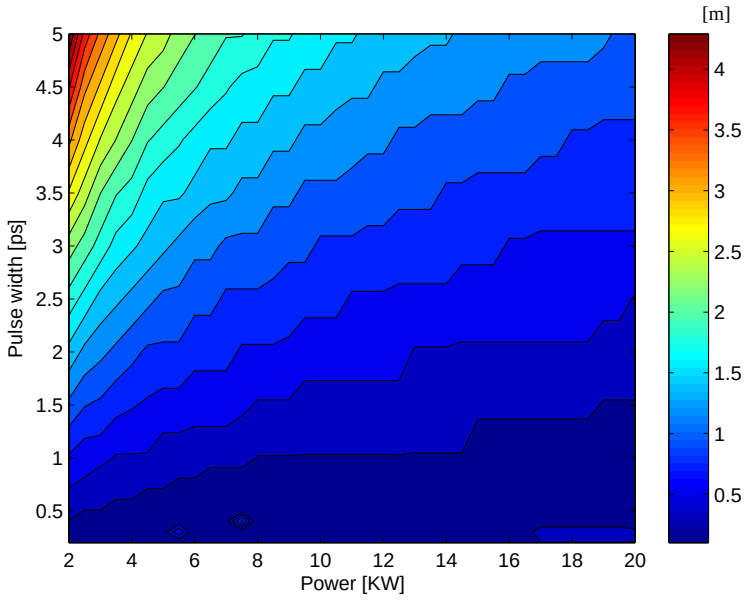

(b)

FIGURE 4.9: a.) Misfit parameter (minimum) for input Gaussian pulse; b.) Taper length where best (minimum) misfit parameter is obtained for input Gaussian pulse, α=0.5 dB/m, d/Λ=0.3

For the second taper, when $d/\Lambda = 0.8$, as the nonlinearity is much higher than when $d/\Lambda = 0.3$, the range of input pulse peak power was 10 W to 1 kW and range of input pulse FWHM was 200 fs to 5 ps. In analogy with the analysis for the first taper, I plotted contour plots of the minimum misfit parameter along the taper length (see Figure 4.13.a) and the corresponding distances (Figure 4.13.b) versus pulse peak powers and FWHM widths.

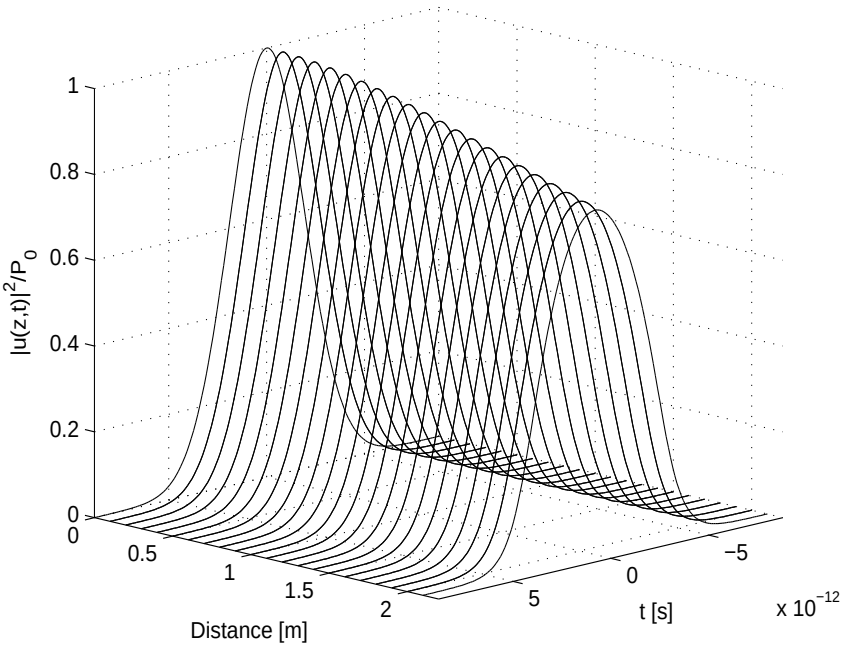

FIGURE 4.10: Parabolic pulse evolution, d/Λ=0.3, α=0

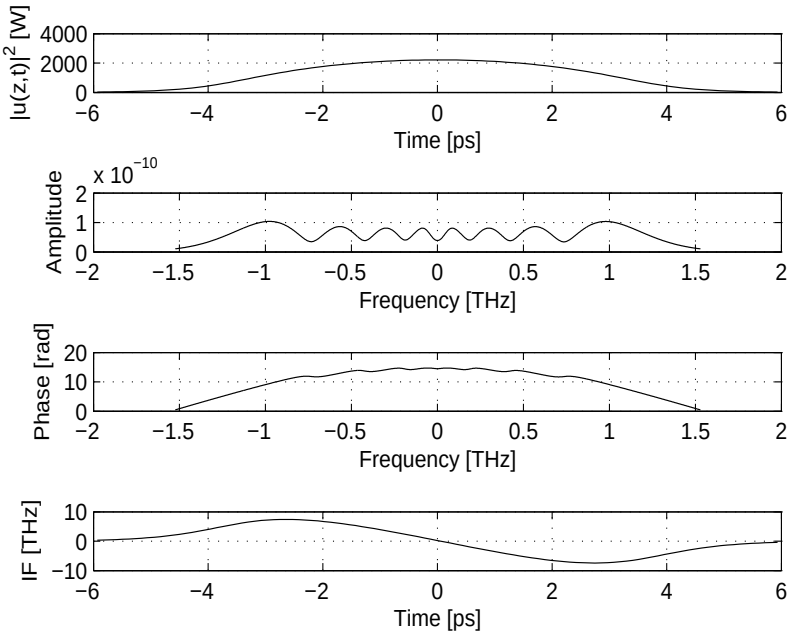

FIGURE 4.11: Pulse envelope, spectrum, phase and chirp coefficient, d/Λ=0.3

From Figure 4.13.a and Figure 4.13.b (as in previous case) the information about the taper length which will provide best misfit parameter can be extracted. The minimum value of misfit parameter, from Figure 4.13.a, is 0.002, obtained for input powers of

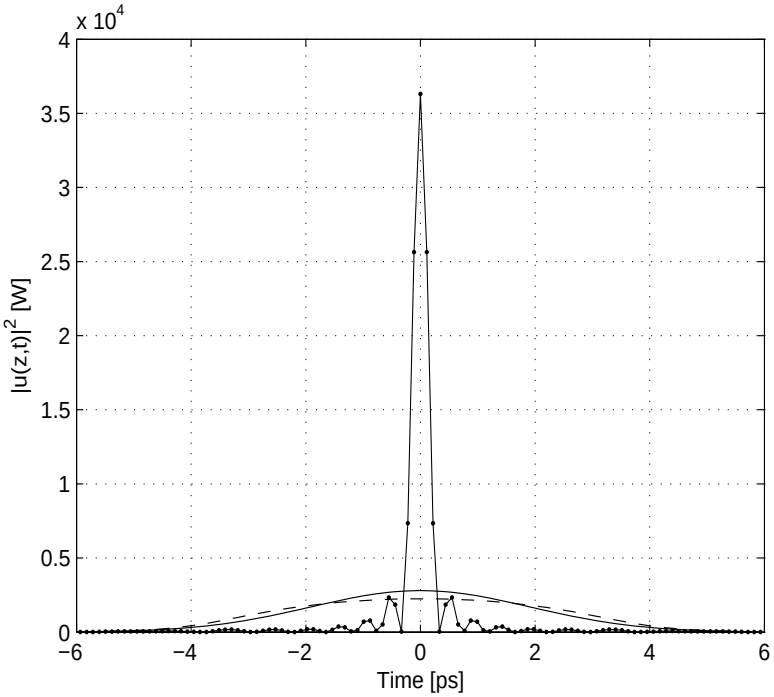

FIGURE 4.12: Initial pulse envelope (-), compressed pulse envelope (•) and parabolic pulse (−−)

around 0.1 kW, for different input pulse widths. The taper length that corresponds to the chosen pulse peak power and width can be determined from Figure 4.13.b. Therefore, from Figure 4.13.a and Figure 4.13.b it is possible to choose values for input pulse peak power, width and the taper length: $P_0 = 0.1$ kW, $T_0 = 2$ ps and z_{max}= 2.3 m, respectively. Analogously to Figures 4.8 and 4.9, these parameters are chosen in accordance to the choice of the taper slope (determined by z_{max}=10 m) and are used for illustrative purposes. Similarly to the taper when $d/\Lambda = 0.3$, from the contour plots given, it can be concluded that there is a range of values of input pulse widths and powers that will enable generation of parabolic pulses.

Figure 4.14 shows parabolic pulse evolution for the chosen parameters of the taper, when $d/\Lambda = 0.8$ and peak power $P_0 = 0.1$ kW, FWHM width $T_0 = 2$ ps and the taper length $z_{max} = 2.3$ m.

Figure 4.15 shows the pulse envelope, spectrum, phase and chirp, for the taper when $d/\Lambda = 0.8$ and the chosen values for the peak power, FWHM width and the taper length. The spectra broadening factor is calculated as B/B0 = 9.25, when d/Λ= 0.8. Result of the numerical pulse compression is shown in Figure 4.16. Initial pulse FWHM is 2 ps and pulse is compressed to 332 fs, so that compression factor of 6 is obtained for this case. The side lobes observed in Figure 4.12 and Figure 4.16 are the theoretical wings of a compressed parabolic pulse.

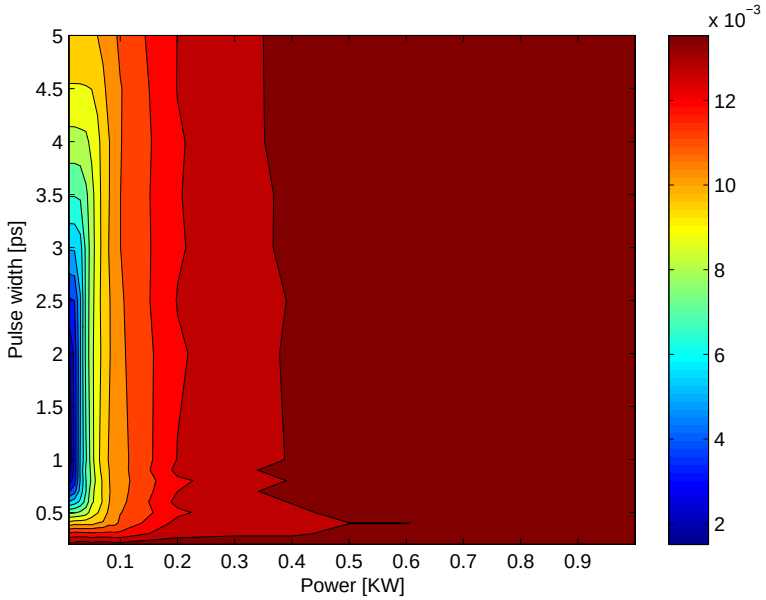

(a)

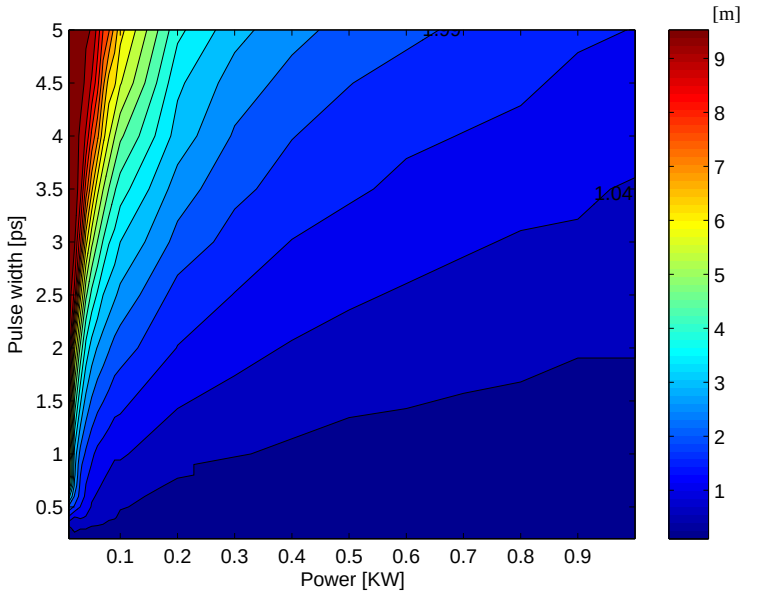

(b)

FIGURE 4.13: a.)Misfit parameter (minimum) for input Gaussian pulse; b.)Taper length where best (minimum) misfit parameter is obtained for input Gaussian pulse, α=0, d/Λ= 0.8

Figure 4.17, for d/Λ= 0.8 presents the pulse envelope at the taper's output, for the parameters: taper length 2.3 m, P_0 = 0.1 kW and T_0 = 2 ps and at the bottom plot the misfit parameter or the error between the pulse intensity profile and the parabolic fit calculated using Equation 4.27. It can be seen that the pulse exhibits the parabolic intensity profile, but with a small discrepancy in the wings of the pulse.

By comparison of Figure 4.17 and Figure 4.7 it can be observed that the minimum misfit

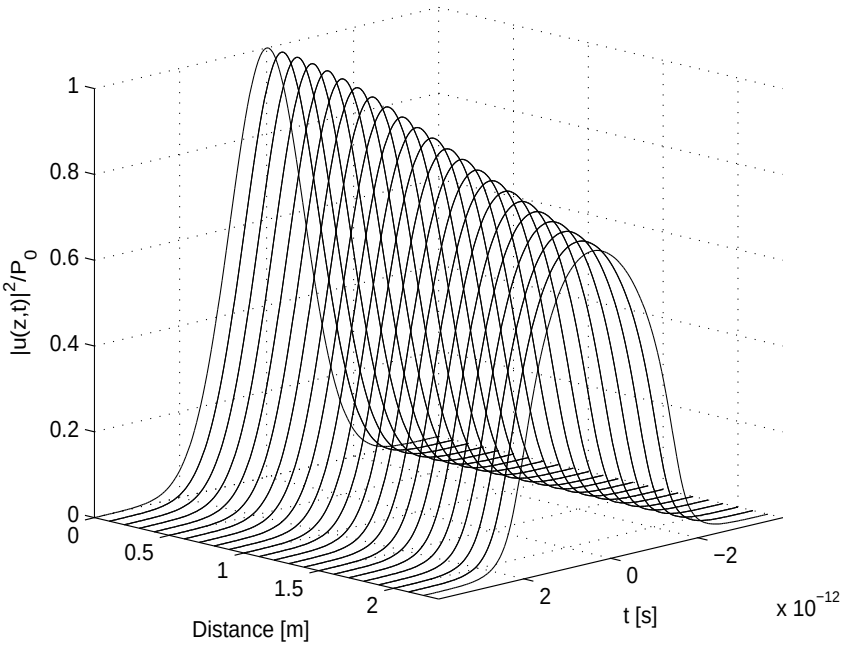

FIGURE 4.14: Parabolic pulse evolution, d/Λ=0.8

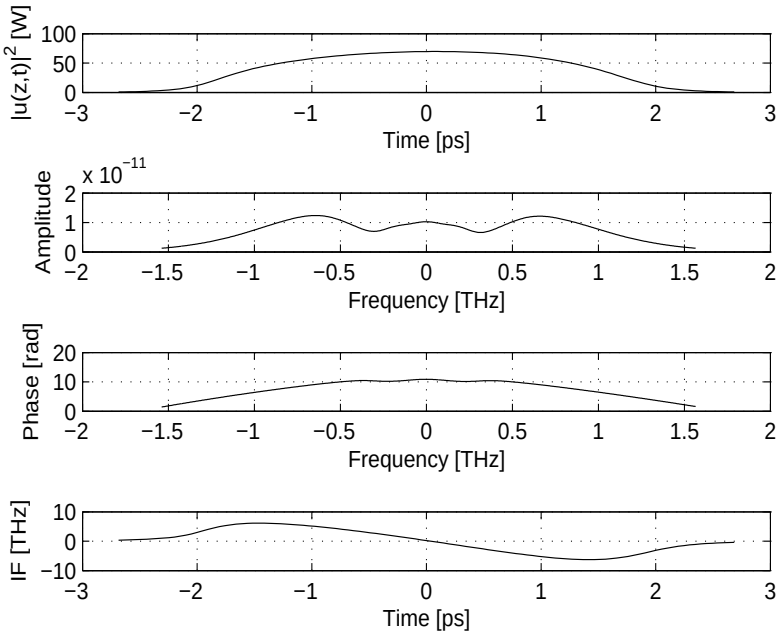

FIGURE 4.15: Pulse envelope, spectrum, phase and chirp coefficient, d/Λ=0.8

parameter has a lower value when d/λ=0.8, so the intensity profile of the pulse for the taper when d/λ=0.8 deviates less from the parabolic shape in comparison to the case when d/λ=0.3, although it deviates slightly more at the top of the pulse. I anticipate

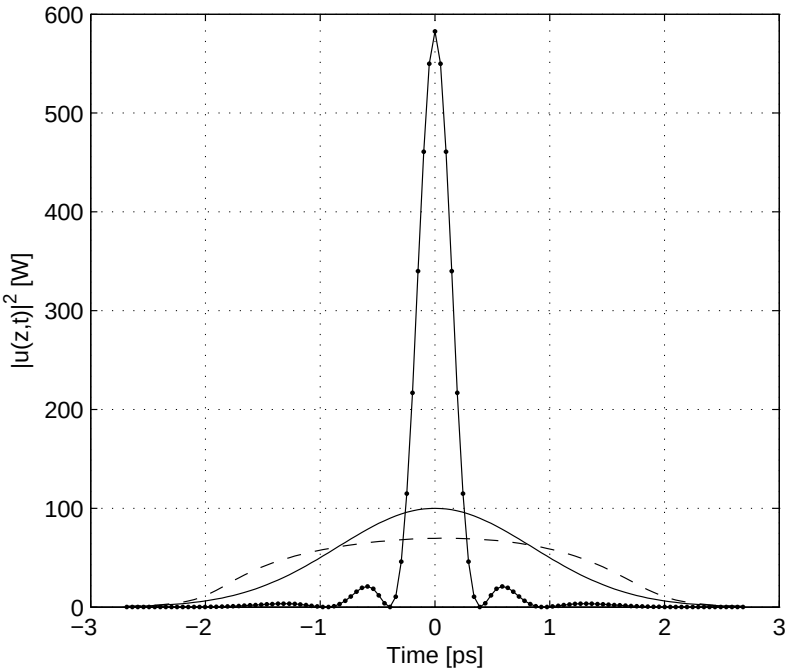

FIGURE 4.16: Initial pulse envelope (-), compressed pulse envelope (•) and parabolic pulse (−−), d/Λ=0.8

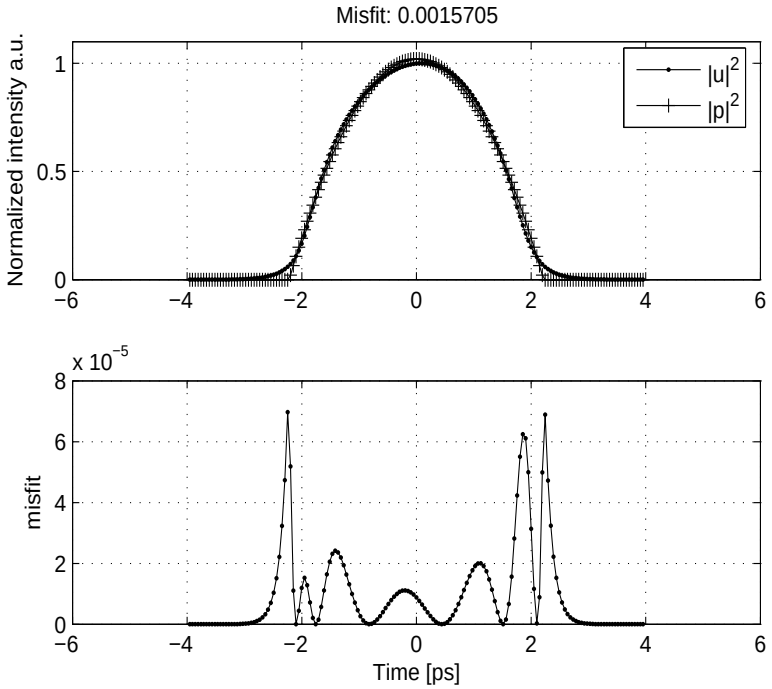

FIGURE 4.17: Top: pulse envelope (normalized $\mid u \mid^2$) against parabolic fit (normalized $\mid p \mid^2$), and bottom: local misfit parameter, d/Λ=0.8

that this asymmetric deviation from the parabolic shape is due to the value of the third order dispersion, which is nearly one order of magnitude higher when d/λ=0.8 in

comparison to the case d/λ=0.3. Also, the higher power of the pulse when d/λ=0.3 is another reason for this greater misfit.

4.4 Conclusion

In this Chapter I have introduced the theoretical background of the parabolic pulse generation in the normally dispersive optical fibre, which relies on the theory of self similarity. The theory shows that in a system described by the ideal lossless NLSE with decreasing dispersion (taper), optical pulse evolution is formally similar to that of a medium with a constant gain and an asymptotic self-similar parabolic pulse solution is found to exist in a taper. Furthermore, I have presented results of modelling and simulation of tapered normally dispersive microstructured optical fibres. I have identified two normal dispersion regions, and outlined a procedure for choosing the parameters of the taper profile for efficient parabolic pulse generation. The design procedure of a fibre taper for parabolic pulse generation followed the steps:

1. Generate optical property maps for the relevant wavelength and pitches;
2. Choose a suitable linear taper;
3. Numerically simulate the propagation of varying peak powers and widths pulses down fibre tapers of different lengths;
4. Compare the output pulse with a parabolic pulse;
5. Choose the taper which gives the best parabolic pulse.

The parameters of the MOF (pitch and the air-filling factor) are determined so that the normal dispersion regime is obtained. For two different values of the air-filling factor 0.3 and 0.8, two different tapers with a linear profile are proposed. In the case when $d/\Lambda = 0.3$ the confinement loss is non-negligible, so it has been taken into consideration. Results show that Gaussian input pulse of different peak power and width can evolve into the parabolic shape with a linear chirp coefficient in both cases. The two different spectra broadening factors are calculated for two different cases, 28 when d/Λ=0.3 and 9.25 when d/Λ=0.8. Also, results show that using the first taper, when d/Λ=0.3, linearly chirped parabolic pulse of FWHM width 4.5 ps can be compressed down to 310 fs, so that compression factor of 14.5 is achieved and for the second taper, when d/Λ=0.8, initial pulse FWHM width 2 ps is compressed to 332 fs, so that compression factor 6 is obtained. The optimal taper length, to achieve the best parabolic characteristic for a range of input powers and pulse widths has also been determined. Results show that due to the different nonlinearity parameters for the two tapers under consideration, best parabolic fit can be achieved for different pulse energies. When d/Λ =0.3, minimum

misfit parameter is achieved for pulse energy in range from 10 nJ to 24 nJ, while when d/Λ=0.8, due to the higher nonlinearity coefficient, the pulse energy range that gives minimum misfit parameter is from 177 pJ to 440 pJ. Therefore, it implies that these results might be of interest where pulse reshaping is conditioned by the initial pulse energy availability. Based on the presented procedure, optimization can be performed to find the best possible taper profile and length for the parabolic pulse generation.

My major contributions presented in this Chapter are:

1. Detailed analysis of the principal method used for modelling of tapered MOF and determination of the parameters of the taper profile;
2. Generating `Matlab` script for calculation of dispersion optical property map;
3. Generating `Matlab` script to model the parabolic pulse generation in tapered MOF. The program could be easily modified to treat any pulse shape propagation through any profile of the tapered MOF (Parts of the `Matlab` code are given in Appendix C).

The possible direction for the future work in this area is the investigation of parabolic pulse generation extended to different taper profiles (such as hyperbolic or exponential) with different dispersion limits in the normal dispersion regime. Alternatively, the design procedure could be conducted in reverse, so that having specified minimum misfit parameter value for the best parabolic pulse fit, the optimum taper profile can be determined.

Following the numerical consideration presented in this chapter, next chapter shows the investigation towards the experimental confirmation.

Chapter 5

Experimental Investigation of Parabolic Pulse Generation in Tapered Microstructured Optical Fibre

5.1 Introduction

It is well known [1], [93], that in the normal dispersion regime, due to the interaction between fibre dispersive and nonlinear effects, high intensity pulses suffer from wave breaking effect [99], which can be avoided if the pulse is characterised by a linear chirp. This can be achieved using parabolic pulses, which have the potential of flat broadband spectra and can be efficiently compressed in the time domain.

It Chapter 4 I described how when a high intensity optical pulse is launched into the fibre, the pulse evolves into a linearly chirped, parabolic pulse in which the nonlinear chirp introduced by the self phase modulation is linearized gradually by normal group velocity dispersion. There are different principles of the parabolic pulses generation, as discussed in Chapter 4, due to the interaction between gain, nonlinearity and dispersion [99] - [115]. In particular, parabolic pulses can be generated in a passive manner using normally dispersive dispersion decreasing fibres (tapers) [104], [105], or fibre gratings etc. [95], [97], [106]. Parabolic pulses generated using tapers are attractive as they are considerably cheaper and less complex to produce when compared to the use of amplifiers.

Tapered MOFs have unique properties, making them ideal for parabolic pulse generation. Tapered MOFs are used for many other applications, as it has been emphasised previously in this thesis, such as pulse compression [35] - [37], stimulated Brillouin scattering

threshold enhancement [31] - [33], supercontunuum generation [38] - [41] etc. Tapered microstructured optical fibres represent an alternative way to produce the required dispersion decreasing fibre. This method is ideal for producing metre-length tapers needed to efficiently generate parabolic pulses using femtosecond pulses, as was shown in Chapter 4. Moreover, in Chapter 3 I presented a design and results of the development of a novel tapering facility capable of fabricating the required metre-long optical fibre tapers.

My experimental investigation[1] towards the parabolic pulse generation in tapered MOFs consists of three sets of measurements, performed using three different tapered MOFs. I modelled and fabricated three tapers, 40 cm - length, 60 cm - length and a 1.8 m - length taper. This Chapter is organized so that first I present results related to the first configuration, using 40 cm - length taper, followed by the results of the second configuration, using 60 cm - length taper and finish by presenting the results of the experiment using 1.8 m - long taper.

5.2 Nonlinear pulse propagation in tapered MOF - first experimental set-up

In this Section I present the modelling results of the tapered MOF, the fabrication of a 40 cm-length taper and the results of the experiment performed using this taper. The results didn't meet expectations, but provided me with important information about how the experiment could be improved.

5.2.1 Taper design and fabrication

Microstructured optical fibres have extended the range of possibilities in optical fibres, by allowing remarkable control of their optical properties (dispersion, nonlinearity, birefringence). However, the microstructured fibre drawing process is challenging, as different types of distortion [2] are introduced through the effects of viscous flow, surface tension and pressure and therefore they are much more expensive in comparison to standard optical fibres.

The major idea behind this experiment was to observe nonlinear phenomena in metre-long tapered MOFs (meso-tapers) [116]. The choice of microstructured optical fibres was limited and the fibre that was initially available for me to use had the following parameters: hole diameter d=1.6 μm, pitch Λ=1.74 μm, d/Λ=0.92, core diameter=1.2 μm. The SEM image of the fibre is shown in Figure 5.1.

[1] I am enormously grateful to Dr Francesca Parmigiani for her help in conducting these experiments.

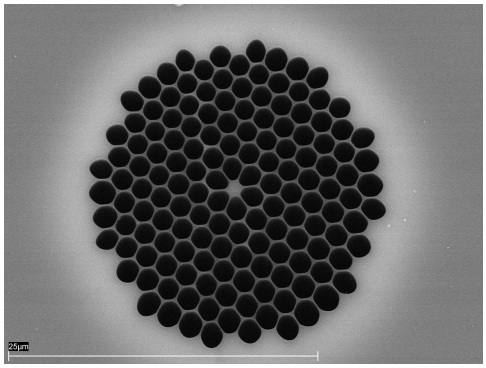

FIGURE 5.1: SEM image of the MOF, scale = 25 μm

As was explained in Chapter 4, after measuring the fibre parameters that determine the fibre optical properties (Λ, d/Λ, core diameter), I used the finite element method to solve for the fibre dispersion, effective area and confinement loss of the lowest order mode. The chromatic dispersion of the fibre in function of pitch calculated at λ=1550 nm is shown in Figure 5.2.a. This graph can be used to determine the minimum and maximum values of parameter Λ (the parameters of the linear taper profile), so that the taper operates in the normal dispersive regime which is of importance for the parabolic pulse generation (previously described in Chapter 4). I chose the same criteria which limits the absolute value of dispersion to practically usable values. However, this fibre operates in the anomalous dispersion regime at wavelength 1550 nm, as can be seen from Figure 5.2.a, whilst zero dispersion is achieved for pitch value approximately 1.19 μm. Therefore, I decided to taper the fibre linearly until the normal dispersion regime it obtained. Using the dispersion profile in Figure 5.2.a the starting and finishing pitch for the linear taper profile are determined to be $\Lambda(0)$=1.14 μm and Λ(end)=1.18 μm, respectively. Similarly to the procedure in Chapter 4, for the sake of simplicity, I chose a linear profile for the taper, determined by fibre pitch at the beginning and the end, given by the Equation 4.25, $\Lambda(0)$= 1.14 μm and $\Lambda(z_{max})$= 1.18 μm.

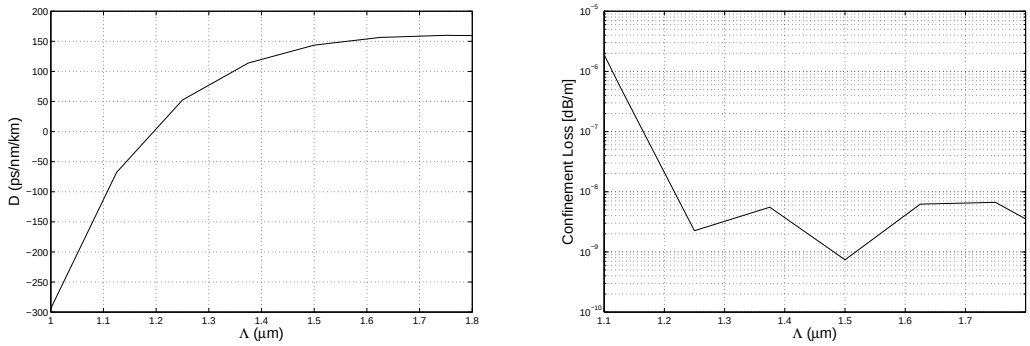

(a) (b)

FIGURE 5.2: a.) Dispersion of the MOF b.) Confinement loss of the MOF

Figure 5.2.b. shows the calculated confinement loss as a function of pitch, which is low for the range of pitch values of interest and so disregarded in further calculations. The parameters of the linear profile taper are summarized in Table 5.1.

	$\Lambda[\mu m]$	$\beta_2[ps^2/m]$	$\beta_3[ps^3/m]$	$\gamma[W^{-1}km^{-1}]$
Start	1.14	0.0624	-0.00131	53.8
End	1.18	0.0065	-0.00117	52.7

TABLE 5.1: Parameters of the tapered fibre ($d/\Lambda = 0.92$)

The next step was to fabricate a taper according to the calculated parameters. As the original MOF has a pitch value Λ=1.74 μm and the anomalous dispersion, I pre-tapered the fibre 18% along first 10 cm of its length, in order to reduce the pitch value from 1.74 μm to 1.18 μm, as it was determined to fall in the region of normal dispersion (see Figure 5.2.a). Then, the fibre was tapered further 4% along 0.4 m of length to obtain the pitch value of 1.18 μm, as previously calculated. The diameter profile of the taper fabricated in this way is shown in Figure 5.3.

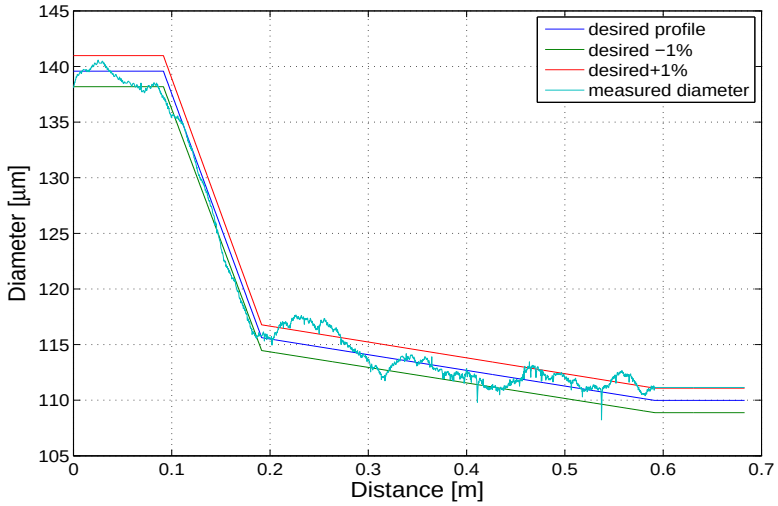

FIGURE 5.3: Taper diameter vs. distance (diameter variation within ±1%)

It can be observed that the diameter variation is within the ±1% of the value of the desired fibre diameter at almost the whole taper's length. However, the taper profile is very demanding and I anticipate that the uncertainties in the tapering process could affect the optical properties of the taper. It should be taken into consideration that the approximation in the numerical and experimental investigation throughout this thesis is the assumption that the structure of the fibre was preserved along the transition region. The taper profiles are complex with highly demanding requirements for their fabrication, but nevertheless the accurate measurements have to be taken in the future

improvements of the system (e.g. by introducing accurate nondestructive measurement of the structure parameters).

Figure 5.4 shows the parameters of the taper (β_2, β_3, Λ and γ) changing with the taper length. As explained in Chapter 4, I calculated the parameters for different pitch values and used them as the interpolation points to calculate the parameters versus taper length, using linear interpolation.

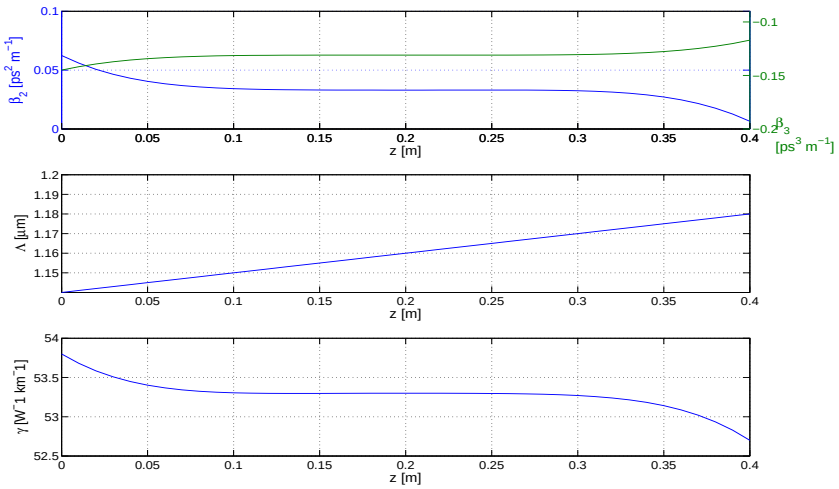

FIGURE 5.4: β_2 and β_3 vs. distance (top), pitch Λ vs. distance and γ vs. distance (bottom)

5.2.2 Results and discussion

The experimental set-up used to study parabolic pulse generation in the fabricated tapered microstructured optical fibre is shown in Figure 5.5.

The input signal was generated by a commercial mode locked Erbium Glass Oscillator (ERGO) producing $\sim$ 2.8 ps Gaussian pulses at 1550 nm and the repetition rate of 10 GHz. The signal was then amplified up to an average power of 33 dBm using a high power Erbium Doped Fibre Amplifier (HP-EDFA). A 5 nm filter was used to filter out the HP-EDFA amplified spontaneous emission (ASE) noise. Assessment of the pulses quality was done using the l-FROG technique [58], [59], explained in Chapter 2. The polarisation controller (PC) was used to align the input signal to the polarisation axis with the higher nonlinear coefficient of the tapered MOF.

The retrieved temporal intensity and phase and the spectra and spectral phase of the ERGO signal is shown in Figure 5.6. The temporal FWHM of the retrieved pulse is 2.85 ps. The spectra at the input and at the output of the taper were measured by an Optical Spectrum Analyzer (OSA).

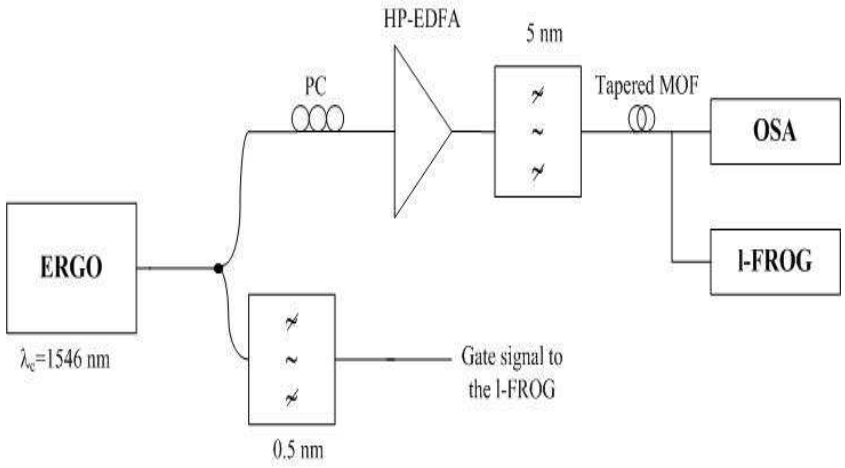

FIGURE 5.5: Experimental set-up for the parabolic pulse shaping

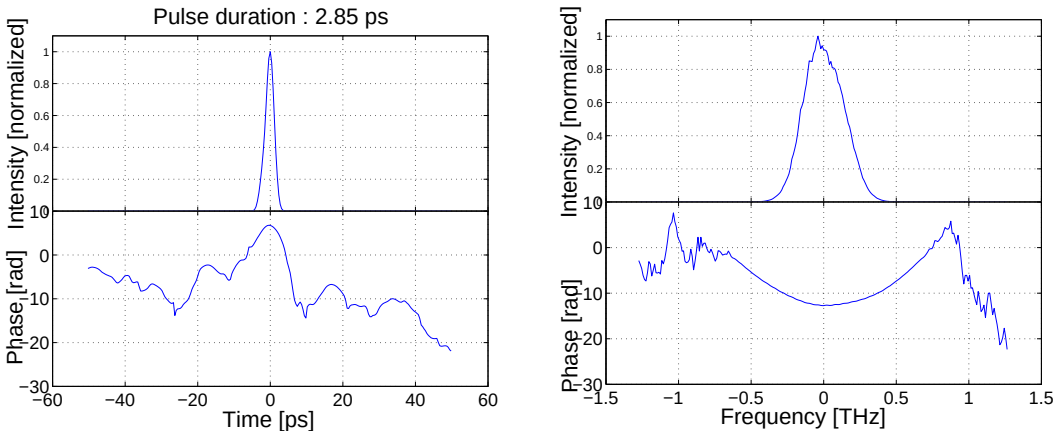

(a) (b)

FIGURE 5.6: a.) Normalized envelope and phase at the output of ERGO. b.) Normalized spectra and spectral phase.

In this experiment the l-FROG measurement was only taken at the taper's output and the corresponding pulses' temporal and spectral intensity were retrieved. However, the same measurement at the taper's input had not been taken and therefore I couldn't use the interpolation data[2] as the input pulse in the simulation and consequently, I couldn't obtain best fitting with the experimental results. This issue was addressed and improved in the experiment that will be described in the Section 5.4. The launching efficiency in

[2]The interpolation data is used in a context of using the discretised signal at the input of the taper, obtained as a result of a l-FROG retrieval, and interpolating the pulse to the number of points used in the split step algorithm which solves the NLSE propagation equation.

this experiment, when the light was coupled into the fibre core of a diameter less than 1 μm, was ~10%. The calculated peak power at the input of the taper, after taking into account system parameters, for the average power of the HP-EDFA of 33 dBm, was 26 W. The calculation is based on the following simple formulaes:

$$E = \frac{P_{av}}{f_{rep}} \tag{5.1}$$

$$P_0 = \eta \frac{1.665E}{\sqrt{\pi} T_{FWHM}} \tag{5.2}$$

where P_{av} is the average power, f_{rep} is the repetition frequency, T_{FWHM} is the Gaussian pulse FWHM temporal width, E is the energy of the Gaussian pulse, P_0 is the pulse peak power at the input of a taper and η is the launching efficiency.

In order to understand the experimental results I compared the pulse intensity profile at the output of the taper with the parabolic fit and quantified the evolution towards the parabolic shape using the misfit parameter defined by Equation 4.27. In this experiment it was observed that when the average power was low, the misfit parameter had very high value so that the pulse intensity profile was significantly different from the desired parabolic shape. The results were getting just marginally better for the increased power. Figure 5.7 shows the results of measurement and simulation for the maximum achievable power of 33 dBm. Figure 5.7.a (top) shows the pulse envelope calculated from the simulation, compared to the ideal parabolic fit. The result shows very high value of the misfit parameter (0.077), implying that no parabolic pulse was achieved. Figure 5.7.a (bottom) presents the comparison of the pulse's envelope measured at the output of the taper using the l-FROG technique and the pulse's envelope obtained from the simulation, when 5 m of SMF fibre from the output of taper to the l-FROG, was taken into account. The discrepancy between these two results can be attributed to the use of a Gaussian pulse as the input pulse in the simulation instead of using the signal obtained from the l-FROG measurement at the input of the taper. Another reason could be that due to the necessity to cleave the fibre to improve the coupling efficiency, a dispersion regime has been reached that wasn't predicted in the model. The results of the pulses' spectra taken by OSA at the taper's output for different power and the spectra obtained as a result of the simulation are shown in Figure 5.7.b. Some spectra broadening in the taper was obtained, as the power was increased, however, some discrepancy with the simulation result can be observed.

In spite of that the results of the experiment were far from the expected, this experiment proved to be an useful start and enabled information about what could be improved in the taper's design and in the measurement procedure in order to progress towards the generation of parabolic pulse in the tapered MOF. The major conclusion from the results taken in this first attempt was that longer optical fibre tapers needed to be fabricated,

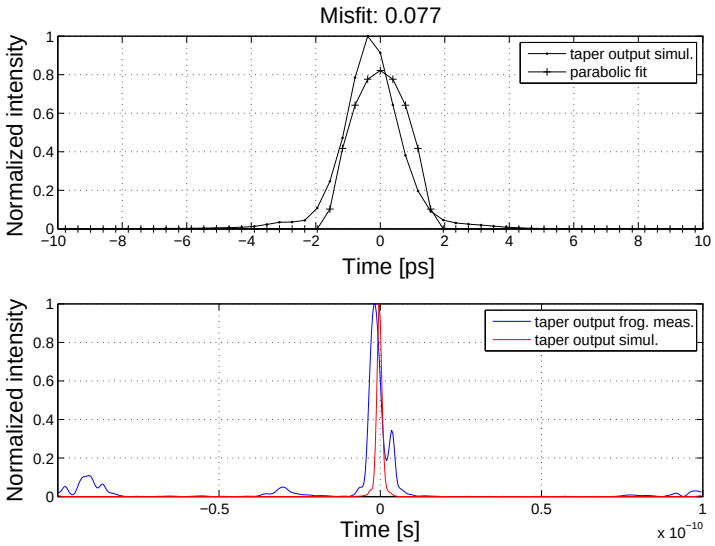

(a)

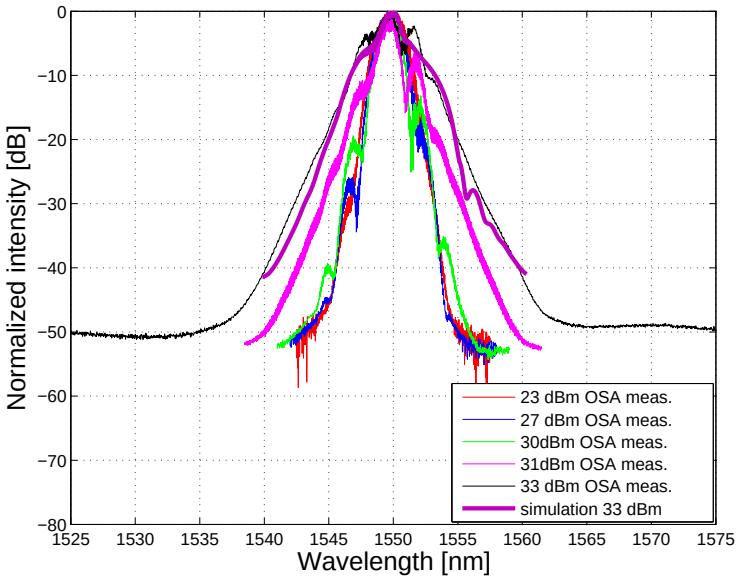

(b)

FIGURE 5.7: a.) Top: Taper output pulse envelope against parabolic fit; Bottom: Pulse envelope at the output of the taper. b.) Normalized spectra at the taper output compared to OSA spectra for different powers.

ideally from the fibre that has normal dispersion at 1550 nm. In addition, another conclusion was that more systematic measurements had to be taken so that the results could be easily validated using numerical modelling. All issues have been addressed and explained in Section 5.4.

5.3 Nonlinear pulse propagation in tapered MOF - second experimental set-up

In this Section I present the modelling results of the tapered MOF, the fabrication of a 60 cm-length taper and the results of the investigation of experimental parabolic pulse generation in tapered MOF, performed using this taper. Although the results do not show the parabolic pulse generation, they provided for me additional important information about the experimental set-up.

5.3.1 Taper design and fabrication

In the second attempt to perform an experiment of parabolic pulse generation in tapered MOF, the appropriate microstructured optical fibre wasn't yet available. Therefore, I used the same fibre as described in the previous section (the fibre parameters were: hole diameter d=1.6 μm, pitch Λ=1.74 μm, d/Λ=0.92, core diameter=1.2 μm). The SEM image of the fibre is shown in Figure 5.1.

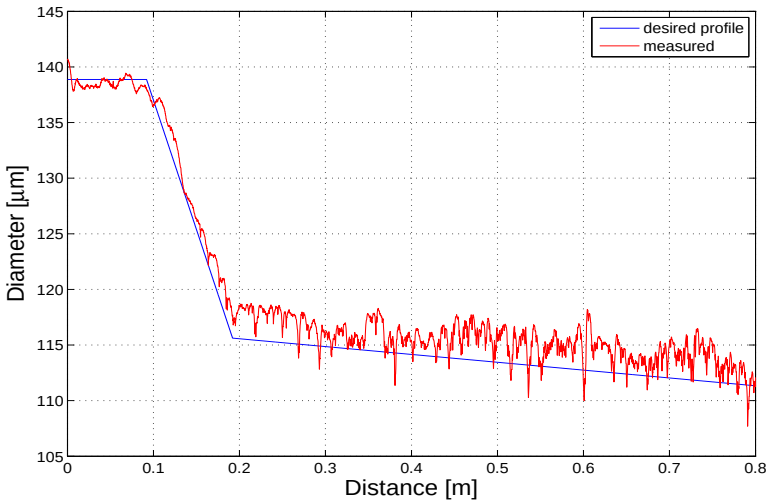

FIGURE 5.8: Taper diameter vs. distance

Bearing in mind the conclusion derived from the first experiment, I attempted to fabricate a longer taper. However, the optical fibre recoater was also not available at the time of the experiment. The problem I faced was difficulty to handle longer tapered fibres (that were so fragile being uncoated), so that the taper I fabricated was only 60 cm long. The variation of taper's diameter along the length of the taper is shown in Figure 5.8. The significant oscillations in the taper diameter, shown in Figure 5.8, originate from the lower temperature of the microheater unit, which at this stage exhibited problems, so that higher temperature, required to reach the silica fibre softening point, couldn't be achieved. This lower temperature led to the increased tension of the fibre, which caused

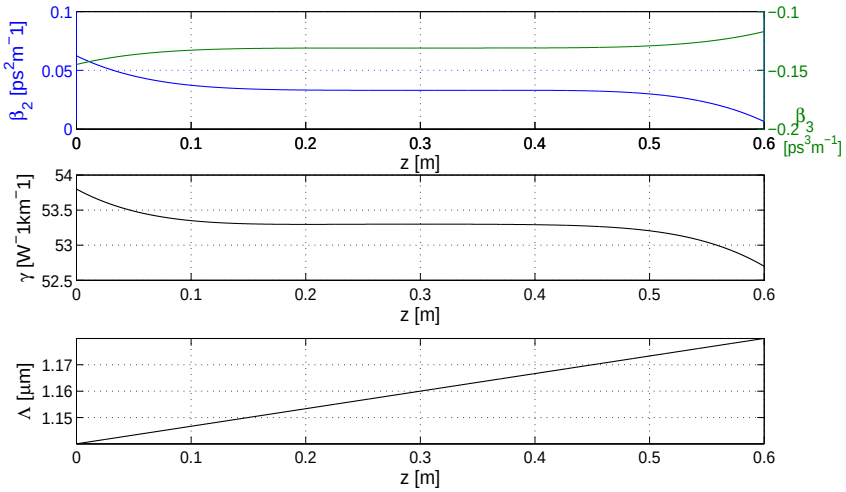

FIGURE 5.9: β_2 and β_3 vs. distance (top), pitch Λ vs. distance and γ vs. distance (bottom)

the oscillations of the fibre during tapering and consequently a ripple in the diameter variation.

The microstructured optical fibre was pre-tapered 18% along first 10 cm of its length, in order to reduce the pitch value from 1.74 μm to 1.18 μm, as it was determined as the region of normal dispersion and afterwards further 4% to reach the pitch value of Λ = 1.14 μm. Figure 5.9 shows the parameters of the taper (β_2, β_3, Λ and γ) changing with the taper length.

5.3.2 Results and discussion

The experimental set-up was the same as described in section 5.2. and shown in Figure 5.5. The input signal was generated from an ERGO source at 1550 nm, which generated $\sim$ 1.5 ps Gaussian pulses, which were gated down by the modulator to produce a 5 GHz train of pulses. The pulses were amplified up to 33 dBm using the HP-EDFA, followed by the 5 nm filter, to reduce the ASE noise. The pulses time and frequency domain profiles were assessed using the l-FROG, just like in the previous experiment.

In this experiment the l-FROG measurements at the taper's input (after the HP-EDFA and the filter) were taken and also at the taper's output. Pulses' temporal and spectral intensity and corresponding phase were retrieved. The launching efficiency in this case was slightly improved, although the fibre core diameter was less than 1 μm, to a value of $\sim$15%. The HP-EDFA introduced nonlinearity, so that both the signal time and frequency domain intensity profiles changed after the propagation through HP-EDFA for high power. The pulse time intensity and spectra after the propagation through HP-EDFA, at 33 dBm, is shown in Figure 5.10. It can be observed that signal time duration

decreased from 1.5 ps that was initial FWHM at the ERGO output, to 0.88 ps at the HP-EDFA output. This result obtained from the FROG retrieval was implemented, after the interpolation, as an input pulse in the simulation in order to provide better fitting with the experimental results.

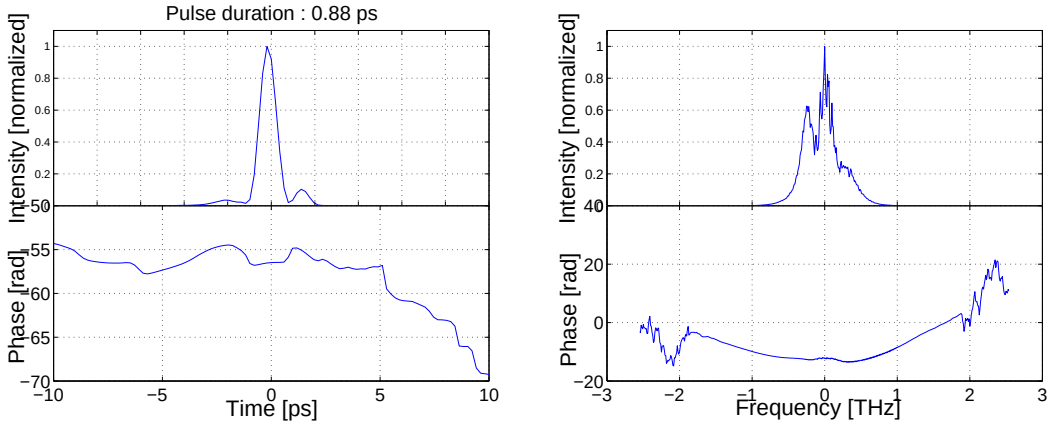

(a) (b)

FIGURE 5.10: a.) Normalized envelope and phase at the output of HP-EDFA. b.) Normalized spectra and spectral phase.

As in the previous section, the HP-EDFA increased the power of the pump signal up to 33 dBm. The peak power of the pulse at the taper's input was in the range from 10 W to 60 W.

Figure 5.11 shows the results of measurement and simulation for the maximum achievable power of 33 dBm. Figure 5.11.a (top) shows the pulse envelope calculated from the simulation, when parameters of the experiment were taken into account and compared to the ideal parabolic fit. The result shows that the value of the misfit parameter is 0.0644, which is lower than the value that was obtained in the previous section (0.077), using a 40 cm long taper, but it is still so high so it implies that no parabolic pulse has been generated. Figure 5.11.a (bottom) shows the comparison of the pulse's envelope measured at the output of the taper using the l-FROG method and the pulse's envelope obtained from the simulation. Agreement between the spectra taken at the output of the simulation and the spectra measured for 33 dBm power at the HP-EDFA can be observed. However, there is still some discrepancy which appears due to the mismatch between the dispersion parameters that were calculated and the dispersion parameters of the actual taper. Another possible reason for the discrepancy could be the mismatch between the actual and estimated pulse peak power. Similar results were obtained when different peak power were used.

In order to validate the results of the experiment, I have taken samples of the taper used in the experiment both at the taper's input and output and used the SEM imaging (using program described in the Appendix A for the automatic post-processing of the

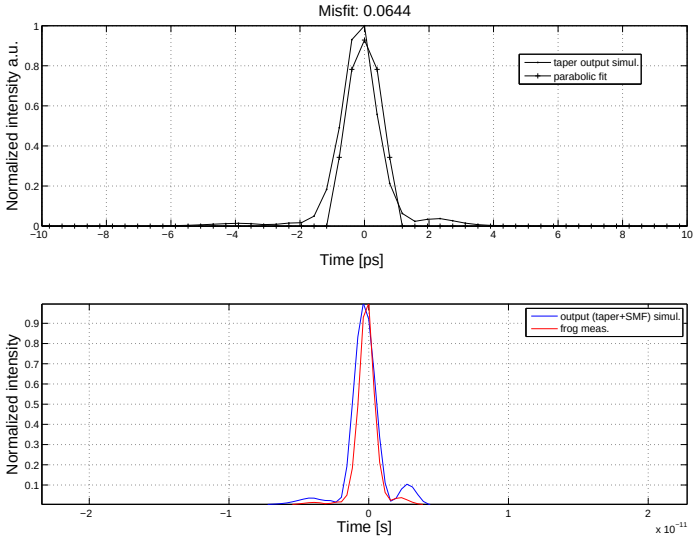

(a)

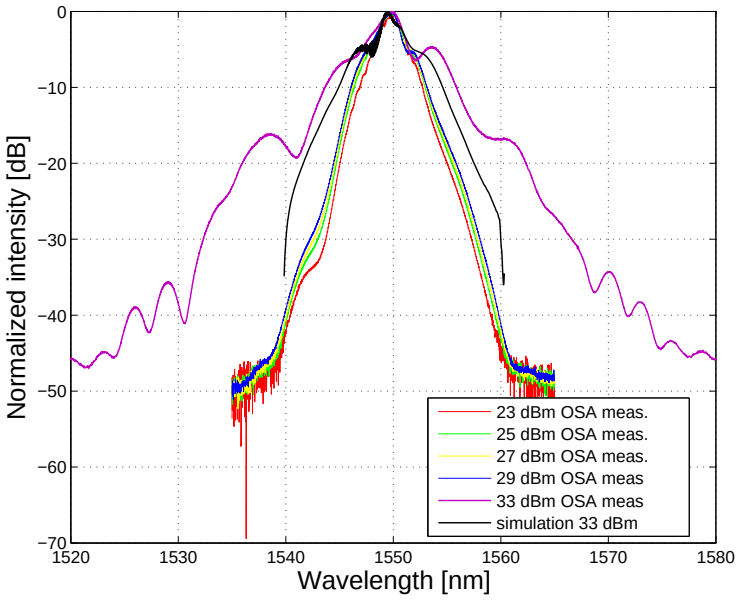

(b)

FIGURE 5.11: a.) Top: Taper output pulse envelope against parabolic fit; Bottom: Pulse envelope at the output of the taper. b.) Normalized spectra at the taper output compared to OSA spectra for different powers.

images) to calculate the taper's parameters. The results showed that the pitch value at the beginning of the taper was Λ=1.3 μm, and d/Λ was 0.9. The parameters measured at the output of the taper were Λ=1.28 μm and d/Λ=0.89. Consequently, the FEM modelling showed that for these parameters the taper was in the region of anomalous dispersion regime, and this can be considered as the most important reason for the discrepancy of results of simulation and the experiment. This important observation clearly led to the conclusion that normally dispersive fibre would be the best choice for

this experiment. These results confirmed that in this attempt I didn't manage to achieve the taper parameters that I was aiming at.

The results of this experiment showed the self phase modulation spectra broadening in the tapered MOF, but still without any confirmation of the evolution towards parabolic pulse waveform. However, this experiment was another step forward in obtaining significant experience and information about the experiment's procedure. Similar conclusion from the results taken in this experiment was obtained as in the experiment with the 40 cm taper, explained above in the previous section. In order to be able to generate parabolic pulses in the tapered MOF, using the source that was available for use, a longer optical fibre taper was needed to be fabricated from the fibre which falls to the closer proximity of the normal dispersion regime at 1550 nm.

5.4 Nonlinear pulse propagation in tapered MOF - third experimental set-up

In previous sections of this Chapter I presented the results of my experimental investigation of parabolic pulse generation, performed using two different tapered microstructured optical fibres. The most important issue in my initial experimental investigation was that the ideal MOF that was appropriate to be tapered and used in the experiment of parabolic pulse generation hadn't been fabricated yet. The fibre that was available for use has the anomalous dispersion at wavelength 1550 nm and I tried to find a way to accommodate this fibre for use in the normal dispersion regime. The idea that led me through my research was to try to set-up the experiment, to build up the experience and to establish the measurement procedure that would all make a good starting point in the later phases of the experiment, when the new fibre would be available for use.

This section is organized so that firstly I present the modelling results for the taper used for parabolic pulse generation, then the fabrication of a 1.8 m-long fibre taper and the corresponding experimental investigation of a parabolic pulse generation. The numerical results are quantified using the misfit parameter which measures the root mean square error between the propagated pulse and its parabolic fit in the time domain (according to Equation 4.27) and are compared with the experimental ones.

5.4.1 Taper design and fabrication

The microstructured optical fibre that was to be used in the experiment[3] has a hexagonal arrangement of six rings of holes and the following parameters: hole diameter d=0.88 μm, pitch Λ=1.42 μm, d/Λ=0.62, core diameter=1.88 μm. SEM images of the fabricated

[3]Fabricated by Dr Marco Petrovich.

fibre are shown in Figure 5.12. The decision to choose this particular fibre was based on the fact that the fibre has low anomalous dispersion at 1550 nm, (which is the wavelength of interest for my application), so that the fibre could be easily tapered to obtain normal dispersion regime and achieve the requirements for the parabolic pulse generation.

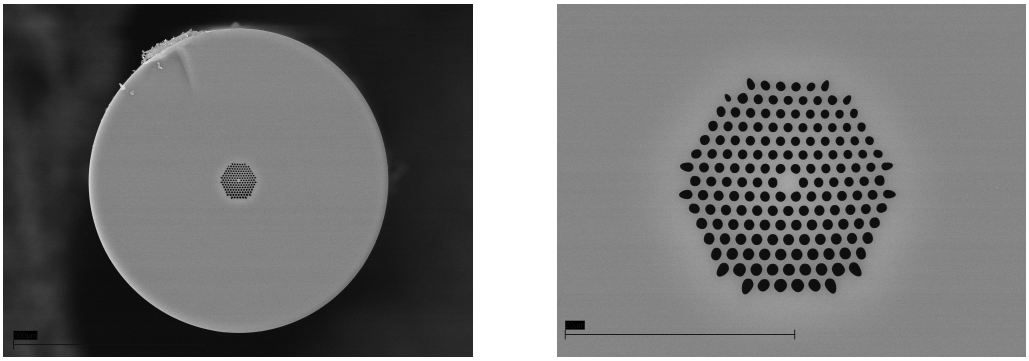

(a) (b)

FIGURE 5.12: SEM images of the MOF; a.) scale = 100 μm, b.) scale = 20 μm

In accordance to the procedure for the fibre taper design explained in Chapter 4, after measuring the fibre parameters, I calculated corresponding dispersion, effective area and confinement loss of the lowest order mode, using the finite element method. The calculated chromatic dispersion profile of the fibre as a function of the pitch at λ=1546 nm is shown in Figure 5.13.a. and the minimum and maximum values of parameter Λ (the parameters of the linear taper profile) can be determined, so that the taper operates in the normal dispersive regime. I chose the criteria which limits the absolute value of dispersion to approximately $\mid D \mid \leq$ 40 ps/nm/km, as this is the regime of particular technological interest (relatively low values of dispersion). Using the dispersion profile in Figure 5.13.a. the starting and finishing pitch are determined, for the linear taper profile, as $\Lambda(0)$=1.29 μm and Λ(end)=1.37 μm, respectively. The fibre dispersion at the corresponding pitch values is D($\Lambda(0)$)=-45.58 ps/nm/km whilst D(Λ(end)=-2.123 ps/nm/km. Note that the original fibre has hole-to-hole spacing of Λ=1.42 μm and parameter D=18.55 ps/nm/km, therefore it is necessary to taper this fibre to reduce its pitch value to 1.37 μm to reach the required normal dispersion regime. Calculations predict that dispersion slope varies between -0.47 ps/nm^2/km at $\Lambda(0)$ and -0.32 ps/nm^2/km at Λ(end). The effective area increases by $\sim$ 8% from 1.76 μm^2 at $\Lambda(0)$ to 1.92 μm^2 at Λ(end). I chose to taper the fibre linearly, as in the previous experiments. Figure 5.13.b shows that calculated confinement loss is $< 10^{-3}$ dB/m and so can be ignored as it is much smaller than the actual loss. The fibre loss of the chosen MOF was measured using a standard cut-back method. The total fibre length used for the cut-back measurement was 12.1 m and the cut-back section was 2.36 m long. The measurement result is shown in Figure 5.13.c and it can be seen that the fibre loss is around 0.4 dB/m at 1550 nm. The parameters of the linear profile taper, calculated using the finite element method, are summarised in Table 5.2.

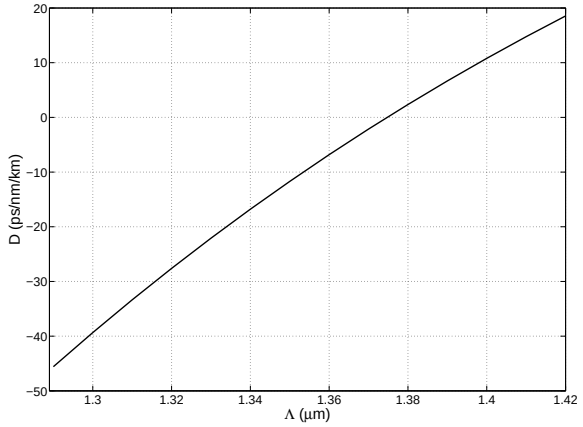

(a)

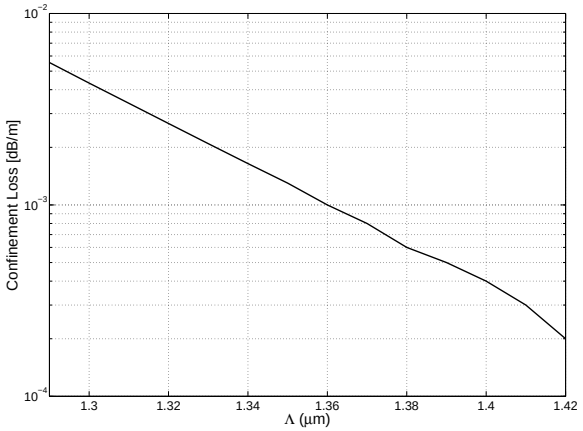

(b)

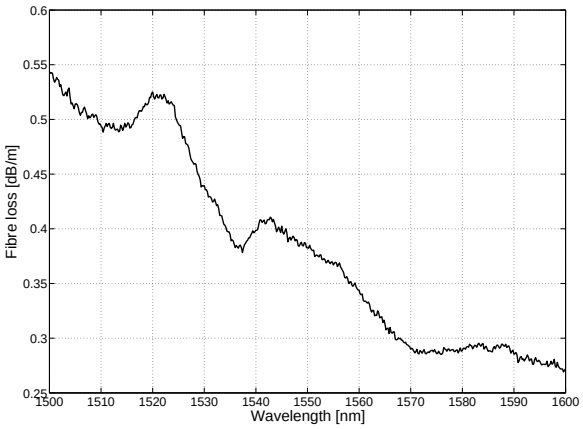

(c)

FIGURE 5.13: a.) Dispersion of the MOF b.) Confinement loss of the MOF c.) Fibre loss

Figure 5.14 shows the parameters of the taper (β_2, β_3, Λ and γ) changing with the taper length. I calculated the parameters for different pitch values and used them as

	$\Lambda[\mu m]$	$\beta_2[ps^2/m]$	$\beta_3[ps^3/m]$	$\gamma[W^{-1}km^{-1}]$
Start	1.29	0.058167	-0.008244	28.99
End	1.37	0.002723	-0.05688	27.8

TABLE 5.2: Parameters of the tapered fibre ($d/\Lambda = 0.62$)

the interpolation points to calculate the parameters versus taper length (using linear interpolation).

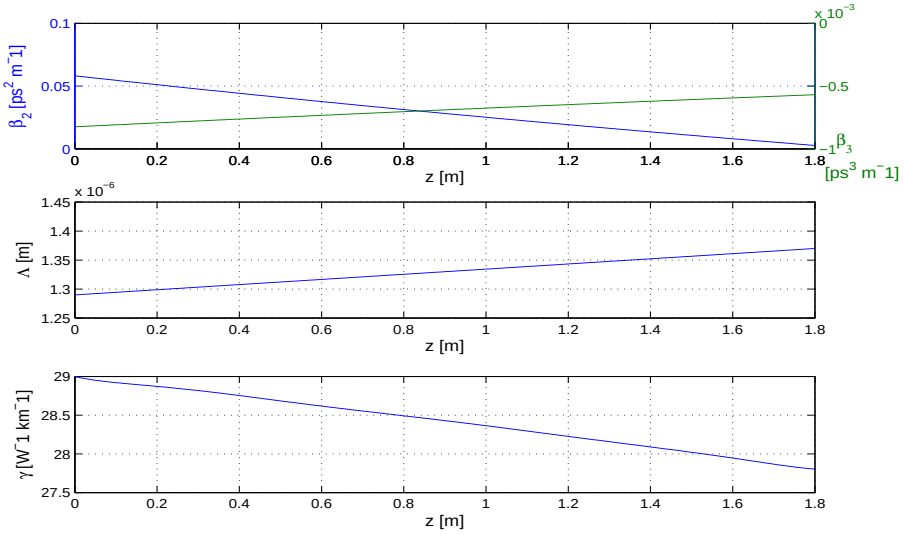

FIGURE 5.14: β_2 and β_3 vs. distance (top), pitch Λ vs. distance and γ vs. distance (bottom)

Next, I used the procedure explained in Chapter 4 to determine the optimum pulse width and the launching conditions for the parabolic pulse generation. I examined the optical propagation of unchirped Gaussian pulses of different temporal widths and peak powers, in an optical fibre with variable dispersion and nonlinearity, described by the NLSE. As it was explained in Chapter 4, I solved the NLSE Equation 4.26 using the symmetrised split-step Fourier method, numerically, for the chosen taper parameters as discussed above.

I computed the evolution of the misfit parameter, M^2, between the pulse intensity profile and the parabolic fit, to quantify the pulse evolution towards the parabolic pulse, according to the Equation 4.27. A local misfit parameter which calculates the difference between the pulse and an ideal parabolic pulse at a particular instant in time is also used. A Gaussian pulse with various peak powers and FWHMs is considered as the initial signal and let propagate from the narrow part of the taper: from Λ= 1.29 μm to Λ= 1.37 μm. The range of input pulse peak power was 10 W to 1 kW and range of input pulse FWHM was 800 fs to 2 ps, in accordance with the signal source and peak powers available in the experiment.

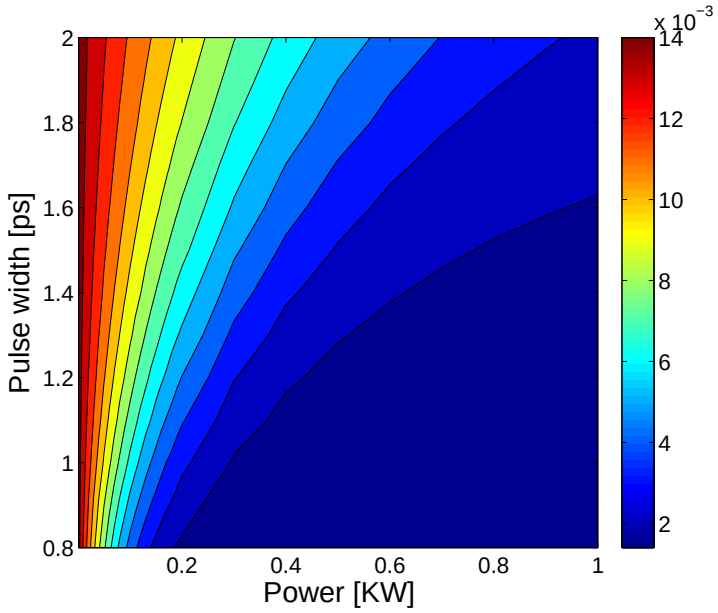

(a)

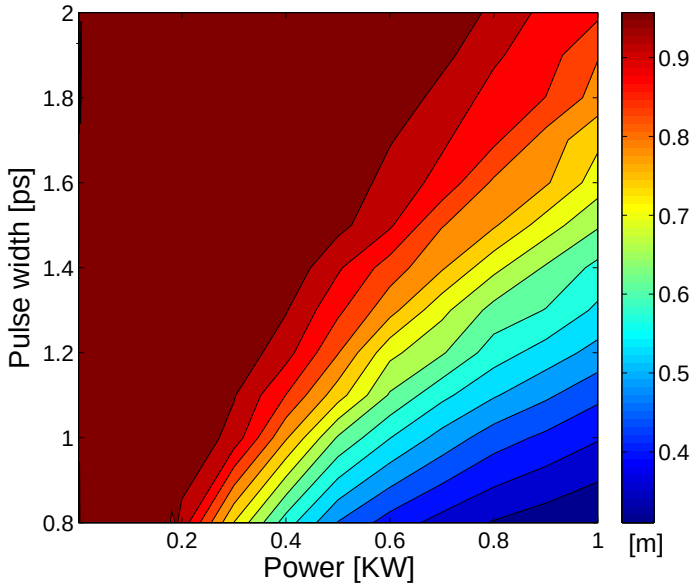

(b)

FIGURE 5.15: a.) Misfit parameter (minimum) for input Gaussian pulse; b.) Taper length [m] where best (minimum) parameter for input Gaussian pulse.

Using the algorithm and procedure shown in Chapter 4, I calculated the misfit parameter and presented as the contour plots showing the minimum values for the misfit parameter M^2 for different launching conditions (see Figure 5.15.a) and the optimum distance along the taper where the misfit has the minimum value (shown in Figure 5.15.b). From Figure 5.15.a. it can be seen that the misfit parameter decreases as the pulse peak power increases. Figure 5.15.a. shows that the minimum values of misfit parameters

could be obtained for the pulse peak powers in the range of 200 W to 1 kW, and the pulse temporal widths between 800 fs and 1.5 ps. Figure 5.15.b shows that the optimum taper's length decreases as peak power launched into the taper increases. However, the source which was available for use and the high power EDFA enable the range of calculated corresponding peak powers at the taper's input to be between 10 W and 100 W, taking into account the launching efficiency when light is coupled into the $\sim 1\mu$m core fibre (which was approximately 20%- 25%). This range of values is much lower than what should be required to get the minimum misfit parameter as shown in Figure 5.15.a). Therefore, to compensate against such low peak powers and in order to achieve better parabolic evolution, which is quantified by the minimum misfit parameter, a longer taper is required, as the contour plots in Figures 5.15.a and 5.15.b indicate (the longer taper is required, if low peak power pulses are used, in order to achieve minimum misfit parameter). Using the novel tapering facility described in Chapter 3, I fabricated an 1.8 m - long taper to achieve the modelled fibre pitches.

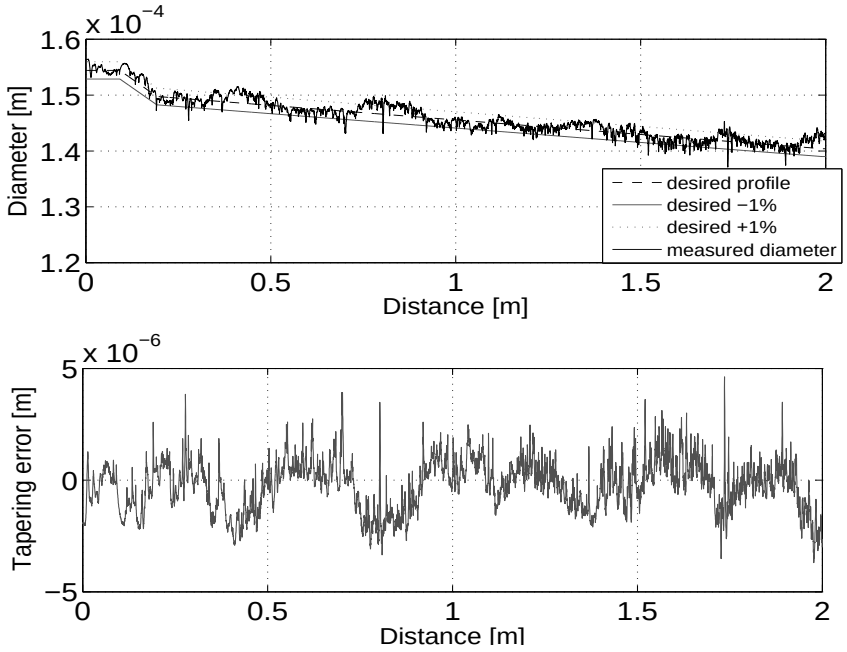

FIGURE 5.16: Top: Taper diameter vs. distance (diameter variation within ±1%); Bottom: Tapering error

However, as the original MOF has a pitch value Λ=1.42 μm which falls in the anomalous dispersion region, I pre-tapered the fibre 4% within first 10 cm of its length, in order to reduce the pitch value from 1.42 μm to 1.37 μm, as it falls in the region of normal dispersion (see Figure 5.13.a). The fibre was then tapered further 5% along 1.8 m of length to get the pitch value of 1.29 μm, as previously calculated. The diameter profile of the taper fabricated in this way is shown in Figure 5.16. (top) where it can be observed that the diameter variation is within the ±1% of the value of the desired fibre diameter, and the tapering error also has a very low value, shown in Figure 5.16. (bottom), too.

This taper represents a record taper length fabricated with the accuracy of ±1%, shown in this thesis.

5.4.2 Experimental Set-up

The experimental set-up is shown in Figure 5.5 (the same set-up was used in the three experiments, with different tapers). The signal at the 90% port of the coupler originates from an Erbium Glass Oscillator (ERGO) at 1546 nm, which generates ∼ 1.4 ps Gaussian pulses with the repetition rate 10 GHz. The pulses are amplified up to 33 dBm using the high power Erbium Doped Fibre Amplifier (HP-EDFA) to form the pump signal. The 5 nm filter is placed to filter out the HP-EDFA ASE noise. The profiles of the pulses in the time and frequency domain was assessed using the l-FROG technique[4].

However, due to the high peak powers involved the signal was undergoing some nonlinear effects in the HP-EDFA, causing the filter to filter out part of the signal itself and then inducing relatively high losses (∼2.3 dB). For this reason measurements with and without the filter were carried out. Assessment of the pulses quality has been done using the l-FROG technique, as in previous experiments. The PC was used to align the input signal to the axis of higher nonlinear coefficient of the tapered MOF.

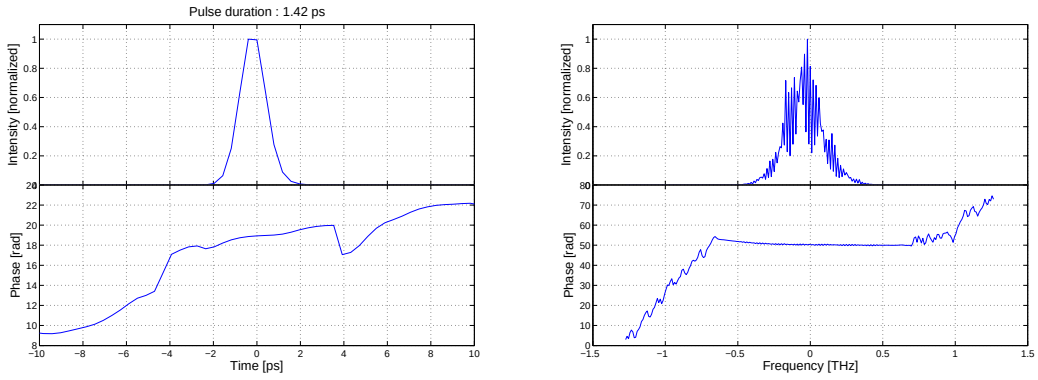

(a) (b)

FIGURE 5.17: a.) Normalized envelope and phase at the output of ERGO. b.) Normalized spectra and spectral phase.

The retrieved temporal intensity and phase and corresponding spectra and spectral phase of the ERGO signal is shown in Figure 5.17 and the reconstructed spectrogram in Figure 5.18. The temporal FWHM of the retrieved pulse is 1.42 ps. The accuracy of the retrieval is confirmed by the good agreement of the retrieved spectrum with the spectrum measured using an OSA (see Figure 5.19. top).

[4]Thanks to Dr Francesca Parmigiani for helping me with the experiment and pulse l-FROG measurement retrieval.

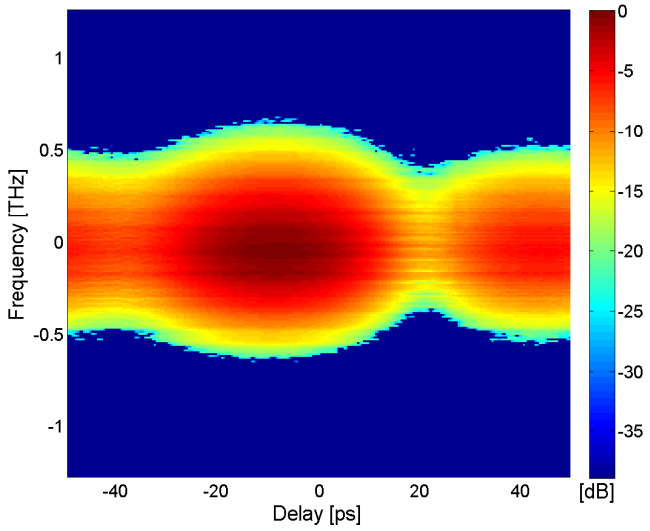

FIGURE 5.18: Reconstructed spectrogram of the retrieved pulses at the output of ERGO

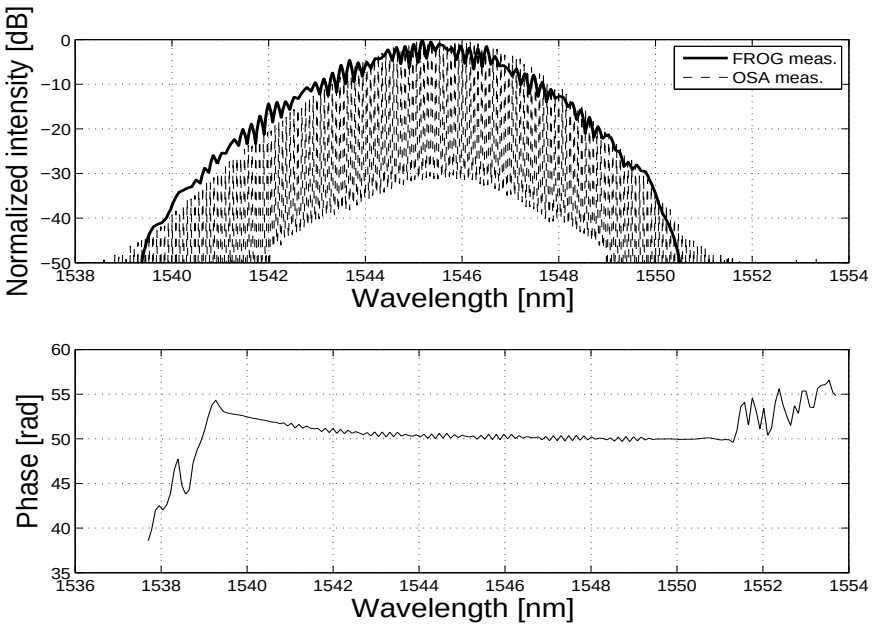

FIGURE 5.19: Normalized spectra and spectral phase vs. λ, comparison between the spectra retrieved from FROG and spectra measured using OSA

The spectra at the input and at the output of the taper were measured using an Optical Spectrum Analyzer (OSA). I considered two configurations of the set-up, as explained above, first when the optical filter is connected after the HP-EDFA, and second when the filter is removed. Figure 5.20 shows the normalized spectra at the taper input and

output for different average powers (27 dBm, 29 dBm, 31 dBm, 32 dBm and 33 dBm), without the use of filter. As can be observed and anticipated before, spectral traces at the output of the HP-EDFA broaden as the power increase implying that the signal undergoes nonlinear propagation along the amplifier. However, it is important to notice that the spectrum broadens further as it propagates along the tapered MOF and this is more noticeable when the optical filter is removed (Figure 5.21). Figure 5.21 shows the normalized spectra at the taper input and output for different average powers (27 dBm, 29 dBm, 31 dBm, 32 dBm and 33 dBm), as well as spectra measurement taken by OSA of the ERGO source. Figure 5.22 shows the normalized spectra at the taper input and output for all powers, at the taper input and output.

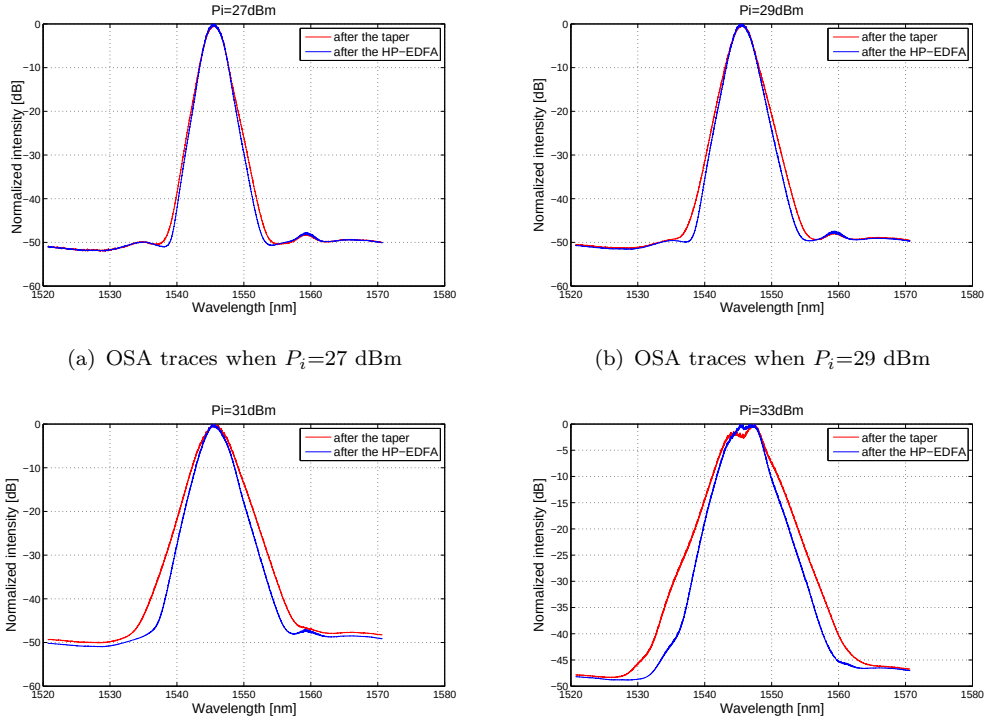

(a) OSA traces when P_i=27 dBm

(b) OSA traces when P_i=29 dBm

(c) OSA traces when P_i=31 dBm

(d) OSA traces when P_i=33 dBm

FIGURE 5.20: Normalized spectra at the taper input and output, with the use of filter, P_i is power of the HP-EDFA

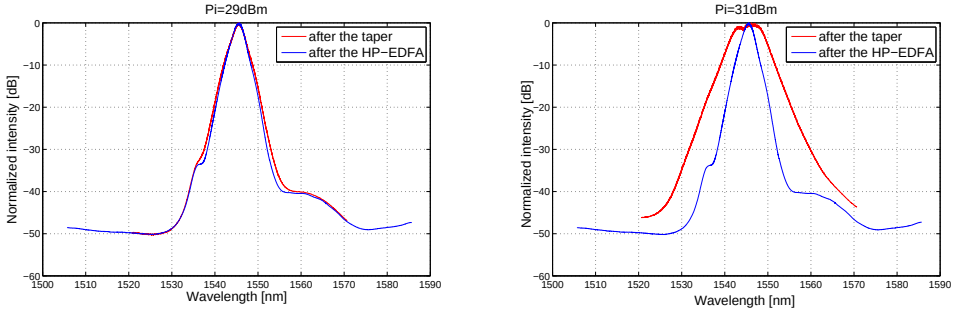

(a) OSA traces when P_i=29 dBm

(b) OSA traces when P_i=31 dBm

(c) OSA traces when P_i=32 dBm

(d) OSA traces when P_i=33 dBm

FIGURE 5.21: Normalized spectra at the taper input and output, without the use of filter, P_i is power of the HP-EDFA

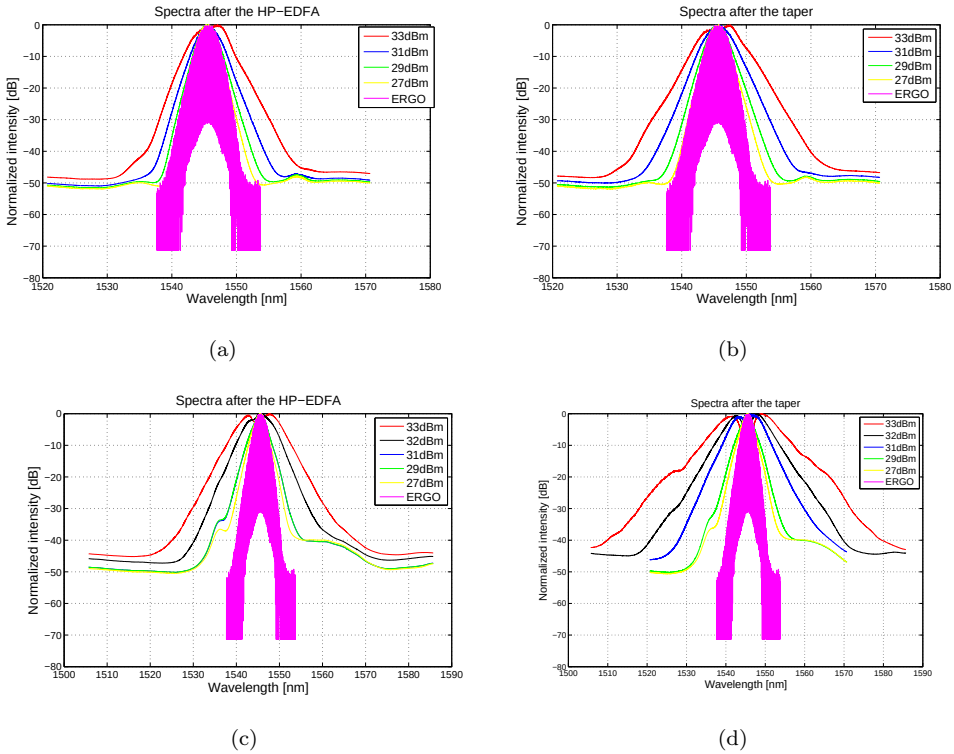

(a)

(b)

(c)

(d)

FIGURE 5.22: Normalized spectra at the taper input and output a.) with the use of filter; b.) with the use of filter; c.) no filter used; d.) no filter used.

5.4.3 Results and discussion

The main objective during the experiment was to perform a systematic measurement of both the spectra using an OSA and temporal traces using a l-FROG in three important points, for different average powers: at the output of the ERGO source, at the input of the taper (i.e. at the output of HP-EDFA) and at the taper output. We then retrieved their temporal and spectral intensity and corresponding phase. As the consequence of the nonlinearity of the HP-EDFA, the pulse temporal FWHM decreased as the HP-EDFA power increased: FWHM of 0.78 ps was measured for power of 31 dBm, FWHM of 0.68 ps for power of 32 dBm and FWHM of 0.59 ps for power of 33 dBm. Figure 5.23 and Figure 5.24 show the retrieved temporal and spectral traces when average powers are 31 dBm, 32 dBm and 33 dBm, for the cases with and without the use of filter in the set-up. These results are used after the interpolation as the input pulses in the simulation, to provide better fitting with the experimental results.

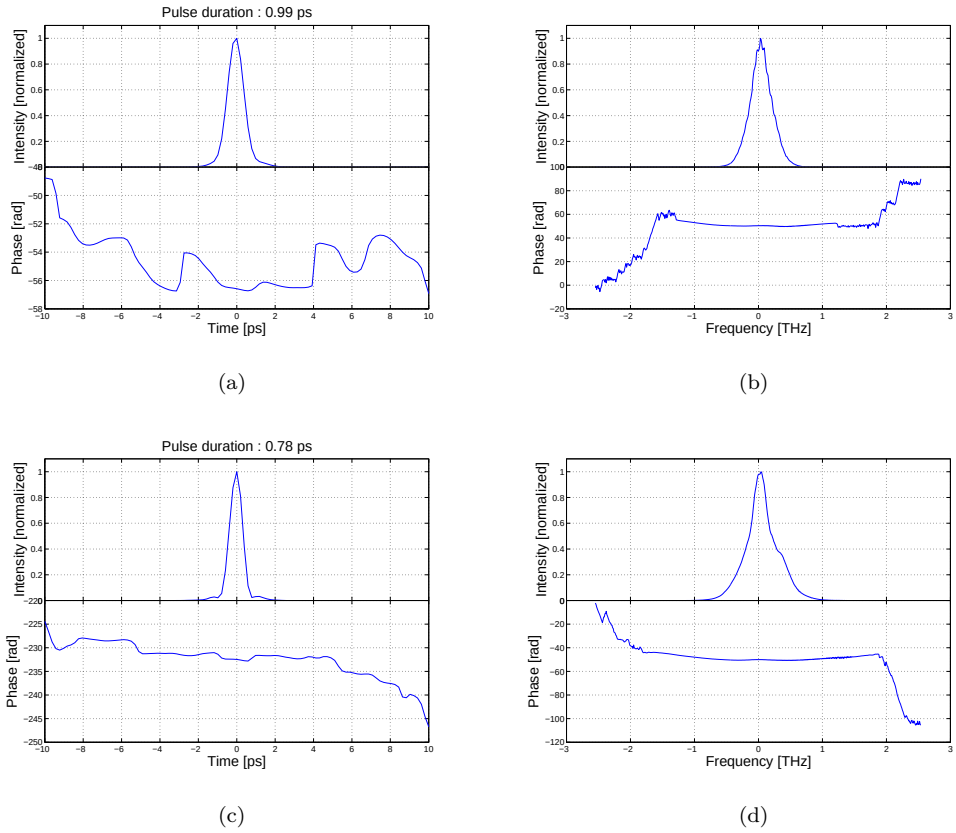

FIGURE 5.23: Normalized time and frequency intensity and phase at the taper input when power is 31 dBm, with the use of filter (a and b) and without the use of filter (c and d)

Next step in the results post-processing was to implement the interpolated pulse as an input pulse in the simulation and to observe pulse propagation for the similar conditions as in the experiment. Due to the taper's fragility and the necessity to cleave the fibre

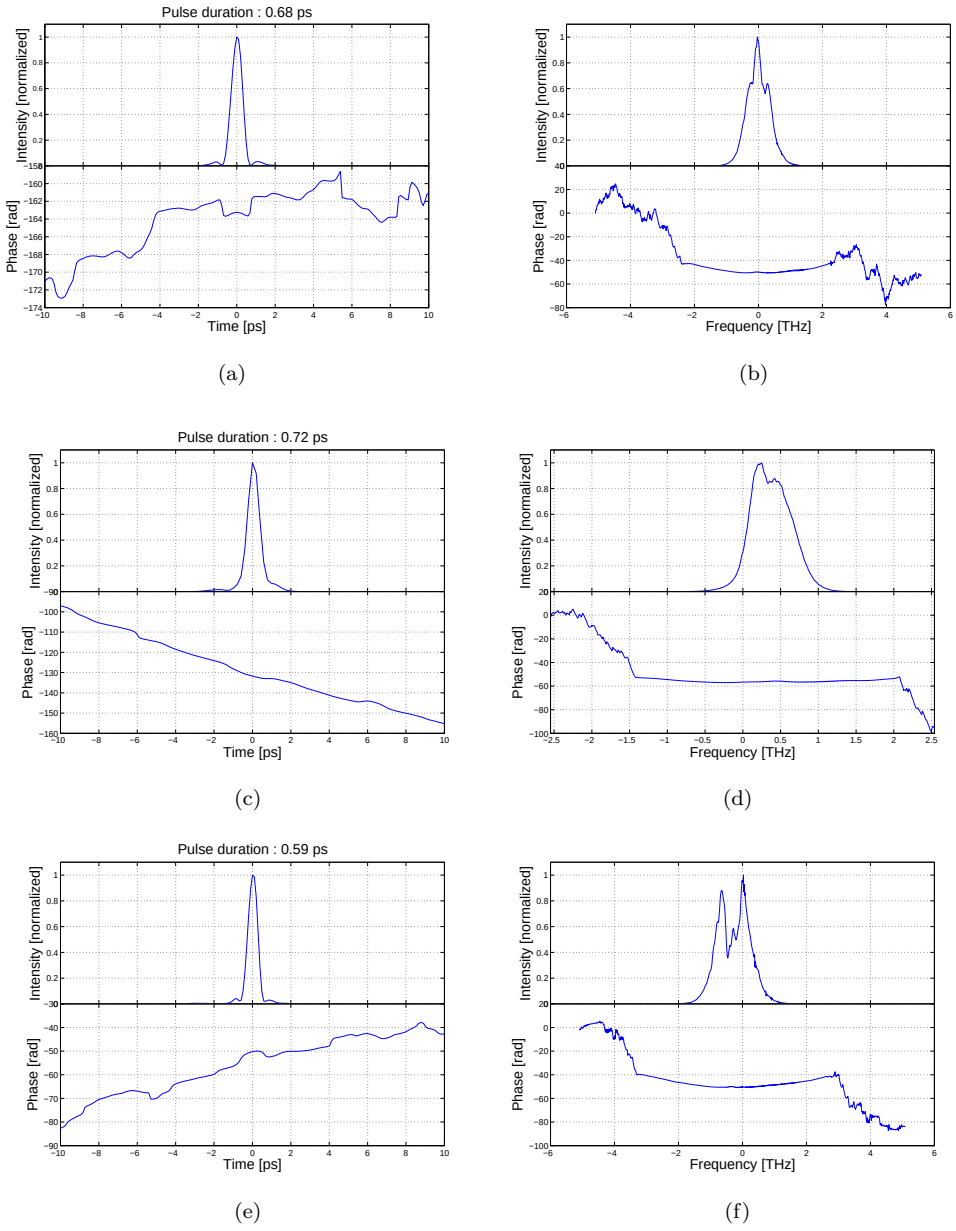

FIGURE 5.24: Normalized time and frequency intensity and phase at the taper input when power is 32 dBm (a and b), filter excluded, and 33 dBm with the use of filter (c and d) and without the use of filter (e and f)

in order to improve the coupling efficiency, the overall taper length was reduced to approximately 1.4 m. The launching efficiency is calculated on the basis of measuring the average power at the taper's input and the output whilst the fibre loss is approximately 0.4 dB/m at the wavelength of 1550 nm. To overcome the problem of the instability of coupling light into a small core fibre and the reduction of the launching efficiency, we used the optical coupler, so that the launching efficiency was constantly monitored and, if necessary, readjusted. The launching efficiency was calculated to be 20%. More significant spectra broadening was observed for higher powers, $\geq$ 31 dBm, therefore we decided to consider pulse propagation in the taper for powers of 31 dBm, 32 dBm and

33 dBm. Note that the 32 dBm was considered only when filter was removed from the set-up. The Gaussian pulse FWHM temporal width obtained from the retrieved signals of the temporal envelope in Figure 5.23 and Figure 5.24. Table 5.3 summarises values of the calculated pump signal peak powers for different values of the average power in case of the filter included in the set-up and when the filter was excluded, calculated for the f_{rep}=10 GHz and launching efficiency of 20%.

	filt. incl. P_{av} [W]	filt. excl. P_{av} [W]	filt. incl. P_0 [W]	filt. excl. P_0 [W]	filt. incl. T_{FWHM} [ps]	filt. excl., T_{FWHM} [ps]
31 dBm	0.74	1.259	14	30	0.99	0.78
32 dBm	0.933	1.58	21	44	/	0.67
33 dBm	1.175	2	28	64	0.72	0.59

TABLE 5.3: Average power (P_{av}), calculated peak power (P_0) at the input of the taper and the pulse T_{FWHM} at the input of the taper.

In order to validate the experimental results I compared the pulse intensity profile at the output of the taper with the parabolic fit and quantified the evolution towards the parabolic shape using the misfit parameter defined by Equation 4.27. For the lowest average power of 31 dBm, and including the filter, the misfit parameter was 0.015 (Figure 5.25.a), implying that the pulse intensity profile is quite different from the desired parabolic shape. The misfit parameter was then calculated for different powers when filter was excluded from the set-up. M^2 is 0.012 for 33 dBm with the use of filter (Figure 5.26.a), and M^2 is 0.0064 for 31 dBm (Figure 5.27.a) and M^2 is 0.0053 for 32 dBm (Figure 5.28.a), without the use of filter. I also compared the spectra of the output pulse obtained from the OSA measurement with the spectra obtained as the result of simulation as well as the pulse intensity profile obtained from the simulations (taking into account 5 m of SMF fibre between the taper output and the l-FROG set-up) and the pulse envelope retrieved from the FROG measurement, for all cases of average powers, in accordance to Table 5.3.

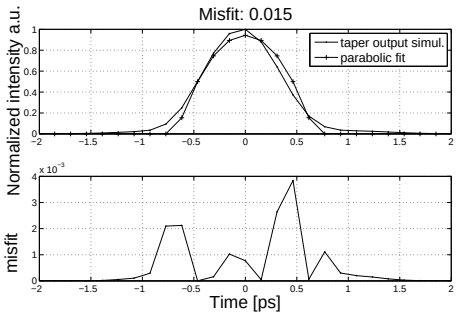

(a) Top: taper output pulse envelope against parabolic fit; Bottom: local misfit parameter

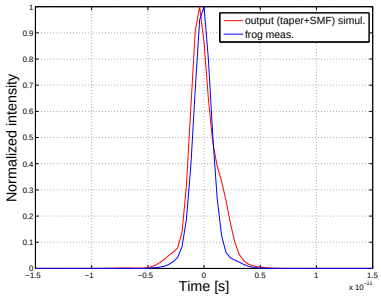

(b) Pulse envelope comparison

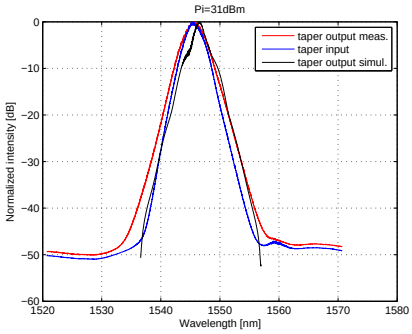

(c) Normalized spectra comparison

FIGURE 5.25: Power 31 dBm, with the use of filter.

Figure 5.25.b shows the comparison between the intensity profile obtained as the result of simulation but with approximately 5 m of SMF fibre between the taper output and l-FROG setup, taking into account the pulse envelope retrieved from the FROG measurement. In Figure 5.25.c the spectra obtained as a result of simulation is compared to the spectra taken using an OSA at the input and at the output of the taper. When the average power of the HP-EDFA was 33 dBm, with the use of filter, the similar set of results is shown in Figure 5.26. Figures 5.25, 5.26, 5.27, 5.28 and 5.29 show the time intensities and spectra of the output pulse obtained from the OSA measurement compared with the spectra obtained as the result of simulation, as well as the pulse intensity profile obtained as the result of simulation (with 5 m of the SMF fibre) compared with the pulse envelope retrieved from the FROG measurement, for different average powers.

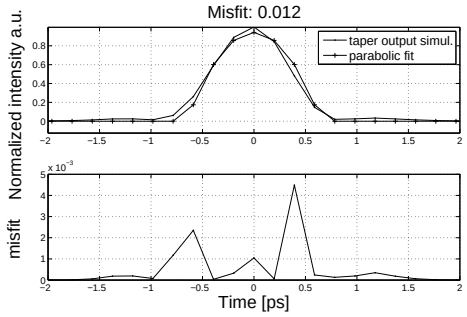

(a) Top: taper output pulse envelope against parabolic fit; Bottom: local misfit parameter

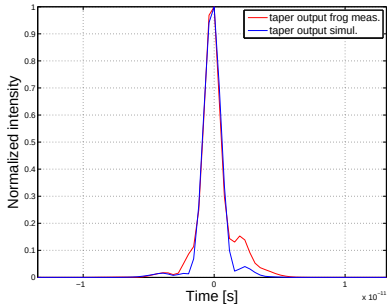

(b) Pulse envelope comparison

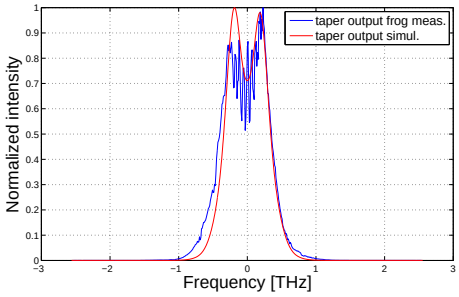

(c) Spectra comparison, with 5 m of SMF fibre

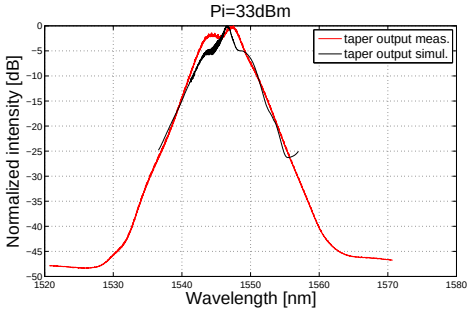

(d) Normalized spectra comparison

FIGURE 5.26: Power 33 dBm, with the use of filter.

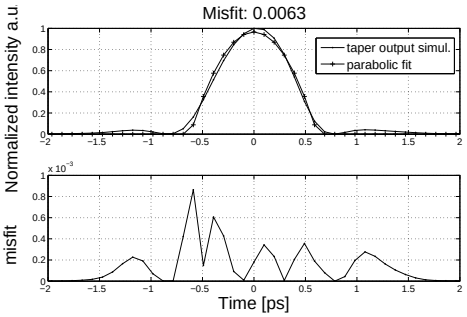

(a) Top: taper output pulse envelope against parabolic fit; Bottom: local misfit parameter

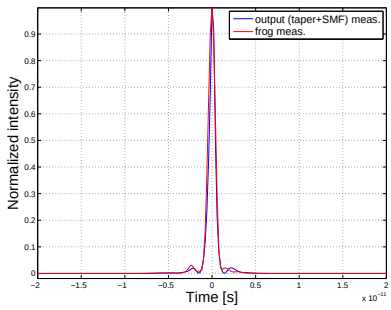

(b) Pulse envelope comparison

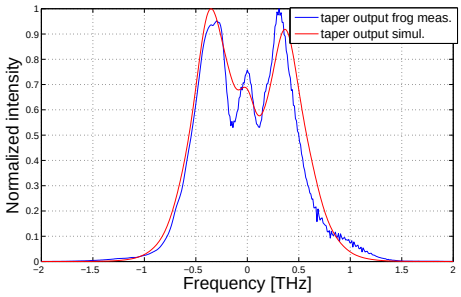

(c) Spectra comparison, with 5 m of SMF fibre

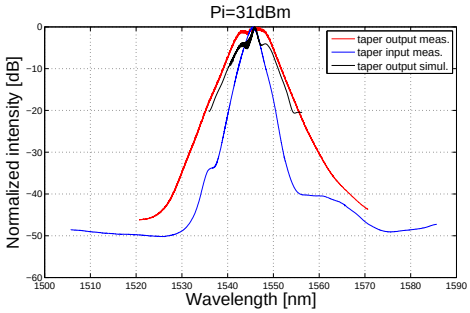

(d) Normalized spectra comparison

FIGURE 5.27: Power 31 dBm, without the use of filter.

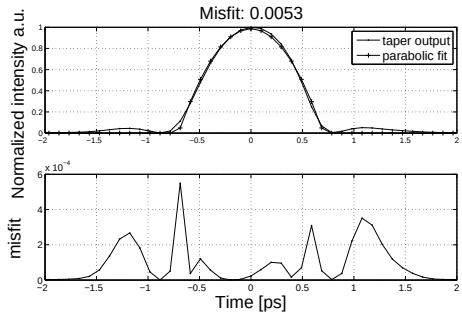

(a) Top: taper output pulse envelope against parabolic fit; Bottom: local misfit parameter

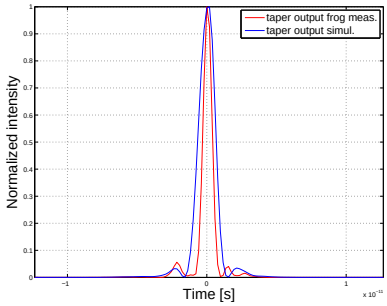

(b) Pulse envelope comparison

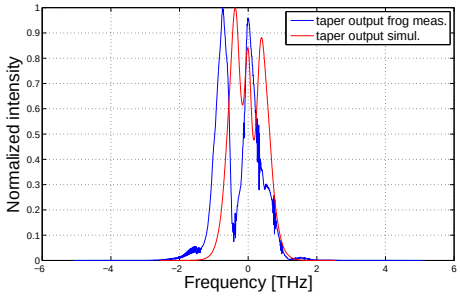

(c) Spectra comparison, with 5 m of SMF fibre

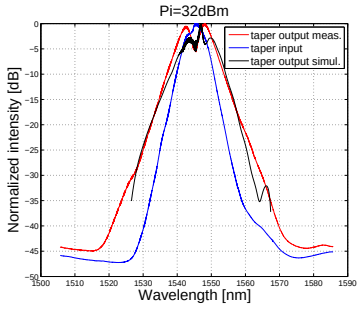

(d) Normalized spectra comparison

FIGURE 5.28: Power 32 dBm, without the use of filter.

I have also considered the case of the average power 33 dBm without the optical filter (that was the maximum power available in the measurement). The misfit parameter calculated in this case was 0.0032, which confirms a continuous decrease in the misfit parameter as the pulse initial peak power increases. However, in this case, the average power corresponds to only 64 W of the peak power of the signal at the taper input. These results of the post-processing are shown in Figure 5.29 and Figure 5.30.

Figure 5.29.a shows the pulse time intensity in comparison with the ideal parabolic fit. The measured FWHM is 1.22 ps, so that during the propagation along the taper the input pulse 0.59 ps FWHM was reshaped into the pulse of 1.22 ps duration. Figure 5.29.b shows the comparison between the simulation and the result of the FROG deconvolution, where FWHM of the pulse obtained from the simulation is 1.49 ps and FWHM of the pulse obtained from the FROG measurement is 1.25 ps. Figure 5.29.c shows the comparison between the spectra obtained as a result of the pulse retrieval at the output of the taper and from the simulation when 5 m of the SMF fibre was taken into account. Figure 5.29.d shows the comparison between the spectra obtained as a result of simulation and from OSA measurement. Figure 5.30 shows pulse envelope, phase and chirp (obtained as the result of simulation) and it can be observed that the phase is almost parabolic, which leads to the nearly linear chirp across the pulse time duration.

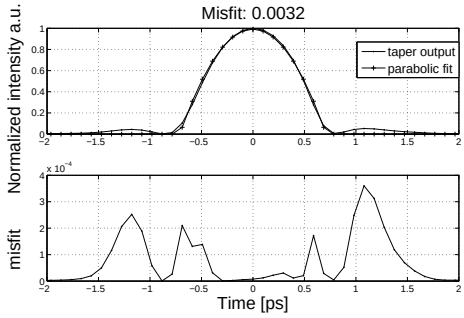

(a) Top: taper output pulse envelope against parabolic fit; Bottom: local misfit parameter

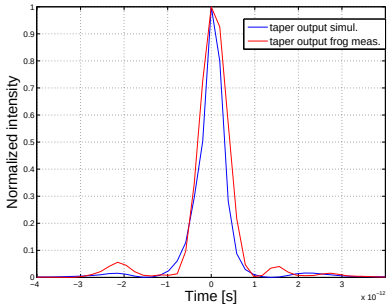

(b) Pulse envelope comparison

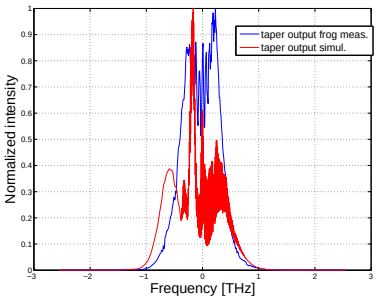

(c) Spectra comparison, with 5 m of SMF fibre

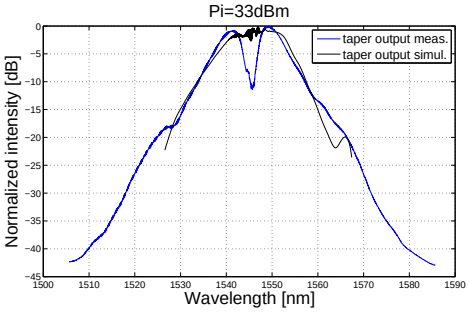

(d) Normalized spectra comparison

FIGURE 5.29: Power 33 dBm, without the use of filter.

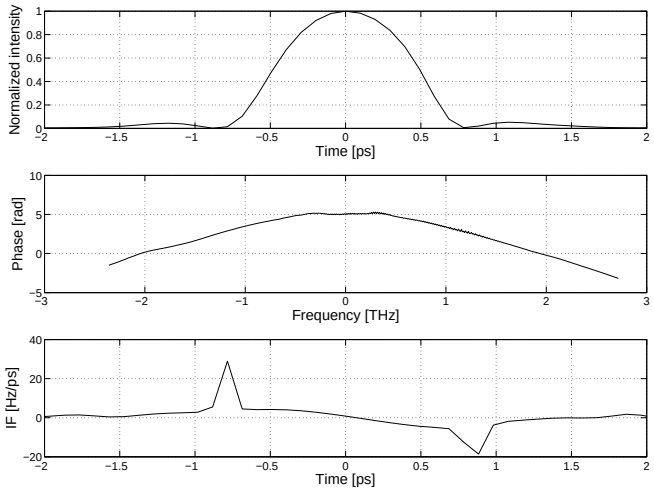

FIGURE 5.30: Pulse envelope, spectra, phase and chirp coefficient; power 33 dBm, no filter.

Results show that a good qualitative agreement between simulations and measurement is achieved for both temporal intensity profiles and spectra for all powers, leading to the conclusion that the simulation adequately models the experimental conditions. Some

discrepancy between numerical simulation and experiment can be explained by the lack of full knowledge of some important parameters, such as exact dispersion along the taper (as the consequence of fibre cleaving) and the exact pulse peak power at the input of the taper due to some instability in the system. Despite the fact that the higher peak power at the input of the taper is needed and the constraints in using the HP-EDFA, the possibility of generating parabolic pulses in the MOF taper has been demonstrated. In the ideal conditions of having higher power into the MOF taper, the parabolic pulse shaping would be even more efficient.

Figure 5.31 shows results of the numerical simulations for the cases of having longer taper length or improved launching efficiency. In this case it has been assumed that the input and output geometries of the taper have been maintained (i.e. $\Lambda(0)$=1.29 μm and Λ(end)=1.37 μm). The input pulse in the simulation was interpolated retrieved pulse at the input of the taper for the HP-EDFA power of 33 dBm. Figure 5.31.a shows that in case of fabricating a taper of 3 m length, while keeping pulse peak power at the input of the taper 64 W, the misfit factor of 0.0028 could be achieved. In another case, when taper length is 1.4 m, while launching efficiency being improved by ∼20%, the misfit parameter becomes 0.0024 (Figure 5.31.b). Finally, if 3 m - long taper is being fabricated and the launching efficiency is improved by ∼20%, the misfit parameter becomes even lower 0.0021. These results confirm the assumption of enhancing the efficiency of the process by further improving the experimental set-up.

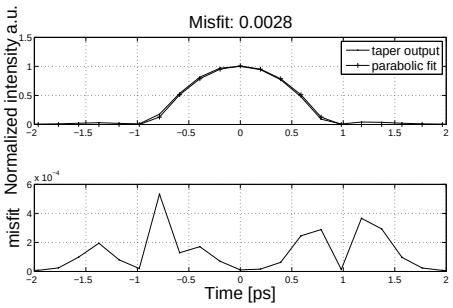

(a) Taper length 3 m, peak power = 64 W

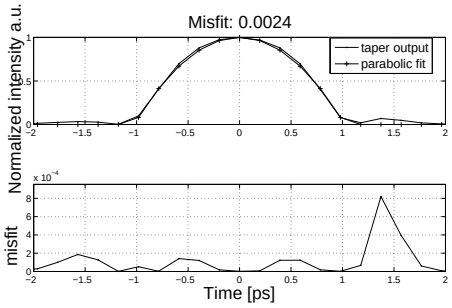

(b) Taper length 1.4 m, peak power = 77 W

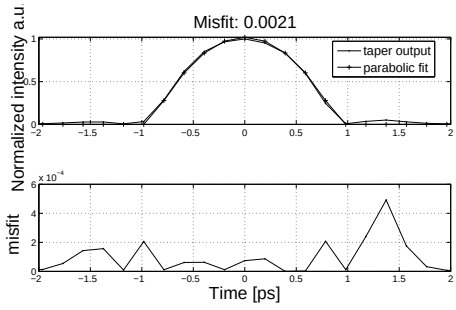

(c) Taper length 3 m, peak power = 77 W

FIGURE 5.31: Top: taper output pulse envelope against parabolic fit; Bottom: local misfit parameter.

5.5 Conclusion

In this chapter I have presented numerical and experimental results of the three sets of experiments that I have done towards the parabolic pulse generation in a tapered microstructured optical fibre with the normal dispersion. However, due to the lack of the appropriate fibre which would be specifically designed for this analysis and experiment, I tried to accommodate the existing MOF to suit my purpose. The fibre that was available for the first two experiments fell far from dispersion values that were desirable for the experiment (anomalous dispersion of 150 ps/nm/km at 1550 nm). Therefore, I made attempts to taper this fibre down to reach the normal dispersion regime, needed for the parabolic pulse shaping in the tapered MOF. This happened to be a very challenging task, and I didn't succeed entirely. Nevertheless, I managed to fabricate two different tapers, first 40 cm - length and second of 60 cm - length and took two different attempts to perform parabolic pulse generation. The experiments showed different problems that appeared along the way, such as difficulty to obtain significantly better launching efficiency (better than 10% - 15%), nonlinearity of HP-EDFA at high powers and insufficiently high pulse peak powers. Also, the experiments showed the necessity to use longer taper, too. The important problem that has been confirmed from the SEM images taken at the taper's input and output in the second experiment, was that pre-tapering and cleaving had led to taper parameters that fell in the anomalous dispersion regime.[5] Although the results of the two experimental attempts were not as desired, these experiments were crucial for performing important changes in order to improve the experimental set-up.

Next I presented numerical and experimental results of the third set of experiments of the parabolic pulse shaping in a microstructured optical fibre taper with the normal dispersion. The microstructured optical fibre was initially in the anomalous dispersion regime (lower dispersion than in previous case, D=18.55 ps/nm/km at λ=1.55 μm) and it was accommodated to have the parameters so that the fibre had low values of the normal dispersion. The fibre parameters were measured and the taper's parameters determined in order to obtain a desirable linear taper profile and a 1.8 m long taper has been fabricated. The experimental study of parabolic pulse generation has been compared with the numerical simulations. The pulse propagating through the taper was characterized using linear FROG method. A qualitative agreement between the results of experiment and simulation was demonstrated. The consistent convergence towards the parabolic pulse at the taper's output is observed for the increase in the input pulse powers. The quality of the parabolic pulses was quantified using a misfit parameter, which reached value of 0.0032, when maximum power has been applied. It

[5]This was the important reason for the dismissal of previous two experiments in favour of the third one (where MOF initially had low value of anomalous dispersion and it was easier to be pre-tapered). This observation leads to the conclusion that there is a need to develop a measuring technique for the structural parameters determination during the tapering process and this will be the subject of future work.

has been shown that the initial pulse FWHM of 0.59 ps has been shaped into a pulse of 1.22 ps FWHM (which has an rms error against the parabolic fit of 0.0032). However, these results and the conclusions assume a perfect fit between the experiments and simulations, although in practice it hasn't been the case. Generally, there were many constraints in conducting these experiments, such as that structural characterisation was only possible using destructive SEM method, so that the taper's parameters were taken into account as the approximative ones. Nevertheless, these results suggest that parabolic pulse shaping can be obtained if the optimum conditions can be achieved. Here, optimum conditions include a perfect fit between the experiment and simulation, tapering with the minimum tapering error and the launching conditions that would enable high input pulse peak powers. In all experiments, the important limitation was the pulse peak power and I anticipate that by increasing peak power at the taper's input or increasing taper's length, the quality parabolic pulse can be produced at the output of the tapered microstructured optical fibre.

Chapter 6

Investigation of Supercontinuum Generation in Tapered Microstructured Optical Fibres

6.1 Introduction

Supercontinuum generation (SC) has become a very active area of research since it was first reported in 1970s by Alfano and Shapiro [116]. SC occurs when high-power ultrashort optical pulses propagate through a nonlinear optical medium resulting in extremely broad spectra often octave spanning. The first observation of SC generation by Alfano and Shapiro was in bulk material, followed by different studies on "super-broadening" [117], [118]. The first results on the SC generation in conventional fibres [119] reported a highly complex process involving coupling between spatial and temporal effects. Work by Gaeta [120] provided a comprehensive explanation based on full three-dimensional simulations of light propagation [52]. More recently the introduction of small core (highly nonlinear) optical fibres and in particular microstructured optical fibres have enabled major advances in obtaining SC spectral broadening over the past decade, leading to the development of new inexpensive and efficient SC sources [121] - [126]. SC generation in MOFs has revolutionized many fields, such as optical frequency metrology and has opened the whole new area of significant applications in telecommunications, sensing, spectroscopy, medical imaging etc. [41], [52]. In telecommunications specifically, it has been proposed the spectral slicing of broadband SC spectra to create multiwavelength optical sources for dense wavelength division multiplexing applications (DWDM) [52]. There have been numerous theoretical and experimental investigations of the supercontinuum generation in different pumping regimes [52], [78] - [80], [123] - [129], using photonics crystal fibres [79], [80], [127] - [136], using single mode [137] or using tapered fibres [78] - [80].

There is also a number of results reported for the longer pulsed regime, quasi-continuous and continuous wave (CW) pumping regime [52]. SC is a complex phenomenon which arises due to the interaction between dispersion and nonlinear effects in the optical fibres. The nonlinear effects that are behind the mechanism of SC generation include self-phase modulation (SPM), four wave mixing (FWM), cross phase modulation (XPM), stimulated Raman scattering (SRS), modulation instability, self-steepening and optical shock formation etc. [52]. Generally, SC characteristics can vary significantly with the particular combination of pulse and fibre parameters used and the SC generation process is driven dominantly by the soliton dynamics in the femtosecond pumping regime, whilst the modulation instability is the dominant effect in longer pumping regimes [52]. Propagation dynamics and broadening mechanisms are characterised by the dispersion length and nonlinear length, which determine the soliton number, according to the formula $N = \sqrt{L_D/L_{NL}}$. Different propagation regimes can be distinguished depending on the combination of GVD regime and pulse parameters [123]:

- ***Anomalous GVD regime with short pump pulses:*** Spectral broadening arises from soliton - related dynamics. The short pulse durations implies that $N \gg 1$ and therefore the pump pulses are higher order solitons. They undergo an initial period of spectral broadening and temporal compression, followed by soliton fission. The characteristic length scale over which the soliton fission occurs is given by $L_{fiss} = L_D/N$. Soliton fission manifests itself as the higher order soliton pulse breaks - up into N distinct fundamental soliton components. The process occurs due to higher order dispersion and stimulated Raman scattering. The initial propagation of these fundamental solitons is associated with the generation of dispersive wave spectral components through resonant transfer of energy across the zero dispersion wavelength [123]. The resonance, due to higher-order dispersion, is narrowband which explains an abrupt short - wavelength edge typically seen on SC spectra in this regime. As the solitons continue propagating, the result is a continuous shift to longer wavelengths through the Raman self frequency shift. Finally, the generated Raman soliton and dispersion waves can couple through XPM to generate additional frequency components that increase the overall bandwidth.

- ***Anomalous GVD regime with pulses of longer durations:*** In this case, when high peak powers are applied the solitons become very large ($N \gg 10$) and the soliton fission process described above becomes less important during initial propagation. This is because fission length increases with the pump pulse duration. Instead modulation instability, MI, (which is equivalent to the generation of FWM) occurs on the same scale regardless of the pulse duration and begins to dominate the phase of initial propagation [123]. The initial MI leads to the temporal breakup of input pulse into subpulses, where each subpulse undergoes further fission, self-frequency shift and dispersive wave generation. Pumping too far into anomalous regime effectively reduces the generated SC, as the initial MI dynamics do not

generate sufficient bandwidth to enable efficient seeding of dispersive wave transfer into the normal dispersive regime [52].

- ***Pumping in the CW regime:*** The conditions explained above are extended in the CW regime. However, the MI develops simultaneously from noise that has dramatic consequence for the pulse time evolution ("rogue" waves) and SC coherence [138].

- ***Normal GVD regime with short pump pulses:*** In this pumping regime, SC broadening arises from the interaction of SPM and GVD of the fibre, with shorter pulses inducing greater nonlinear broadening. The extent of nonlinear broadening is limited, as the combination of these effects leads to the temporal broadening and decrease in peak power in the beginning of propagation. For pump wavelength approaching the zero dispersion wavelength and across into the anomalous dispersion regime, the soliton dynamics plays an important role as well [123]. FWM and SRS also take part and contribute to the transfer of energy into the anomalous dispersion regime. Generally, closer to the zero dispersion wavelength, the FWM becomes more important, since the parametric gain is higher than the Raman gain.

More recently much of the theoretical emphasis concerning SC has shifted from understanding the fundamentals to optimising the generation of SC for particular applications. Since each application has particular requirements the results of one study cannot in general be applied to different applications. Many such studies have concentrated on optimising the visible supercontinuum in MOFs [139]. For example Wadsworth et al. [135] designed and fabricated a MOF and showed that by pumping the MOF in the near-infrared anomalous GVD, SC generation from the ultraviolet to the infrared can be seen. This requires considerable dispersion engineering of the fibres in order to modify the zero dispersion point and as a result the dispersion profiles used cannot be extended to other wavelengths ranges since such fibres have to be specifically designed to satisfy different requirements.

In this Chapter I will present results of modelling and simulation of SC generation at 1.55 μm in tapered MOFs with the emphasis on the procedure for finding the dispersion profile and launching conditions that achieve the best width and flatness of the SC spectra. Such sources would be of considerable interest for telecommunications applications such as spectral splicing for high density DWDM sources (here spectral flatness is of considerable importance). In addition the MOF can be spliced directly to a high power short pulse fibre laser making a convenient and compact SC source suitable for telecoms applications, remote sensing etc. From numerical and experimental results obtained at wavelengths around 780 nm [127] it is known that pumping in the anomalous dispersion regime and controlling the position of the zero dispersion wavelength relative to the pump wavelength, are vital to controlling the SC process. Thus the initial design target

is to ensure that the fibres have near zero GVD at 1.55 μm. I chose to taper these fibres, since, as it was pointed out in [52], dispersion control is enhanced in tapered fibres, thus potentially improving the quality of the generated SC and this Chapter presents the results of my investigation.

Specifically, my intention here was to investigate SC generation in metre-long tapers which could be easily fabricated (using the tapering facility described in Chapter 3) from a "standard" MOF (which hasn't been under strict design requirements that would probably initiate different constraints and difficulties in its fabrication). Therefore, the starting point in the investigation that I performed was consideration of the likelihood of having the typical MOF available for use and hence the optimisation of the tapered MOF, rather than the design optimisation of the MOF with respect to the SC generation.

6.2 Taper design for SC generation

As it was explained in the introduction, the "standard" design of a microstructured optical fibre was considered for tapering. The geometry of the MOF used for modelling and simulation was a hexagonal pattern with 6 layers of holes, (see Figure 6.1.a). The use of the finite element method (in `Comsol Multiphysics`) allows the restriction of the computational domain to only one quarter of the structure (according to the group theoretic analysis) for the fundamental mode, thus saving considerable on the computational time, as stated previously in this thesis. The magnitude of Poynting vector of the fundamental mode of a MOF, for illustrative purposes, is shown in Figure 6.1.b. It can be observed that the light is well confined to the core region and penetrates only slightly into the cladding region.

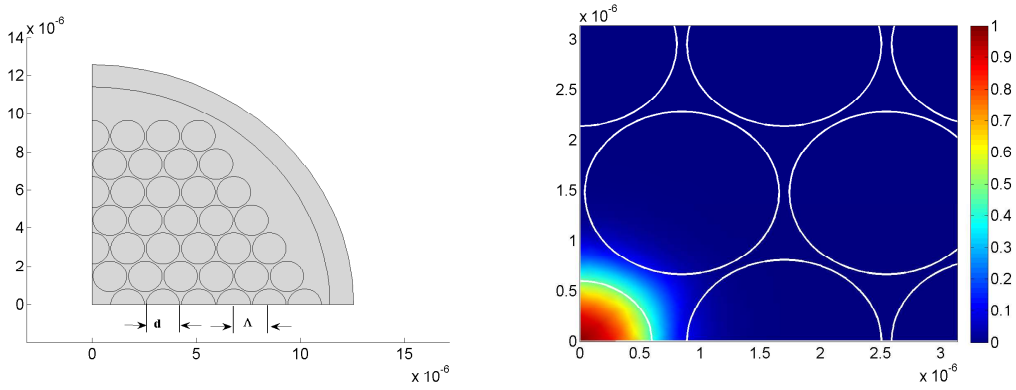

(a) (b)

FIGURE 6.1: a.) Cross section of the MOF with 6 rings of holes (d-hole diameter, Λ-pitch). b.) The magnitude of Poynting vector for the fundamental mode.

The principal properties of each fibre under consideration, such as dispersion, effective area and confinement loss of the lowest order mode, are numerically determined. A mode solver within the `Comsol Multiphysics` program is used to find the effective index n_{eff}, so that the result is post-processed to find the mode propagation constant β using the Equation 2.3 and hence the corresponding derivatives of the mode propagation constant, from the Equation 2.46.

In all cases considered in this investigation the confinement loss (proportional to the imaginary part of n_{eff}) is below 10^{-6}dB/m and so can be neglected for these fibres. Analogously to the analysis in Chapter 4, I used the optical maps representation to display the optical properties of the MOF. Figure 6.2 shows an optical map of the calculated dispersion (dispersion parameter D [ps/nm/km]) of various MOFs at 1.55 μm (the wavelength mostly used in communications applications) in function of Λ and d/Λ. The optical map is plotted for Λ between 1 μm and 2 μm and the range of d/Λ is 0.65 to 0.95.

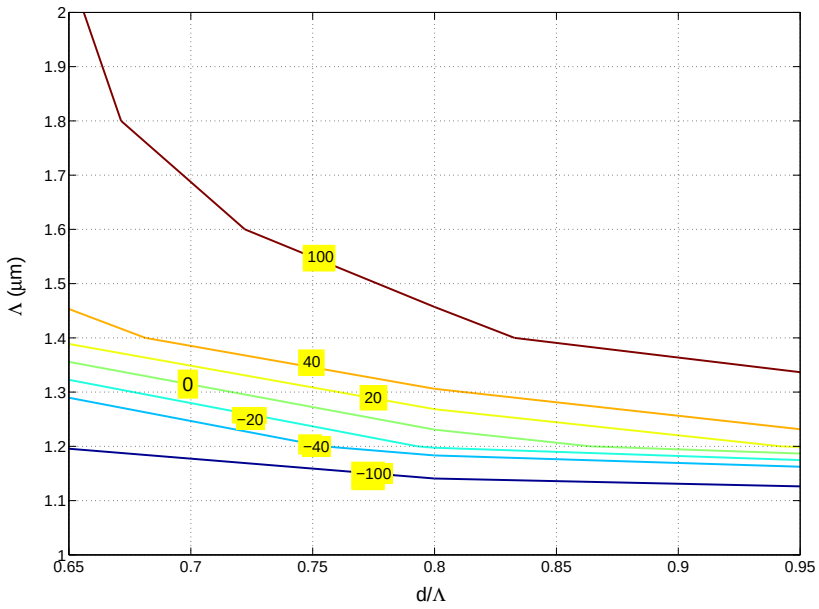

FIGURE 6.2: Dispersion, D [ps/nm/km], contour plot at λ=1.55 μm.

This plot enables finding the range of values for Λ (pitch) and d/Λ (relative hole size) that would provide the required dispersion regime (normal or anomalous) of the fibre. Note that any value of D between $\pm$100 ps/nm/km is possible through correct selection of fibre parameters. Since every taper corresponds to a path in (Λ, d/Λ) space, the desired profile can be immediately read off the graph. For ease of fabrication, the taper design requires a constant d/Λ [115] and so corresponds to vertical paths in the graph (although using pressurisation any taper can be fabricated). Choosing a large d/Λ maximizes the effective nonlinearity and so I chose d/Λ =0.95. Equally important for

SC generation is the GVD vs. wavelength, due to the wide bandwidth. Hence Figure 6.3 shows the characteristic of dispersion in function of wavelength, for the case d/Λ=0.95 and Λ=1.2 μm. It can be observed that the chosen parameters of the fibre enable two well separated zero dispersion wavelengths (ZDW). The zero GVD is in the vicinity of 1.55 μm (that was the initial design target, as pointed out above). Moreover, it has been reported in Ref. [126] that by increasing the separation of the two ZDW, i.e. increasing the width of anomalous dispersion region, the phase matched range is increased, too, which consequently increases the SC bandwidth.

As stated previously, the fibre is a typical highly nonlinear fibre and I aim to see how the SC process can be improved through tapering. The MOF was chosen with the focus on the dispersion at pump wavelength, although the design of the fibre with different overall dispersion profile (which looks at the dispersion slope etc.) could improve the generated SC. My aim here was to simplify the taper design so that it could be easily fabricated (to be applied in the future experiment) and to focus on the use of the procedure for finding the optimum launching conditions.

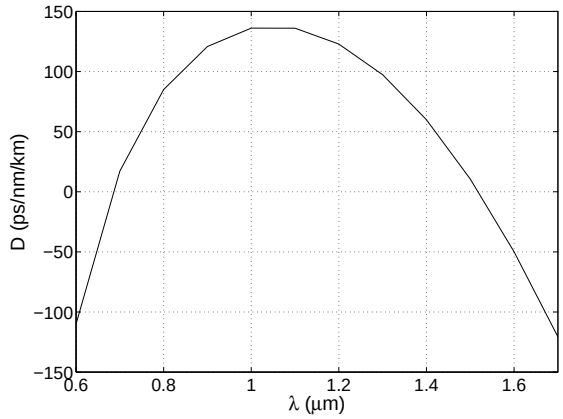

FIGURE 6.3: Dispersion in function of wavelength, d/Λ=0.95, Λ=1.2 μm.

Compared to most previous studies on SC generation, [52], [122], in this particular choice of MOF, we have the opposite sign of β_3 and thus as the wavelength increases the dispersion becomes normal. This makes the dynamics of SC generation different since the Raman self-frequency shift will move the soliton towards a region of normal dispersion and thus is not as likely to be as strong as in a fibre with the opposite sign of β_3.

In the process of the taper's parameters determination, I fixed $d/\Lambda = 0.95$, and then next step was to determine the range of pitch values that would determine the linear profile of the taper. Figure 6.4.a shows the range of possible dispersions obtainable through tapering ($d/\Lambda = 0.95$), whilst Figure 6.4.b shows the confinement loss (CL) versus (Λ) (d/Λ=0.95) for a MOF with six rings of holes (as seen in Figure 6.1.a). From Figure 6.4.a the parameters of the taper can be chosen, with two values of the pitch

determined by the condition of the relatively low absolute dispersion of approximately ±40 ps/nm/km (starting pitch 1.14 μm and finishing pitch 1.22 μm). These parameters suggest that shallow tapering (< 10%) is needed and that the fabrication of metre-long, shallow tapers is achievable using our tapering facility, [115], described in Chapter 3. Even knowing the starting and finishing values of the dispersion there is still an infinite range of possible tapers to consider. For the sake of simplicity I chose a linear profile for the taper.

The parameters of the MOF that change with tapering are: the chromatic dispersion β_2, higher order dispersion terms β_k (where terms β_3 - β_{10} were considered) and nonlinear coefficient γ. Note that it is the effective area that changes along the taper and hence γ does as well. Table 6.1 summarises taper parameters for region d/Λ=0.95. In all cases the parameters are calculated for different pitch values and are stored to be used as the interpolation nodes. Then, the parameters are calculated versus taper length using linear interpolation. For the illustration purposes Figure 6.5 shows the parameters of the taper (Λ, D and γ) changing with the taper length (in the graph the chosen taper length is 1 m, however it can be optimised as it will be shown in section 6.4).

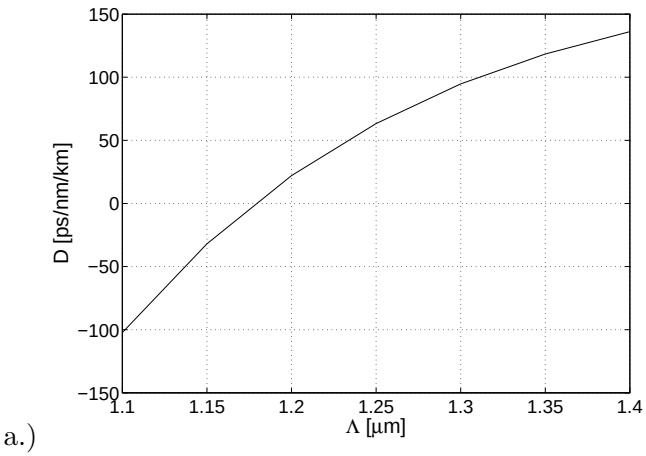

a.)

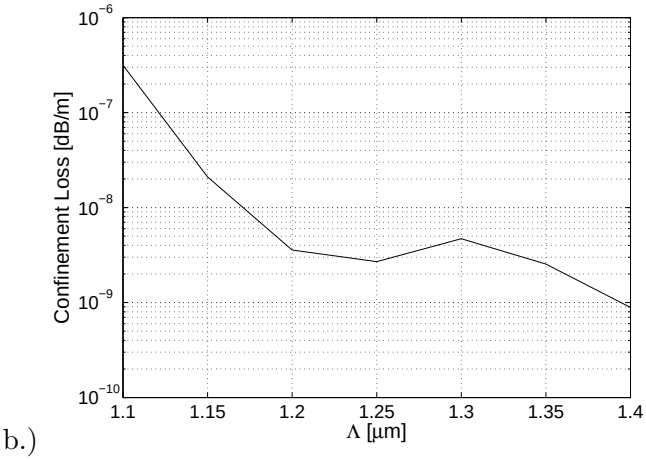

b.)

FIGURE 6.4: a.) Dispersion (D) vs. Λ at λ=1550 nm b.) Confinement loss vs. Λ for fixed d/Λ=0.95.

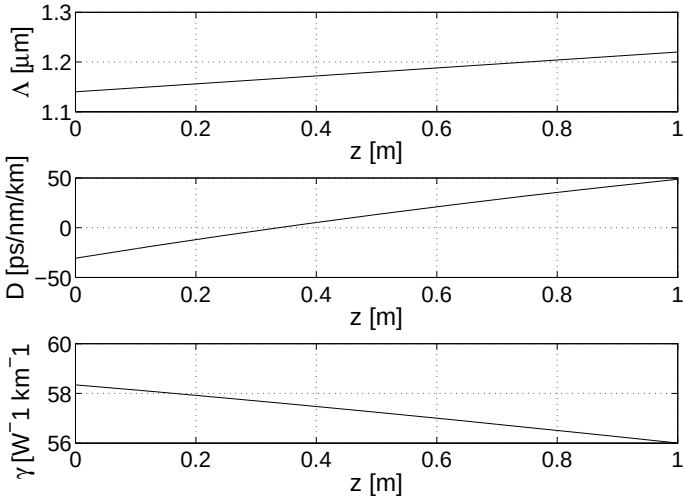

FIGURE 6.5: Pitch, dispersion and γ vs. distance.

	Start	Stop
Λ [μm]	1.14	1.22
β_2 [ps^2/km]	39.131	-62.1121
β_3 [ps^3/km]	-1.4425	-0.898497
β_4 [ps^4/km]	1.00012x10^{-2}	7.3367x10^{-3}
β_5 [ps^5/km]	-6.03832x10^{-5}	-4.8947x10^{-5}
β_6 [ps^6/km]	3.34176x10^{-7}	3.141549x10^{-7}
β_7 [ps^7/km]	-1.35702x10^{-9}	-1.8402x10^{-9}
β_8 [ps^8/km]	-3.309644x10^{-12}	7.57013x10^{-12}
β_9 [ps^9/km]	1.84503x10^{-13}	2.946656x10^{-14}
β_{10} [ps^{10}/km]	-1.7648569x10^{-15}	-6.211819x10^{-15}
γ [W$^{-1}km^{-1}$]	58.3419	56.0038

TABLE 6.1: Parameters of the tapered fibre ($d/\Lambda = 0.95$)

6.3 Results and Discussion

The next step, after the determination of tapered MOF parameters, is to model the optical propagation through the taper. The propagation of pulses in an optical fibre is described by the generalised nonlinear Schrödinger equation (GNLSE). The GNLSE, in the co-moving frame, can be written as:

$$\frac{\partial A}{\partial z} + \frac{i}{2}\beta_2\frac{\partial^2 A}{\partial t^2} - \frac{1}{3!}\beta_3\frac{\partial^3 A}{\partial t^3} + \cdots + \frac{\alpha}{2}A = i\gamma(1 + \frac{i}{\omega_0}\frac{\partial}{\partial t})(A(z,t)\int_0^\infty R(t')|A(z,t-t')|^2 dt') \tag{6.1}$$

where $A(z,t)$ is the slowly varying envelope of the electric field, z is the distance along the fibre, t is time in a copropagating time-frame. The equation takes into account

the effect of dispersion through β_k, the effect of nonlinearity through γ and fibre loss through parameter α, as discussed in Chapter 2.

The self-steepening and optical shock effects are characterized by a time scale of $\tau_{shock} = 1/\omega_0$. The numerical model includes the calculated dispersion curve from Figure 6.4.a. In order to correctly model the real dispersion, contribution of up to 10 terms of the dispersion has to be taken into account [1], [52]. The higher order dispersion coefficients are obtained in the simulation by fitting the dispersion data with a 15^{th} order polynomial.

In this investigation I employed the fourth order Runge Kutta in the interaction picture method [54] to solve the GNLSE. An array size of 2^{14} points is used and I set the temporal resolution to approximately 0.8 fs, which corresponds to a spectral resolution of 80 GHz. An algorithm with an adaptive step size control is applied so that a sufficiently small step size has been chosen, which was in the range of 10 - 100 μm, in order to follow rapid spectral changes with propagation.

6.3.1 Method for improving flatness of the SC

SC broadening process strongly depends on the fibre type, pulse duration and pulse energies used, whilst the figure of merit of the quality of spectra is either the spectra bandwidth or the best flatness. The major idea that led me through this investigation was to develop an efficient procedure that could enable determination of optimum launching conditions that would enhance the flatness of the SC at 1.55 μm (for any MOF under consideration). This could be particularly interesting in application of spectral slicing for dense WDM applications. The important characteristic of the procedure is that it can be generalized, i.e. it can be applied to other wavelengths or different fibres of interest. The procedure will be presented via the use of short tapered MOFs which can be easily modelled.

As pointed out earlier in this Chapter, I chose to examine a region of a standard hexagonal structure MOFs for the fixed value of the relative hole size (d/Λ=0.95) (shown in Figure 6.1.a) and to taper fibres linearly with the profile determined by fibre pitch at the beginning and the end. Hyperbolic secant pulses with the central wavelength of 1550 nm are launched into the taper. I chose to examine pulses with a temporal width between 100 fs - 600 fs and with the peak powers between 1 kW - 5 kW (although clearly other peak powers and time durations can be considered, depending on the the choice of the optical signal source). The supercontinuum generation for this particular range of widths and powers is dominated by the Raman scattering and soliton fission [2].

I modelled two different possible cases of propagation through the chosen taper, where firstly, the pulse is launched from anomalous dispersion regime and propagates to normal dispersion regime and secondly, the pulse is launched from anomalous dispersion regime and propagates to normal dispersion regime. For comparison I have also modelled a

case of an untapered MOF (Λ=1.2 μm, d/Λ=0.95) in the anomalous dispersion regime. Figure 6.6 shows the normalized spectrum versus wavelength for three different cases, when the input pulse peak power is chosen as 2 kW, input pulse FWHM 100 fs and the fibre length is 0.5 m. It can be observed that the tapered fibre in the case of tapering from anomalous to normal dispersion regime has broader spectra and better flatness, too. Further analysis showed that the SC obtained using these fibres had the same behaviour for different input pulse parameters, as well. In the analysis that follows the fibre loss is neglected since the taper length is at most a couple of meters and the loss of MOFs over this distance can be ignored.

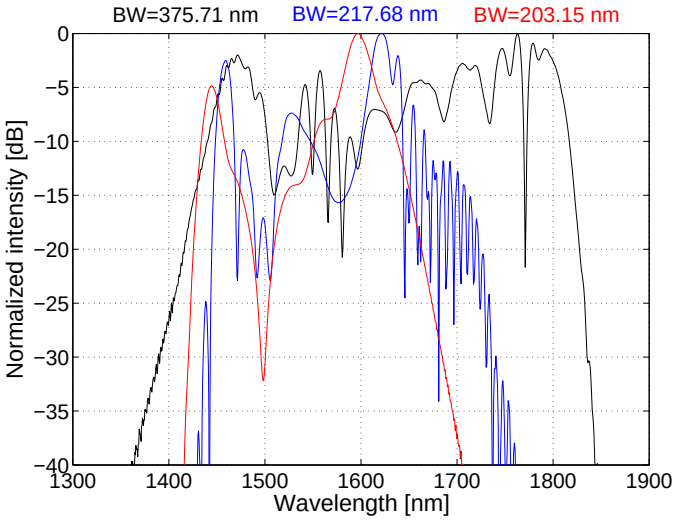

FIGURE 6.6: Normalized spectrum vs. λ when fibre is tapered from anomalous disp. regime to normal (black), when fibre is tapered from normal to anomalous (blue) and for the untapered fibre (red); P_0=2 kW, T_0=100 fs, z=0.5 m.

Since the input pulse parameters are not optimized, the next step is to determine the optimum launching conditions, such as the input pulse peak power and duration, as well as the optimum taper length. The method for determination the optimum conditions for the widest and best spectra flatness is based on calculating the widest SC bandwidth (B), calculated as - 20 dB width, and the taper length at which it can be achieved and plotting the corresponding contour plots versus input pulse peak powers and FWHM durations. Alternatively, maximum of the ratio of the bandwidth and the standard deviation of the spectra (B/Std), as a measure of the flatness and taper's corresponding length are calculated and plotted as contour plots in function of input pulse peak powers and time durations.

6.3.1.1 SC generation in a tapered fibre from anomalous to normal dispersion regime

Here I show the results of the first case of tapering from anomalous to normal dispersion regime. Figure 6.7 shows results of calculation of B and Figure 6.8 the taper′s corresponding length where the maximum bandwidth has been achieved. The sech pulse is launched in the anomalous dispersion regime where D=48.7 ps/nm/km, when Λ=1.22 μm and propagates in the linear taper until the end of the taper is reached, which corresponds to D = -30.68 ps/nm/km, when $\Lambda = 1.14\,\mu$m.

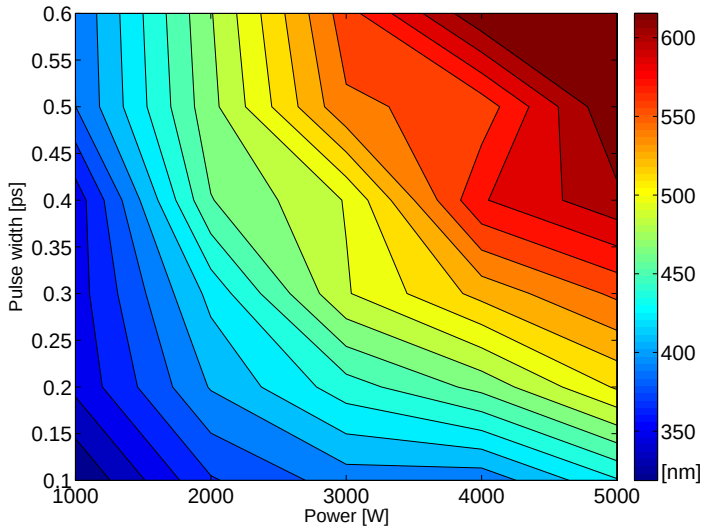

FIGURE 6.7: Maximum SC bandwidth (B), tapered from anomalous to normal, Λ changes from 1.22 μm to 1.14 μm.

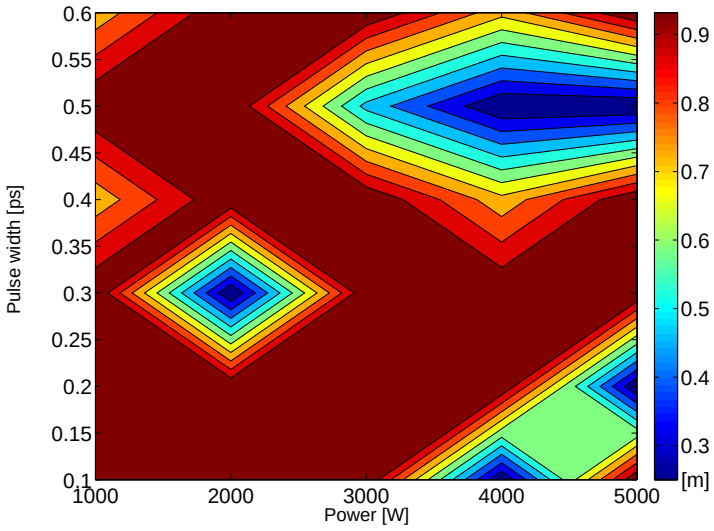

FIGURE 6.8: Taper length for maximum SC bandwidth (B), tapered from anomalous to normal, Λ changes from 1.22 μm to 1.14 μm.

In this case the contour plots show that the maximum spectra broadening of about 600 nm can be achieved for the input pulse temporal widths between 450 fs to 600 fs, with the peak powers between 3.5 kW to 5 kW for the taper 0.3 to 0.9 m long. This result is expected as broadest SC is achieved for higher pulse energies, as seen in Figure 6.7. As the energy of the input pulse increases, by increasing either pulse temporal width or peak power, the required taper length decreases correspondingly, as shown in Figure 6.8 - the minimum taper length corresponds to the higher pulse energies, although it is not as clear cut as Figure 6.7.

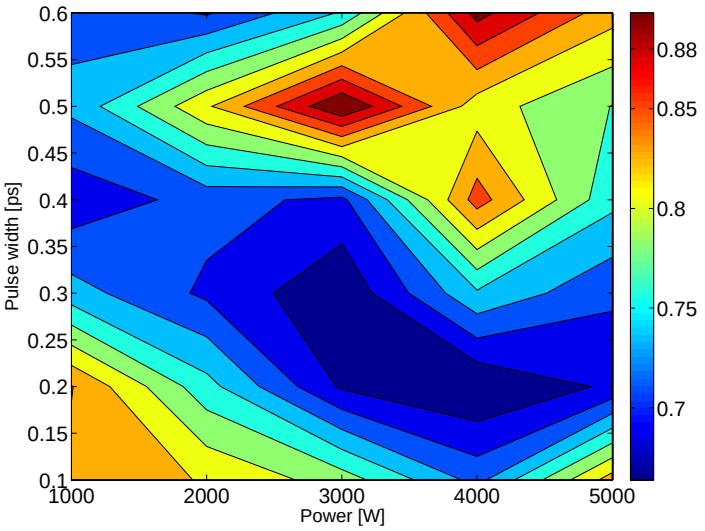

FIGURE 6.9: Maximum B/Std for tapered fibre when Λ changes from 1.22 μm to 1.14 μm, d/Λ=0.95, λ=1.55 μm.

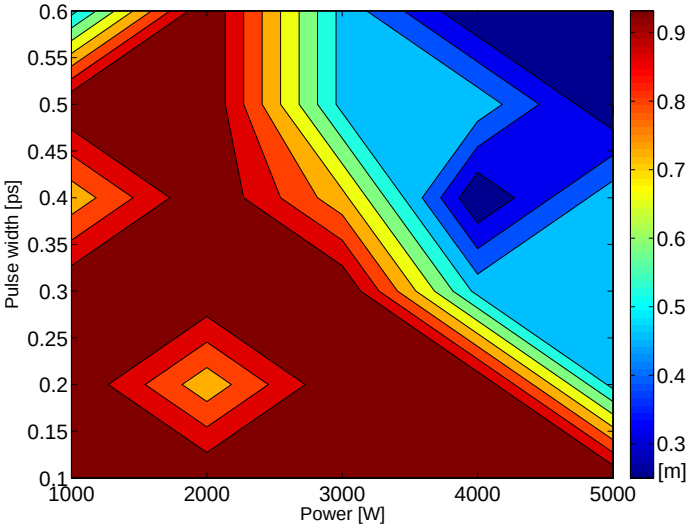

FIGURE 6.10: Taper length where best (maximum) B/Std for tapered fibre, when Λ changes from 1.22 μm to 1.14 μm, d/Λ=0.95, λ=1.55 μm.

Alternatively, the measure of the maximum spectra flatness can be calculated and plotted as contour plots, too. The maximum of the ratio of the bandwidth and the standard deviation (B/Std) and the corresponding taper length is shown in Figure 6.9 and Figure 6.10, respectively. This procedure enables defining the spectra width to determine the best flatness, in case if the specific application sets such a requirement. However, there are some features in the contour plots that are the product of the rapid spectral changes during the propagation and are determined by the number of points used for their calculation. Figure 6.11 shows individual spectra plots for the parameters extracted from Figure 6.9, in the vicinity of the area of maximum in the contour plot. It can be observed that the -20 dB points are similar for the three plots, but there are less spectral fluctuations for the pulse with the parameters P_0=3 kW, T_0=500 fs; z=0.5 m, which fall in the region of the maximum in Figure 6.9.

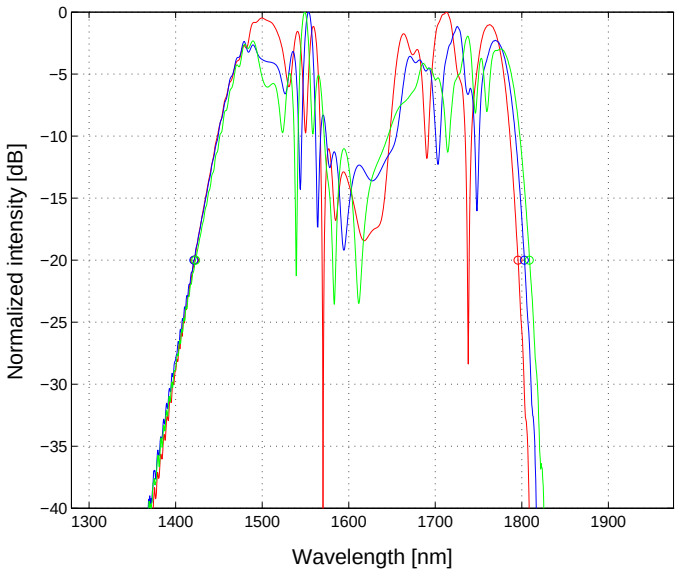

FIGURE 6.11: Spectra for the pulse parameters in the vicinity of the area of maximum in Figure 6.9: (red) P_0=2.6 kW, T_0=500 fs; z=0.6 m, (blue) P_0=3 kW, T_0=500 fs; z=0.5 m; (green) P_0=3.6 kW, T_0=500 fs; z=0.4 m.

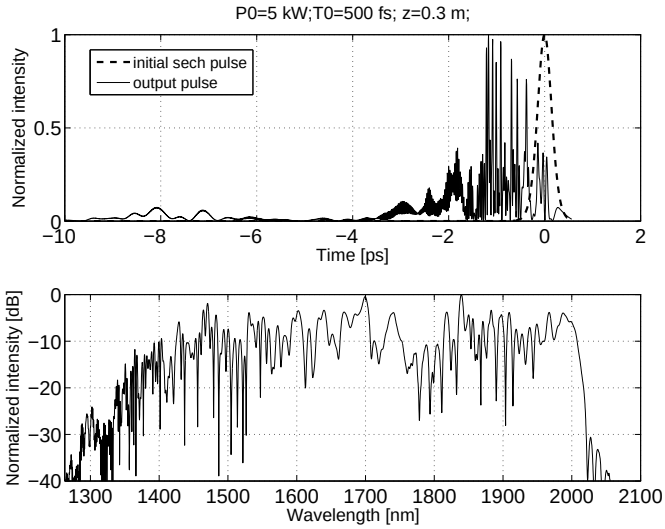

FIGURE 6.12: Top: pulse envelope, input (dashed) and output (solid) for the tapered fibre from anomalous to normal dispersion regime, when Λ changes from 1.22 μm to 1.14 μm; Bottom: normalized spectrum vs. wavelength.

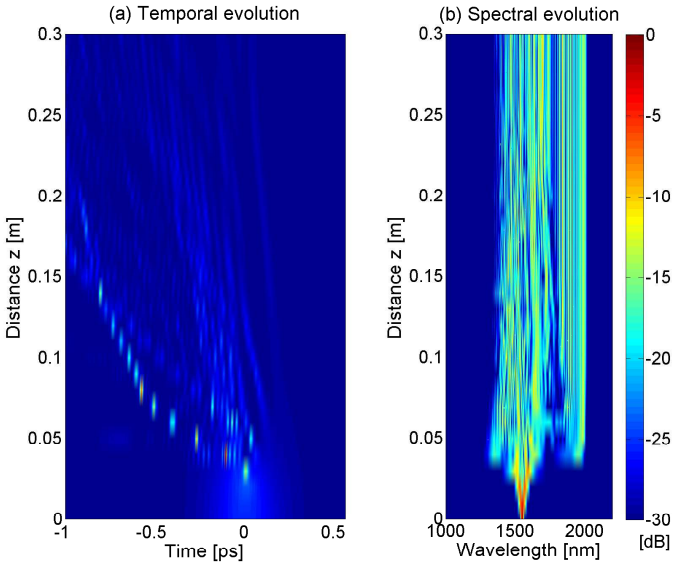

FIGURE 6.13: Temporal and spectral evolution in the tapered fibre for selected propagation distance; P_0=5 kW, T_0=500 fs; z=0.3 m.

From the analysis of the contour plots in Figure 6.9 and Figure 6.10 clear optimum parameters to obtain maximally broad but at the same time maximally flat spectra (minimum standard deviation) could be determined. The B/Std factor has its maximum value of 0.88, and in this case the input pulse duration is 500 fs, for the peak powers in the range 2.6 kW to 3.2 kW, for the taper length between 0.45 m and 0.8 m.

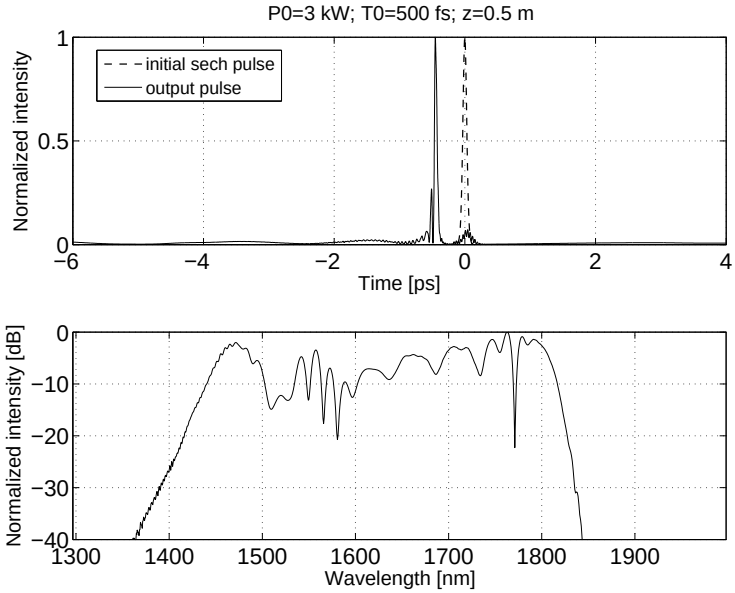

FIGURE 6.14: Top: pulse envelope, input (dashed) and output (solid) for the tapered fibre from anomalous to normal dispersion regime, when Λ changes from 1.22 μm to 1.14 μm; Bottom: normalized spectrum vs. wavelength.

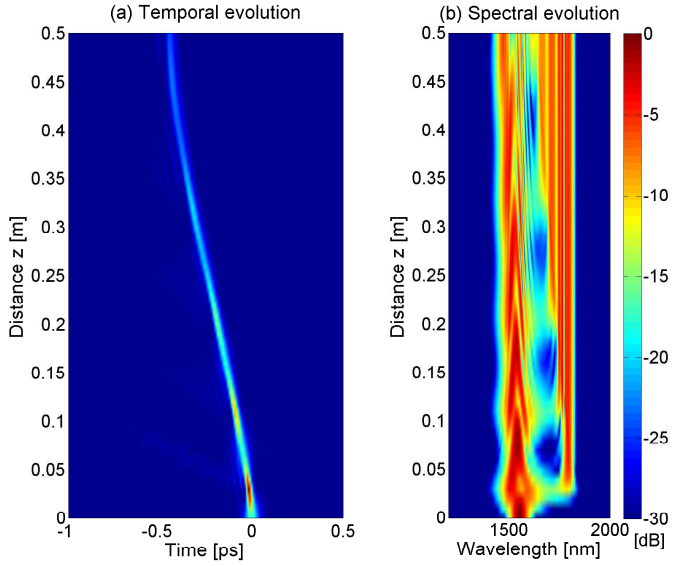

FIGURE 6.15: Temporal and spectral evolution in the tapered fibre for selected propagation distance; P_0=3 kW, T_0=500 fs; z=0.5 m.

This region of the optimum launching conditions is different from Figure 6.7 as the highest pulse energy or the maximum spectra bandwidth does not necessarily imply the best spectra flatness. According to the optimum launching conditions obtained from contour plots in Figure 6.7 and Figure 6.8 the widest spectra could be achieved when the input pulse peak power is chosen to be 5 kW and the duration of 500 fs FWHM,

whilst the corresponding optimum taper's length is 0.3 m. Based on these parameters Figure 6.12 and Figure 6.13 show the resulting output spectrum and time intensity, as well as the temporal and spectral evolution, for the taper of 0.3 m length.

The resulting spectra bandwidth is approximately 600 nm in this case, as expected from the contour plot in Figure 6.7. However, if we take into consideration spectra flatness as well, referring to the contour plots in Figure 6.9 and Figure 6.10 and we choose to launch the sech pulse with the input pulse peak power 3 kW and 500 fs FWHM width in the taper 0.5 m long, then the resulting normalized spectrum is within - 20 dB in the range from approximately 1420 nm to 1840 nm (shown in Figure 6.14 and Figure 6.15).

It can be easily seen that although the normalized spectra is much wider in the former, better spectra flatness is achieved in the latter case. This result validates the significance of this approach that could be used when optimization of the input conditions to achieve the best SC is needed and shows the advantages of this procedure that enables ease of determination of the input pulse conditions and taper parameters to achieve quality in SC. Alternatively, it would be possible to search for the best SC width based on the spectra flatness that is tolerable, depending on the application. This will be implemented into the procedure in the future work.

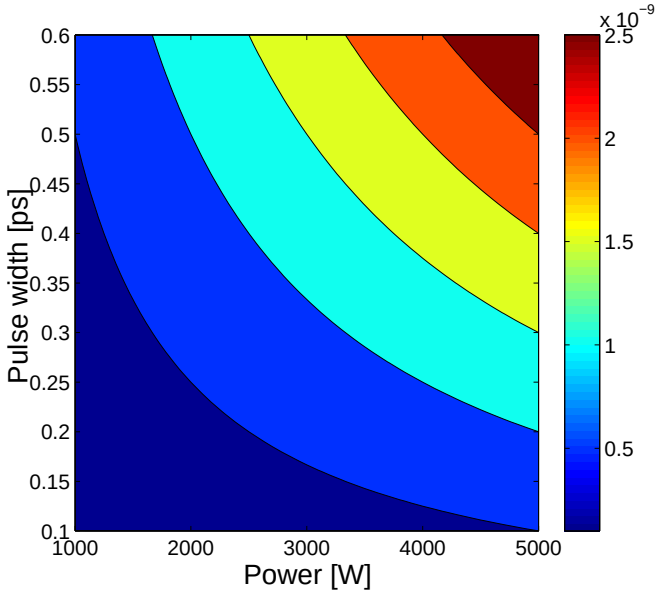

FIGURE 6.16: Constant energy contour plot; calculated contours of the energy of the sech pulse $E = 2T_0P_0$, where P_0 is input pulse peak power and $T_0 = T_{FWHM}/1.76$.

The results of the SC evolution for the tapered fibre from anomalous to normal dispersion region show that different SC generation mechanisms take place. Due to the short pulse durations ($T_{FWHM} = 500fs$), the soliton number is $N = 19$ when $P_0 = 5\ kW$ i.e. $N = 15$ when $P_0 = 3\ kW$, implying that pump pulses are higher order solitons

and nonlinear effects dominate over dispersion effects. An initial period of spectral broadening and temporal compression, followed by the soliton fission and formation of fundamental solitons after several cm of propagation, can be observed. Pumping in the anomalous dispersion regime, such as in this case, leads to the phase matched generated components at short and long wavelengths via FWM [126]. Due to the intrapulse Raman scattering i.e. the soliton self frequency shift (SSFS), these fundamental solitons are subsequently shifted to longer wavelengths. As approaching ZDW and across into normal dispersion regime the extent of nonlinear broadening becomes limited and leads to the temporal broadening. At this stage the process is associated with the generation of dispersive wave spectral components.

Figure 6.16 shows constant energy contour plot for the *sech* pulse of various peak powers and widths. It can be observed that the shape of contours is in an agreement with the contours of the maximum SC bandwidth presented in Figure 6.7. This result shows that in a case of tapering from anomalous to normal dispersion regime the maximum SC bandwidth is determined by the increasing input pulse energy, whilst it is not the case when the best spectra flatness is required (as seen from Figure 6.9).

6.3.1.2 SC generation in a tapered fibre from normal to anomalous dispersion regime

In this section I show the results of the first case of tapering from normal to anomalous dispersion regime. Figure 6.17 shows results of calculation of the maximum SC width, B, and Figure 6.18 the taper′s corresponding length where the maximum bandwidth has been achieved, when sech pulse propagates from the taper's end that falls in the normal dispersion regime towards anomalous. In this case the contour plots show that the maximum spectra broadening of about 550 nm can be achieved for the input pulse temporal width of about 350 fs, with the peak power larger than 5 kW and the corresponding taper's length is larger than 0.9 m.

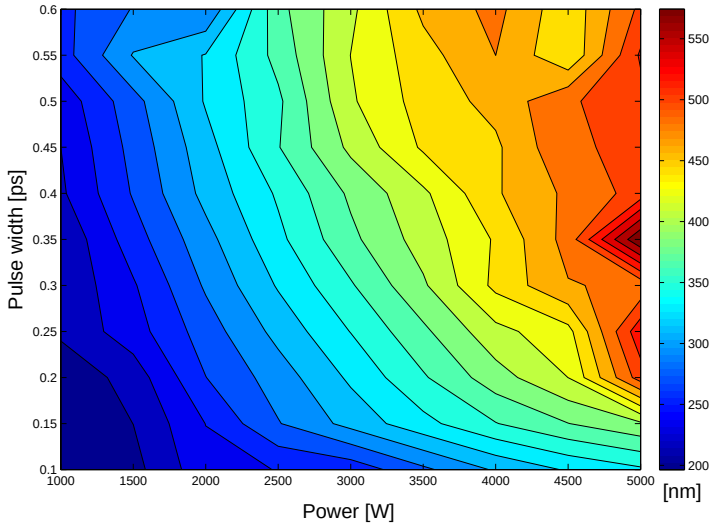

FIGURE 6.17: Maximum SC bandwidth (B), tapered from normal to anomalous, when Λ changes from 1.14 μm to 1.22 μm, d/Λ=0.95, λ=1.55 μm.

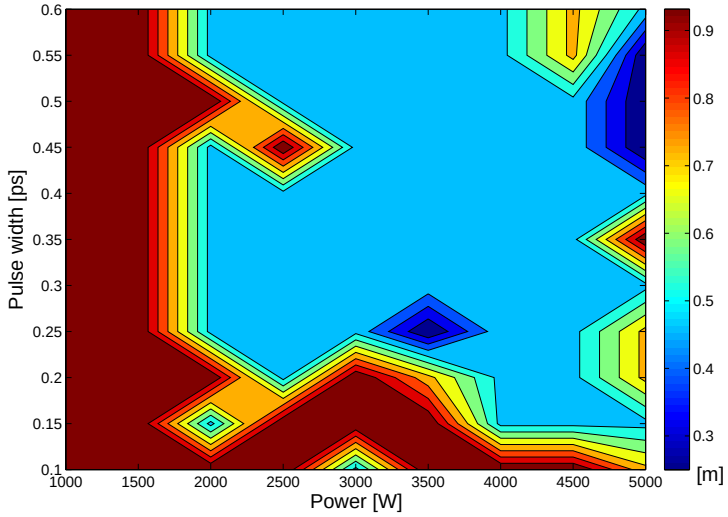

FIGURE 6.18: Taper length for maximum SC bandwidth, when Λ changes from 1.14 μm to 1.22 μm, d/Λ=0.95, λ=1.55 μm.

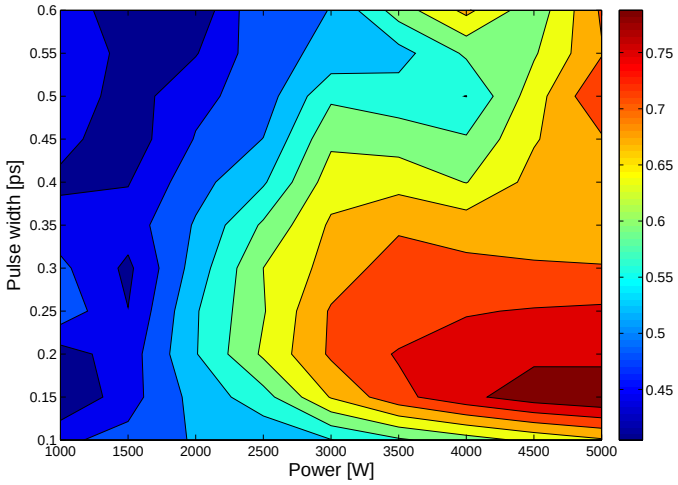

FIGURE 6.19: Maximum B/Std for tapered fibre when Λ changes from 1.14 μm to 1.22 μm, d/Λ=0.95, λ=1.55 μm.

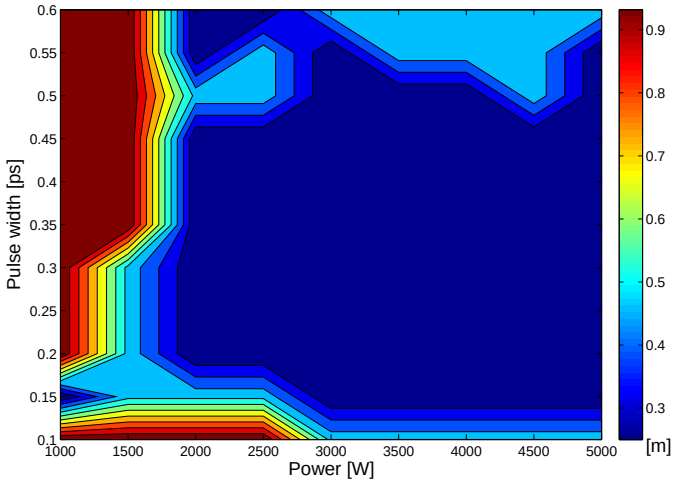

FIGURE 6.20: Taper length where best (maximum) B/Std for tapered fibre, when Λ changes from 1.14 μm to 1.22 μm, d/Λ=0.95, λ=1.55 μm.

This result shows that in order to achieve better SC characteristics, higher pulse energies are needed than in case of pulse propagation when pulse is launched from the end which falls in the anomalous dispersion regime. Contour plots in Figure 6.19 and Figure 6.20 show different optimum launching conditions if B/Std is considered, as in the previous case, with the maximum value of 0.75 which is significantly lower than 0.88 (that is obtained in case of pulse propagation from anomalous end of the taper).

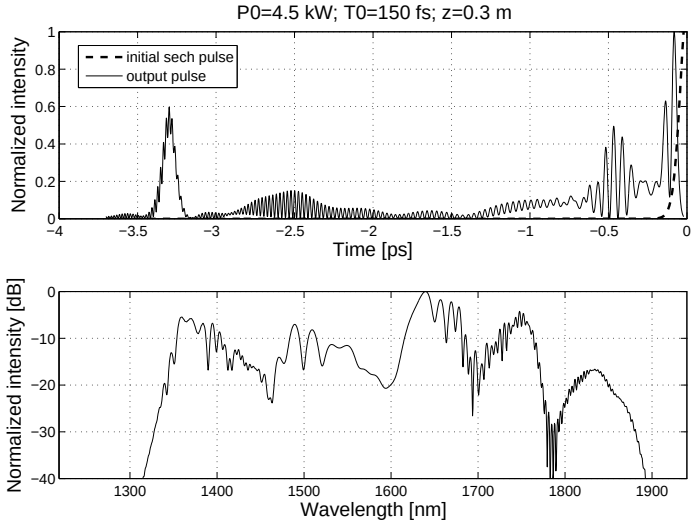

FIGURE 6.21: Top: pulse envelope, input (dashed) and output (solid) for the tapered fibre from normal to anomalous, when Λ changes from 1.14 μm to 1.22 μm; Bottom: normalized spectrum vs. wavelength.

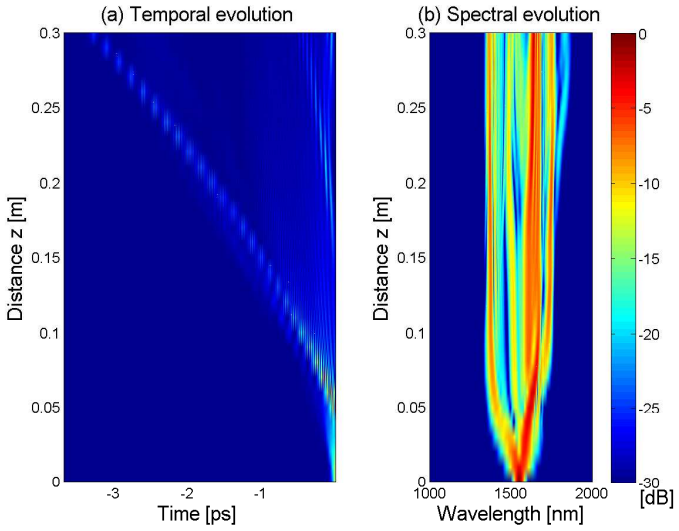

FIGURE 6.22: Temporal and spectral evolution in the tapered fibre for selected propagation distance; P_0=4.5 kW, T_0=150 fs; z=0.3 m.

According to the optimum launching conditions obtained from contour plots in Figure 6.18 and Figure 6.19 the optimum launching conditions could be achieved when the input pulse peak power is chosen to be 4.5 kW and the time FWHM duration is 150 fs, whilst the corresponding optimum taper's length is 0.3 m. Based on these parameters Figure 6.21 and Figure 6.22 show the resulting output spectrum and time intensity, as well as the temporal and spectral evolution, for the taper of 0.3 m length.

6.3.1.3 SC generation in an untapered fibre in the anomalous dispersion regime

Finally, the same analysis has been done for the case of the untapered microstructured fibre in the anomalous dispersion regime.

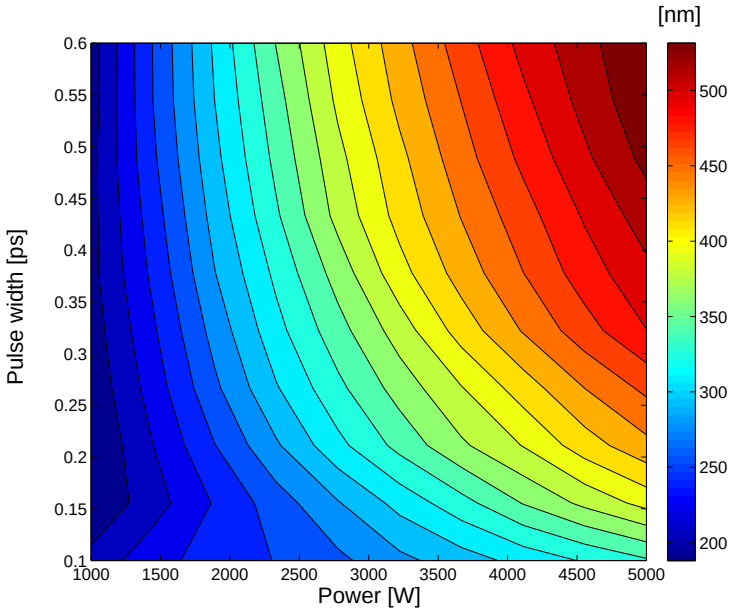

FIGURE 6.23: Maximum SC bandwidth (B), untapered fibre, when Λ = 1.22 μm, d/Λ=0.95, λ=1.55 μm.

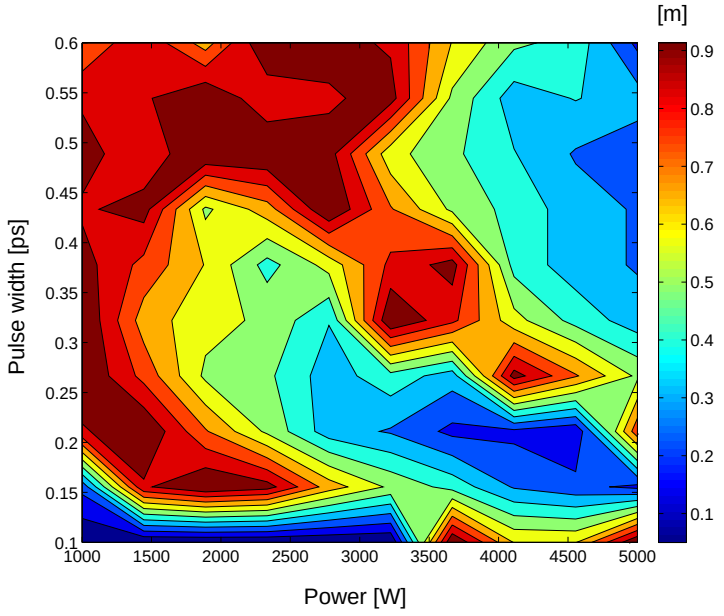

FIGURE 6.24: Taper length for maximum SC bandwidth for untapered fibre, when Λ=1.22 μm, d/Λ=0.95, λ=1.55 μm.

The contour plots of the maximum SC bandwidth (B) and B/Std and the corresponding taper length versus input pulse widths and peak powers, are shown in Figures 6.23 and 6.24, and it can be seen the broadest spectra of about 500 nm (which can be achieved for peak powers of around 5 kW and pulse FWHM of about 550 fs).

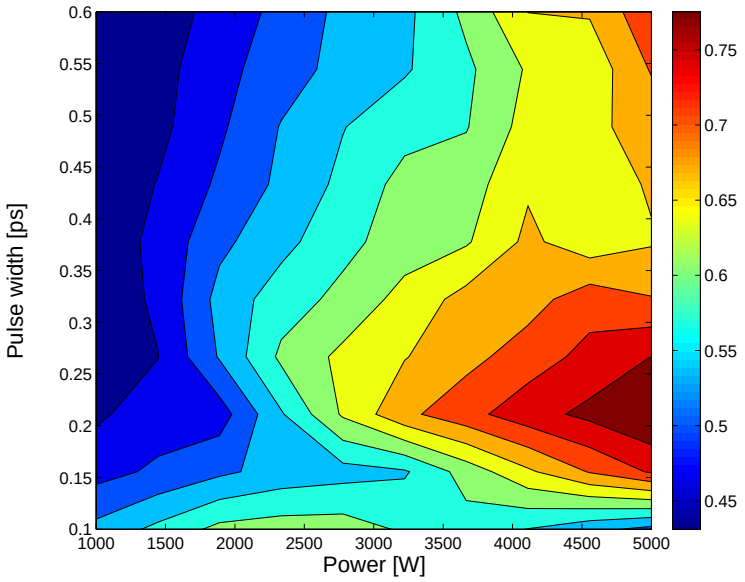

FIGURE 6.25: Maximum B/Std for untapered fibre when Λ = 1.22 μm, d/Λ=0.95, λ=1.55 μm.

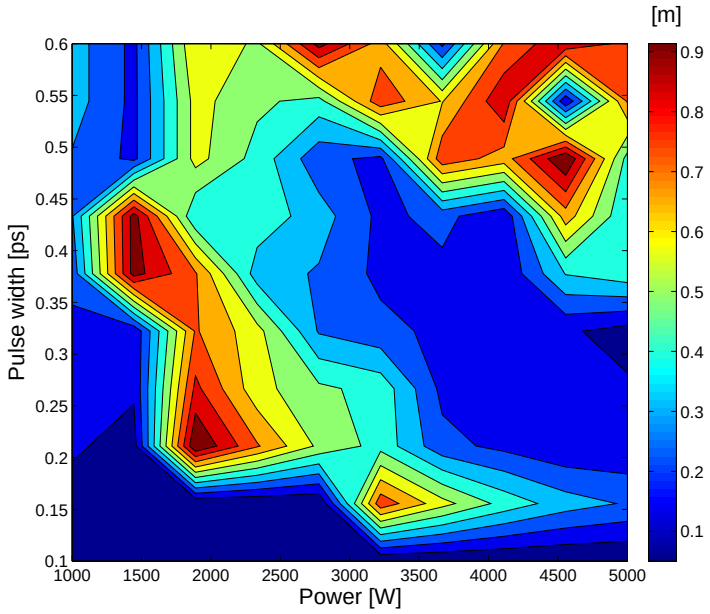

FIGURE 6.26: Taper length where best (maximum) B/Std for untapered fibre, when Λ=1.22 μm, d/Λ=0.95, λ=1.55 μm.

Figures 6.25 and 6.26 show contour plots of best B/Std factor (which has maximum value of 0.75 for 300 fs pulse duration and peak power range 4.5 - 5 kW) and the corresponding taper's lengths. Results show that both the SC width and B/Std are lower when compared to the fibre tapered from anomalous to normal dispersion regime.

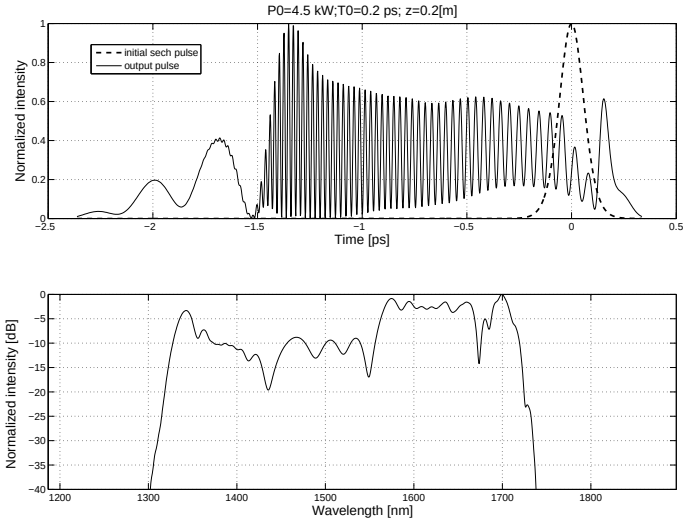

FIGURE 6.27: Top: pulse envelope, input (dashed) and output (solid) for the untapered fibre, when Λ =1.22 μm; Bottom: normalized spectrum vs. wavelength.

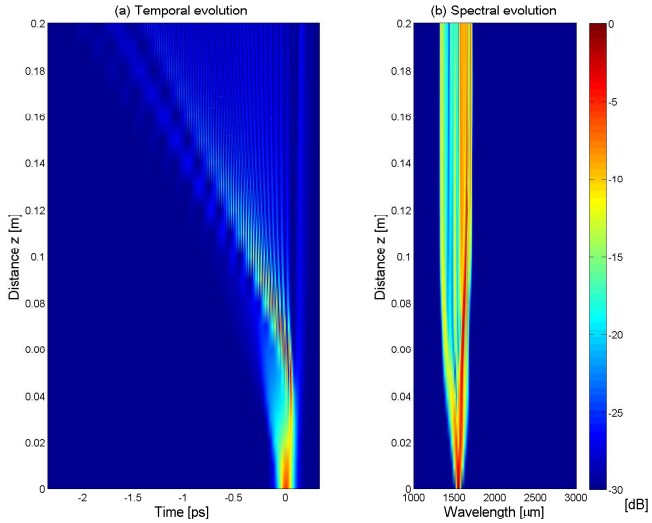

FIGURE 6.28: Temporal and spectral evolution in the untapered fibre for selected propagation distance; P_0=4.5 kW, T_0=200 fs; z=0.2 m.

According to the optimum launching conditions obtained from contour plots in Figure 6.25 and Figure 6.26 the optimum launching conditions could be achieved when the input pulse peak power is chosen to be 4.5 kW and the time FWHM duration is 200 fs,

whilst the corresponding optimum taper's length is 0.2 m. Based on these parameters Figure 6.27 and Figure 6.28 show the resulting output spectrum and time intensity, as well as the temporal and spectral evolution, for the taper of 0.2 m length.

6.4 Conclusion

In this Chapter I have proposed a method for improving flatness of a SC based upon tapering the microstructured optical fibres. This approach provides a simple way for determination of the taper parameters (pitch and relative hole size), to achieve the required dispersion regime. I chose to taper a MOF with d/Λ=0.95 and determined parameters of the taper in terms of starting and finishing pitch values.

The modelling was based on sech pulse propagation in the tapered MOF using GNLSE, which is solved numerically using the RK4IP method. The SC spectra width (B) and the ratio of spectra width and spectra standard deviation, which is figure of merit of the spectra flatness, (B/Std), are calculated and presented as contour plots versus input pulse durations and peak powers, for the case of tapering from the anomalous to normal dispersion regime.

These results show better SC features when compared to another case of tapering from normal to anomalous regime as well as for the case of untapered fibre. I have also shown that by taking into account the spectra standard deviation it is possible to find conditions to significantly improve flatness of the supercontinuum, as well. The method proved to be efficient for easy determination of the optimum launching conditions, thus providing a simple way of enhancing the spectra properties of SC, which is of the fundamental and practical interest.

My major contributions in the investigation of SC generation in tapered MOFs are:

1. MOF modelling using finite element method (using `Matlab` scripts for `Comsol Multiphysics`);
2. Generating optical property map for the relevant parameters of the MOF;
3. Generating `Matlab` script for `Comsol Multiphysics` to calculate the higher order dispersion coefficients (β_3 to β_{10}) by fitting the dispersion data with a 15^{th} order polynomial, using Richardson's interpolation (using difference approximation for derivative of n^{th} order);
4. Generating `Matlab` script to solve GNLSE, using RK4IP method (Appendix D);
5. Numerical simulation of the pulse propagation in different fibre tapers;

6. Designing an algorithm/procedure for determination of optimum parameters for widest/(best flatness) SC.

Directions for future work are towards implementing complete optimisation of the microstructured optical fibre by taking into account consideration of the overall dispersion profile of the MOF. This implies that even better SC generation would be achieved if the optimally designed MOF has been considered.

Chapter 7

Conclusions

In this thesis I have investigated fabrication of the intermediate length tapers and explored theoretically and experimentally nonlinear propagation in these tapers. Microstructured optical fibre technology has an important role within the nonlinear fibre optics techniques, in terms of offering unique control of optical properties. In my work I have combined the MOF technology and the novel tapering facility in an attempt of achieving some new applications in the field of nonlinear optics.

In a first step, I have presented the development of the novel optical fibre tapering system. The new tapering system is based on the `Matlab` code which controls the motor controllers processor units and the diameter measuring gauge, using serial RS-232 interface. The system setup is described in details and the algorithm for setting up the desired tapering profiles is presented. Furthermore, I have shown work done to improve the system performance by reducing the variation of the measured fibre diameter. I have described the design steps of the control system feedback loop algorithm. The control system feedback loop algorithm is used for the implementation of the PI controller with the associated noise filter. I have presented how starting from the PI controller and noise filter transfer functions in the Laplace domain, through the discrete time equivalents in the z domain, I derive the corresponding inverse z transforms, which led to their software implementation. Subsequently, I have presented several sets of experimental results of tapering step-index and MOF fibres. Firstly, for the non-monotonically varying fibre profile, the diameter variation is shown for the cases with and without the control feedback loop in the system. By means of minimum mean error and standard deviation, these results justify an improvement achieved with the implementation of the control feedback loop. The capabilities of the novel tapering system were demonstrated further on two more examples: a.) step index fibre tapered periodically along 60 cm of length and b.) step index fibre tapered linearly 70% along 20 cm of length. Finally, the experimental result of tapering the solid-core MOF 50% along 60 cm length, is shown. In this case the SEM images of this taper were taken at different propagation distances, which confirmed the structural change within the taper.

As a second step, I have explored theoretically the application of parabolic pulse generation in the new, intermediate range MOFs tapers. I have demonstrated a procedure for modelling and simulation of a MOF taper. In the proposed method, starting from the optical map, the parameters of the MOF taper, needed for the parabolic pulses generation, are determined. I proposed two different tapers with a linear pitch profile, for two values of the air-filling factor. The nonlinear pulse propagation is performed using numerically solving the NLSE. I have shown how initial Gaussian pulses of various input peak powers and temporal widths propagating in the tapered MOF, evolve into parabolic pulses characterised by a linear chirp. Results are quantified using the misfit parameter, which measures the root mean square error between the propagated pulse and its parabolic fit in the time domain. Significantly, the modelling procedure enables determination of the optimum launching conditions and taper's length that enables best parabolic pulse generation. The optimisation can be important in cases when pulse reshaping is conditioned by the initial pulse energy availability.

Then, I extended this work into the area of the experimental investigation of the parabolic pulse generation in the intermediate range tapers. I have presented numerical and experimental results of the three experiments conducted using three different tapers. The various lengths (40 cm, 60 cm and 1.8 m) tapers were fabricated using the novel tapering facility. The pulse propagating through the taper was characterized using linear FROG method. In this investigation the results of experiment and simulation were compared confirming the overall good agreement between them. The results show consistent convergence towards the parabolic pulse at the taper's output, with the increase in the input pulse power levels.

Finally, I have shown the results of investigation of the supercontinuum generation in tapered MOFs. I have proposed a method which ultimately improves flatness of a SC. This method consists of several steps. It starts with the use of optical maps to find the taper parameters, just as the parabolic pulse generation modelling starts. However, in this case, the nonlinear pulse propagation is modelled using GNLSE, which is solved numerically using the RK4IP method. Then, the SC spectra width and the ratio of spectra width and spectra standard deviation, which is figure of merit of the spectra flatness, are calculated. In analogy to the procedure for the best parabolic pulse generation, these calculated measures of the SC property are presented as contour plots for various input pulse durations and peak powers. In this method, the enhancement of the spectra properties of SC is confirmed by tapering MOF. Significantly, the method proved to be efficient for easy determination of the optimum launching conditions, which consequently leads to better spectra flatness or wider bandwidth.

Future work

The work conducted in this thesis has identified several areas of research for the future investigation.

The results presented in Chapter 3 demonstrated good accuracy in the taper diameter variation. In order to achieve better control of the dispersion and nonlinearity I have chosen to taper MOFs. However, tapering of such fibres with the tapering ratios of >10% leads to problems of holes collapse, as seen in [116]. Therefore, to overcome problems due to the surface tension which causes holes to collapse, the pressurisation needs to be applied during the tapering. Active pressurisation during the tapering process would enable selective control over the hole size and pitch of the MOF, during the tapering procedure. There have been references to the controlled hole expansion in MOFs by heating the fibre while holes were pressurised [140], [141]. Fully understanding and controlling the process of pressurisation will require monitoring the structural parameters during the tapering process. Previously, I have used the SEM technique to analyse structural parameters of the tapers, which is a destructive method and is not suitable for this purpose. Therefore, there is a need to develop alternative measuring technique. The possible solution has been experimentally demonstrated by other researchers [65]. It has been shown that in the transverse plane microstructured optical fibres exhibit bandgaps whose central frequency scales linearly with Λ [65]. The strength of the bandgaps depend on the d/Λ, so transverse probing of the fibre with the white light source can allow structural parameter determination.

Various applications may benefit from the novel fibre tapering facility. For the application such as adiabatic soliton compression, which is an attractive technique extendable to the femtosecond domain, this new approach can be of a particular interest. An adiabatic soliton compression requires the control of the fibre diameter with a longitudinal precision which couldnt be achieved with the existing techniques. By using this technique it is possible to make suitable tapers which should have low loss since the mode is still well confined in the core. The novel tapering facility could be, also, potentially used to fabricate tapers used for the efficient Brillouin suppression, as tapers needed require constant Λ and decreasing d/Λ. It has been shown theoretically that by modulating the Brillouin gain bandwidth along the length of the fibre the effective threshold for stimulated Brillouin scattering can be increased [31].

Research conducted in the area of parabolic pulse shaping could be extended to the goal of producing compressed pulse within the fs range and ultimately single cycle pulses. Having available the tapering facility able to produce arbitrary taper shapes, the investigation of parabolic pulse generation could be also extended to different taper profiles (such as hyperbolic or exponential) with different dispersion limits in the normal dispersion regime. Also, an inverse MOF taper design could be applied, so that having

specified minimum misfit parameter value, search for the optimum taper profile can be conducted.

The experimental results presented in Chapter 5 demonstrated early stages of the parabolic pulse generation and convergence towards the parabolic pulse with the increase of the input power. However, it is possible to further improve the experimental conditions. The main limiting factor in the experiments was the lack of the appropriate fibre and the difficulty to handle long tapers without being recoated. The fibre recoater became available near to the end of my work, therefore it hasn't been fully exploited in the experiments. This is definitely the obvious way of improving the MOF taper robustness, allowing fabrication of significantly longer taper lengths. Another drawback of the experiment was limitation of the peak power input into the taper. This can be overcome in the future work, by using high power amplifier capable of producing higher powers and by improving the coupling efficiency into the fibre taper (e.g. by splicing the single mode fibre to the highly nonlinear fibre, thus obtaining smaller spot size of the incident beam or by using the nanopositioning piezo-electric xyz stages).

It has been shown in Chapter 6 that tapering strategies provide great scope of achieving enhanced properties of SC spectra. The investigation in this chapter has suggested the direction for possible future work. Further steps could be conducted in the direction of the complete optimisation of the MOF, by considering overall dispersion of the fibre.

Appendix A

Automatic `Matlab` based post processing of the SEM images

This appendix presents a tool for post processing the images obtained using Scanning Electron Micrograph in order to find the geometry parameters of the fibres under examination. Using this tool it is possible to automatically measure parameters of the MOFs such as hole diameter, pitch value, d/Λ ratio or the core diameter. The program is written in `Matlab` and is based on using the `Image` toolbox. This program was developed due to the practical importance to post process the results of the structural parameters analysis using SEM technique and was used throughout this thesis. The example used for illustration purposes corresponds to the Figure 3.18.a, now shown in Figure A.1.

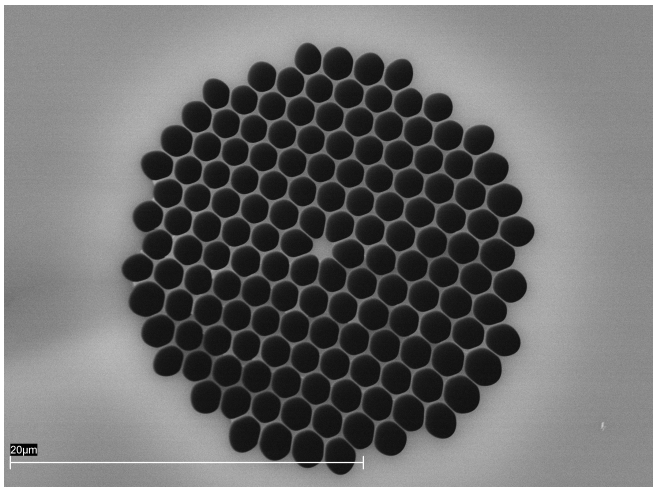

FIGURE A.1: The SEM image at the start of the post processing procedure

In the first step the function `bwareopen`, which reads grayscale image from the graphic file, is called. This function removes from a binary image all connected objects that are

smaller than tens of pixels producing another binary image. It is followed by function `bwboundaries`, which traces the exterior boundaries as well as boundaries of holes inside objects.

Afterwords, the function `regionprops`, which measures properties of the image regions, is called. The properties of the image region are: area, centroids, perimeter, equivalent diameter etc. The diameter of the holes can be quickly calculated by finding the average value of all equivalent diameters of the structure (or apart from the last ring of holes which usually expands the most). In the next phase the image is being labeled so that holes are associated with numbers, as in Figure A.2.

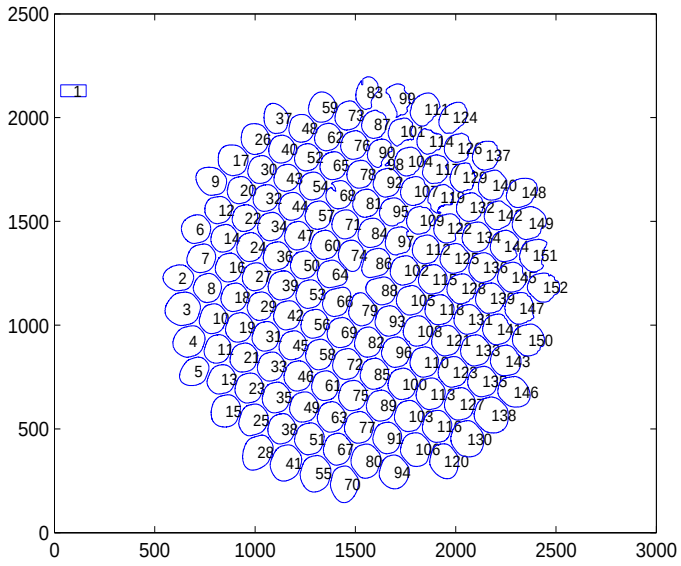

FIGURE A.2: The MOF cross section with the holes being labeled

From Figure A.2 we can distinguish which rows of holes we wish to use for the parameters determination. Just as we would do it manually, we could choose number of rows containing holes. We could exclude the last ring of holes (which expanded mostly) and the holes whose size is inappropriate (due to the imperfections while drawing the fibre or due to the low quality of the SEM image taken). Also, in manual treatment we would choose holes in three different axis (planes) of the cross section. In the tool proposed two methods are available for the geometry parameters measurement. The first method (uses function `calc_dist`) for finding values of the pitch is based on calculating the distance between the centres of the holes (for the chosen arrays of holes in different directions) and finding the average of this. Using this method, for the example chosen we measured the $\Lambda = 1.8443$ μm, $d = 1.6414$ μm and consequently $d/\Lambda = 0.89$.

In the second method (shown in Figure A.3) we find automatically the cross points between the hole (circle) and the line we draw across the chosen array of holes in different directions (as we would do manually), using function `cross_points`. The pitch value is

calculated as the total distance between the first and the last cross point divided by the number of holes in between.

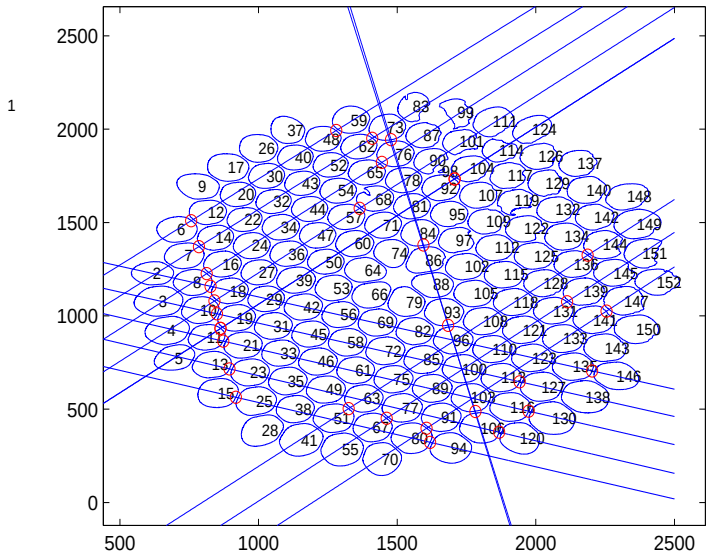

FIGURE A.3: The MOF cross section used for Λ calculation

Using the second method, for the example chosen in Figure A.3 we measured $\Lambda = 1.8236$ μm, $d = 1.7324$ μm and consequently $d/\Lambda = 0.95$.

The comparison of the first and the second method shows that there is small discrepancy of the results, but we could consider both methods similar and approximately correct and reliable. The advantage of using this proposed tool for the geometry parameters measurements is that the procedure is much faster and it offers better accuracy in comparison to the manual method. Important point is, that regardless of which method we use the accuracy of the measurement depends on the quality of the SEM image.

```
% Natasha Vukovic, ORC Southampton, 06/06/2007
% script enables post processing of the images obtained using
% SEM, in order to find the geometry
% parameters of the fibre under examination

% uses following functions and scripts:

% a.)  calc_dist: calculates equivalent distances between centres
% of the centroids of the structure
% function drowm=calc_dist(row,cent)


% b.) cross_points: finds automatically the cross points between the
```

```
% hole (circle) and the line drawn across the chosen array of
% holes in different directions (as it is done manually)
% [pitch,xk,yk]=cross_points(B,cent,rw,scale)

% calculates parameters:

% a.) D1:  the average value of all equivalent diameters
% (equ_diam - obtained from regionprops), of the structure
% b.) pitch_1: the average value of the pitches
% c.) ratio1: calculated d/Lambda using the first method
% d.) D2:  the average value of all equivalent
% diameters (equ_diam) of the structure
% e.) pitch_2: the average value of the pitches
% f.) ratio2: calculated d/Lambda using the second method

clear all;
clc;
close all;
file_name = 'ST13-1A-S3-M9000-P26.jpg';
I = imread(file_name);
figure(1),imshow(I),hold on,
Ibw = (I<=60);
% remove all object containing fewer than 30 pixels
Ibw = bwareaopen(Ibw,30);
% fill any holes, so that regionprops can be used to estimate
% the area enclosed by each of the boundaries
Ibw = imfill(Ibw,'holes');
[B,L] = bwboundaries(Ibw,'noholes');
s = regionprops(L,'area','centroid','EquivDiameter');
areas = cat(1,s.Area); areas = areas(1:end,:);
centroids = cat(1, s.Centroid); cent=centroids(1:end,:);
equ_diam = cat(1,s.EquivDiameter);
for ind = 1:length(B)
    boundary = B{ind};
    figure(3),plot(boundary(:,2),boundary(:,1)),hold on,
    text(cent(ind,1),cent(ind,2),num2str(ind),'Fontsize',8)
end


%FIRST METHOD: calculates equivalent distances between centres
% of the centroids of the structure for the chosen array
```

```
% of holes in different directions
scale = 20e-6/1501;
row1=[15,25,38,51,67,80,94];
drowm(1)=calc_dist(row1,cent);
.
. % FOR BREVITY REASONS AVERAGING OVER DIFFERENT ROWS
. % IS NOT SHOWN
.
D1 = mean(equ_diam)*scale;
pitch_1=mean(drowm)*scale;
ratio1=D1/pitch_1;


% SECOND METHOD: Calculates the distance between
%cross points between the
% hole (circle) and the line drawn across the chosen array of
% holes in different directions (as it is done manually)
rw1=[15,80,5];
[pitch(1),xk,yk]=cross_points(B,cent,rw1,scale);
D(1) = mean(equ_diam([25,38,51,67,80]))*scale;
.
. % FOR BREVITY REASONS AVERAGING OVER DIFFERENT ROWS
. % IS NOT SHOWN.
.
D2=mean(D);
pitch_2 = mean(pitch);
ratio2 = D2/pitch_2;

return;
```

Appendix B

Matlab code for the tapering rig control system implementation

This appendix contains the relevant bits of code, that I have written in Matlab, for the application that controls the feeding and drawing motors of the tapering system. Only parts of the code associated with the preprocessing of the diameter profile parameters are shown below. The full code is available in the laboratory for use.

The important variable in the code is Feedback_Closed. It determines if the feedback loop is closed (=1) or it is open (=0). Another important variable is SwitchFeed. If it is set to zero, it enables the speed profile in which feeding motor speed is kept constant and exit motor speed changes according to Equation 3.1 (shown in Figure 3.4.a). Otherwise, If variable SwitchFeed set to one, that enables the speed profile in which exit motor speed is kept constant and feeding motor speed decreases in relevance the chosen diameter profile, in accordance to Equation 3.1 (shown in Figure 3.4.b). Third important variable is MaxSpeedActive. If it is set to value of one, speed profile similar to Figure 3.4.c (it depends on the chosen taper profile) could be obtained.

```
% Natasha Vukovic, ORC Southampton, 01/04/2007
% script enables determination of the parameters needed for the tapering
% control system and calculation of the taper profile
linv_rotv = 9.1e-6;  % linear velocity 9.1um per rotation
pure_delay = 0.09;   % distance btw heater and the measurement head
dist_mh_exitm = 0.05;   % distance btw the measurement head and the exit motor
exit_motor_length =0.2; % the exit motor length
bad_fiber = 2e-3;    % to allow for fibre to be placed into the heater
Dfeed = 125e-6;      % Start diameter
vstart = 3000;       % feed motor start velocity [rpm]
v_inital_min = 60;   % velocity [rpm] at the beginning of tapering,
```

```
 %to avoid problems with slow movement
Dstart = Dfeed*sqrt(1-v_inital_min/vstart); % Desired exit diameter at the begin.
MaxSpeedActive = 0;  % (=1) or (=0)
SwitchFeed = 1;      % if (SwitchFeed=1) feed motor speed drops
Feedback_Closed = 1; % Feedback closed/open

ini_rat = Dstart/Dfeed;

%periodic taper profile
Diam_Dist_vect=[0.2, 0.2, ini_rat,ini_rat,0.2, 0.2,ini_rat;
                                0.1, 0.2,   0.3,  0.4,    0.5, 0.6, 0.7];

% Append initial segment of length pure_delay (no feedback on this segment)
Diam_Dist_vect = [ini_rat,ini_rat,Diam_Dist_vect(1,:);
                  0,pure_delay, Diam_Dist_vect(2,:)+pure_delay];

Diam_Dist_vect(1,:) = Dfeed*Diam_Dist_vect(1,:);

No_segm = size(Diam_Dist_vect,2)-1;

a_D = diff(Diam_Dist_vect(1,:))./diff(Diam_Dist_vect(2,:));
b_D = Diam_Dist_vect(1,1:end-1)-a_D.*Diam_Dist_vect(2,1:end-1);

Lend = Diam_Dist_vect(2,end); % taper length
 % total tapering length:
Lfinal = Lend+pure_delay+dist_mh_exitm+exit_motor_length;


%%...SOME PARTS OF THE CODE ARE NOT SHOWN

%NF filter used for filtering the control (exit velocity)
wnf = 2*pi/500;
% gamma and delta used to implement low pass filter
gamma = exp(-Ts*wnf);
delta = 1-gamma;
% alpha and beta used to implement PI controller
Ki = 2*pi/2000;
ll = 2;Kp = 1/ll;
alpha = exp(-Ki*ll*Ts);
beta =   1/ll;
```

```
%%...SOME PARTS OF THE CODE ARE NOT SHOWN
FirstSwitch = 0;
Ts = 0.5;
while(l2(ind_t)<Lfinal)
    ind_t = ind_t+1;
    l1(ind_t) = l1(ind_t-1)+Ts*vfeed_filt(ind_t-1)*linv_rotv/60;
    l2(ind_t) = l2(ind_t-1)+Ts*vfeed_filt(ind_t-1)*linv_rotv/60;
    if (l2(ind_t)<(Lend+pure_delay))
    % based on distance find which a_D and b_D to use
        ind_segment = min(No_segm,max(find(l2(ind_t)>Diam_Dist_vect(2,:))));
        Ddes(ind_t) = a_D(ind_segment)*min(Lend,max(0,(l2(ind_t))))+,...
         b_D(ind_segment);
        that_ratio = (Dfeed/Ddes(ind_t))^2;
        vfeed(ind_t) = vfeed(ind_t-1);
        vexit(ind_t) = vfeed(ind_t-1)*that_ratio;
if (MaxSpeedActive)
     if ((vexit(ind_t)-vfeed(ind_t))>MaxSpeedDif) % decrease vfeed
                vfeed(ind_t) = round((SpeedHeadRoom*MaxSpeedDif)/(that_ratio-1));
                vexit(ind_t) = vfeed(ind_t)*that_ratio;
                FirstSwitch = 1;
      elseif (FirstSwitch==1) && (vexit(ind_t)-vfeed(ind_t) <,...
       SpeedHeadRoom*MaxSpeedDif) % increase vfeed
                vfeed(ind_t) = min(vstart,round(abs((MaxSpeedDif)/(that_ratio-1))));
                vexit(ind_t) = vfeed(ind_t)*that_ratio;
      end
end
    if (SwitchFeed)
            vexit(ind_t) = vexit(ind_t-1);
            vfeed(ind_t) = vexit(ind_t)/that_ratio;
    else
        vexit(ind_t) = vexit_delay;
        vfeed(ind_t) = vfeed_delay;
        Ddes(ind_t) = Dfeed*sqrt(vfeed(ind_t)/vexit(ind_t));
   end
        vfeed_filt(ind_t) = vfeed(ind_t);
        vexit_filt(ind_t) = vexit(ind_t);

end
```

Appendix C

`Matlab` code for the simulation of parabolic pulse generation in tapered MOFs

This appendix contains part of the code that I have written in `Matlab`, which simulates parabolic pulse generation in tapered MOFs. This code was used to generate the results both in Chapter 4 and Chapter 5. Numerical solution of the NLSE is based on the symmetrized split step Fourier method, implemented in the function `sspropc` [53].

Firstly, in the program, previously calculated GVD, third order dispersion and nonlinearity coefficient are polynomially fitted to the number of pitch values, then used as the interpolation points to calculate the respective parameters versus taper length, using linear interpolation. The program supports three different taper profiles: linear pitch, linear GVD and hyperbolic GVD. Although during the simulation I have examined parabolic pulse generation in three different taper profiles, for the reason of ease of fabrication, I focused on the linear pitch profile. The propagation is observed for the input Gaussian pulse of various input FWHM and peak powers. The results are quantified using the misfit parameter, M^2, using function `fit_pulse_params`. This function governs a Nelder-Mead nonlinear optimization algorithm to ensure the best fit of the output pulse to the parabolic profile. In addition, for a number of steps of diameter changes, the results are saved in an array `AllParams`. This array enables contour plots representation of the minimum misfit parameter and corresponding taper length in function of pulse FWHM and peak power. Only some parts of the code are shown below for clarity.

```
% Natasha Vukovic, ORC Southampton 14/03/2007
% script shows parabolic pulse formation for normal dispersion MOF for
% linear change of pitch for different tapers (d_L=0.2; 0.3; 0.8)
```

```
% USES FUNCTIONS AND SCRIPTS:
% sspropc - free licence software that solve the NLSE using split step Fourier method
%u1=sspropc(u0,dt,dz,nchange,alpha,betap,gammap),
% where:
% u1- output optical field;
%u0 - input optical field, complex, slowly varying envelope of
%the optical field; dt - the time increment between adjacent
%points of the vector u0;
% dz - the
%step-size to use for propagation;
%nchange - the number of
%steps to take;
% alpha - the linear
%power attenuation coefficient;
% betap - polynomial expressing dispersion;
% gammap - nonlinear coefficient of the fibre
% fit_beta_gamma_L: this script fits beta and gamma as a
% polynomial function of L
% fit_pulse_params: wrapper for pulse parameter fitting
% [params,errval] = fit_pulse_params(t,pulse,pulse_choice,plot_opt)
% impulse_fit: to calculate fit error used in fminsearch
% error_sum = impulse_fit(params,pulse_choice,puls,t,t0,plot_opt)
% pulse_bandwidth: to calculate freq. domain pulse characteristics
% [bandw,maxA,AdB,f0,f1,dirty] = pulse_bandwidth(amplitude,f,drop_dB)
% Saves AllParams array with the following format:
% AllParams = [zmax,power, Pulse_width, distance,Bx/B0,misfit,P0,...
% nt - No of samples (power of 2)
% plot_divider - Every plot_divider distance step is plotted and
%pulse parameters fitted
% pulse_choice - parabolic fit;

% Distance parameters: tapering is performed from L0 at z=0 to L1 at z = L1.
%Changing Max_z changes the diameter gradient of tapering.
% No_z              -> Number of lengths in [Min_z,Max_z] to simulate
% lengths available  in z_array
% Min_z             -> minimum distance
% Max_z             -> maximum distance
% z_array           -> array of distances

% INITIAL PULSE POWERS
```

```
% No_power          -> No. of diff. init. powers in [Min_Power Max_Power] range
% Min_Power         -> minimum initial power
% Max_Power         -> maximum initial power
% powerv            -> vector of initial powers

% INITIAL PULSE WIDTHS
% No_width          -> No. of diff. init. pulse widths in [Min_Width, Max_Width] rang
% Min_Width         -> minimum initial width
% Max_Width         -> maximum initial width
% pwidths           -> vector of initial pulse widths

% No_change         -> Number of diameter changes


echo off;
clc;
clear all;
close all;

nt = 2^14;
cc=2.997924580105029e+08;

plot_divider = 1;   % plot and fit pulse/pulse params every plot_divider steps
plot_opt = 1;             % 1 enable fit plot, 0 disable fit plot
pulse_choice = 'parabolic';  % parabolic fit
taper_profile = 'linear_L';
%taper_profile = 'linear_beta';
%taper_profile = 'hyperbolic_beta';

z_array=[1.8];
No_z=length(z_array);

% Number of different initial powers
Min_Power = 2e3;        % [W]
Max_Power = 20e3;      % [W]
No_power=30;
powerv = linspace(Min_Power,Max_Power,No_power);% vector of initial powers

% Number of different initial pulse widths
Min_Width = 0.4e-12;                                %
Max_Width = 5e-12;
```

```
No_width=30;
pwidths = linspace(Min_Width,Max_Width,No_width);  % vector of initial pulse widths

% re-calculate beta and gamma as f(distance) No_change times
No_change = 100;

% polyfit beta and gamma as a function of L
%fit_beta_gamma_L;  %data for d_L=0.3 - taper B
fit_beta_gamma_LA;  %data for d_L=0.8 - taper A
%fit_beta_gamma_LC;  %data for d_L=0.2 - taper C
alpha=0; %fibre loss

AllParams = zeros(No_z*No_power*No_width*(No_change+1)/plot_divider,10);

curr_ind = 0;
start_time = clock;

for ind_z = 1:No_z,

    z = z_array(ind_z);
    dz=1e-5;                          % step size [m]
    z_nor=1;                          % normalized distance 1m
    nz=(z*z_nor)/dz;                  %total numer of steps
    nchange = round(nz/No_change);    % Number of steps per change
    nz = nchange*No_change;           % recalculated total number of steps


%main loop
    for ind_p=1:No_power,
        power=powerv(ind_p);

        for ind_width = 1:No_width,
            Pulse_width = pwidths(ind_width);

            if (Pulse_width<0.5e-12)   % short pulses expand more
                T = 350*Pulse_width;   % Time interval [ps]
            else
                T = 100*Pulse_width;
            end

            dt = T/nt;                % Sample time [s]
```

```
Fs = 1/dt;                % Sampling Frequency [Hz]
Fmax = Fs/2;              % Maximum Frequency without aliasing [Hz]
df = 1/T;                 % Frequency resolution [1/Hz]
t = ((-T/2):dt:(T/2)-dt)';
f = (-Fmax:df:Fmax-df)';  % frequency vector
w = 2*pi*[(0:nt/2-1),(-nt/2:-1)]'/(dt*nt);% angular freq. vector
lambda_wav=1.55e-6;
f_wav = cc/lambda_wav;
Omega = 2*pi*cc/lambda_wav;
lambda_w=2*pi*cc./fftshift(w+Omega);
[sort_lambda,ind_sorted] = sort(lambda_w);

u0 = gaussian(t,0,Pulse_width,power);

zv = (z/No_change)*(0:No_change);
u = zeros(length(t),length(zv));
u(:,1) = u0;

UX =dt*fftshift(fft(fftshift(u(:,1))));
UMAG    = abs(UX);
UPHASE  = angle(UX);

[B0,maxA,AdB,f0,f1,dirty] = pulse_bandwidth(UMAG,f,-3); % 3dB bandwidth
[params,misfit] = fit_pulse_params(t,u0,pulse_choice,plot_opt);
curr_ind = curr_ind +1;
AllParams(curr_ind,:) = [z,power,Pulse_width,0,1,dirty,misfit,params];

for ii = 1:No_change,
    Curr_distance = ii*nchange*dz;
    if isequal(taper_profile,'linear_L') %linear L
        L=lin_a*Curr_distance+lin_b;
        betap=[0,0,polyval(beta_pol,L,[],Mu_beta)];

    elseif isequal(taper_profile,'hyperbolic_beta')%hyperbolic beta2
        curr_beta2 = (fit_struc.max_beta2)/(1+Gamma_0*Curr_distance);
        L = polyval(L_beta_pol,curr_beta2,[],Mu_L_beta);
        betap = [0,0,curr_beta2,polyval(beta3_pol,L,[],Mu_beta3)];

    elseif isequal(taper_profile,'linear_beta')%linear  beta2
        curr_beta2 = lin_a*Curr_distance + lin_b;
        L = polyval(L_beta_pol,curr_beta2,[],Mu_L_beta);
```

```
                    betap = [0,0,curr_beta2,polyval(beta3_pol,L,[],Mu_beta3)];
                end

                gammap=polyval(gamma_pol,L,[],Mu_gamma);

                u(:,ii+1) = sspropc(u(:,ii),dt,dz,nchange,alpha,betap,gammap);

                % Every plot_divider distance will be plotted and fitted
                if (mod(ii,plot_divider)==0)

                  UX =dt*fftshift(fft(fftshift(u(:,ii+1))));
                  UMAG   = abs(UX);
                  UPHASE = angle(UX);
                  [Bx,maxA,AdB,f0,f1,dirty] = pulse_bandwidth(UMAG,f,-3); %3dB bandw.

[params,misfit] = fit_pulse_params(t,u(:,ii+1),pulse_choice,plot_opt);
curr_ind = curr_ind +1;
AllParams(curr_ind,:) = [z,power,Pulse_width,Curr_distance,Bx/B0,dirty,misfit,params]

%%...

        end %plot_divider
       end  % for initial pulse widths
    end % loop for power

end % loop for z

return;
```

Appendix D

`Matlab` code for the SC generation simulation based on RK4IP method

This appendix contains part of the `Matlab` code that I have written which solves GNLSE using RK4IP method, [54]. Model includes the following effects: fibre loss, higher order dispersion, Kerr effect, Raman delayed response, self-steepening and optical shock effect. The function used is `ssprope`, which is called using the following command:

```
function [u1,h,tol] = ssprope(u0,dt,dz,nz,alpha,betap,gamma,fr,w0,tol,maxiter)
```

The function returns the output pulse envelope u1, propagation step h and tolerance tol (they are adaptively changed). The input parameters are: u0 - starting field amplitude (vector), dt - time step, dz - propagation step size, nz - number of steps to take, i.e., ztotal = dz*nz, alpha - power loss coefficient, i.e. P=P0*exp(-alpha*z), betap - dispersion polynomial coefficients, [β_0 ... β_m], γ - nonlinearity coefficient, fr - the fractional contribution of the delayed Raman response to nonlinear polarization, w0 - parameter related to optical shock effect, maxiter - max number of iterations, tol - convergence tolerance.

For illustrative purposes, the SC evolution according to the numerical example in Ref. [52], (Fig. 3), is given. In accordance to Ref. [52], input parameters are: sech input pulse, pulse FWHM is T_0=50 fs, pulse peak power P_0=10 kW, shock effect τ_{shock}=0.56 fs, propagation distance z=0.15 m. The operating wavelength is 835 nm, nonlinearity coefficient γ=0.11 $W^{-1}m^{-1}$ and Taylor series expansion coefficients from β_2 to β_{10} are given in the code.

Figure D.1 presents graphs of the pulse temporal and spectral evolution. Figure D.2 shows pulse envelope at the input and after the propagation distance of 15 cm and the

normalized spectrum after 15 cm of propagation. Figure D.3 and Figure D.4 present pulse temporal and spectral evolution for selected propagation distances. The results show excellent agreement with the results after Ref. [52] and confirm the agreement between the results obtained using RK4IP method and SSFM (used in Ref. [52]) and so validate the accuracy of the simulation. This `Matlab code` was used for the simulation throughout Chapter 6 in this thesis.

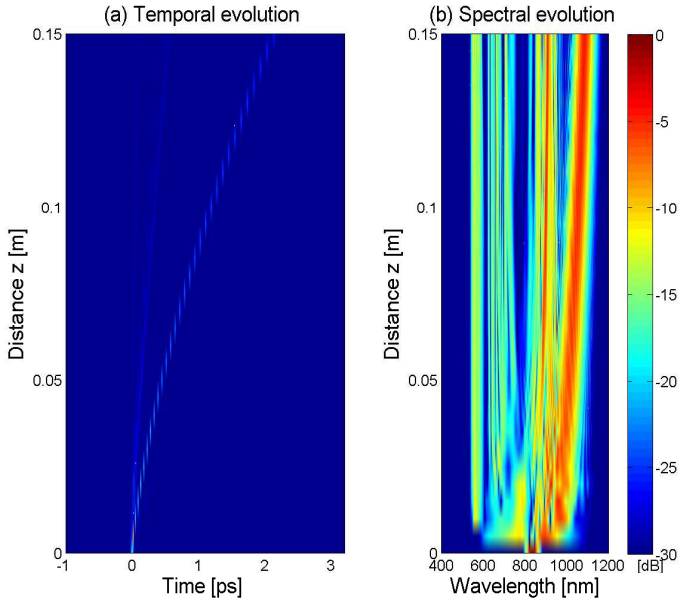

FIGURE D.1: Temporal and spectral evolution

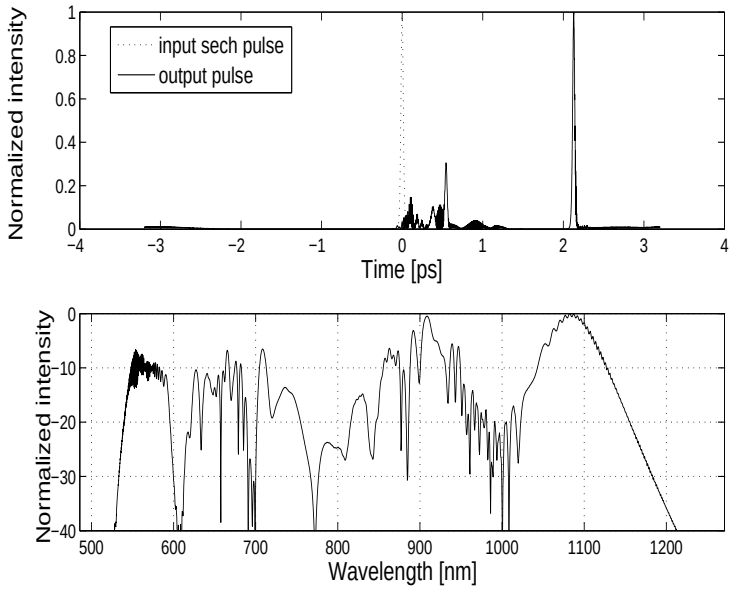

FIGURE D.2: Top: pulse envelope; Bottom: Normalized spectrum [dB] vs. wavelength

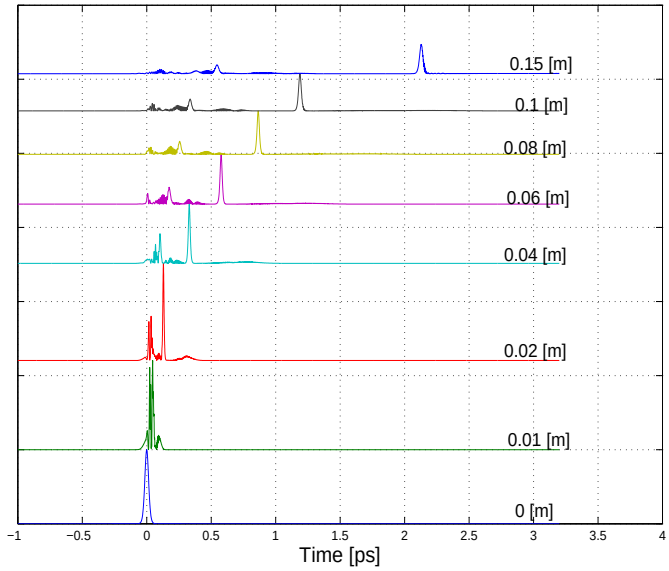

FIGURE D.3: Temporal evolution for selected propagation distances

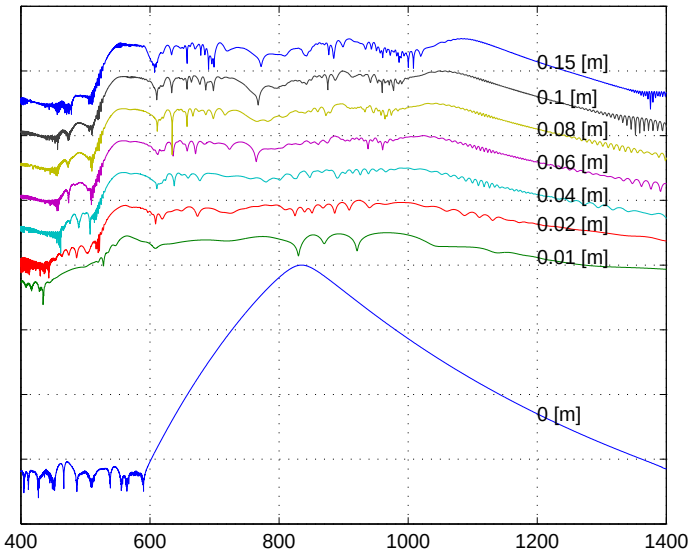

FIGURE D.4: Spectral evolution for selected propagation distances

```
% Natasha Vukovic, ORC Southampton 9/06/2008
%calculates SC using split step F. method for Dudley's example
%uses function ssprope.m (based on RK4IP method)
clc;
clear all;
close all;
```

```
% initial parameters
ps = 1e-12;
pss_per_m = ps.^[2:10]/1000;
%Taylor series expansion coefficients
beta=[0,0,[-11.83 8.1038e-2 -9.5205e-5 2.0737e-7 -5.3943e-10,...
1.3486e-12 -2.5495e-15 3.0524e-18 -1.714e-21].*pss_per_m];
gamma=0.11;
fr=0.18;
w0 = 1/(0.56e-15);
z = 0.15;  %propagation distance
nt = 2^14; % No of samples
Sstep = 0.005;
power = 10e3;
Pulse_width = 50*1e-15;
z_vect = [0:Sstep:z];
No_z = length(z_vect);
T =128*Pulse_width; %Time interval
dt = T/nt;           % Sample time [s]
Fs = 1/dt;          % Sampling Frequency [Hz]
Fmax = Fs/2;    % Maximum Frequency without aliasing [Hz]
df = 1/T;             % Frequency resolution [1/Hz]
t = ((-T/2):dt:(T/2)-dt)'; % time vector [s]
f = (-Fmax:df:Fmax-df)'; % frequency vector

w = 2*pi*[(0:nt/2-1),(-nt/2:-1)]'/(dt*nt); % angular frequency vector

cc = 2.997924580105029e+08;
lambda_wav=835e-9; %wavelength
Omega = 2*pi*cc/lambda_wav;
lambda_w=2*pi*cc./fftshift(w+Omega);
f_wav = cc/lambda_wav;
Omega = 2*pi*cc/lambda_wav;
lambda_w=2*pi*cc./fftshift(w+Omega);
[sort_lambda,ind_sorted] = sort(lambda_w);

%input pulse
u0=sechpulse(t,0,Pulse_width,power);
nz = round(z/Sstep);
u = zeros(length(u0),nz);
UX = zeros(length(u0),nz);
```

```
u(:,1) = u0;
UX(:,1) = fftshift(abs(dt*fft(u(:,1)/sqrt(2*pi)).^2));

%sorting wavelengths
[magnor,LambdaBw,LambdaArea,lambda_min,lambda_max,LambdaStd,LambdaMean] =,...
lambdadata(UX(:,1),lambda_w);

No_end_prop = nz;
StepTol = zeros(No_end_prop+1,2);
dz = Sstep;
tol = 0.05;

for ii = 1:No_end_prop,
StepTol(ii,:) = [dz,tol];

[u(:,ii+1),dz,tol] = ssprope(u(:,ii),dt,dz,round(Sstep/dz),0,beta,gamma,fr,w0,tol);

UX(:,ii+1) = fftshift(abs(dt*fft(u(:,ii+1)/sqrt(2*pi)).^2));
 Curr_distance = z_vect(ii)+Sstep;
 pulse=u(:,ii+1);
 [magnor,LambdaBw,LambdaArea,lambda_min,lambda_max,LambdaStd,LambdaMean] =,...
 lambdadata(UX(:,ii+1),lambda_w);

end
...
```

Chapter 8

References

[1] G. Agrawal, *Nonlinear Fiber Optics*, Fourth Edition, Academic Press, San Francisco, 2007.

[2] P. St. J. Russell, "Photonic-Crystal Fibers", *Journal of Lightwave Technology*, vol. 24, no. 12, pp. 4729-4749, 2006.

[3] P. St. J. Russell, "Photonic-Crystal Fibers", *Science*, vol. 299, no. 5605, pp. 358-362, 2003.

[4] T. A. Birks, P. J. Roberts, P. St, J. Russell, D. M. Atkin, T. J. Shepherd, "Full 2-D Photonic Bandgaps in Silica/Air Structures", *Electronics Letters*, vol. 31, pp. 1941 - 1943, 1995.

[5] J. C. Knight, T. A. Birks, P. St. J. Russell, D. M. Atkin, "All-silica Single-mode Optical Fiber with Photonic Crystal Cladding", *Optics Letters*, vol. 21, pp. 1547 - 1549, 1996.

[6] J. C. Knight, T. A. Birks, P. St. Russell, J. P. de Sandro, "Properties of Photonic Crystal Fibre and Effective Index Model", *Journal of Optical Society of America B*, vol. 15, pp. 748-752, 1998.

[7] H. Ebendorff - Heidepriem, K. Furusawa, D. R. Richardson, T. M. Monro, "Fundamentals and Applications of Silica and Non-Silica Holey Fibers", SPIE Proceedings 5350-06, Photonics West, San Jose, pp. 359, 2004.

[8] T. A. Birks, J. C. Knight, P. St. J. Russell, "Endlessly Single-Mode Photonic Crystal Fiber", *Optics Letters*, vol. 22, no. 13, pp. 961 - 963, 1997.

[9] J. C. Knight, J. Arriaga, T. A. Birks, A. Ortigosa-Blanch, W. J. Wadsworth, P. St. J. Russell, "Anomalous Dispersion in Photonic Crystal Fiber", *IEEE Photonics Technology Letters*, vol. 12, pp. 807-809, 2000.

[10] B. T. Kuhlmey, R. C. McPhedran, C. M. de Sterke, P. Robinson, G. Renversez, D. Maystre, "Microstructured Optical Fibers: Where's the Edge?", *Optics Express*, vol. 10, no. 22, pp. 1285-1290, 2002.

[11] D. J. Richardson, F. Poletti, J. Y. . Leong, X. Feng, H. Ebendorff Heidepreim, V. Finazzi, K. E. Frampton, S. Asimakis, R. C. Moore, J. C. Baggett, J. R. Hayes, M. N. Petrovich, M. L. Tse, R. Amezcua, J. H. V. Price, N. G. R. Broderick, P. Petropoulos, T. M. Monro, "Advances in Microstructured Fiber Technology", Conference Proceedings, WFOPC 2005, Palermo, 22-24 June 2005.

[12] N. G. R. Broderick, T. M. Monro, P. J. Bennett, D. J. Richardson, "Nonlinearity in Holey Optical Fibres: Measurement and Future Opportunities", *Optics Letters*, vol. 24, no. 20, pp. 1395 - 1397, 1999.

[13] N. G. R. Broderick, P. Bennett, D. Hewak, T. M. Monro, D. J. Richardson, Y. D. West, "Nonlinearity in Holey Optical Fibres", Conference Proceedings, LEOS 2000, Puerto Rico, 13-16 November 2000.

[14] A. Ortigosa-Blanch, J. C. Knight, W. J. Wadsworth, J. Arriaga, B. J. Mangan, T. A. Birks, P. St. J. Russell, "Highly Birefringent Photonic Crystal Fibers", *Optics Letters*, vol. 25, no. 18, pp. 1325 - 1327, 2000.

[15] J. C. Baggett, T. M. Monro, K. Furusawa, D. J. Richardson, "Comparative Study of Large-Mode Holey and Conventional Fibers", *Optics Letters*, vol. 265, no. 14, pp. 1045 - 1047, 2001.

[16] T. M. Monro, D. J. Richardson, N. G. R. Broderick, P. J. Bennett, "Holey Optical Fibers: an Efficient Modal Model", *Journal of Lightwave Technology*, vol. 17, pp. 1093-1102, 1999.

[17] J. C. Flanagan, R. Amezcua, F. Poletti, J. R. Hayes, N. G. R. Broderick, D. J. Richardson, "The Effect of Periodicity on the Defect Modes of Large Mode Area Microstructured Fibers", *Optics Express*, vol. 16, no. 23, pp. 18631-18645, 2008.

[18] V. Finazzi, T. M. Monro, D. J. Richardson, "Small Core Silica Holey Fibers: Nonlinearity and Confinement Loss Trade-off", *Journal of Optical Society of America B*, vol. 20, no. 7, pp. 1427-1436, 2003.

[19] K. Saitoh, M. Koshiba, "Unique Dispersion Properties of Photonic Crystal Fibers", Conference Proceedings, ICICS-PCM, 1A7.3, pp. 171-175, 2003.

[20] F. Zolla, G. Renversez, A. Nicolet, B. Kuhlmey, S. Guenneau and D. Felbacq, *Photonic Crystal Fibres*, London, Imperial College Press, 2005.

[21] J. C. Baggett, M. N. Petrovich, J. R. Hayes, V. Finazzi, F. Poletti, R. Amezcua, N. G. R. Broderick, D. J. Richardson, T. M. Monro, P. L. Salter, G. Proudley, E. J.

O'Driscoll, "Microstructured Fibers for High Power Applications", SPIE Proceedings, Nanophotonics for Communication: Materials and Devices II, Boston, 2005.

[22] F. Poletti, "Direct and Inverse Design of Microstructured Optical Fibres", *Ph.D. thesis*, 2007.

[23] G. Agrawal, *Fiber Optic Communications Systems*, Third Edition, John Wiley & Sons, 2002.

[24] G. Kakarantzas, L. Prill-Sempere, P. St. Russell, "Up-tapering of Optical Fibers Using a Conventional Flame Tapering Rig", Proceedings of Conference CLEO 2007.

[25] K. Imoto, M. Sumi, G. Toda and T. Suganuma, "Optical Fiber Drawing Method with Gas Flow Controlling System", *Journal of Lightwave Technology*, vol. 7, no. 1, pp. 115-121, 1989.

[26] U. C. Paek, "High-Speed High-Strength Fiber Drawing", *Journal of Lightwave Technology*, vol. LT-425, no. 8, pp. 1048-1059, 1986.

[27] U. C. Paek, "Laser Drawing of Optical Fibers", *Applied Optics*, vol. 13, no. 6, pp. 1383-1386, 1974.

[28] T. A. Birks, W. J. Wadsworth and P. St. J. Russell, "Supercontinuum Generation in Tapered Fibers", *Optics Letters*, vol. 25, no. 19, pp. 1415-1417, 2000.

[29] A. Kudlinski, A. K. George, J. C. Knight, J. C. Travers, A. B. Rulkov, S. V. Popov, J. R. Taylor, "Zero-dispersion Wavelength Decreasing Photonic Crystal Fiber for Ultraviolet-extended Supercontinuum Generation", *Optics Express*, vol. 14, no. 12, pp. 5715-5722, 2006.

[30] F. Gerome, K. Cook, A.K. George, W.J. Wadsworth, J.C. Knight, "Delivery of sub 100 fs Pulses through 8 m of Hollow Core Fiber using Soliton Compression", *Optics Express*, vol. 15, no. 12, pp. 7126 - 7131, 2007.

[31] F. Poletti, K. Furusawa, Z. Yussoff, P. Petropoulos, N. G. R. Broderick, T. M. Monro, D. J. Richardson, "Nonlinear Tapered Holey Fibers with High SBS Threshold and Controlled Dispersion", *Journal of Optical Society of America B*, Vol.24, No. 9, pp. 2185-2194, 2007.

[32] K. Furusawa, Z. Yusoff, F. Poletti, T. M. Monro, N. G. Broderick, D. J. Richardson, "Brillouin Characterization of Holey Optical Fibers", *Optics Letters*, vol. 31, no. 17, pp. 2541-2543, 2006.

[33] F. Poletti, K. Furusawa, Z. Yussoff, P. Petropoulos, N. G. R. Broderick, T. M. Monro, D. J. Richardson, "Brillouin Suppression through Longitudinal Structural Variation in High Nonlinearity Silica Holey Fibers", *OFC*, Anaheim, OWI10, 2006.

[34] J. Hu, B. S. Marks, C. Menyuk, "Pulse Compression Using a Tapered Microstructured Optical Fiber", *Optics Express*, vol. 14, no. 9, pp. 4026-4036, 2006.

[35] M. L. V. Tse, P. Horak, J. H. V. Price, F. Poletti, F. He, D. J. Richardson, "Pulse Compression at 1.06 μm in Dispersion-decreasing Holey Fibers", *Optics Letters*, vol. 31, no. 23, pp. 3504-3506, 2006.

[36] S. V. Chernikov, P. V. Mamyshev, "Femtosecond Soliton Propagation in Fibers with Slowly Decreasing Dispersion", *Journal of Optical Society of America B*, vol. 8, no. 8, pp. 1633-1641, 1991.

[37] J. C. Travers, B. A. Cumberland, A. B. Rulkov, S. V. Popov, J. R. Taylor, "Pulse Compression in Dispersion Decreasing Photonic Crystal Fiber", Proceedings of CLEO 2007.

[38] M.G. Welch, K. Cook, R.A. Correa, F. Gerome, W.J. Wadsworth, A.V. Gorbach, D.V. Skryabin, J.C. Knight, "Solitons in Hollow Core Photonic Crystal Fiber: Engineering Nonlinearity and Compressing Pulses", *Journal of Lightwave Technology*, vol. 27, no. 11, pp. 1644-1652, 2009.

[39] G. Brambilla, F. Koizumi, V. Finazzi, J. Mills, D. Richardson, "Long-Wavelength Supercontinuum-Generation in Tapered Bismuth Silicate Fibres", *CLEO/IQEC-Pacific Rim Tokyo*, 2005, QWL4-3.

[40] P. Falk, M. H. Frosz, O. Bang, "Supercontinuum generation in a Photonic Crystal Fiber with Two Zero-dispersion Wavelengths Tapered to Normal Dispersion at all Wavelengths", *Optics Express*, vol. 13, no. 19, pp. 7535-7540, 2005.

[41] W. J. Wadsworth, A. Ortigosa-Blanch, J. C. Knight, T. A. Birks, T. P. M. Man, P. St. J. Russell, "Supercontinuum Generation in Photonic Crystal Fibers and Optical Fiber Tapers: a Novel Light Source", *Journal of Optical Society of America B*, vol. 19, pp. 2148-2155, 2002.

[42] X. Liu, C. Xu, W. Knox, J. Chandalia, B. Eggleton, S. Kosinski, R. Windler, "Soliton Self-frequency Shift in a Short Tapered Air-silica Microstructure Fiber", *Optics Letters*, Vol. 26, no 6, pp. 358-360, 2001.

[43] T. A. Birks, G. Kakarantzas and P. St. J. Russell, "All - fibre Devices Based on Tapered Fibres", Proceedings of the OFC, ThK2, 2004.

[44] J. C. Baggett, T. M. Monro, J. R. Hayes, V. Finazzi, D. J. Richardson, "Improving Bending Losses in Holey Fibres", Conference Proceedings, OFC 2005, Anaheim, March 2005.

[45] J. C. Baggett, T. M. Monro, K. Furusawa, D. J. Richardson, "Understanding Bending Losses in Holey Optical Fibers", *Optics Communications*, Vol. 227, pp. 317-335, 2003.

[46] A. Hasegawa, F. Tappert, "Transmission of Stationary Nonlinear Optical Pulses in Dispersive Dielectric Fibers. I. Anomalous dispersion", *Applied Physics Letters*, vol. 23, no. 3, pp. 142-172, 1973.

[47] A. Hasegawa, F. Tappert, "Transmission of Stationary Nonlinear Optical Pulses in Dispersive Dielectric Fibers. II. Normal dispersion", *Applied Physics Letters*, vol. 23, no. 4, pp. 171-172, 1973.

[48] P. Dumais, F. Gonthier, S. Lacroix, J. Bures, A. Villeneuve, P. G. J. Wigley, G. I. Stegeman, "Enhanced Self-phase Modulation in tapered Fibers", *Optics Letters*, vol. 18, no. 23, pp. 1996-1998, 1993.

[49] R. H. Stolen, J. P. Gordon, W. J. Tomlinson, H. A. Haus, "Raman Response Function of Silica-core Fibers", *Journal of Optical Society of America B*, vol. 6, no. 6, pp. 1159-1166, 1989.

[50] K. J. Blow and D. Wood, "Theoretical Description of Transient Stimulated Raman Scattering in Optical Fibers", *IEEE Journal of Quantum Electronics*, Vol. 25, pp. 2665–2673, 1989.

[51] C. Hile, W. Kath, "Numerical Solution of Maxwell's Equations for Nonlinear-optical Pulse Propagation", *Journal of Optical Society of America B*, vol. 13, no. 6, pp. 1135-1145, 1996.

[52] J. M. Dudley, G. Genty, S. Coen, "Supercontinuum Generation in Photonic Crystal Fiber," *Review of Modern Physics*, Vol. 78, pp. 1135-1184, 2006.

[53] T. E. Murphy, simulation software SSPROP, University of Maryland, *www.photonics.umd.edu/software/ssprop*.

[54] J. Hult, "A Fourth-order Runge-Kutta in the Interaction Picture Method for Simulating Supercontinuum Generation in Optical Fibers", *Journal of Lightwave Technology*, Vol. 25, pp. 3770–3775, 2007.

[55] P. L. Francois, "Nonlinear Propagation of Ultrashort Pulses in Optical Fibers: Total Field Formulation in the Frequency Domain", *Journal of Optical Society of America B*, vol. 8, no. 2, pp. 276-293, 1996.

[56] I. Cristiani, R. Tediosi, L. Tartara and V. Degiorgio, "Dispersive Wave Generation by Solitons in Microstructured Optical Fibers", *Optics Express*, vol. 78, 124-135 (2003).

[57] B. M. Caradoc-Davies, "Vortex Dynamics in Bose-Einstein Condensates", PhD thesis, 2000.

[58] R. Trebino, *Frequency-Resolved Optical Gating: The Measurement of Ultrashort Laser Pulses*, Kluwer Academic Publishers, Boston, Ma., 2000.

[59] M. A. F. Roelens, "Precise Intensity and Phase Characterisation of Optical Telecommunication Signals", *Ph.D. thesis*, 2006.

[60] C. Dorrer, I. Kang, "Simultaneous Temporal Characterization of Telecommunication Optical Pulses and Modulators by use of Spectrograms", *Optics Letters* Vol. 27, 1315-1317 (2002).

[61] D. J. Richardson, R. P. Chamberlin, L. Dong and D. N. Payne, "Demonstration of 100GHz Dark Soliton Generation and Propagation using a Dispersion Decreasing Fibre", *Electronics Letters*, vol. 30, pp. 1326−1327, 1994.

[62] D. J. Richardson, R. P. Chamberlin, L. Dong, D. N. Payne, "High Quality Soliton Loss Compensation in 38 km Dispersion-decreasing Fibre", *Electronics Letters*, vol. 31, no. 19, pp. 1681-1682, 1995.

[63] E. C. Magi, P. Steinvurzel and B. J. Eggleton, "Tapered Photonic Crystal Fibers", *Optics Express*, vol. 12, no. 5, pp. 776-784, 2004.

[64] E. C. Magi, P. Steinvurzel, B. J. Eggleton, "Transverse Characterization of Tapered Photonic Crystal Fibers", *Journal Applied Physics*, vol. 96, no. 7, pp. 3976-3982, 2004.

[65] P. Domachuk, A. Chapman, E. Magi, M. J. Steel, H. C. Nguyen, B. J. Eggleton, "Transverse Characterization of High Air-fill Fraction Tapered Photonic Crystal Fiber", *Applied Optics*, vol. 44, no. 19, pp. 3885-3892, 2005.

[66] D. Donlagic, "In-line higher order mode filters based on long highly uniform fiber tapers", *Journal of Lightwave Technology*, vol. 24, pp. 3532-3539, 2006.

[67] J. K. Chandalia, B. J. Eggleton, R. S. Windeler, S. G. Kosinski, X. Liu, C. Xu, "Adiabatic Coupling in Tapered Air-silica Microstructured Optical Fiber", *IEEE Photonics Technology Letters*, Vol. 13, pp. 52-54, 2001.

[68] K. Imoto, M. Sumi, G. Toda and T. Suganuma, "Optical Fiber Drawing Method with Gas Flow Controlling System", *Journal of Lightwave Technology*, vol. 7, no. 1, pp. 115−121, 1989.

[69] J. Hu, B. S. Marks and C. Menyuk, "Pulse Compression using a Tapered Microstructured Optical Fiber", *Optics Express*, vol. 14, pp. 4026−4036, 2006.

[70] W. J. Tomlinson, R. H. Stolen, C. V. Shank, "Compression of Optical Pulses Chirped by Self-phase Modulation in Fibres", *Journal of Optical Society of America B*, vol. 1, no. 2, pp. 139-149, 1984.

[71] J. C. Travers, J. M. Stone, A. B. Rulkov, B. A. Cumberland, A. K. George, S. V. Popov, J. C. Knight, J. R. Taylor, "Optical Pulse Compression in Dispersion Decreasing Photonic Crystal Fiber", *Optics Express*, vol. 15, no. 20, pp. 13203-13211, 2007.

[72] M. L. V. Tse, P. Horak, F. Poletti, D. J. Richardson, "Designing Tapered Holey Fibers for Soliton Compression", *Journal of Quantum Electronics*, vol. 44, pp. 192-198, 2008.

[73] D. G. Ouzounov, C. J. Hensley, A. L. Gaeta, N. Venkateraman, M. T. Gallagher, K. W. Koch, "Soliton Pulse Compression in Photonic Band-Gap Fibers", *Optics Express*, vol. 13, no. 16, pp. 6153-6159, 2005.

[74] B. Kibler, R. Fischer, P.-A. Lacourt, F. Courvoisier, R. Ferriere, L. Larger, D. N. Neshev, J. M. Dudley, "Optimised One-step Compression of Femtosecond Fibre Laser Soliton Pulses around 1550 nm to below 30 fs in Highly Nonlinear Fibre", *Electronics Letters*, vol. 43, no. 17, 2007.

[75] C. Finot, B. Barviau, G. Millot, A. Guryanov, A. Sysoliatin and S. Wabnitz, "Parabolic Pulse Generation with Active or Passive Dispersion Decreasing Optical Fibres", *Optics Express*, vol. 15, no. 24, pp. 15824-15835, 2007.

[76] A. Latkin, A. Sysoliatin, P. Harper, J. Harrison, A. Plocky, S. Turitsyn, "Optical Spectral Broadening and Parabolic Pulse Generation Using Tapered Fibre with Normal Dispersion", Proceedings of ECOC, 2007.

[77] N. Vukovic, N.G.R. Broderick, F. Poletti", "Parabolic Pulse Generation using Tapered Microstructured Optical Fibres", *Advances in Nonlinear Optics*, ID 480362, pp. 1-10, 2008.

[78] W. J. Wadsworth, N. Joly, J. C. Knight, T. A. Birks, F. Biancalena, P. St. J. Russell, "Supercontinuum and Four-wave Mixing with Q-switched Pulses in Endlessly Single-mode Photonic Crystal Fibres", *Optics Express*, vol. 12, no. 2, pp. 299 - 309, 2004.

[79] P. Falk, M. H. Frosz, O. Bang, "Supercontinuum Generation in a Photonic Crystal Fiber with Two Zero-Dispersion Wavelengths Tapered to Normal Dispersion at all Wavelengths", *Optics Express*, vol. 13, no. 19, pp. 7535-7540, 2005.

[80] J. K. Ranka, R. S. Windeler, A. J. Stentz, "Visible Continuum Generation in Air-Silica Microstructure Optical Fibres with Anomalous Dispersion at 800 nm", *Optics Express*, vol. 25, pp. 25-27, 2000.

[81] F. P. Payne, C. D. Hussey, "Fibre-taper Devices", *Microelectronics&Photonics*, pp. 845-851, 1987.

[82] T. A. Birks, Y. W. Li, "The Shape of Fiber Tapers", *Journal of Lightwave Technology*, vol. 10, no. 4, pp. 432-438, 1992.

[83] R. P. Kenny, T. A. Birks, K. P. Oakley, "Control of Optical Fiber Taper Shape", *Electronics Letters*, vol. 27, no. 18, pp. 1654-1656, 1991.

[84] V. A. Bogatyrev et al., "The Single Mode Fiber with Chromatic Dispersion Varying Along the Length", *Journal of Lightwave Technology*, vol. 9, pp. 561-566, 1991.

[85] A. Mulpur, C. Thompson, "Nonlinear Control of Optical Fiber Diameter Variations", *IEEE Transactions of Control Systems Technology*, Vol. 4, No.2, March 1996, pp. 152-162.

[86] L. Tong, J. Lou, Z. Ye, G. Svacha, E. Mazur, "Self-modulated Taper Drawing of Silica Nanowires", *Nanotechnology*, vol. 16, pp.1445-1448, 2005.

[87] G. E. Town, J. T. Lizier, "Tapered Holey Fibers for Spot-size and Numerical aperture Conversion", *Optics Letters*, vol. 26, no. 14, pp. 1042-1044, 2001.

[88] H. C. Nguyen et al., "Leakage of the Fundamental Mode in Photonic Crystal Fiber Tapers", *Optics Letters*, vol. 30, no. 10, pp. 1123 - 1125, 2005.

[89] D. H. Smithgall and R. E. Frazee, "Characterization of the Preform Stretching Process", *Journal of Lightwave Technology*, vol. LT−5, no. 12, pp. 1755−1762, 1987.

[90] F. T. Geyling, "Basic Fluid-Dynamic Considerations in the Drawing of Optical Fibers", *The Bell System Technical Journal*, Vol. 55, no. 8, pp 1011-1056, 1976.

[91] S. Xue, M. van Eijkelenborg, G. Barton and P. Hambley, "Theoretical, Numerical and Experimental Analysis of Optical Fiber Tapering", *Journal of Lightwave Technology*, vol. 25, no. 5, pp. 1169-1176, 2007.

[92] R. H. Doremus, "Viscosity of Silica", *Journal Applied Physics*, vol. 92, no. 12, pp. 7619-7629, 2002.

[93] D. Anderson, M. Desaix, M. Lisak, M. L. Quiroga-Teixeiro, "Wave Breaking in Nonlinear Optical Fibers", *Journal of the Optical Society of America B*, vol. 9, no. 8, pp. 1358-1361, 1992.

[94] D. Anderson, M. Desaix, M. Karlson, M. Lisak and M. L. Quiroga-Teixeiro, "Wave-breaking-free Pulses in Nonlinear-Optical Fibers", *Journal of Optical Society of America B*, vol. 10, no. 7, pp. 1185-1190, 1993.

[95] F. Parmigiani, P. Petropoulos, M. Ibsen, D. J. Richardson, "Pulse Retiming Based on XPM Using Parabolic Pulses Formed in a Fiber Bragg Grating", *EEE Photonics Technilogy Letters*, vol. 18, No. 7, pp. 829-831, 2006.

[96] M. Nakazawa, T. Hirooka, F. Futami, S. Watanabe, "Ideal Distortion-Free Transmission Using Optical Fourier transformation and Fourier Transform-Limited Optical Pulses", *IEEE Photonics Technology Letters*, vol. 16, no. 4, pp. 1059-1061, 2004.

[97] F. Parmigiani, C. Finot, K. Mukasa, M. Ibsen, M. A. F. Roelens, P. Petropoulos and D. Richardson, "Ultra-flat SPM-broadened Spectra in a Highly Nonlinear Fiber Using

Parabolic Pulses Formed in a Fiber Bragg Grating", *Optics Express*, vol. 14, no. 17, pp. 7617-7622, 2006.

[98] V. I. Kruglov, A. C. Peacock, J. D. Harvey, "Exact Solutions of the Generalized Nonlinear Schrodinger Equation with Distributed Coefficients", *Physical review*, vol. 71, pp. 056619-1-056619-19, 2005.

[99] V. I. Kruglov, A. C. Peacock and J. D. Harvey, "Self-similar Propagation of Parabolic Pulses in Normal-dispersion Fiber Amplifiers", *Journal of Optical Society of America B*, vol. 19, no. 3, pp. 461-469, 2002.

[100] M. E. Fermann, V. I. Kruglov, B. C. Thomsen, J. M. Dudley, J. D. Harvey, "Self-Similar Propagation and Amplification of Parabolic Pulses in Optical Fibers", *Physics Rev. Letters*, vol. 84, no. 26, pp. 6010 - 6013, 2005.

[101] C. Finot, F. Parmigiani, P. Petropoulos, D. J. Richardson, "Parabolic Pulse Evolution in Normally Dispersive Fiber Amplifiers Preceding the Similariton Formation Regime", *Optics Express*, vol. 14, no. 8, pp. 3161-3170, 2006.

[102] F. O. Ilday, J. R. Buckley, W. G. Clark and F. W. Wise, "Self-similar Evolution of Parabolic Pulses in a Laser", *Physics Review Letters*, vol. 92, pp. 2734-2736, 2004.

[103] A. Ruehl, O. Prochnow, M. Schultz, D. Wandt, D. Kracht, "Impact of Third-Order Dispersion on the Generation of Wave-breaking Free Pulses in Ultrafast Fiber Lasers", *Optics Letters*, vol. 32, no. 17, pp. 2590-2592, 2007.

[104] J. M. Dudley, C. Finot, G. Millot, D. J. Richardson, "Parabolic Pulse Generation with Active or Passive Dispersion Decreasing Optical Fibers", *Optics Express*, vol. 15, no. 24, pp. 15824-15835, 2007.

[105] T. Hirooka, M. Nakazawa, "Parabolic Pulse Generation by Use of a Dispersion-decreasing Fiber with Normal Group-velocity Dispersion", *Optics Letters*, vol. 29, no. 5, pp. 498-500, 2004.

[106] D. Krcmarik, R. Slavik, Y. Park, J. Azana, "Nonlinear Pulse Compression of Parabolic-like Pulses Synthesized with a Long Period Fiber Grating Filter", *Optics Express*, vol. 17, pp. 7074-7087, 2009.

[107] C. Finot, L. Provost, P. Petropoulos, D. Richardson, "Parabolic Pulse Generation Through Passive Nonlinear Pulse Reshaping in a Normally Dispersive Two Segment Fiber Device", *Optics Express*, vol. 15, no. 3, pp. 852-864, 2006.

[108] B. Kibler, C. Billet, P.-A. Lacourt, R. Ferriere, L. Larger, J. M. Dudley, "Parabolic Pulse Generation in Comb-like Profiled Dispersion Decreasing Fibre", *Electronics Letters*, vol. 42, no. 17, 2006.

[109] A. Latkin, S. Tuitsyn, A. Sysoliatin, "Theory of Parabolic Pulse Generation in Tapered Fiber", *Optics Letters*, vol. 32, no. 4, pp. 331-333, 2007.

[110] T. P. White, R. C. McPhedran, C. M. de Sterke, L. C. Botten, M. J. Steel, "Confinement Loss in Microstructured Optical Fibers", *Optics Letters*, vol. 26, no. 21, pp. 1660-1662, 2001.

[111] P. R. McIsaac, "Symmetry-induced Modal Characteristics of Uniform Waveguides. I. Summary of Results", *IEEE Transactions of Microwave Theory and Technology*, vol. 23, pp. 421-429, 1975.

[112] M. J. Steel, T. P. White, C. M. de Sterke, R. C. McPhedran, "Symmetry and Degeneracy in Microstructured Optical Fibers", *Optics Letters*, vol. 26, no. 8, pp. 488-490, 2001.

[113] C. Finot, S. Pitois, G. Millot, C. Billet, J. M. Dudley, "Numerical and Experimental Study of Parabolic Pulses Generated via Raman Amplification in Standard Optical Fibers", *IEEE Journal of Selected Topics in Quantum Electronics*, Vol. 10, pp. 1211-1218, 2004.

[114] A. Plocky, A. A. Sysoliatin, A. I. Latkin, V. F. Khopin, P. Harper, J. Harrison and S. K. Turitsyn, "Experiments on the Generation of Parabolic Pulses in Waveguides with Length-varying Normal Chromatic Dispersion", *JETP Letters*, Vol. 85, pp. 319-322, 2007.

[115] A. Plotski, A. Sysoliatin, M. Y. Salganskii, P. Harper, J. Harrison, S. K. Turitsyn, A. I. Latkin, "High Power Parabolic Pulse Generation in Dispersion Decreasing Tapered Fibre", Proceedings of CLEO Europe 2009, Proceedings OTuJ2, 2009.

[116] N. Vukovic, N. Broderick, M. Petrovich, G. Brambilla, "Novel Method for the Fabrication of Long Optical Tapers", *IEEE Photonics Technology Letters*, Vol. 20, pp. 1264-1266, 2008.

[117] R. R. Alfano and S. L. Shapiro, "Emission in the Region 4000 to 7000 $\AA$ via Four-Photon Coupling in Glass", *Physics Review Letters*, vol. 24, pp. 584-587, 1970.

[118] N. G. Bondarenko, I. V. Eremina, V. I. Talanov, "Broadening of Spectrum in Self-focusing of Light in Crystals", *JETP Letters*, vol. 12, pp. 85-87, 1970.

[119] W. Werncke, A. Lau, M. Pfeiffer, K. Lenz, H.-J. Wegmann, C. D. Thuy, "An Anomalous Frequency Broadening in Water", *Optics Communications*, vol. 4, pp. 413-415, 1972.

[120] A. L. Gaeta, "Nonlinear Propagation and Continuum Generation in Microstructured Optical Fibers", *Optics Letters*, vol. 27, pp. 924-926, 2002.

[121] S. Coen, A. H. L. Chau, R. Leonhardt, J. D. Harvey, J. C. Knight, W. J. Wadsworth, P. St. J. Russell, "White-light Supercontinuum with 60 ps Pump Pulses in a Photonic Crystal Fiber", *Optics Letters*, vol. 26, pp. 1356-1358, 2001.

[122] G. Genty, S. Coen, J. M. Dudley, "Fiber Supercontinuum Sources", *Journal of Optical Society of America B*, vol. 24, no. 8, pp. 1771-1785, 2007.

[123] J. C. Travers, A. B. Rulkov, B. A. Cumberland, S. Popov, J. R. Taylor, Non-linear Applications of Microstructured Optical Fibres", *Opt. Quantum Electronics*, vol. 39, pp. 963-974, 2007.

[124] A. Ortigosa-Blanch, J. C. Knight, P. St. J. Russell, "Pulse Breaking and Supercontinuum Generation with 200-fs Pump Pulses in Photonic Crystal Fibers", *Journal of Optical Society of America B*, vol. 19, no. 11, pp. 2567-2572, 2002.

[125] J. M. Dudley, S. Coen, "Numerical Simulations and Coherence Properties of Supercontinuum Generation in Photonic Crystal and Tapered Optical Fibers", *IEEE Journal of Selected Topics in Quantum Electronics*, vol. 8, pp. 651-659, 2002.

[126] M. L. V. Tse, P. Horak, F. Poletti, N. G. R. Broderick, J. H. V. Price, J. R. Hayes, D. J. Richardson, "Supercontinuum Generation at 1.06μm in Holey Fibers with Dispersion Flattened Profiles", *Optics Express*, vol. 14, pp. 4445-4451, 2006.

[127] A. I. Gaeta, "Nonlinear Propagation and Continuum Generation in Microstructured Optical Fibers", *Optics Letters*, vol. 27, pp. 924-926, 2002.

[128] J. M. Dudley, L. Provino, N. Grossard, H. Maillotte, R. S. Windeler, B. J. Eggleton, S. Coen, "Supercontinuum Generation in Air-Silica Microstructured Fibers with Nanosecond and Femtosecond Pulse Pumping", *Journal of Optical Society of America B*, vol. 19, pp. 765-771, 2002.

[129] T. Schreiber, T. V. Anderson, D. Schimpf, J. Limpert, A. Tunnermann, "Supercontinuum Generation by Femtosecond Single and Dual Wavelength Pumping in Photonic Crystal Fibers with Two Zero Dispersion Wavelengths", *Optics Express*, vol. 13, pp. 9556-9569, 2006.

[130] A.V. Husakou, J. Herrmann, "Supercontinuum Generation of Higher-order Solitons by Fission in Photonic Crystal Fibers", *Physics Review Letters*, vol. 87, no. 203901, 2001.

[131] A. V. Husakou, J. Herrmann, "Supercontinuum Generation, Four-Wave Mixing, and Fission of Higher-order Solitons in Photonic-Crystal Fibers", *Journal of Optical Society of America B*, vol. 19, no. 9. pp. 2171-2182, 2002.

[132] S. Coen, A. H. L. Chau, R. Leonhardt, J. Harvey, J. C. Knight, W. J. Wadsworth, P. St. J. Russell, Supercontinuum Generation by Stimulated Raman Scattering and

Parametric Four-Wave Mixing in Photonic Crystal Fibers", *Journal of Optical Society of America B*, vol. 19, pp. 753-763, 2002.

[133] G. Chang, T. B. Norris, H. G. Winful, "Optimization of Supercontinuum Generation in Photonic Crystal Fibers for Pulse Compression", *Optics Letters*, vol. 28, pp. 546-548, 2003.

[134] K. M. Hilligsoe, T. V. Andersen, H. N. Paulsen, C. K. Nielsen, K. Molmer, S. Keiding, R. Kristiansen, K. P. Hansen, J. J. Larsen, Supercontinuum Generation in a Photonic Crystal Fiber with Two Zero Dispersion Wavelengths", *Optics Express*, vol. 12, pp. 1045-1054, 2004.

[135] W. J. Wadsworth, N. Joly, J. C. Knight, T. A. Birks, F. Biancalana P. St. J. Russell, "Supercontinuum and Four-Wave Mixing with Q-switched Pulses in Endlessly Single-Mode Photonic Crystal Fiber", *Optics Express*, vol. 12, pp. 299-308, 2004.

[136] G. Genty, S. Coen, P.-A. Lacourt, B. Kibler, J. M. Dudley, "Highly Coherent Supercontinuum Generation in Dispersion Increasing Fibers", *Nonlinear Photonics* OSA Tech. Digest, NThC2, 2007.

[137] K. Mori, H. Takara, S. Kawanishi, Analysis and Design of Supercontinuum Pulse Generation in a Single-Mode Optical Fiber", *Journal of Optical Society of America B*, vol. 18, pp. 1780-1792, 2001.

[138] J. M. Dudley, G. Genty, B. Eggleton, "Harnessing and Control of Optical Rogue Waves in Supercontinuum Generation", *Optics Express*, vol. 16, no. 6, pp. 3644-3651, 2008.

[139] D. Mogilevtsev, T. A. Birks, P. St. Russell, "Group Velocity Dispersion in Photonic Crystal Fibers", *Optics Letters*, vol. 23, pp. 1662-1664, 1998.

[140] W. J. Wadsworth, A. Witkowska, S. G. Leon-Saval, T. A. Birks, "Hole Inflation and Tapering of Stock Photonic Crystal Fibres", *Optics Express*, vol. 13, no. 17, pp. 6541-6549, 2005.

[141] A. Witkowska, "Post-processing of Photonic Crystal Fibres and Standard Fibres", PhD thesis, 2009.

List of Publications

Jounal papers

N. Vukovic, N. G. R. Broderick, M. N. Petrovich, G. Brambilla, "Novel method for the fabrication of long optical tapers", *IEEE Photonics Technology Letters*, vol. 20, no. 14, pp. 1264-1266, 2008.

N. Vukovic, N. G. R. Broderick, F. Poletti, "Parabolic pulse generation using tapered microstructured optical fibres", *Advances in Nonlinear Optics*, ID 480362, pp. 1-10, 2008.

Conference papers

N. Vukovic, F. Parmigiani, A. Camerlingo, M. N. Petrovich, P. Petropoulos, N. G. R. Broderick, "Experimental investigation of a parabolic pulse generation using tapered microstructured optical fibres", accepted for *SPIE Photonics Europe 2010*, Brussels, 12-16 Apr 2010.

N. G. R. Broderick, N. T. Vukovic, G. Brambilla, P. Horak, D. J. Richardson, F. Poletti, "Fun things to do with fibre tapers", submitted for *ACOFT 2009*, Adelaide, 29 Nov-3 Dec 2009 (Invited).

N. Vukovic, N. G. R. Broderick, "Improved flatness of a supercontinuum at 1.55 μm in tapered microstructured optical fibres", *CLEO Europe - IQEC 2009*, 2009.

N. Vukovic, N. G. R. Broderick, M. N. Petrovich, G. Brambilla, "Fabrication of metre-long fibre tapers", *CLEO/QELS 2008*, San Jose, 4-9 May 2008.

N. Vukovic, N. G. R. Broderick, "Parabolic pulse formation in tapered microstructured optical fibres", *TELSIKS 2007*, Nis, 26-28 Sep 2007.